Icy Dust Grains in the Interstellar Medium:

Their Properties and Impact

Alexander Rosu-Finsen

Submitted for the degree of Doctor of Philosophy

Heriot-Watt University

School of Engineering and Physical Sciences

October 2016

Abstract

The behaviour of atoms and molecules on interstellar dust grain analogue surfaces has been probed with surface science techniques such as reflection-absorption infrared spectroscopy (RAIRS) and temperature programmed desorption (TPD). Chemical systems under investigation include O atoms, O_2, CO, H_2O and N_2O as deposited either on a silica (SiO_2) surface representative of an interstellar dust grain or on H_2O surfaces.

As H_2O is the dominant solid state chemical species in the interstellar medium (ISM) preliminary experiments have been conducted to investigate one of its formation pathways. Such experiments involved bombarding SiO_2 or H_2O surfaces with O atoms, producing O_2 and O_3 molecules as determined by RAIRS and TPD.

During the initial stages of H_2O growth on dust grains in the ISM, only small quantities will be found in the solid state. The de-wetting behaviour of such quantities was investigated by directly dosing H_2O onto the SiO_2 surface and observing the νOH vibrational band with time and temperature. Through such experiments, H_2O has been observed to de-wet even at cryogenic temperatures of 17 K with an activation energy of about 2 kJ mol^{-1}. The effect of this in the ISM is that bare dust grain surfaces will be left exposed for other molecules, such as CO, to interact with. Such interactions may be stronger than those of the molecules directly interacting with a water surface, meaning molecules will reside in the solid state for longer times.

As icy mantles develop throughout the lifetime of a molecular cloud, adsorbed CO becomes a large part of the icy mantle. Multilayers of CO were investigated and shown to exhibit a bulk potential. This charge is due to a spontaneous electric (spontelectric) field arising as certain dipolar molecules align in the solid state. To investigate the spontelectric effect in CO, N_2O was first examined and shows a correlation between IR features and the direct measurement of the spontelectric potential of N_2O. Such a link was found through the temperature dependent shifts in the LO-TO splitting of the N_2O. CO exhibits the same temperature dependence and spontelectric parameters have been extracted to show that a spontelectric potential of 6.7 mV per monolayer is created as multilayers adsorb on a surface. The effect of this in the ISM would be to reduce the gas-phase charge and ionisation fractions in molecular clouds of the ISM which in itself has the potential to have wide-reaching implications.

Acknowledgements

The work that has gone into this thesis, both experimental and written, could not have been done without the help, advice and guidance of many people. Firstly, I would like to express my sincere gratitude to Prof. Martin R. S. McCoustra for the opportunity to experience the world of scientific research. The years have been filled with joys and frustration when the experimental kit either worked perfectly or needed reparations. Whatever the state of the laboratory, Prof. McCoustra was always there with advice and encouragement.

I am also grateful for the assistance and help from the astrochemistry group itself. This includes Mark, Ali and Skandar for their inspiring scientific conversations and to a great extent, I am very thankful for the friendship of Jerome and Demian. The two of them have had the patience to teach me how to work with the different experimental setups in the laboratories. Further to this, they have supplied me with a multitude of great comments and suggestions during the process of writing this thesis.

Prof. David Field and Dr. Andrew Cassidy at Aarhus University have also been a big part of the work gone into this project and thesis. Without their collaboration and input this thesis would have been very different.

Throughout the years at Heriot-Watt University I have gotten to know a number of great people who have always created a wonderful working environment everyday of the week. These people include all on the ground floor of the William Perkin Building and in particular Mary, Allan and Iain.

A life outside of the work has always been important to me. All the people in my life have been hugely important to me and have always been there for me. They have been able to let me remove my focus from work in the best of ways. These people know who they are and will always hold a special place in my life.

The author would also like to acknowledge the support of a James Watt Scholarship from Heriot-Watt University throughout the years of this Ph.D. program.

Lastly, and very importantly, I would like to thank my family for helping me in all possible ways. Without their help, this work would not have been possible.

ACADEMIC REGISTRY
Research Thesis Submission

Name*:*	Alexander Rosu-Finsen		
School/PGI:	Engineering and Physical Sciences – Institute of Chemical Sciences		
Version: *(i.e. First, Resubmission, Final)*	Final	Degree Sought (Award **and** Subject area)	Ph.D. in Physical Chemistry

Declaration

In accordance with the appropriate regulations I hereby submit my thesis and I declare that:

1) the thesis embodies the results of my own work and has been composed by myself
2) where appropriate, I have made acknowledgement of the work of others and have made reference to work carried out in collaboration with other persons
3) the thesis is the correct version of the thesis for submission and is the same version as any electronic versions submitted*.
4) my thesis for the award referred to, deposited in the Heriot-Watt University Library, should be made available for loan or photocopying and be available via the Institutional Repository, subject to such conditions as the Librarian may require
5) I understand that as a student of the University I am required to abide by the Regulations of the University and to conform to its discipline.

* *Please note that it is the responsibility of the candidate to ensure that the correct version of the thesis is submitted.*

Signature of Candidate*:*		Date:	

Submission

Submitted By *(name in capitals):*	
Signature of Individual Submitting:	
Date Submitted:	

For Completion in the Student Service Centre (SSC)

Received in the SSC by *(name in capitals):*			
Method of Submission *(Handed in to SSC; posted through internal/external mail):*			
*E-thesis Submitted (**mandatory for final theses)***			
Signature:		Date:	

Please note this form should bound into the submitted thesis.

Updated February 2008, November 2008, February 2009, January 2011

Table of Contents

List of Table Captions

Chapter 1

1.1: The different regions of the ISM with their general temperatures in K, state of hydrogen and the ionization fraction of the atoms/molecules. The density as stated in molecules cm^{-3} concerns the concentration of atomic hydrogen in the first four regions and molecular hydrogen in the mCNM. The last column, A_V, is the extinction of light as it travels through the different media. The question marks indicate that the exact value of the magnitude is unknown, but have been assumed to be zero due to the lack of molecules [11, 12].

1.2: This table illustrates the range of molecular complexity as observed in molecular clouds in the ISM. More than 190 different molecules have been observed until this point in time [13–15].

Chapter 2

2.1: Indicating the approximate times taken for a complete monolayer to be formed at a given pressure. In general, this indicates how long a surface remains clean at a certain pressure. The calculations have been done for N_2 and times will vary depending on the molecule of interest.

2.2: This table shows the values for the intercept, $\ln(P_0)$, and the gradient, C_m, as obtained from the pump–down curves from **Figure 2.16**.

2.3: O atom transitions with the corresponding emission peak from the spectrometer [16, 22]. The 777 nm transition is the strongest signal with the supplied energy as measured by the fiber optic cable linked to the spectrophotometer.

2.4: This table indicates the different gradients from **Figure 2.20**. The change in gradient indicates that an increase of about 58% O_2 desorption occurs when the plasma source is on and when every other experimental aspect, flux and time, is kept constant.

Chapter 3

3.1: This table shows the IR frequencies composing the O_3 band displayed in **Figure 3.7** which have been compared to literature values.

3.2: This table shows the result of resolving the components of the O_3 band when fitted with Gaussians and their comparison with literature values.

3.3: This table shows the results of the different limits put onto the CKS model for investigating the O_2 and O_3 formations in columns two and four (labelled O_2:O_3) and O_3 destruction (labelled O_3:O_2) in columns three and five. As can be seen, a greater extent of O_3 is produced than observed in the TPD experiments with negligible destruction.

3.4: This table shows the TPD results of O_2 desorption. The first column of values is of O_2 desorption after having been beam dosed onto the bare SiO_2 sample. The other columns are of O_2 having been dosed with the atomic beam onto the different surfaces.

3.5: This table summarises all the values of the O_3 band from the different surfaces after they have been fitted with Gaussians as compared to the literature values [16].

Chapter 4

4.1: This table shows the areas of the νOH band after the spectra have been baseline corrected and smoothed. The correction of the A_∞ value comes as a result of **Figure 4.6**.

4.2: This table shows the next step in the analysis using **Equation 3**. The areas used come from smoothing of the spectra for the 24 K de–wetting experiment.

4.3: This table shows the individual values of the rate constant, *k*, with respect to its annealing temperature. Plotting the inverse temperature and the ln(*k*) will lead to the associated energy through **Equation 4**.

4.4: This table shows the gradients for the linear fits of **Figure 4.8a** and **4.8b**.

4.5: This table reports the activation energy values associated with the de–wetting process of H_2O (rising edge) and the subsequent region (plateau) where isolated H_2O molecules have formed a greater bulk.

4.6: This table has been made to show the difference in the rate constant (*k*) as the coverage changes in p–ASW films and the film itself is changed to c–ASW and CSW.

Chapter 5

5.1: This table shows the peak positions and the difference in the LO–TO splitting for the annealing data (upper section) and the different deposition temperature data (lower part) from **Figures 5.10** and **5.11**. Only data at ≥48 K have been included due to the more clearly defined peaks.

5.2: This table produces a more clear sight of the peak shifts of CO as the deposition temperature changes. A contraction is observed which is indicative of a spontelectric material.

5.3: This table shows the peak positions with respect to deposition temperatures for CO on p–ASW, c–ASW and CSW. The data in this table can also be seen in **Figure 5.24**.

5.4: This table describes the different terms that the models use to relate the experimental RAIRS data to the surface potential measurements for N_2O and to show the possible extent of the spontelectric effect of solid state CO.

5.5: This data is from the experiment where N_2O is deposited at different temperatures [19]. The first four columns are the same as seen in the bottom part of **Table 5.1**.

5.6: This table shows the values as calculated from the model and compared to the observed RAIRS data for N_2O. Explanations for each column can be found in the text [19].

5.7: This table shows the data used for the modelling of the CO RAIRS data. The first four columns are taken directly from the experiments with the last two being calculated from the experimental data [28].

5.8: This table illustrates the variety of Ω as the deposition temperatures change when calculated through **Equation 25** [28].

5.9: This table shows how the values of E_S (upper and lower values) vary with the deposition temperature as calculated through **Equation 24** [28].

5.10: This table shows the values of the degree of dipole orientation as the temperature and spontelectric field vary. The subscripts *u* and *l* refer to the upper and lower branch as calculated for E_S [28].

5.11: This table shows the overall result of the spontelectric parameters and the dipole orientation when CO multilayers are deposited onto different types of H_2O while the deposition temperature is changed. The * marks where the deposition temperature is 21 K which is only the case for the c–ASW experiments [31].

5.12: This table summarises the results obtained through the analysis of the RAIRS data of N_2O and CO. As can be seen for the CO data, peculiar results are obtained when the substrate is changed as already discussed in the text.

5.13: This table sums up the estimated timescales for a species (electron or proton) to encounter an interstellar dust grain as calculated through **Equation 28** [31].

Chapter 6

6.1: This table shows the overall results of all the RAIR spectra of O_3 and the interactions leading to the IR spectra. These values can be compared to literature values as stated in the last column.

6.2: This table shows the full range of TPD results of O_2 desorption from the different surface investigated (SiO_2, p–ASW, c–ASW and CSW). The main body of the results is of O atomic beam dosing with O_2 molecular beam dosing results shown as a comparison.

6.3: This table shows the calculated values of the spontelectric effect of CO when deposited onto SiO_2, p–ASW, c–ASW and CSW.

List of Figure Captions

Chapter 1

1.10: The Eley–Rideal mechanism illustrating how one gas phase species only interacts with an adsorbed molecule to create a new species. The gas phase molecule does not come into contact with the surface at any point.

1.11: The Harris–Kasemo mechanism can be thought of as one part reverse E–R and one part L–H mechanisms. A molecule breaks apart on the surface creating one fragment with excess energy (B) which can diffuse on or in an ice lattice. This hot atom can then react with other molecules to produce (E).

Chapter 2

2.1: The Propst diagram shows what surface science processes are possible and studied in various fields of physical sciences. The main aspects of interest for this work are; electric fields, heat and neutral species.

2.2: A picture of the UHV rig used for this work and the main experimental aspects labelled with red arrows.

2.3: A detailed sketch of the UHV rig used for this work. The atomic beams have not been shown, but will be detailed later in **2.3.5**. The sketch is not to scale.

2.4: A sketch of the entire manipulator with the closed–cycle He cryostat cooling the sample to a minimum base temperature observed for this work of 17 K. The sample has XYZ translations and a virtual 360^{o} rotation.

2.5: The sample itself located at the end of the cryostat. The Cu block is coated with SiO_2 and a cartridge heater selectively heats only the sample block. Two KP–type thermocouples register the temperature throughout experimental work.

2.6: To the left is a schematic of the SiO_2 deposition chamber reaching base pressure of 10^{-6} mbar. To the right is a picture of the chamber as viewed from the left side of the rig. The SiO_2 is placed in the path of an electron beam which evaporates it, the sample is positioned directly above the SiO_2 and the rate of deposition is monitored by a QCM.

2.7: Two spectra showing the difference between a clean Cu sample, black, and one with SiO_2, red, deposited onto it. The 1241 cm^{-1} feature is the LO mode and the 1065 cm^{-1} is the TO optical mode of SiO_2.

2.8: This shows a simple test to verify if a layer of SiO_2 has been deposited, where droplets of H_2O appear to wet SiO_2 and clusters on Cu. The cloudy material on the

left side of the sample is SiO_2 which has not stuck properly to the sample and would not be used in the UHV rig, however for the H_2O test this will suffice.

2.9: A diagram showing the connection of the dosing lines to the leak valves of the UHV chamber. The lines are regularly evacuated and a small volume of gas or vapour containing the molecules of interest is expanded into the dosing bulbs for experimental use.

2.10: This graph shows the potential energy diagram of O_2 and what energy levels are needed to excite, dissociate and ionise O_2. The region labelled l with a red circle is the atoms of interest, $O(^3P)$, for this work.

2.11: Grotrian diagram for O showing all the electronic transitions possible. With the plasma source on, the $^5P \rightarrow {}^5S^0$ transition, labelled as OI IR3 to the left of the diagram, is the strongest.

2.12: A general schematic of the atomic beam sources and their overall construction. The source to the left is for the production of O atoms while the right side is for H atoms (not used in this work). The UHV chamber is as follows from **Figure 2.2**.

2.13: To the left is a picture of the plasma tube during reconstruction. The white discs, made of alumina so as to minimise O atom recombination after cracking, hold in place the aperture disc. The 5-hole grid in the centre of the aperture disc allows for the O beam to pass. The right picture is of the fully assembled plasma tube.

2.14: A sketch of the entire O atom plasma source. The inductively coupled radio frequency source sparks the O_2 gas when enough power is supplied. The air capacitors are to contain and focus as much power as possible towards the molecular gas. A fiber optic cable records the plasma emission in real time by a spectrometer.

2.15: The pump–down curve used to assess the beam flux when for O atom experiments. The rise in the MS counts of m/z = 32 is due to the gate valve, separating the plasma chamber and the central UHV chamber, being opened. The count rate is allowed to stabilise and the red line shows the gate valve being closed and the O_2 pumped out of the central UHV chamber. The experiments were done with a room temperature cryostat.

2.16: The result of the pump down curves form **Figure 2.15** when the MS counts have been converted to pressure, *P*, and each pumping curve has been set to zero to allow for individual and simple analysis.

2.17: The temperature programmed desorption of O_2 beam dosed onto the sample indicate ML formation between 5 – 10 minutes. The beam flux and nature of the surface have effects of the monolayer formation time.

2.18: This shows the generally obtained spectra of the O atom plasma as monitored through the fiber optic cable linked to the manual tuning unit (see **Figure 2.14**). The minor peaks correspond to various transitions of O atoms, with a slight contamination of OH, but the strongest signal is observed at 777 nm, corresponding to the ($3p\ ^5P$) → ($3s\ ^5S$) transition in the O atom.

2.19: The traces here initially indicate only a background of O, m/z = 16, the red trace, and O_2, m/z = 32, the black trace. As the gate valve between the plasma chamber and the central chamber is opened, a sharp rise in the counts happens. As this plateaus an initial measurement of the fragments monitored by the QMS is made (the blue vertical line). The plasma source is then turned on which cracks O_2 into O (the green vertical line). The source is left to stabilise and reach optimum operational conditions and the cracking fraction of the plasma source can be estimated (the brown vertical line).

2.20: This figure shows the integrated and normalised areas of O_2 TPD traces when dosing the O_2 molecular beam (black data set) and atomic O beam (blue data set) for 1, 2, 5 and 10 minutes. The areas have been normalised through integrated area of the 1 minute TPD traces for the O atom beam and the O_2 molecular beam to allow for comparison between the different experiments. The insert shows the difference in the TPD traces when the atomic beam is off or on.

2.21: This figure show the formation of a TPD trace. Initially molecules are deposited onto a surface of a certain quantity, θ_s, before the sample is heated. As the sample and the film heat up the coverage decreases as the rate constant, k_d increases. The point where the two curve intersect is the peak of desorption and the area under this newly created curve, v_{des}, is proportional to the amount of species deposited.

2.22: The traces above indicate the ideal desorption behaviours of chemical films deposited onto a surface. The top graph shows zero order kinetics where the leading edges align and a bulk material desorbs. The second graph is of 1st order where all the peaks line up to the same peak temperature of desorption which is expected for sub–monolayer desorption. The bottom graph is of 2nd order desorption where the trailing edges align indicative of recombination of molecules on the surface during desorption.

2.23: A schematic of the electric field vectors on a surface from parallel polarised light (to the left) and perpendicular polarised light (on the right). As can be seen, the electric field is cancelled in the left diagram and enhanced in the right.

2.24: This graph shows how the phase changes as polarised light perpendicular (**a**) and parallel polarised (**b**) is incident on a metal surface at a given angle. As can be seen, (**b**) has a greater phase change as the angle of incidence changes. Figure is adapted from [29].

2.25: The MSSR is important when conducting IR experiments on a pure metal surface. As can be seen, the molecules oriented perpendicular to the surface will have an overall enhanced dipole moment due to the image dipole arising in the metal surface. This effect is cancelled out when the molecules are aligned parallel to the surface.

2.26: RAIRS spectra of the νNN mode of 14 ML N_2O on Cu, blue, 200 nm SiO_2, red, and 300 nm SiO_2, black. As can be seen the TO mode of N_2O is silent when deposited directly on Cu. This mode then activates as it is physically removed from the surface of the Cu by SiO_2 spacers.

2.27: A similar diagram to that describing the MSSR in Figure 2.25. However, a SiO_2 layer has been placed between the metal and the adsorbed dipolar molecular film illustrating how the roughness can circumvent the MSSR.

2.28: This cartoon shows how the LO and TO modes behave in a solid. The LO mode arises as the phonons in the solid interact longitudinally, or along, the electric field when the IR beam hits the surface of the Cu substrate. The TO mode behaves oppositely and interacts transversely with the electric field.

2.29: This figure illustrates the experimental setup in Aarhus for measuring the surface potential of spontelectric molecules. Photo–ionisation of argon gas (S1–3) produces near–zero kinetic energy electrons which are focussed (L1–4) onto the sample [37].

Chapter 3

3.1: This figure indicates a variety of routes of H_2O in the solid phase on interstellar dust grains. The focus point of this chapter will be in the top line where O atoms lead to O_2 which can lead to O_3. This figure is taken from [3].

3.2: This figure shows the results of the TPD experiments of molecular oxygen beam dosed onto SiO_2 for 1, 2, 5, 10, 20 and 50 minutes. A clear change can be seen

between 5 and 10 minute dosing, this is due to the change from sub–monolayer to multilayers of O_2. This change is more clearly shown in the insert of 1, 2, 5 and 10 minute dosages.

3.3: This figure shows the results of the leading edge analysis of the pure O_2 molecular beam dosing TPD experiment. Two separate regions can be distinguished where the lower three points relate to the coverages of 1, 2 and 5 minute beam dosing and the latter three points are of the 10, 20 and 50 minute dosing. These two regions are the sub–monolayer and multilayer respectively.

3.4: This figure shows the Arrhenius plot of the TPD trace after the molecular oxygen beam has dosed the bare SiO_2 surface for 50 minutes. The black dots correspond to the experimental data and the red dots highlight the leading edge of the TPD profile from the same 50 minute TPD trace in **Figure 3.2**.

3.5: This figure shows the TPD results of 50 min molecular oxygen dosing onto SiO_2 (black scatter) with the CKS model as a red solid line.

3.6: As can be seen in this figure, O_3 is produced as the O atom beam bombards the bare SiO_2. As the dosing time is increased a peak at about 1045 cm^{-1} is seen to grow as dosing time is increased.

3.7: This figure shows the fit between the RAIRS data (black) and the fit (red) which is made by three Gaussians in blue. The result of the fit has been listed in **Table 3.1**. Further to this, the top of the figure shows the residuals from the experimental data and the overall fit.

3.8: This figure shows the results when the O atomic beam is dosed onto SiO_2 for a duration of 50 minutes. The O_2 TPD trace, measured through m/z = 32 shows two main peaks, the low temperature peak corresponds to sample desorption while at higher temperatures O_2 is released from the cold finger. The insert shows O_3 desorption, m/z = 48, as measured simultaneously with O_2 cold–finger desorption.

3.9: This is the Arrhenius plot of the desorption profile from the TPD trace in **Figure 3.8**. The black scatter is representative of the inverted TPD trace after the atomic beam has bombarded the bare SiO_2 for 50 minutes with the red points being the leading edge of the TPD trace.

3.10: This figure shows the comparison between the experimental data (black scatter) and the CKS model (red solid line). This fit has been created with an E_{des} of 6.7 kJ mol^{-1} and 5×10^{27} molecules cm^{-2} s^{-1}.

3.11: This figure shows the formation of O_3 when the O atom beam bombards 20 ML p–ASW. As can be seen, the shape and character of the feature is similar to when O atoms probe the bare SiO_2 surface.

3.12: This figure shows the three regions of interest in the IR spectrum. These are difference spectra showing the difference of the p–ASW film ($A_{p–ASW}$) after O atom bombardment ($A_{O\ atoms}$). The red boxes indicate the specific regions where H_2O_2 features are expected if formed, however no such features are observed.

3.13: This figure is of the 20 ML p–ASW film after 50 minute O atom bombardment as it desorbs. The species of interest in this figure is O_2 as it leaves the surface, the shape and temperature at which it leaves the surface is due to the porosity of H_2O. The insert is an Arrhenius plot where the red dots (the leading edge of desorption) are used to extract the kinetic information of the desorption process.

3.14: This figure shows the comparison between the experimental data (black) of O_2 desorption from 20 ML p–ASW and the model (red).

3.15: This figure shows the desorption of O_3 after 20 ML p–ASW has been bombarded by O atoms for 50 minutes. A change is observed in the temperature region above 62 K as O_3 begins to leave the surface.

3.16: The two panels in this figure illustrate the lack of H_2O_2 during the experiments. Panel **(A)** shows the desorption of O_2 which **(B)** is of H_2O as followed through different mass fragments. The two spectra are expected to be more similar in the high time end if H_2O_2 is desorbed.

3.17: This figure shows the O_3 peak after the O atom beam has bombarded a multilayer surface of c–ASW for 50 minutes. There are no other observed differences in the IR spectrum.

3.18: This figure illustrates what happens after the O atoms have bombarded a multilayer surface of c–ASW for 50 minutes. Desorption is seen to initiate at about 25 K and a more clear peak is observed as compared to a similar amounts of O_2 desorbing from p–ASW. The insert shows the Arrhenius plot of the desorption from which kinetic parameters can be extracted.

3.19: This figure shows the attempt at fitting O_2 desorption from c–ASW (black scatter) with a CKS model (red solid line). The O atoms beam is believed to alter the morphology of the molecular film leading to the experimental data appearing as presented.

3.20: This figure shows the result, when looking at O_3, when a 20 ML CSW film has been bombarded with O atoms for 50 minutes. No other change in the 800 – 4000 cm^{-1} region was observed.

3.21: The figure illustrates the shape as O_2 is desorbed from SiO_2 after a 50 minute atomic beam dose. The reason for the long trailing edge of this multilayer desorption spectra is believed to be due to the O atom beam affecting the morphology of the CSW surface. The insert sheds light on the desorption kinetics through linear analysis of the red points.

3.22: This figure shows the similarity in the leading edge of the experimental data and the CKS model of O_2 desorption from CSW after 50 minute O atoms beam dosing.

3.23: This figure shows the result of adding all the TPD spectra into one graph. A clearly defined peak is observed which can be used for further analysis.

3.24: This inverted figure leads to the desorption energy through the gradient of the red line while the intercept gives an indication of the pre–exponential factor.

3.25: This figure shows the correlation between the experimental data (black scatter) and the model (red solid line) of O_3 desorption.

3.26: This figure shows the results as gathered from the CKS model and presented in **Table 3.3**. Formation of O_3 **(A)** occurs as expected, however to a greater extent than shown in the experimental TPD data. O_3 destruction **(B)** has also been shown in this figure and is considered not to be the cause for the lack of O_3 signal during desorption in the TPD experiments.

Chapter 4

4.1: Temperature programmed RAIRS of 0.5 ML H_2O on SiO_2 showing an increasing intensity of the νOH band as the temperature increases. The magenta band shows a 20 ML spectrum of H_2O, as can be seen, the annealed appear similar to the multilayer. The sharp features are due to gas–phase water in the optics boxes on the air side of the UHV apparatus. This figure is taken from [2] and [8].

4.2: This plot shows the correlation between pressure in mbar and counts of m/z = 18 as monitored by the QMS. This linear relationship between pressure and counts was used throughout to note the background H_2O pressure during an experiment.

4.3: These spectra show the deposition of 0.5 ML H_2O (black) on SiO_2 followed by TPD of that film. After the partial pressure of H_2O has decreased to $<2 \times 10^{-10}$ mbar the sample was cooled and another spectrum was taken (red). Re–adsorption of H_2O on the timescale of the experiment is not significant due to the low H_2O partial pressure.

4.4: The result of depositing 0.5 ML H_2O onto SiO_2 at 18 K. The time between each RAIR spectrum was one hour as this was determined to be the average time between scans when H_2O is annealed at the other temperatures investigated. The sharp peaks are due to gas–phase H_2O in the optics boxes on the air side of the UHV apparatus.

4.5: The result of depositing 0.5 ML H_2O onto SiO_2 at 100 K for a total of 500 sec before annealing to the $A_{infinity}$ times, A_∞, factor. The sharp peaks at 3500 – 3600 cm^{-1} are due to gas–phase H_2O in the optics boxes on the air side of the UHV rig.

4.6: These spectra show the change when depositing 0.5 ML H_2O at 17 K before annealing to 100 K for 20 minutes and again for 120 minutes.

4.7: This figure shows the linear relationship of **Equation 3**. The slope is the rate constant, *k*, for the isolated H_2O to a bulk process. The values for this figure are obtained from **Table 4.2**.

4.8: This figure shows the Arrhenius plot where two regimes can be observed. The first regime, **a)**, illustrates a rising edge while **b)** indicates a plateau. A series of fits have been done to estimate an average gradient for each **a)** and **b)** in order to obtain an activation energy, however a clear change is apparent as the temperature increases. The figures have been shown in two parts for clarity with matching colours for the linear fits.

4.9: This figure shows the final step after analysis with an indication of the best linear fits to the two data regions in the experimental results.

4.10: This figure shows the effect of O atom bombardment on 0.5 ML H_2O. The large sharp peaks are due to gas phase H_2O in the optics boxes outside of the UHV chamber.

4.11: This figure is of 1 ML p–ASW as O atoms bombard the sample for a total of 50 minutes. The same trend is seen here, however to a greater extent, as is seen in **Figure 4.10**.

4.12: As can be seen in this figure, 1 ML of c–ASW does not behave as the p–ASW films. Throughout O atom irradiation for 50 minutes, the band is invariant, however has the same shape as the p–ASW spectra presented in this work.

4.13: This figure shows the effect of O atoms bombarding a 1 ML CSW film. The atomic beam was dosed in steps for a total of 50 minutes. The bump seen in the 1 ML CSW spectrum (red spectra) at about 3350 cm^{-1} disappears during O atom bombardment.

4.14: This figure shows the H_2O as isolated (i) converting into clusters (c) with time through a heating rate of 1 K $century^{-1}$ **(a)** and the corresponding temperature for the cluster formation **(b)**. The simulation has been done for 0.5 ML H_2O with an E_{act} of 1.8 kJ mol^{-1} and a pre–exponential factor of 10^{12} s^{-1}.

4.15: This figure shows what happens as H_2O adsorbs onto an interstellar dust grain as during cloud collapse and freeze–out as the temperature falls from 110 K to 10 K. Gas phase molecules (g) will either adsorb as isolated or clustered H_2O. As the temperature is above the energy needed for de–wetting, isolated molecules instantly become crystalline or clustered depending on temperature. The simulation has been done for 0.5 ML H_2O with an E_{act} for de–wetting of 1.8 kJ mol^{-1} and a pre–exponential factor of 10^{12} s^{-1} with a cooling rate of 1 K $century^{-1}$.

4.16: This figure shows the behaviour of CO as it adsorbs onto an interstellar dust grain with H_2O already present. Assuming an equal probability of CO initially adsorbing onto H_2O or SiO_2, CO then migrates to the preferred SiO_2 sites until all SiO_2 sites are inhabited leaving H_2O sites open for interactions as compared to the less favoured CO multilayer formation.

4.17: This cartoon represents the onset of H_2O cluster formation and the de–wetting process even at temperatures of 10 K on dust grains, brown substrate, in the cores of molecular clouds. The red circles are representative of O atoms, black circles are H atoms, blue ovals are H_2O molecules and green ovals are molecules of CO. This figure draws inspiration from [8].

Chapter 5

5.1: This figure shows how the surface potential varies proportionately with amount of N_2O. A decrease in the potential is observed as the deposition temperature rises. At temperatures above 65 K, N_2O does not stick effectively to the gold surface under UHV conditions and no measurements are made [1].

5.2: This cartoon illustrates the thermodynamically most favoured structure for a dipolar molecular solid **(A)** and the likely molecular orientation in the spontelectric phase **(B)**.

5.3: This figure shows the TPD results of depositing various amounts of N_2O onto SiO_2 and desorption of the molecular films. N_2O detected as m/z = 44 is recorded as a function of temperature of the substrate. As can be seen, a clear change is observed between 6 L and 7 L which is the change between the sub–monolayer and the multilayer regimes as explained in **Chapter 2**.

5.4: This figure shows the full range of the spectrum obtained when having deposited 14 ML N_2O onto SiO_2 at 50 K. The peaks of interest at about 2250 cm^{-1} have been highlighted in the insert [19].

5.5: This figure indicates that changing the amount of N_2O from 1.4 ML to 28 ML has little bearing on the peak positions. The N_2O films were deposited at 50 K to ensure the sharp features of the LO–TO splitting. The dashed lines are a guide to the eye to show peak shifts as compared to the centre of the peak of the 14 ML N_2O spectrum.

5.6: This figure shows 14 ML N_2O on SiO_2 being annealed from base temperature. The red arrows indicate the movement of the peaks as they shift with increasing temperature. N_2O deposited at 18 K is believed to be amorphous and the higher temperature spectra (>48 K) are crystalline. When the film is annealed to 48 K characteristics of both structural states can be observed.

5.7: This figure shows the effect of changing the deposition temperature of 14 ML of N_2O. A greater contraction of the LO–TO splitting is observed as compared to **Figure 5.6**. To make the figure easier to read, only five experiments have been shown instead of the full range [19].

5.8: This figure shows the comparison between the experimental data (open circles), and the Gaussian fits (solid red line) to the LO–TO splitting of N_2O with the residuals shown in the box above the graph.

5.9: This figure shows the result of plotting the data outlined in **Table 5.1** where squares and dots correspond to the LO and TO peaks, respectively. Further to this, the black and red represent the annealing and deposition temperature experiments, respectively. As can be seen, a contraction occurs with increasing temperature, and greater so when the deposition temperature is increased [19].

5.10: This figure shows the change in the inhomogeneous broadening of the LO–TO splitting of N_2O from the annealing experiment (black squares) and the different deposition experiments (red dots) [19]. The data points were calculated by measuring the intensity at 2150 cm^{-1} and normalising the data from **Figures 5.6** and **5.7**.

5.11: This figure shows the desorption of different CO coverages from SiO_2. As can be seen, a clear change in behaviour is observed between 15 L and 20 L indicating that this is the completion of the first monolayer.

5.12: This figure shows the whole spectrum when depositing 5 ML of CO onto SiO_2 at 20 K. The feature of interest, the CO stretch, at about 2140 cm^{-1} has been highlighted in the insert to show the LO–TO splitting. The sharp bands at >3500 cm^{-1} and in the 1250–2000 cm^{-1} range are of gas–phase H_2O with the negative bands at about 2300 cm^{-1} being gas–phase CO_2 in the optics boxes outside of the UHV chamber [28].

5.13: This data shows that as the amount of CO is increased from 2.5 ML to 10 ML a slight change above the spectrometer resolution is observed when the film thickness is doubled. However, considering the general uncertainty of background dosing being about 20%, the amount of molecules on the surface can be said to have no impact of the LO–TO peak positions.

5.14: This shows the LO–TO splitting as the 5 ML CO film is annealed from 20 K to 26 K. Observing shifts of the peaks over the resolution of the spectrometer is impossible.

5.15: This figure shows the results of depositing 5 ML CO onto SiO_2 at different temperatures. A slight shift in the LO–TO splitting of the ν*CO band is now observed which is greater than the resolution of the spectrometer (0.1 cm^{-1}) [28].

5.16: This figure shows the comparison between the experimental RAIRS data of the ν*CO band of 5 ML CO on SiO_2 at 20 K and the fit with Gaussians with the residuals shown above the data and fit.

5.17: This figure shows the position of the LO and TO modes of the ν*CO band of 5 ML CO on SiO_2 as the deposition temperature changes from 20 K through to 26 K [28].

5.18: This figure shows another way of looking at the order of dipoles in the 5 ML CO film as the temperature of deposition is increased from 20 K through to 26 K [28].

5.19: This figure shows all the RAIRS data collected when 20 ML CO is deposited onto multilayers of p–ASW (A), c–ASW (B) and CSW (C) at the indicated temperatures in the 20 K to 24 K range. A shift in the LO–TO splitting of ν*CO is observed as the temperature increases [31].

5.20: This figure displays the data from **Table 5.3** of the LO (squares) and TO (circles) modes of the ν*CO band contracting with increasing deposition temperature. As can be seen, a greater splitting is observed at 20 K for p–ASW (blue) as compared to the other c–ASW (black) and CSW (red) [31].

5.21: This figure shows the inhomogeneous broadening as measured at 2141 cm^{-1} between the LO and TO modes of the *ν*CO band of 20 ML CO on H_2O ice. The blue data points are from CO on p–ASW, black is c–ASW and red is CSW. The linear regressions of the points give an idea of the similarity of environments of CO on H_2O surfaces [31].

5.22: This figure shows the relationship with the spontelectric contribution to the LO–TO splitting and the dipole alignment for N_2O. A linear relationship exists as expected except for the 66 K data point due to the decrease in the sticking coefficient when the temperatures approaches the desorption temperature of N_2O [19].

5.23: This figure shows the final result comparing the observed RAIRS data (black scatter) with the modelled data (red solid line). The dashed red lines indicate the level of uncertainty in the modelled data (± 0.8 cm^{-1}) [19].

5.24: This figure shows the linear relationship between the value of the LO–TO splitting of CO on SiO_2 with respect to the inverse temperature. The intercept with the y–axis leads to an approximation for the intrinsic component of the LO–TO splitting of CO [28].

5.25: The two graphs show the depletion of CO from the gas phase **(A)** as the molecules condense onto the cold interstellar dust grain **(B)** with time. Both graphs have been done with typical astronomical conditions as found in the core of B68 [31].

5.26: This figure shows how CO initially aggregates onto a dust grain. The spontelectric effect in CO starts when a multilayer is formed thereby creating a positively charged surface. This attracts electrons, which in turn attracts cations and together they can recombine leading to the cycle starting over.

Chapter 6

6.1: This figure shows the surface potential measurements of methyl formate as the temperature increases. As can be seen, methyl formate behaves as a typical spontelectric material initially before changing behaviour at about 70 – 80 K. Above this temperature the surface potential increases along with the temperature until the Curie point is reached at about 90 K [21, 22].

List of Abbreviations

aCNM	Atomic Cold Neutral Medium
(p, c)-ASW	(porous, compact)-Amorphous Solid Water
CSW	Crystalline Solid Water
E-R	Eley-Rideal
FTIR	Fourier Transform Infrared
FWHM	Full Width at Half the Maximum
GMC	Giant Molecular Cloud
H-K (H-A)	Harris-Kasemo (Hot Atom)
HIM	Hot Ionised Medium
HOPG	Highly Oriented Pyrolitic Graphite
IR	Infrared
ISM	Interstellar Medium
ISO	Infrared Space Observatory
ISRF	Interstellar Radiation Field
L-H	Langmuir-Hinshelwood
LO	Longitudinal Optical
mCNM	Atomic Cold Neutral Medium
MCT	Mercury Cadmium Telluride
MS	Mass Spectrometry
MSSR	Metal Surface Selection Rule
NASA	National Aeronautics and Space Administration
OFHC	Oxygen Free High Conductivity
PAH	Polycyclic Aromatic Hydrocarbon
QMS	Quadrupole Mass Spectrometer
RAIRS	Reflection-Absorption Infrared Spectroscopy
SN	Supernova

SWS	Short Wavelength Spectrometer
TO	Transverse Optical
TPD	Temperature Programmed Desorption
UHV	Ultrahigh Vacuum
VSE	Vibrational Stark Effect
(V)UV	(Vacuum) Ultraviolet
WIM	Warm Ionised Medium
WNM	Warm Neutral Medium

List of Publications and Conference Presentations

Publications

Laboratory Investigations of Irradiated Acetonitrile-Containing Ices on an Interstellar Dust Analog: A.G.M. Abdulgalil, D. Marchione, A. Rosu-Finsen, M.P. Collings and M.R.S. McCoustra, *J. Vac. Sci. Technol. A*, 2012, **30**, 0415051

Investigations Into the Nature of Spontelectrics: Nitrous Oxide Diluted in Xenon: A. Cassidy, O. Plekan, J. Dunger, R. Balog, N.C. Jones, J. Lasne, A. Rosu-Finsen, M.R.S. McCoustra and D. Field, *Phys. Chem. Chem. Phys.*, 2014, **16**, 23843

Laboratory Surface Astrochemistry Experiments: V.L. Frankland, A. Rosu-Finsen, J. Lasne, M.P. Collings and M.R.S. McCoustra, *Rev. Sci. Instrum.*, 2015, **86**, 055103

Probing Model Interstellar Grain Surfaces with Small Molecules: M.P. Collings, V.L. Frankland, J. Lasne, D. Marchione, A. Rosu-Finsen and M.R. S. McCoustra, *Mon. Not. R. Astron. Soc.*, 2015, **449**, 1826

Spontaneous Electrical Solids in a New Light: J. Lasne, A. Rosu-Finsen, A. Cassidy, M.R.S. McCoustra and D. Field, *Phys. Chem. Chem. Phys.*, 2015, **17**, 20971

Spontaneous Electrical Fields in Solid Carbon Monoxide: J. Lasne, A. Rosu-Finsen, A. Cassidy, M.R.S. McCoustra and D. Field, *Phys. Chem. Chem. Phys.*, 2015, **17**, 30177

Spontaneous Polarization of Solid CO on Water Ices and some Astrophysical Implications: A. Rosu-Finsen, J. Lasne, A. Cassidy, M.R.S. McCoustra and D. Field, *Phys. Chem. Chem. Phys.*, 2016, **18**, 5159

Enabling Star Formation via Spontaneous Molecular Dipole Orientation in Icy Solids: A. Rosu-Finsen, J. Lasne A. Cassidy, M.R.S. McCoustra and D. Field, Submitted to *Astrophys. J.*

N_2O phase change: A. Cassidy, M.R.V. Jørgensen, A. Rosu-Finsen, J. Lasne, J.H. Jørgensen, A. Glavic, V. Lauter, B.B. Iversen, M.R.S. McCoustra, and D. Field, Submitted to *J. Phys. Chem. C*

Photodesorption and Physical Properties of CO Ice as a Function of Temperature: G.M. Munoz Caro, Y.-J. Chen, S. Aparicio, A. Rosu-Finsen, J. Lasne and M.R.S. McCoustra, *Astron. Astrophys.*, 2016, **589**, A19

Electron-promoted Desorption of H_2O from Interstellar Dust Grain Surfaces: A.G.M Abdulgalil, A. Rosu-Finsen, D. Marchione, J.D. Thrower and M.R.S. McCoustra, *Phys. Chem. Chem. Phys.*, In Preparation

Electron-promoted Desorption from Core Dust Grain Surfaces: D. Marchione, A.G.M. Abdulgalil, J., J. Thrower, A. Rosu-Finsen and M.R.S. McCoustra, *Mon. Not. Roy. Astron. Soc.*, In Preparation

Peeling the Astronomical Onion: A. Rosu-Finsen, D. Marchione, T. Salter, J. Stubbing, W. Brown and M.R.S. McCoustra, In Preparation

Wetting and De-wetting Behaviour on Model Interstellar Dust Grains
D. Marchione, A.G.M. Abdulgalil, A. Rosu-Finsen, and M.R.S. McCoustra, In Preparation

H_2O behaviour on Interstellar Dust Grains; A Closer Examination: A. Rosu-Finsen, D. Marchione and M.R.S McCoustra, In Preparation

Methyl Formate Spontelectrics: S. Taj, A. Rosu-Finsen, J. Lasne, A. Cassidy, M.R.S. McCoustra and D. Field, In Preparation

O atom Chemistry: A. Rosu-Finsen and M.R.S. McCoustra, In Preparation

Using CO as a Probe of the Characteristics of Heterogeneous Surfaces: D. Baird, S. Taj, A. Rosu-Finsen and M.R.S. McCoustra, In Preparation

Conference Presentations

Spontelectric Effect in Solid Nitrous Oxide (N_2O): A RAIRS Study of Dipole Alignment: Poster presented at the 11th European Conference on Atoms, Molecules and Photons, Aarhus University, Aarhus, Denmark, 24th – 28th of June, 2013

Desorption of O_2, CO and N_2 from Astronomically Relevant Surfaces: Talk presented at the 19th International Vacuum Conference - Astrosurf, Le Palais des Congres de Paris, Paris, France, 9th –13th of September, 2013

Poster presented Faraday Discussions 168: Astrochemistry of Dust, Ice and Gas; NH Conference Centre, Leiden, NL, 7th – 9th of April, 2014.

Probing Model Interstellar Grain Surfaces with Small Molecules: Talk presented at the Joint Royal Society of Chemistry/Royal Astronomical Society, Milton Keynes, United Kingdom, 15th – 16th of Januray, 2015

Chapter 1

The Interstellar Medium

Contents of this chapter

1.1 Introduction

In all its expanding glory, the 13.8 billion years old Universe can be divided into two types of regions. The first of these categories encompasses all stellar systems with possible orbiting planets and satellites and the second category is the regions between these systems called the interstellar medium (ISM). Various fields of study have been formed dedicated to understanding the different processes and phenomena observed in the Universe; astrophysics, astrochemistry and astrobiology. Astrophysics focuses on the physical laws that formed and control the Universe through theoretical studies, laboratory experiments and observations. At present, it is believed that baryons (baryonic matter is the 'normal' matter composing the visible Universe, as opposed to dark matter and dark energy) make up about 4% of the mass of the Universe, while 23% is believed to be dark matter and 73% being dark energy [1–3]. Baryons define matter composed of protons, neutrons and electrons, and can therefore be detected by methods such as infrared (IR), ultraviolet (UV), radio, microwave and rotational spectroscopy. Dark matter was first mentioned by Fritz Zwicky in 1933 who referred to it as 'dunkle Materie' (dark matter) [4] and is only inferred by its gravitational effects [5, 6]. Dark energy was first introduced in 1998 by Michael Turner [4] and is believed to cause the acceleration of the Universe's expansion [6]. Both dark matter and energy are not seen in the electromagnetic spectrum, however with the discovery of gravitational waves, more can possibly be learned in the future.

Astrochemistry is, as the name suggests, the study of chemistry both in our Solar system and outside it. The general challenge in this field is to obtain a unified model for the chemical reactions occurring, both gas–phase and surface chemistry, to explain the observations of molecules and their abundances as surveyed by ground– and space–based observatories such as the Atacama Large Milimeter/submilimeter Array (ALMA) and telescopes such as the Hubble or James Webb telescopes. The latter, and youngest, field of astroscience, astrobiology has recently gained a lot of attention since many exoplanets have been discovered orbiting stars [7]. Some of these exoplanets can be found in the 'Goldilocks' zone, which is the distance from a star where the temperature can support the presence of liquid water on their surface. While it has been difficult to determine the composition of exoplanetary atmospheres due to 'flat' signals meaning specific molecular features cannot be distinguished, recent progress has been made. The exoplanet of 55 Cancri e is not in the 'Goldilocks' zone and has a surface temperature of

about 2000 K, however observations have shown that the atmosphere of this celestial body contains large amounts of H and He, this is the first detection of an exoplanet's atmosphere [8]. This observation was done with the Hubble Space Telescope, one telescope of many investigating and observing the farthest reaches of the Universe. One of the most famous examples of astrophysical observation of dark clouds is of the well–known Barnard 68 as seen in **Figure 1.1** [9].

Figure 1.1: These pictures are of a molecular cloud named Barnard 68. The picture to the left shows the cloud as observed through optical based telescopes while the right picture is presented in false colour showing the IR background radiation from the stellar landscape behind the cloud.

The pictures in **Figure 1.1** show various regions of the ISM, the lack of colour in the left being from interstellar clouds obscuring visible light from passing through due to a greater concentration of gas and dust. This lack of gas and dust in the regions around the cloud means that the stellar landscape can be observed. To contrast the stark change in molecular cloud and stellar landscape in the picture to the left, the right hand side shows the same regions as seen in the near–IR. The dust and gas in the molecular cloud does not absorb and scatter all manners of radiation leaving the astronomers who captured this picture as calling it 'Seeing the light through the dark' [10]. This picture illustrates the point that the ISM cannot be wholly empty and that different regions must exist.

The ISM can be divided into five regions according to their physical and chemical properties: the hot ionized medium (HIM), the warm ionized medium (WIM), the warm neutral medium (WNM), the atomic cold neutral medium (aCNM), and the molecular cold neutral medium (mCNM). These regions of space do not have specific boundaries

with each other, but are blended together. **Table 1.1** shows the typical traits associated each region [11, 12].

ISM Region	**Common Name(s)**	**Temperature / K**	**Density / molecules cm^{-3}**	**State of Hydrogen**	**Ionization Fraction**	A_V **/ mag**
Hot Ionized Medium (HIM)	Coronal Gas	10^6	0.003	H^+	1	?
Warm Ionized Medium (WIM)	Diffuse Ionized Gas (DIG)	10^4	≥10	H^+	1	?
Warm Neutral Medium (WNM)	Intercloud H_I (^1H)	8×10^3–10^4	0.1	H	0.1	~0.5
Atomic Cold Neutral Medium (aCNM)	Diffuse Cloud	100	10–100	H / H_2	10^{-3}	0.5–1
Molecular Cold Neutral Medium (mCNM)	Molecular Cloud	1–50	10^3–10^5	H_2	10^{-7}–10^{-8}	~5

Table 1.1: The different regions of the ISM with their general temperatures in K, state of hydrogen and the ionization fraction of the atoms/molecules. The density as stated in molecules cm^{-3} concerns the concentration of atomic hydrogen in the first four regions and molecular hydrogen in the mCNM. The last column, A_V, is the extinction of light as it travels through the different media. The question marks indicate that the exact value of the magnitude is unknown, but have been assumed to be zero due to the lack of molecules [11, 12].

As can be seen in **Table 1.1**, the density in the HIM is the lowest of all five parts and the temperature is extremely high. The HIM is created after supernova (SN) explosions [11] when stars scatter their atoms farther than the boundaries of their previous stellar system, leading to the low density and high temperature observed. The WIM are the regions beyond the HIM, the aftermath of the prior SN events, where temperatures have fallen and pressures have risen slightly. The amount of radiation is still enormous, leading to a similar ionization fraction and thereby state of H^+ as seen in **Table 1.1**. Regions where the radiation is less, but the temperature is still high are the WNM. Here the radiation mostly leads to atoms recombining or keeping their electrons, thereby remaining neutral. When gravitational forces increase, gas and dust grains form regions such as the atomic cold neutral medium (aCNM also called diffuse clouds). Here the pressures are greater and temperatures lower (about 100 K) than other regions of the ISM due to shielding caused by the dust and gas. Gas phase chemistry is responsible for reactions leading to small amounts of molecules such as H_2 along with lesser parts of HCN, NH_3, CO and H_2CO in these clouds [11, 12]. The low density of molecules is a part of the reason for the lack of chemical diversity in the aCNM, however such clouds are still vulnerable to external vacuum UV (VUV) radiation which is the dominant reason for the atomic nature of diffuse clouds. This harsh VUV field causes photodissociation leading to molecular destruction. These diffuse clouds are seen to envelope dense clouds leading to a density and temperature gradient from the outer reaches to the cold core [11]. An intermediate stage in this cloud envelope is termed translucent clouds; this regime bridges the gap in density, temperature, ionisation fraction and extinction of **Table 1.1**. This means such clouds typically have temperatures ranging from 50 – 100 K, densities between $10^2 – 10^3$ molecules cm^{-3} and A_V of 1 – 5 mag. The state of hydrogen changes from H towards dominance of H_2 [12].

As the gravitational forces continue to pull on the diffuse cloud, the density increases further leading to a greater UV shielding effect which therefore means a lower temperature is found in the cores of the molecular cold neutral medium (mCNM also called dark or dense clouds). This temperature can approach absolute zero and so these are some of the coldest regions known. These dense clouds, are the focus of this thesis due to the variety of molecules observed, over 190 so far as listed in **Table 1.2** [13–15]. Referring back to **Figure 1.1(A)**, it can be seen that bright stars and at the border of B68 fewer stars are observed along with greater darkness. This is the diffuse cloud regime leading to the total darkness in the center of the figure which is the dense cloud. While

Two Atoms		Three Atom		Four Atoms	Five Atoms	Six Atoms	Seven Atoms	Eight Atoms	Nine Atoms	≥Ten Atoms
H_2	ArH^+	C_3	C_2N	c–C_3H	C_5	C_5H	C_6H	CH_3C_3N	CH_3C_4H	CH_3C_5N
AlF	NO^+	C_2H	SiCSi	l–C_3H	C_4H	l–H_2C_4	CH_2CHCN	$HC(O)OCH_3$	CH_3CH_2CN	$(CH_3)_2CO$
AlCl	TiO	C_2O	HO_2	C_3N	C_4Si	C_2H_4	CH_3C_2H	CH_3COH	$(CH_3)_2O$	$(CH_2OH)_2$
C_2	SH	C_2S	TiO_2	C_3O	l–C_3H_2	CH_3CN	HC_5N	C_7H	CH_3CH_2OH	CH_3CH_2CHO
CH	AlO	CH_2	KCN	C_3S	c–C_3H_2	CH_3NC	CH_3CHO	C_6H_2	HC_7N	HC_9N
CN		HCN	FeCN	C_2H_2	H_2CCN	CH_3OH	CH_3NH_2	CH_2OHCHO	C_8H	CH_3C_6N
CO		HCO	H_2Cl^+	NH_3	CH_4	CH_3SH	c–C_2H_4O	l–HC_6H	$CH_3C(O)NH_2$	C_2H_5OCHO
CP		HCS^+	AlOH	HC_2N	HC_3N	HC_3NH^+	H_2C_2HOH	CH_2CHCHO	C_3H_6	C–C_6H_6
SiC		HOC^+	C_2P	HCNH	HC_2NC	HC_2CHO	CH_3NCO	CH_2C_2HCN	CH_3CH_2SH	$C_2H_5OCH_3$
HCl		H_2O		HNCO	HCOOH	NH_2CHO		H_2NCH_2CN		n–C_3H_7CN
KCl		H_2S		HNCS	H_2CNH	C_5N		CH_3CHNH		$HC_{11}N$
NH		HNC		$HOCO^+$	H_2C2O	l–HC_4N		$(NH_2)_2CO$		C_{60}^+
NO		HNO		H_2CO	H_2NCN	l–HC_4H				C_{70}
NS		MgCN		H_2CN	HNC_3	c–H_2C_3O				CH_3COOCH_3
NaCl		MgNC		H_2CS	SiH_4	H_2C_2NH				C_2H_7CN
OH		N_2H^+		H_3O^+	H_2COH^+	HNCHCN				
PN		N_2O		C–SiC_3	HC(O)CN	H_2NCO^+				
SO		NaCN		CH_3	HNCNH	C_5S				
SiN		OC_S		C_3N^-	CH_3O	SiH_3CN				
SiO		SO_2		PH_3	NH_3D^+					
SiS		c–SiC_2		HCNO	NC_2NH^+					
CS		CO_2		HOCN						
HF		NH_2		HSCN						
FeO		H_3^+		H_2O_2						
O_2		SiCN		HMgNC						
CF^+		AlNC		MgC_2H						
SiH		SiNC		NC_2P						
PO		HCP		HC_2O						

Table 1.2: This table illustrates the range of molecular complexity as observed in molecular clouds in the ISM. More than 190 different molecules have been observed until this point in time [13–15].

the different cloud regions have been described as separate environments, they can be considered as co–existing and mingled together. Still, the definitions simplify explanations when describing the ISM. The last column in **Table 1.1** refers to the extinction of light from stellar sources behind a region being studied. This has briefly been mentioned as changing as the environment of the ISM changes. When observing a dense molecular cloud, the light transmitted from a star behind the cloud is absorbed and scattered as it travels through the cloud where the decrease in emission is referred to as the extinction, A_v, [16]. It is based on a logarithmic scale (**Equation 1**) where A_v = 5 (dense cloud) means that the flux of photons from a stellar source (F^0_λ) is 100 times less after the light has passed through a region (F_λ).

$$A_v = 2.5\log\left(\frac{F_\lambda^0}{F_\lambda}\right) \qquad \textbf{Equation 1}$$

1.2 Molecular Clouds

Molecular clouds are considered as organic syntheses factories and as seen in **Table 1.2**, a huge variety of molecules are observed. This is the reason for this region being of importance and interest in this work. The life cycle of a typical cloud is pictured below in **Figure 1.2** as going from diffuse to dense, protostellar to stellar system and a supernova (SN) event resets the cycle. If a stellar system does not reach a SN event, the chemical richness of the system can still be released back into the gas–phase to a certain extent as the star ages. As this happens, the star will expand and vaporise most of the material in its system.

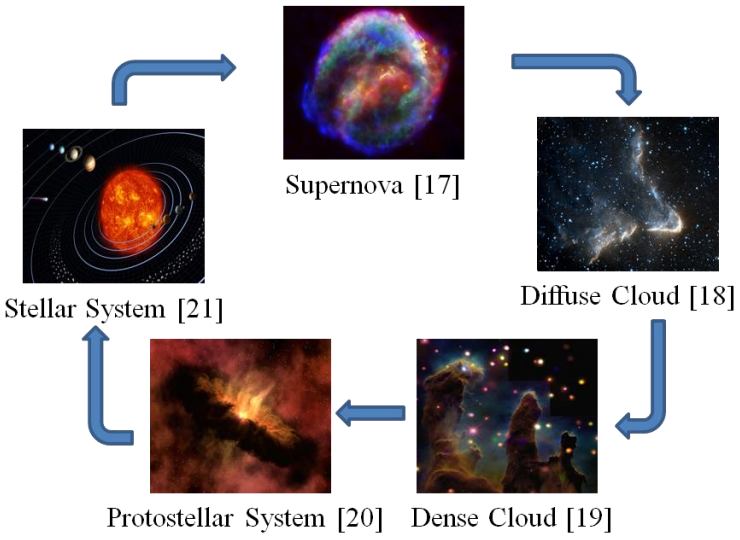

Figure 1.2: These combined pictures show the life–cycle of an interstellar cloud from birth to destruction and rebirth as mentioned in the text.

A dense cloud can be thought of as a diffuse cloud succumbing to gravitational pressure, leading to the highest densities observed in the ISM. As seen in **Table 1.1**. the density can range between $10^3 – 10^5$ molecules cm^{-3} (corresponding to $10^{-13} – 10^{-15}$ mbar as calculated with the ideal gas law and a temperature of 10 K) in molecular cloud cores which increases the efficiency of suitable gas–phase reactions. This is the dominant process, as in diffuse clouds, with a minor contribution from chemistry on surfaces leading to the overall observations of molecules as listed in **Table 1.2** [13–15]. The surface reactions happen on dust grains covered by an icy mantle of various molecules, this will be discussed in greater detail later. As stated in **Table 1.1** molecular clouds are very low in temperature, have a high density dominated by H_2 and a low ionization fraction due to the high extinction factor. The parameters above are linked together through the presence of dust particles found in greater concentration in molecular clouds than in any other region of the ISM. The grains shield the molecular cloud core from UV radiation [11]. This lack of external UV radiation leads to lower temperatures, approaching 10 K [22], as compared to the other regions in the ISM. The dust grains also play a pivotal role in the formation of small hydrides leading to the dominance of H_2 *versus* H in diffuse clouds; this will be discussed in more detail in a later chapter.

Most molecular clouds have a mass of about 10^4 $M_\odot$ ($M_\odot$ = Solar mass) or less [11], but immense clouds have been observed with estimated masses of $10^5 – 10^6$ $M_\odot$ [23, 24]. Such clouds are called giant molecular clouds (GMC), and range in size from $10^1 – 10^2$ light–years across [24]. It was previously mentioned that 4% of the mass of the ISM is baryonic material, and of this 1% is gaseous [25]. GMCs contain most of that percentage of gas even though the volume they occupy is only about 1 – 2% of a galaxy [11]. Regular molecular clouds account for most of the volume of the ISM; they are turbulent systems where the varied chemistry accounting for the numerous chemical species reported in **Table 1.2** can be found. As mentioned, these clouds are considered to be organic molecular factories, and besides giving birth to stars and planets, could also potentially contain the molecules needed for the birth of life. The origins of life are an aspect which generally falls into two distinct categories; endogenous formation or exogenous delivery of molecules necessary for life to appear on Earth.

The endogenous theory involves the very basic elements and molecules being present on a planet after its formation, and through various reactions create bigger and more

complex organic molecules eventually leading to simple and complex life. This thought and approach to the origins of life was revitalised in the scientific community with the Miller–Urey experiments in the 1950's [26, 27]. These experiments are of great importance as they show the possibility of creating over 20 different amino acids, for example glycine and alanine, and several other organic compounds, such as urea, formic acid and lactic acid, from simple starting reagents such as H_2, NH_3, CH_4 and H_2O in conditions believed to be relevant to the early Earth. However, early Earth's atmosphere contained less methane and more carbon monoxide making it less reducing. Another factor concerning the Miller–Urey experiments and the origins of life is that the experiment produced a racemic mixture of amino acids. However, amino acids and sugars contained in human bodies are chiral, where most amino acids are left-handed (or levorotary/sinister) and most sugars are right-handed (or dextrorotary/rectus). Even though the Miller–Urey experiments have some drawbacks, the experimental results are still of great importance as amino acids were created out of simple starting materials.

The other theory is the exogenous delivery of all the starting reagents where the precursors to life are synthesised in molecular clouds and transported to planets *via* comets and meteorites [28]. Amino acids are the building blocks of proteins and contain the necessary elements incorporated in nucleobases. None of these molecules have been unambiguously observed in the ISM, but the necessary elements to form them are present in clouds. Some credence to the exogenous theory has been given due to the detection of chiral amino acids in meteorites and asteroids. The Murchison meteorite which landed in Australia contained various amino acids including glycine and alanine [29, 30] where the L-enantiomer of amino acids has been found to be in excess [30]. The origin of the organic material found in this meteorite has been under debate, the possibility of the meteorite having been contaminated with organic compounds from Earth being the central point of conflict. The conclusion that the organic material found on the Murchison meteorite was of an extraterrestrial origins was determined due to a substantially higher isotopic abundance of ^{15}N than found on Earth [30]. Another meteorite that landed in Antarctica was found to contain similar amino acids to the Murchison meteorite, including glycine and alanine [31]; the organic matter from this meteorite is not under dispute due to the inhospitable Antarctic environment. Various simple organic species, potential precursors of amino acids, such as isocyanic acid and acetonitrile have also been detected to contain in the Hale–Bopp asteroid [32]. Renewed interest with comets and molecules present on them was sparked when the Philae lander

touched down on the 67P / Churyumov–Gerasimenko comet 515 million kilometres from Earth through the Rosetta mission [33]. Measurements on the surface have shown signs of water [34] and organic molecules [35] such as methyl isocyanate, acetone, propionaldehyde, and acetamide which have previously not been noted as being part of comets [36].

For molecules such as HNCO and CH_3CN to be formed, chemical reactions must occur in the ISM. With temperatures approaching absolute zero, and UV radiation not being able to penetrate the cloud cores, only energetically barrierless reactions would have to occur to keep chemistry alive. Barrierless reactions do occur in the ISM between two neutral molecules (more about this in a later section). An energy source is required to create ions and radicals to react with similar or neutrals species, or to bring energy to overcome a potential reaction barrier.

1.3 Sources of Energy

Energy is needed to create species that can undergo barrierless reactions, and it can be used for other reactions to overcome small possible reaction barriers. All of the energy sources can be considered as having their origins from stellar objects. The energy sources discussed in this section can be seen in **Figure 1.3** and their approximate energy in the electromagnetic spectrum [25].

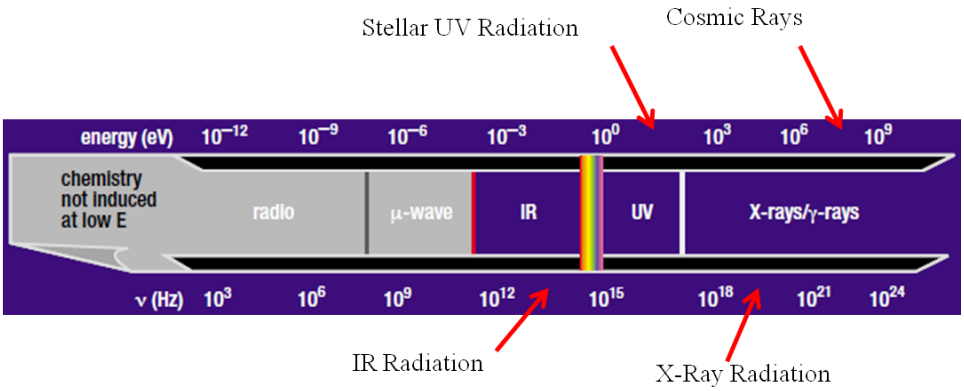

Figure 1.3: This cartoon shows the ranges of energies as found in the ISM used for reactions. The various sources are highlighted here and discussed in the text. This cartoon is taken and adapted from [25].

1.3.1. Cosmic Rays

Cosmic rays can be created in different ways, one is with the release of a stellar wind. These winds are also known as coronal mass discharge, and in our Solar system lead on

to the well known natural phenomenon of aurora. A second way for cosmic rays to be produced is through the violent and widely known event of supernova (SN) explosions [37]. Cosmic rays are composed of different kinds of particles, the most common and abundant is the proton (about 84%) [38]. The helium nucleus is also present but less common, about 14% [39]. The remaining 2% are consistent of many different particles such as electrons, but all of these rays are energetically powerful, as much as 1 GeV [37]. They pass through matter with ease; breaking bonds, ionising or exciting molecules, and the cosmic rays will continue to have energy for further reactions [39]. In this way, a cosmic ray leaves a trail of reactive molecules, ions, electrons or excited molecules, which can react readily. The electrons created are a secondary effect, and a new energy source is created by the cosmic ray referred to as secondary electrons [40, 41] which can lead to chemical reactions or electron promoted desorption. Also, since the cosmic rays have a physical presence, sputtering can occur as they bombard an icy mantle of a dust grain leading to collision–induced desorption.

1.3.2. Photons

Photochemistry is an important factor in the chemistry occurring in the ISM. Photons come in a variety of energies, but the most typical is the Lyman α photon at about 10.2 eV. This photon is emitted when the electron of the hydrogen atom relaxes from the second orbital (n = 2, where n refers to the principle quantum number) back to the first orbital (n = 1) [42].

The UV radiation available for chemical reactions can arise from different sources with stellar UV sources being the most abundant. These photons are used, not only for reactions, but also for the astronomical observations and determination of extinction of light as it goes through different regions in the ISM. The effect the environments (extinction) have on the energy of UV photons can be seen in **Figure 1.4** [43] which is of the interstellar radiation field (ISRF) in a giant molecular cloud.

As has been mentioned earlier, a molecular cloud has a typical extinction factor, A_v, of about 5. From **Figure 1.4**, a drop is observed as A_v changes from 0 through to 200 indicating the difficulty of UV photons to penetrate the cores of dark clouds. Mathis *et al.* concluded that the initial 0.1 – 8 μm of the ISRF traces arise from stellar heating while the remaining 8 – 1000 μm of field comes from re–emitted radiation from the

present dust grains. As these dust grains absorb and scatter UV photons a decrease in photon abundance follows which has been estimated as a 10^4 photon cm^{-2} s^{-1} reduction at $A_v = 5$ as compared to $A_v = 0$ [44].

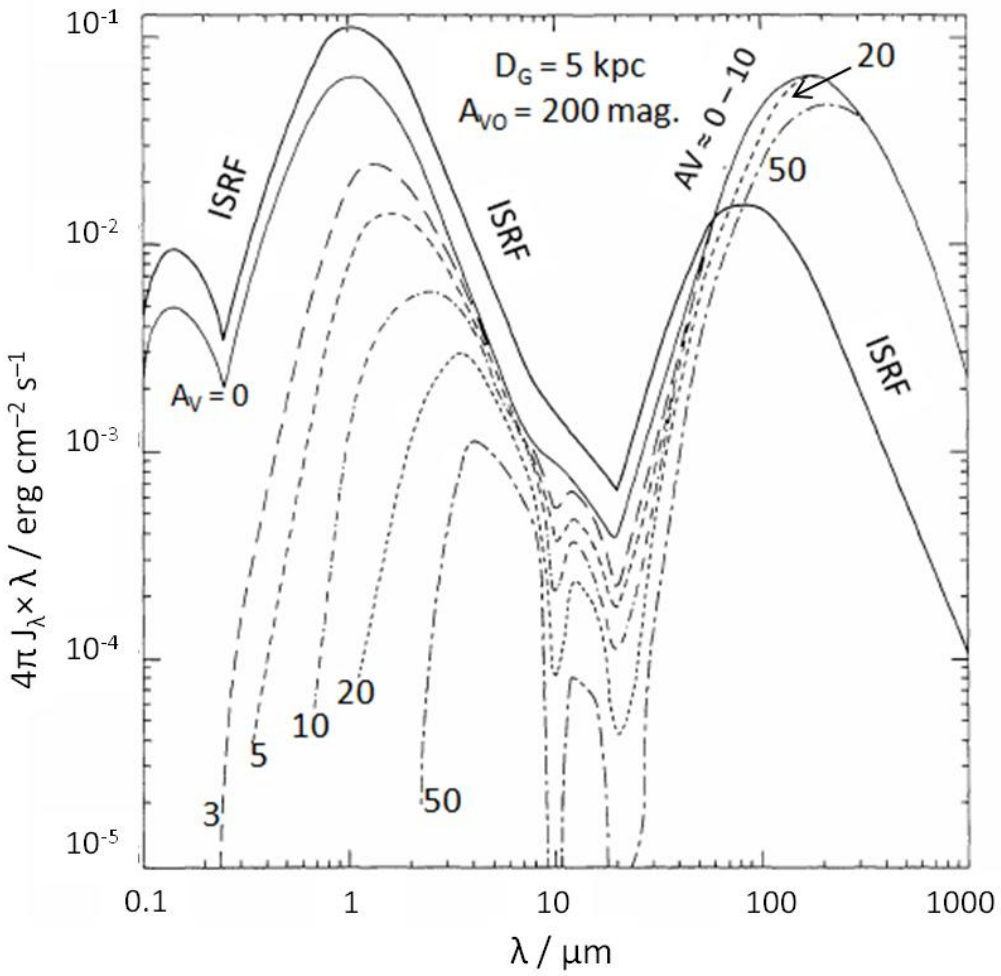

Figure 1.4: This figure is of the ISRF of a molecular cloud. As can be seen, the flux and energy of UV photons decreases as the extinction factor, A_v, increases due to the presence of interstellar dust grains. This figure is taken from [43].

Another type of stellar–based UV radiation is when a star dies. During the SN event when the core of the star collapses, the shockwave created converts the thermal energy of the star's remnants into radiation [45]. Also occurring from a SN event are the cosmic rays mentioned earlier and by their extension the secondary electrons. The electrons can partake in reactions as described above, the products created need to relax back to a ground state and one method for this is by emission of a photon. When this happens an internal UV field is created in molecular clouds; such an internal field can also be created by protostars in a molecular cloud [46].

IR radiation is also a present photon energy source. When a protostar is in the early stages of evolution the main emissions lie in the IR wavelengths and are emitted from the core of the protostar. After about 10^6 years, as the protostar grows, the core becomes optically opaque which prevents the IR radiation from escaping. This typically happens when the protostellar object has reached temperatures of 1500 – 2000 K [39].

Another form of a photon energy source is X–ray radiation which is high in energy. Observations of the galaxy Centaurus A indicated that most of the X–ray emission was below 10^3 eV. They are emitted by young stars and by shockwaves [47], but energies can reach up to 10^4 eV and higher [48].

1.3.3. Thermal Shocks

The same shockwaves described above can also cause a temperature increase when it strikes a gas cloud [1, 49], at the shock front of the cloud the temperature can reach as much as 2000 K [25]. Another source of thermal energy is a protostellar core inside a molecular cloud. The temperature of the protostar depends on the stage of evolution, but it can range from typical molecular cloud temperatures to 10^6 K [39]. As the temperature increases in the vicinity of icy dust grains, the sublimation temperature can be reached releasing molecules into the gas–phase.

1.4 Astrochemistry

Much is known about the chemistry in the ISM, but even more is still to be discovered. In the previous sections, a description of what is present in the astrophysical environment and the different energy sources responsible for the chemical diversity observed in **Table 1.2** has been given. Knowing the above, this section will describe the reactions through which molecules can be created. Only two general types of chemistry exist in the ISM, gas–phase chemistry and surface and solid state chemistry.

1.4.1 Gas–Phase Chemistry

Gas–phase chemistry is the dominant pathway for new molecules to be created in the ISM. It is the dominant process due to gas making up about 99% of baryonic matter in the ISM [50], and under the influence of the various energy sources, *e.g.* UV–photons, cosmic rays and electrons, products listed in **Table 1.2** can arise. Although the

conditions in the ISM are hostile, as explained earlier, gas–phase chemistry still persists through neutral–ion reactions due their barrierless character. These reactions take place between two bodies, while three–body reactions are rare due to the low density even in cold molecular cores [50]. A recent theory concerning desorption from solid surfaces speculates that the icy mantle coating the dust grains in dense clouds could "explode" due to energy being released after the formation of H_2 in the bulk of the ice [51, 52]. The instant after the explosion, the gas–phase density would be similar to the density of the solid ice, which could mean that three–body reactions may be more common than initially thought.

Gas–phase reactions generally happen through one of three pathways; formation of new molecules, bond–rearrangement and destruction of a species [25, 50, 53]. The reactions are reversible, so the opposite of formation reactions can be thought of as destructive mechanisms.

The formation pathways are concerned with the synthesis of larger molecules from smaller starting materials (hereafter denoted as A and B). There are different types of reactions for the formation of molecules;

- Radiative Association:
  - $A + B \rightarrow AB + h\nu$ **Equation 2 (A)**
- Three–Body Reactions (M is the third body):
  - $A + B + M \rightarrow AB + M$ **(B)**
- Negative Ion Reactions:
  - $A + A^- \rightarrow A_2 + e^-$ **(C)**
  - $A + B^- \rightarrow AB + e^-$ **(D)**

An example of a bond formation reaction is for H_2 formation as seen in **Equation 3** through the negative ion reaction pathway (as seen in the generalised **Equation 2(C)**).

$$H^- + H \rightarrow H_2 + e^- \qquad \textbf{Equation 3}$$

This reaction is believed to be one of the primary sources of H_2 in the early stages of the Universe, where H^- forms through radiative association with an electron (reaction **Equation 8(C)** later) [53, 54].

The bond–rearrangement pathways happen between already formed molecules and atoms or other molecules. Below are the general characteristics of such reactions;

- Neutral Exchanges:
  - $AB + D \rightarrow A + BD$ **Equation 4 (A)**
- Ion–Molecule Reaction:
  - $AB + D^+ \rightarrow A + BD^+$ or $A + B^+ + D$ **(B)**
  - $AB + D^+ \rightarrow AB^+ + D$ (charge transfer) **(C)**

An example of a bond re–arrangement reaction can again be displayed through the use of H_2 as in **Equation 5**.

$$H_2^+ + H_2 \rightarrow H_3^+ + H \qquad \textbf{Equation 5}$$

The H_2^+ ion in reaction **Equation 5** can be formed from cosmic ray interaction with H_2. The resulting H_3^+ cation is very important as it reacts with neutral molecules (E) to form hydrogenated molecular cations (EH^+) and molecular hydrogen [50] as displayed in reaction **Equation 6**:

$$H_3^+ + E \rightarrow EH^+ + H_2 \qquad \textbf{Equation 6}$$

The last of the three pathways, destruction, is a reaction route where molecules splinter into smaller fragments. Generic examples are written in the reaction equations below;

- Photodissociation:
  - $AB + h\nu \rightarrow A + B$ **Equation 7 (A)**
- Collisional Dissociation:
  - $AB + M \rightarrow A + B + M$ **(B)**
- Dissociative Recombination:
  - $AB + e^- \rightarrow A + B^-$ **(C)**
  - $AB^+ + e^- \rightarrow A + B$ **(D)**

From the H_3^+ created in **Equation 5**, an electron can be added to create one part H_2 and one part H. This would produce the effect of a dissociative recombination reaction as seen for **Equation 7(D)**.

Another reaction pathway also occurs which is important for the formation of the ions used in the above examples or yielding neutral products and radiation. These reactions usually involve electrons, the source of which can come from cosmic rays;

- Radiative Recombination:
  - $A^+ + e^- \rightarrow A + h\nu$ **Equation 8 (A)**
- Radiative Association:
  - $A + M + e^- \rightarrow A^- + M + h\nu$ **(B)**
  - $A + e^- \rightarrow A^- + h\nu$ **(C)**

From **Equation 8**, the released radiation (hν) can be the formation of the internal UV field present in molecular clouds. There is considerable potential for chemistry *via* these general reactions involving A and B of the above equation when considering the atoms and molecules present in the ISM. Molecular hydrogen is the most abundant molecule in the Universe and has been discussed in the equations above, however larger and unsaturated molecules are also produced through gas–phase chemistry when smaller molecules come together. Generalised examples of the formation of carbon and carbon–nitrogen chain molecules are shown below [55];

- $C_2H + C_mH_n \rightarrow C_{m+2}H_n + H$ **Equation 9 (A)**
- $C_bH_2 + C_aN \rightarrow HC_{a+b}N + H$ **(B)**

where m, n, b and a can have values as leading to the molecules listed in **Table 1.2**.

Many examples of these reactions have been studied in the laboratory and databases have been developed over the years to compile the known gas–phase chemistry, such as the UMIST (Univeristy of Mancherster Institute of Science and Technology) database for astrochemistry (UDfA) [56–60]. Presently, this database contains 6173 gas–phase reactions involving 467 molecules (this includes ions and isotopes) taking into account varying reaction rates in different environments, from dense clouds to stellar regions. Other databases include the OSU (Ohio State University) database [61, 62] and KIDA (Kinetic Database for Astrochemistry) [63]. The input data for these databases are generally the same experimental and theoretical results, however differences between the databases exist due to their individual approach to solving problems and questions. The variations can come in approximating temperature dependence of reactions (if there is one), chosen input values if more than one exists in the literature and if no values

exist (such as rate coefficients) then variations can be seen in how the database has estimated such values.

Many reactions are possible with a pure gas–phase chemistry, and most molecules are made through the pathways introduced. However, when considering all the models and production pathways of small hydrides (H_2, H_2O, NH_3 *etc.*), one finds that the calculated abundances do not match the significantly greater values of abundance observed in the ISM. This leads to the conclusion that other formation mechanisms must be present. This is where heterogeneous chemistry occurring at the surface of interstellar dust grains plays its key role in filling in the gap for the models to account for the observed abundances.

1.4.2 Dust Grain Core

Before an explanation of the heterogeneous chemistry begins, a description of what dust grains and their icy mantle in dense clouds are made of will be given. Observations of dust dates back a long time, and for a long time the grains were considered an irritant as they obscured starlight. From this, the first facts about dust grains can be made; they absorb and scatter certain types of radiation, *e.g.* UV light, and are therefore why molecular clouds appear as black spots in the sky in the UV range [64].

While humankind does not yet have direct access to the ISM and its dust grains, more than 50 particles from comet 81P/Wild 2 were identified by the NASA Stardust Interstellar Dust Collector whereof seven of these are believed to have an interstellar origin [65]. More interstellar dust grains are naturally needed to create a full characterisation of their composition, but for now the exact composition of the dust grains core is not known. Analysis of these collected dust grains revealed that the main component was amorphous silica (SiO_2). This analysis corroborates the spectroscopic data of interstellar dust grains showing strong features in the mid–IR region (1300 cm^{-1} and 500 cm^{-1}) characteristic of the Si–O stretching vibration and O–Si–O bending vibration. However, all interstellar dust grains are likely not mainly made of SiO_2, as the IR frequencies of SiO_2 disappear when observations are turned towards carbon–rich stars. Also the destruction rate of SiO_2 is greater than all interstellar sourced SiO_2 formation rates by about an order of a magnitude [66–68]. Considering this, a general consensus has been agreed upon leading to two kinds of grain cores; one mainly made

of silicate, mostly amorphous, and the other mainly of carbon–containing material of which some is believed to be mainly amorphous [69]. **Figure 1.5 (A)** below shows the contributions of the core material due to the extinction of light by dust grains.

As can be seen in **Figure 1.5 (A)**, SiO_2 (core grain material as shown in the figure), carbonaceous and polycyclic aromatic hydrocarbon (PAH) material are believed to be

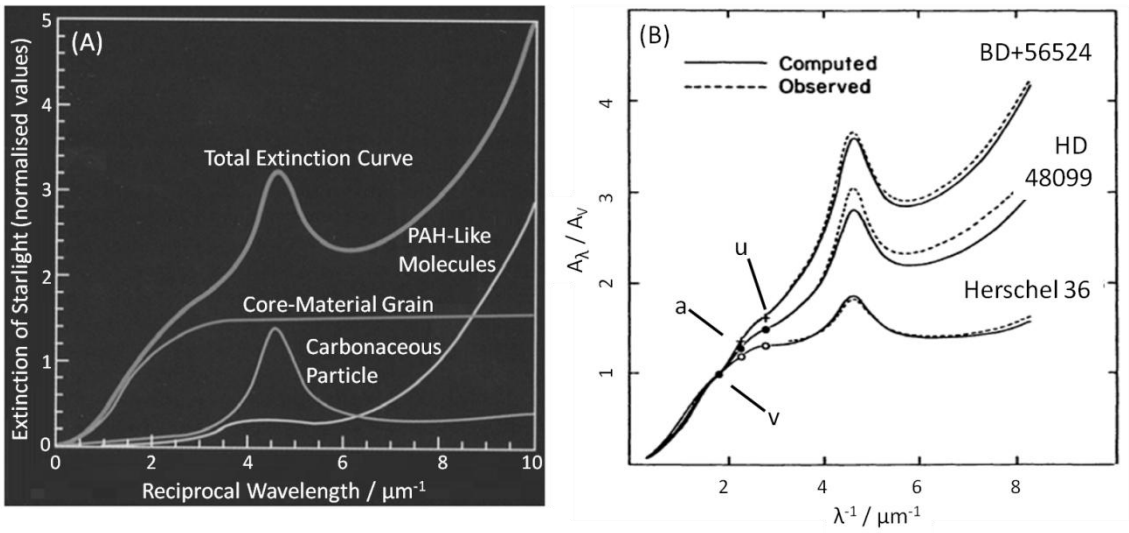

Figure 1.5: These two spectra are of interstellar dust grains. Panel **(A)** [70] shows the various core components of dust grains as being part SiO_2, part carbon–based and possible PAHs. Panel **(B)** [71] shows how the extinction of light due to dust grains change in differing environments, however the general contributions to the profile are still present. This means dust grains are generally made of the same components regardless of location in the ISM.

the main components of interstellar dust grains. This general trend of extinction increasing with the wavelength along with the feature at about 4.6 μm^{-1} are seen throughout the ISM in differing environments as shown in panel **(B)**. The various features highlighted in panel **(B)** in the lower wavelength section are thought to be due to aromatic carbon complexes and H_2O at about 3 μm^{-1} marked as ‘u’. The ‘bump’ at about 4.6 μm^{-1} is thought to be due to carbonaceous material.

Various concentrations of silicate and carbonaceous material along with different metals can be found in the grains. Of the heavier elements present in these cores, one finds iron and magnesium in the greatest abundances [16, 64, 70–72]. Iron metal centres are thought to initially be in the cationic form and as a result of space weathering become iron nanoparticles [73]. With the presence of these metal centres, the chemical structure

of the grains will change. Exact compositions will vary depending of the location, space weathering and environment of the SiO_2 dust grain, however two separate families, orthosilicates and metasilicates are generally accepted. The family classified as $Mg_{2x}Fe_{2(1-x)}SiO_4$ are the orthosilicates can be further characterised as Fayalite (x = 0), Olivine (0 < x < 1) and Forsterite (x = 1). For the metasilicate family, the general chemical formula is $Mg_xFe_{(1-x)}SiO_3$ with further characterisations of Ferrosilite (x = 0), Orthopyroxene (0 < x < 1) and Enstatite (x = 1). Different compounds of PAH are also found as part of dust grains, however these and the orthosilicates and metasilicates families are not studied in this thesis, further details can be found in reference [74]. All in all, the chemically varying components make grains of various sizes, the largest ones being about 0.1 μm [70]. However, recently there has been a pull to re–think the size distribution of dust grains in order to include bigger grains [75,76]. The size and shape of the dust grains have been inferred from observational data as light passes through a dust cloud. An extinction curve can be modelled from the data of absorbed and scattered light as a function of wavelength by incorporating a grain size distribution. Also, considering how star light is not polarised, however becoming polarised as it travels through a molecular cloud gives an idea of the general ellipsoidal shape of dust grains [77].

The lifetime of the grains is not definitely known and varies depending on grain location and environment. Grains in molecular clouds near protostellar regions can be incorporated into the forming star. When a star dies and explodes, *i.e.* during SN events, the shockwave destroys anything within reach. Comet formation is believed to start with dust grains, and is another way dust grains are removed from molecular clouds and the remaining ISM. One estimate of grains' lifetime reaches 5 billion years, spread over a specific cycle each lasting 100 million years. This cycle [70] is described below;

1) In the aCNM (diffuse clouds) the gas and dust grains are thinly dispersed. The dust is composed of a mix of SiO_2, carbonaceous and PAH species.
2) mCNM (dense clouds) is where atoms and molecules adsorb onto the dust grains forming an icy mantle. Dust grains can also clump together to form greater dust grain cores.
3) More complex organic molecules can be synthesised through energetic processing of the icy mantle.

4) As the dense cloud forms a protostar, most of the dust grains are scattered, however some can also form comet nuclei.
5) The dispersed dust grains re–enter the diffuse cloud media. This means more harsh radiation destroys the icy mantle.
6) Following stellar expansion as a star ages or a SN event, dust grains can be shattered along with any remaining organic molecules.

Further to this, dust grain in stellar systems are positively charged through processes including strong stellar UV fields, plasma charging and secondary electron emission of the dust grains [78, 79]. In the interstellar medium, dust grains can either be positively or negatively charged depending on environment. One factor in dust grain charging is the photoelectric emission of an electron as caused by energetic photons can excite electrons in the near–surface forcing them into the gas phase. This could be a process occurring in diffuse clouds due to the presence of VUV radiation and will leave the dust grain positively charged. In denser regions and without the presence of VUV radiation dust grains can become negatively charged due to bombardment of free electrons in the gas phase [77, 80].

1.4.3 Icy Mantle

As stated in the second step of the grain cycle above, an ice mantle is present on grains in the dense clouds of the ISM. These mantles are the second part of describing dust grain composition. The ice is thought mainly to be compact amorphous solid water (c–ASW) [81], and the mechanism for its formation is shown on **Figure 1.6** [82] of which the first line comprising the pure O chemistry will be introduced in **Chapter 3**.

Figure 1.6 shows a great variety and method for the production of H_2O, all of which are possible in the ISM when considering the simple starting materials and energy sources. Various groups have studied the different aspects of this diagram such as O_3 formation [83–86] where hydrogenation leads to H_2O [87]. Direct hydrogenation of O atoms has also been studied going through stages of OH and H_2O_2 [88] of which the formation of H_2O_2 itself has also been investigated [89].

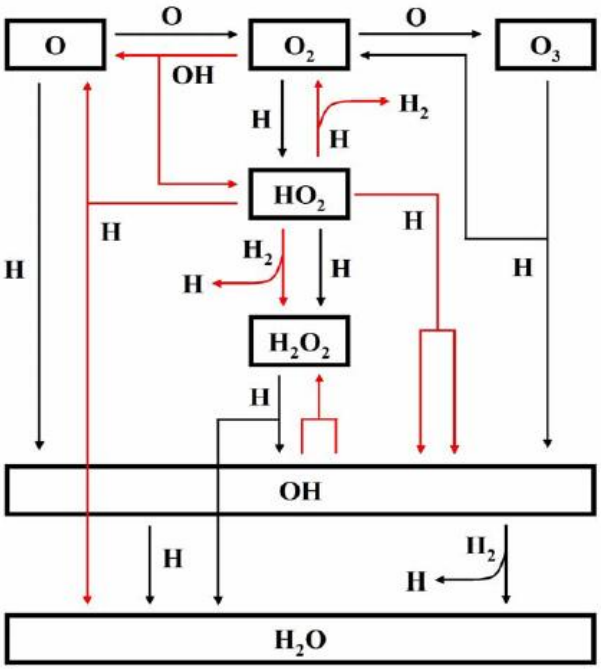

Figure 1.6: This diagram illustrates the formation routes of H_2O on a surface such as an interstellar dust grain. This figure is taken from [82].

No matter the formation pathway, when H_2O forms on interstellar dust grains, a typical 'hit–and–stick' ballistic deposition model is assumed leading to an unstructured network of H–bonds; an amorphous solid. The amorphous structure of ice in the ISM leads to changes in porosity, permeability, surface area and surface chemical activity as compared to crystalline solid water (CSW) [90]; porosity and permeability can be considered to be related as permeability changes with porosity. Temperature–Programmed Desorption (TPD) and Reflection–Absorption Infrared Spectroscopy (RAIRS) laboratory experiments looking at desorption of small molecules, acetone, ether, acetonitrile, chloroform and others, from ASW and CSW have been done. The results lead to the understanding that porosity, permeability and surface area do not have a major effect on adsorbate reactions, but the surface chemical difference plays a role. The reason for this is that H–bond capability decreases by a factor of six as the H_2O changes from ASW to CSW [90, 91].

The icy mantle of the dust grains in the ISM is "dirty" and the many other molecules coating the grains are made on the surfaces or stick to the surfaces from the gas phase. A diagram of a possible "dirty" ice covering a grain of dust can be seen on **Figure 1.7** [92].

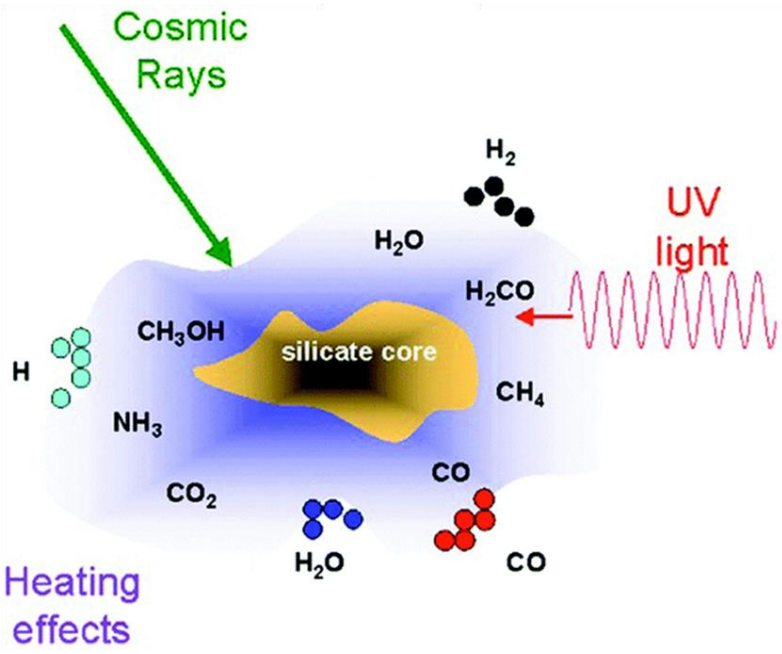

Figure 1.7: This cartoon illustrates a typical interstellar dust grain in the core of a molecular cloud. A mantle of a variety of molecules have adsorbed or accreted onto the silica surface of which H_2O is the dominant species. Also illustrated are various energy sources available for reactions, adapted from [92].

CH_3OH, CO_2, CO and CH_4 are some of the molecules known to be present in the ice coating the dust grains in the ISM, as shown in **Figure 1.8** [93].

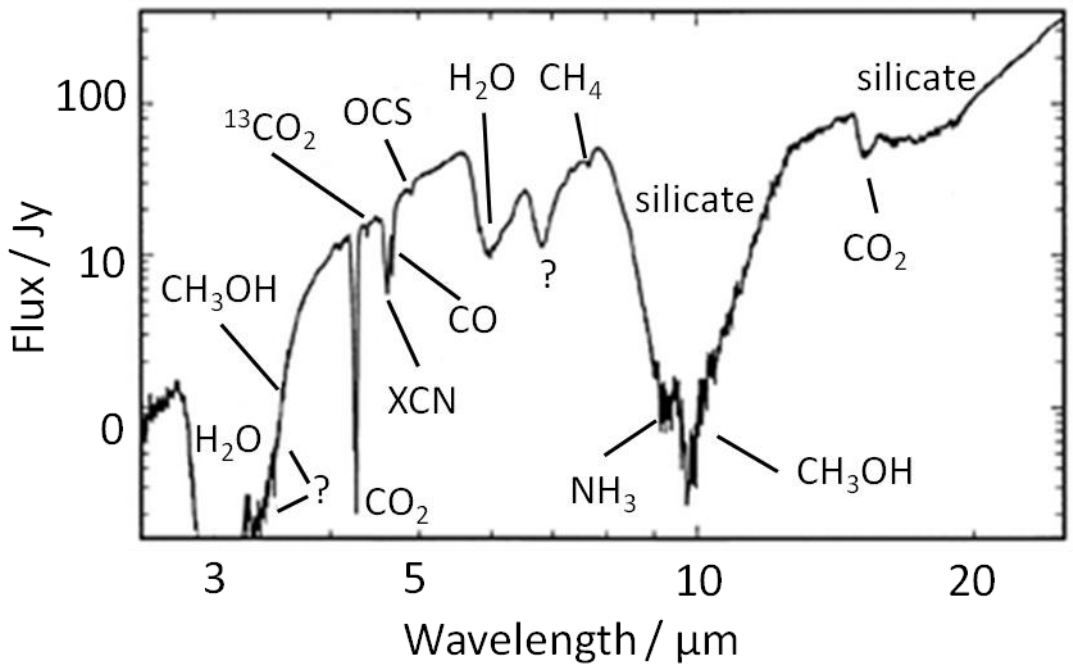

Figure 1.8: This spectrum is of an icy mantle showing the variety of molecules present. This is a spectrum from the Short Wavelength Spectrometer (SWS) of NGC 7538 IRS9 adapted from [93].

As can be seen in **Figure 1.8**, only dominant species and species with very distinct spectral features will be detected in an icy mantle. Also, IR inactive molecules such as O_2 and N_2 which are expected to be found in great concentrations in the ISM [94] cannot be observed in such spectra. Exact number densities of molecules are difficult to determine due to modes overlapping. Ultimately, the composition of the ice is impossible to determine through observational IR spectroscopy alone.

As the Voyager spacecrafts have just left the Solar system, scientists and researchers have naturally not been able to study the composition of dust grain and their mantle by any other means than telescopes. This means that only estimates of the relative abundances of molecules in an icy mantle have been made, but not how molecules are organised. The Onion model has been introduced as a way of visualising how an interstellar dust grain in a dense cloud is composed [95, 96]. This model refers to the bare dust grain being covered in a polar layer which itself is covered by an apolar layer. The terms polar and apolar in this case refer to the H–bond capability meaning that the polar layer is rich in H–bonds (such as H_2O) and the apolar layer is poor (such as CO). Therefore, the Onion model proposes a pure layer of H_2O covering the entire grain surface and molecules such as CO interacting with the surface of H_2O, however not with the grain surface. This idea is understandable considering H_2O being the dominant solid state species in the interstellar grain mantles. However, questions arise when considering the astronomical observations of Pontoppidan *et al.* [97] with a report of three CO features; two for bulk CO and a feature at 2136.5 cm^{-1} which was left unassigned. The work of Collings *et al.* [98] later noted that this feature matched experimental data for CO physisorbed on a SiO_2 surface. The same 2136.5 cm^{-1} feature could also be CO mixed with CH_3OH [99] as this is the final product after hydrogenations reaction. Further experiments with a sub–monolayer of H_2O on SiO_2 have shown that H_2O seems to move from isolated molecules to clustered groups at similar cryogenic temperature as found in dense clouds [98, 100]. The idea of this Onion model will be further investigated in **Chapter 4**.

As seen in the life–cycle of a dust grain in a dense cloud, a multilayer of ice will naturally be formed coating this grain core. Dust grain charges have been mentioned previously and the icy mantle can be charged when excited by one of the energy sources also mentioned. However, the molecular layers of specific species can possibly also produce a noticeable surface charge in the dense regions of the ISM. This can occur

through a spontaneous electric field created as certain dipolar molecules [101–109] such as CO are deposited onto the dust grain [110–112]. This will be discussed in more detail in **Chapter 5**.

1.4.4 Surface Chemistry

As stated earlier, the amount of chemical reactions on surfaces in the ISM is minor compared to gas phase chemistry, but their role is crucial. The importance of dust has been known for a long time [11], but all reaction processes are not known. General reaction pathways are known for model systems and as are possible desorption mechanisms of molecular species after formation. Studying specific reactions will allow for an understanding of chemical processes in molecular clouds, explaining abundances of molecules and possibly clarifying the origins of unknown spectroscopic features observed in the ISM.

In general three different pathways are considered when referring to dust grain surface chemistry: these are the Langmuir–Hinshelwood (L–H), the Eley–Rideal (E–R) and the Harris–Kasemo (H–K) mechanisms which is also known as the Hot Atom mechanism [113].

The L–H mechanism concerns molecules (A and B) firstly adsorbing onto the surface. When the reagents (A and B) diffuse and meet, a bimolecular reaction occurs and the product (C) can desorb from the surface if enough energy is present [72], as represented schematically on **Figure 1.9**. Naturally, the atoms or molecules adsorbing onto the surface might not meet and if they do, they might not react, also A and B might desorb again if they possess enough energy to overcome the adsorption barrier.

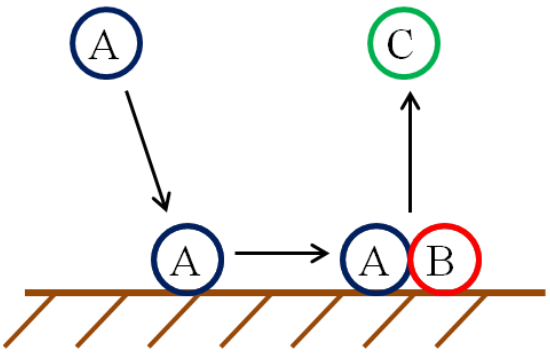

Figure 1.9: The Langmuir–Hinshelwood mechanism, illustrating how atoms or molecules adsorb, diffuse, react and desorb on a surface. As can be seen, both species must be present in the surface.

The E–R mechanism depicted in **Figure 1.10** revolves around one chemisorbed or physisorbed atom or molecule already being present on the surface (B). A second atom or molecule (A) in the gas phase reacts with B, while A never interacts with the surface [72].

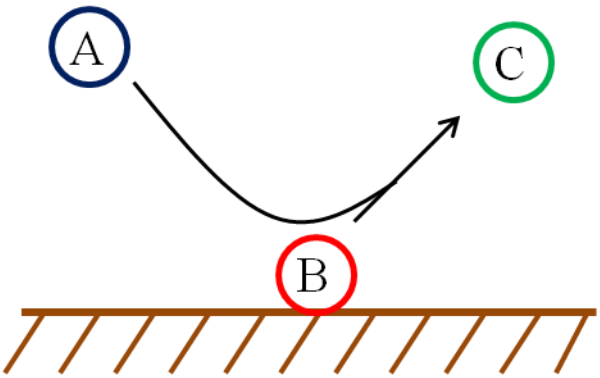

Figure 1.10: The Eley–Rideal mechanism, illustrating how one gas phase species only interacts with an adsorbed molecule to create a new species. The gas phase molecule does not come into contact with the surface at any point.

Both processes above (L–H and E–R) are reversible, possibly leading back to dissociation of molecules into atoms or molecular fragments. When considering the reverse of these reactions, a third mechanism is possible. This process is the H–K mechanism and starts with molecular dissociation. The reverse of the L–H process leads to two species both adsorbed on the surface before molecular formation. The reverse of the E–R mechanism is a molecule breaking into two species where one is adsorbed and the other is in the gas phase. This gas–phase molecule can be high in energy and is now termed a 'hot atom' which might not be released into the general gaseous environment, but can be trapped and can easily diffuse in the ice lattice [114]. This hot atom can now take part in a traditional L–H or E–R mechanism. A general diagram of the H–A mechanism is shown below, **Figure 1.11**.

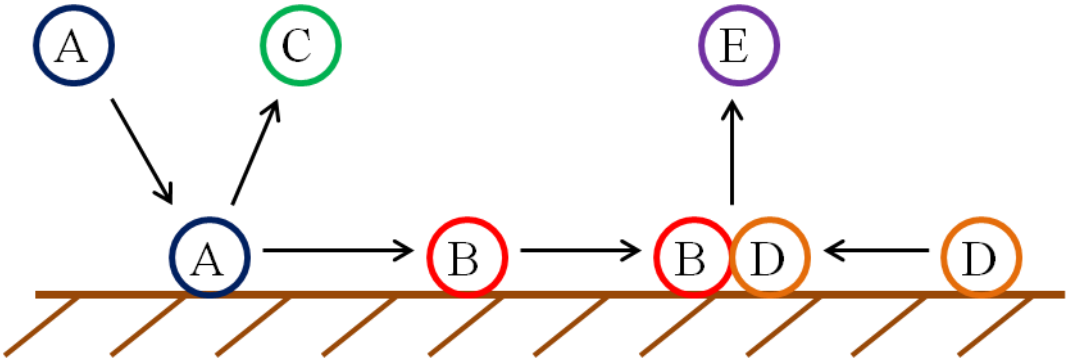

Figure 1.11: The Harris–Kasemo mechanism can be thought of as one part reverse E–R and one part L–H mechanisms. A molecule breaks apart on the surface creating one fragment with excess energy (B) which can diffuse on or in an ice lattice. This hot atom can then react with other molecules to produce (E).

1.5 Thesis Overview

Throughout this chapter, references to later chapters have been introduced. These chapters span three regions of the dust grain cycle from bare dust grains to icy films. Preliminary results about one of the H_2O formation pathways will be discussed, then how small quantities of H_2O behave on a model interstellar grain surface before studying bulk films as found on the dust grain surfaces. A more detailed account of this has been listed below:

- **Chapter 2** will only focus on the experimental theory, equipment and techniques used to obtain results presented in the later chapters.
- **Chapter 3** is the chapter to start a more detailed discussion of how H_2O is formed on a SiO_2 surface at about 20 K which acts as a model interstellar dust grain. These results are currently preliminary, however initial results have shown the formation of O_2 and O_3 from an atomic O beam. To investigate these reactions temperature programmed desorption (TPD) and reflection–absorption infrared spectroscopy (RAIRS) were utilised.
- **Chapter 4** discusses the next step in the grain cycle. Now H_2O has begun to form on the surface and this chapter will investigate the movement of a sub–monolayer coverage H_2O on a SiO_2 surface. The Onion model suggests that H_2O covers the grain surface, however experimental results indicate that the barrier for H_2O to de–wet on a silica surface are negligible. This means H_2O forms islands even in the coldest parts of a molecular cloud leaving bare dust grain surfaces exposed for other molecules to bind and interact with. The results of these experiments were obtained by use of RAIRS.
- **Chapter 5** investigates the multilayers of interstellar dust grains. Multilayers amounts of CO on SiO_2 and a variety of H_2O are studied through RAIRS, however before this N_2O is studied to set a precedent. N_2O has already been shown to harbour a surface potential which in this chapter is studied indirectly through observations of the longitudinal optical and transverse optical splitting as it changes with temperature. Multilayers of CO are then studied with the same technique and view–point to determine the extent and implications of a possible surface potential in such films on interstellar dust grains.
- **Chapter 6** will only look at the conclusions from **Chapters 3**, **4** and **5** while also discussing various and possible future experiment.

1.6 References

[1] C. Sagan, *Cosmos: The Story of Cosmic Evolution, Science and Civilisation* (Abacus, London, 1995)

[2] N.D. Tyson and D. Goldsmith, Origins – *Fourteen Billion Years of Cosmic Evolution* (W. W. Norton & Company, New York, 2014)

[3] S. Miller, *The Chemical Cosmos, A Guided Tour* (Springer, New York, 2012)

[4] R. Panek, *The 4% Universe* (Oneworld Publications, London, 2012)

[5] S. Capoziello, V.F. Cardone and A. Troisi, *J. Cosmology & Astroparticle Phys*., 2006, **08**, 1

[6] L. Amendola, G.C. Campos and R. Rosenfeld, *Phys. Rev. D*, 2007, **75**, 83506

[7] J.T. Wright, O. Fakhouri, G.W. Marcy, E. Han, Y. Feng, J.A. Johnson, A.W. Howard, D.A. Fischer, J.A. Valenti, J. Anderson and N. Piskunov, *Publ. Astron. Soc. Pac.*, 2011, **123**, 412

[8] A. Tsiaras, M. Rocchetto, I.P. Waldmann, O. Venot, R. Varley, G. Morello, M. Damiano, G. Tinetti, E.J. Barton, S.N. Yurichenko and J. Tennyson, accepted for publication in *Astrophys. J.*, arXiv:1511.08901

[9] (a) http://apod.nasa.gov/apod/ap141214.html last accessed: 22/03/16, (b) http://www.eso.org/public/news/eso9934/ last accessed: 22/03/16

[10] J. Alves, C. Lada and E. Lada, *Messenger*, 2001, No. 1, **1**, 15

[11] D.H. Wooden, S.B. Charnley and P. Ehrenfreund, *Comets II* (University of Arizona, Tucson, 2004)

[12] B.E. Turner, *Astrophys. J.*, 2000, **542**, 837

[13] University of Manchester Institute of Science and Technology (UMIST) http://www.udfa.net/

[14] National Institute of Standards and Technology (NIST) http://physics.nist.gov/PhysRefData/Micro/Html/tab1.html last accessed: 22/03/16

[15] the Astrochymist website http://www.astrochymist.org/astrochymist_ism.html last accessed: 22/03/16

[16] J.S. Mathis, *Annu. Rev. Astron. Astrophys.*, 1990, 28, 37

[17] Supernova event: http://www.nasa.gov/multimedia/imagegallery/image_feature_219.html

[18] Diffuse cloud; http://cos.colorado.edu/~burgh/research.html

[19] Dense cloud: http://www.nasa.gov/mission_pages/chandra/multimedia/photos07-019.html

[20] Protostellar: http://isc.astro.cornell.edu/~spoon/crashcourse/protostellar.disk.jpg

[21] Stellar system: http://planetfacts.org/the-solar-system/

[22] P.F. Goldsmith and W.D. Langer, *Astrophys. J.*, 1978, **222**, 881

[23] N. Murray, *Astrophys. J.*, 2011, **729**, 133

[24] N. Murray and M. Rahman, *Astrophys. J.*, 2010, **709**, 424

[25] H.J. Fraser, M.R.S. McCoustra and D.A. Williams, *Astron. & Geophys.*, 2002, **43**, 2.10

[26] S.L. Miller and H.C. Urey, *Science*, 1959, **130**, 245

[27] A.M. Saitta and F. Saija, *Proc. Nat. Acad. Sci. USA*, 2014, **111**, 13768

[28] G.M. Munoz Caro and E. Dartois, *Chem. Soc. Rev.*, 2013, **43**, 2173

[29] M.P. Callahan, K.E. Smith, H.J. Cleaves II, J. Ruzicka, J.C. Stern, D.P. Glavin, C.H. House and J.P. Dworkin, *P. Natl. Acad. Sci.*, 2011, **108**, 13995

[30] M.H. Engel and S.A. Macko, *Nature*, 1997, **398**, 265

[31] K.L.F. Brinton, C. Engrand, D.P. Glavin, J.L. Bada and M. Mauette, *Origins Life Evol. B.*, 1998, **28**, 413

[32] D. Bockelée-Morvan, D.C. Lis, J.E. Wink, D. Despois, J. Crovisier, R. Bachiller, D.J. Benford, N. Biver, P. Colom, J.K. Davies, E. Gerard, B. Germain, M. Houde, D. Mehringer, R. Moreno, G. Paubert, T.G. Phillips and H. Rauer, *Aston. Astrophys.*, 2000, **353**, 1101

[33] J.-P. Bibring, M.G.G.T. Taylor, C. Alexander, U. Auster, J. Biele, A. Ercoli Finzi, F. Goesmann, G. Klingelhoefer, W. Kofman, S. Mottola, K.J. Seidensticker, T. Spohn and I. Wright, *Science*, 2015, **349**, 493

[34] G. Filacchione, M.C. De Sanctis, F. Capaccioni, A. Raponi, F. Tosi, M. Ciarniello, P. Cerroni, G. Piccioni, M.T. Capria, E. Palomba, G. Bellucci, S. Erard, D. Bockelee-Morvan, C. Leyrat, G. Arnold, M.A. Barucci, M. Fulchignoni, B. Schmitt, E. Quirico, R. Jaumann, K. Stephan, A. Longobardo, V. Mennella, A. Migliorini, E. Ammannito, J. Benkhoff, J.P. Bibring, A. Blanco, M.I. Blecka, R. Carlson, U. Carsenty, L. Colangeli, M. Combes, M. Combi, J. Crovisier, P. Drossart, T. Encrenaz, C. Federico, U. Fink, S. Fonti, W.H. Ip, P. Irwin, E. Kuehrt, Y. Langevin, G. Magni, T. McCord, L. Moroz, S. Mottola, V. Orofino, U. Schade, F. Taylor, D. Tiphene, G.P. Tozzi, P. Beck, N. Biver, L. Bonal, J-Ph. Combe, D. Despan, E. Flamini, M. Formisano, S. Fornasier, A. Frigeri, D. Grassi, M.S. Gudipati, D. Kappel, F. Mancarella, K. Markus, F. Merlin, R. Orosei, G. Rinaldi, M. Cartacci, A. Cicchetti, S. Giuppi, Y. Hello, F. Henry, S. Jacquinod, J.M. Reess, R. Noschese, R. Politi and G. Peter, *Nature*, 2016, **529**, 368

[35] I.P. Wright, S. Sheridan, S.J. Barber, G.H. Morgan, D.J. Andrews and A.D. Morse, *Science*, 2015, **349**, aab0673

[36] F. Goesmann, H. Rosenbauer, J.H. Bredehoft, M. Cabane, P. Ehrenfreund, T. Gautier, C. Giri, H. Kruger, L. Le Roy, A.J. MacDermott, S. McKenna-Lawlor, U.J. Meierhenrich, G.M. Munoz Caro, F. Raulin, R. Roll, A. Steele, H. Steininger, R. Sternberg, C. Szopa, W. Thiemann and S. Ulamec, *Science*, 2015, **349**, aab0689

[37] J.C. Everett and E.G. Zweibel, *Astrophys. J.*, 2011, **739**, 60

[38] C.J. Bennett, B. Jones, E. Knox, J. Perry, Y.S. Kim, and R.I. Kaiser, *Astrophys. J.*, 2010, **723**, 641

[39] A.M. Shaw, *Astrochemistry; From Astronomy to Astrobiology* (Wiley, Chichester, 2006)

[40] G.E Morfill, *Astrophys. J.*, 1982, **262**, 749

[41] D. Flower, *Molecular Collision in the Interstellar Medium* 2nd Edition (Cambridge University Press, Cambridge, 2007)

[42] S. Lyman, *Physical Processes in the Interstellar Medium* (Wiley, Birkach, 1977)

[43] J.S. Mathis, P.G. Mezger and N. Panagia, *Astron. Astrophys.*, 1983, **128**, 212

[44] S.S. Prasad and S.P. Tarafdar, *Astrophys. J.*, 1983, **267**, 603

[45] J.C. Raymond, W.P. Blair, K.S. Long, O. Vancura, R.J. Edgar, J. Morse, P. Hartigan and W.T. Sanders, *Astrophys. J.*, 1997, **482**, 881

[46] A.G. Yeghikyan and L. Barsamyan, *Astrophys.*, 2013, **56**, 443

[47] R.P. Kraft, S.E. Vazquez, W.R. Forman, C. Jones and S.S. Murray, *Astrophys. J.*, 2003, **592**, 129

[48] A.E. Jaskot, D.K. Strickland, M.S. Oey, Y.-H. Chu and G. Garcıa-Segura, *Astrophys. J.*, 2011, **729**, 28

[49] J.C. Raymond, *Astrophys. J. Supp. Series*, 1979, **39**, 1

[50] R. Carbo and A. Ginebreda, *J. Chem. Edu.*, 1985, **62**, 832

[51] J.M.C. Rawlings, D.A. Williams, S. Viti, C. Cecchi-Pestellini and W.W. Duley, *Mon. Not. Roy. Astron. Soc.*, 2013, **430**, 264

[52] C. Cecchi-Pestellini, J.M.C. Rawlings, S. Viti and D.A, Williams, *Astrophys. J.*, 2010, **725**, 1581

[53] A.G.G.M. Tielens, *The Physics and Chemistry of the ISM* (Cambridge University Press, Cambridge, 2005)

[54] F. Islam, *Ph.D. Thesis* (University College London, London, 2009)

[55] I. Cherchneff and A. Glassgold, *Astrophys. J.*, 1993, **419**, L41

[56] D. McElroy, C. Walsh, A.J. Markwick, M.A. Cordiner, K. Smith and T.J. Millar, *Astron. Astrophys*, 2013, **550**, 1

[57] T.J. Millar, A. Bennett, J.M.C. Rawlings, P.D. Brown and S.B. Charnley, *Astron. Astrophys.*, 1991, **87**, 585

[58] T.J. Millar, P.R.A. Farquhar and K. Willacy, *Astron. Astrophys.*, 1997, **121**, 139

[59] Y.H. Le Teu, T.J. Millar and A. J. Markwick, *Astron. Astrophys.*, 2000, **146**, 157

[60] J. Woodall, M. Agundez, A.J. Markwick and T.J. Millar, *Astron. Astrophys.*, 2007, **466**, 1197

[61] S.S. Prasad and J.W.T. Huntress, *Astrophys. J.*, 1980, **43**, 1

[62] E. Herbst, http://faculty.virginia.edu/ericherb/research.html last accessed: 22/03/16

[63] V. Wakelam, H.E., J.-C. Loison, I.W. M. Smith, V. Chandrasekaran, B. Pavone, N.G. Adams, M.C. Bacchus-Montabonel, A. Bergeat, K.Bero, V.M. Bierbaum, M. Chabot, A. Dalgarno, V.E.F., A. Faure, W.D. Geppert, D. Gerlich, D. Galli, E.Hebrard, F. Hersant, K. M. Hickson, P. Honvault, S.J. Klippenstein, S. Le Picard, G. Nyman, P. Pernot, S. Schlemmer, F. Selsis, I.R. Sims, D. Talbi, J. Tennyson, J. Troe, R. Wester and L. Wiesenfeld, *Astrophys. J. Suppl. Ser.*, 2012, **199**, 21

[64] B.T. Draine, *The Evolution of the ISM; Proceedings of the Conference, Berkeley, CA. USA*, (Astronomical Society of the Pacific, 1990) page 193

[65] A.J. Westphal, M.R. Stroud, H.A. Bechtel, F.E. Brenker, A.L. Butterworth, G.J. Flynn, D.R. Frank, Z. Gainsforth, J.K. Hillier, F. Postberg, A.S. Simionovici, V.J. Sterken, L.R. Nittler, C. Allen, D. Anderson, A. Ansari, S. Bajt, R.K. Bastien, N. Bassim, J. Bridges, D.E. Brownlee, M. Burchell, M. Burghammer, H. Changela, P. Cloetens, R. Davis, A.M. Doll, C. Floss, E. Grun, P.R. Heck, R. Hoppe, B. Hudson, J. Huth, A. Kearsley, A.J. King, B. Lai, J. Leitner, L. Lemelle, A. Leonard, H. Leroux, R. Lettieri, W. Marchant, R. Ogliore, W.J. Ong, M.C. Price, S.A. Sandford, J.A. Sans Tresseras, S. Schmitz, T. Schoonjans, K. Schreiber, G. Silversmit, V.A. Sole, R. Srama, F. Stadermann, F. Stephan, J. Stodolna, S. Sutton, M. Trielo, P. Tsou, T. Tyliszczak, B.

Vekemans, L. Vincze, J. von Kor, N. Wordsworth, D. Zevin, M.E. Zolensky and Stardust@home, *Science*, 2014, **345**, 6198

[66] A.P. Jones, A.G.G.M. Tielens, D.J. Hollenbach and C.F. McKee, *Astrophys. J.*, 1994, **433**, 797

[67] B.T. Draine and E.E. Salpeter, *Astrophys. J.*, 1979, **28**, 37

[68] C.F. McKee, *Interstellar Dust, Proceedings of the International Astronomical Union, Santa Clara, CA., USA*, IAU Symposium 135,Kluwer Academic Publishers, Dordrecht, 1988) page 431

[69] M. Jura, *Astrophys. J.*, 1986, **303**, 327

[70] J.M. Greenberg, *Sci. Am.*, 2000, **283**, 46

[71] B.T. Draine, *Annu. Rev. Astron. Astrophys.*, 2003, **41**, 241

[72] D.A. Williams and S.D. Taylor, Q.J.R. *Astron. Soc.*, 1996, **37**, 565

[73] S. Sasaki, K. Nakamura, Y. Hamabe, E. Kurahashi and T. Hiroi, *Nature*, 2001, **410**, 555

[74] A.G.G.M Tielens, *Rev. Mod. Phys.*, 2013, **85**, 1021

[75] J. Steinacker, C.W. Ormel, M. Andersen and A. Bacmann, *Astron. Astrophys.*, 2014, **564**, A96

[76] J. Steinacker, M. Andersen, W.-F. Thi, R. Paladini, M. Juvela, A. Bacmann, V.-M. Pelkonen, L. Pagani, C. Lefevre, T. Henning and A. Noriega-Crespo, 2015, http://arxiv.org/pdf/1508.04691.pdf

[77] B.T. Draine, *Physics of the Interstellar and Intergalactic Medium* (Princeton University Press, Princeton, 2011)

[78] D.A. Mendis and M. Rosenberg, *Annu. Rev. Astron. Astrophys.*, 1994, **32**, 419

[79] Q. Ma, L.S. Matthews, V. Land and T.W. Hyde, *Astrophys. J.*, 2013, **763**, 75

[80] L. Spitzer, *Astrophys. J.*, 1941, 93, 369, H.-P. Gail and E. Sedlmayr, *Astron. Astrophys.*, 1975, **41**, 359

[81] E.F. van Dishoeck, E. Herbst and D.A. Neufeld, *Chem. Rev.*, 2013, **113**, 9043

[82] H.M. Cuppen, S. Ioppolo, C. Romanzin and H. Linnartz, *Phys. Chem. Chem. Phys.*, 2010, **12**, 12077

[83] M. Minissale, E. Congiu and F. Dulieu, *J. Chem. Phys.*, 2014, **140**, 074705.1

[84] D. Jing, J. He, J.R. Brucato, G. Vidali, L. Tozzetti and A. De Sio, *Astrophys J.*, 2012, **756**, 98

[85] J. He, D. Jing and G. Vidali, *Phys. Chem. Chem. Phys.*, 2014, **16**, 3493,

[86] B. Sivaramen, C.S. Jamieson, N.J. Mason and R.I. Kaiser, *Astrophys. J.*, 2007, **669**, 1414

[87] H. Mokrane, H. Chaabouni, M. Accolla, E. Congiu, F. Dulieu, M. Chehrouri, and J.L. Lemaire, *Astrophys. J.*, 2009, **705**, L195

[88] H.M. Cuppen and E. Herbst, *Astrophys. J.*, 2007, **668**, 294

[89] M.J. Loeffler, U. Raut, R.A. Vidal, R.A. Baragiola, R.W. Carlson, *Icarus*, 2006, **180**, 265

[90] J.E. Schaff and J.T. Roberts, *J. Phys. Chem.*, 1996, **100**, 14151

[91] J.E. Schaff and J.T. Roberts, *Langmuir*, 1999, **15**, 7232

[92] E. Herbst, *Phys. Chem. Chem. Phys.*, 2014, **16**, 3344

[93] D.J. Burke and W.A. Brown, *Phys. Chem. Chem. Phys.*, 2010, **12**, 5947

[94] E. Dartois, *ISO Science Legacy*, 2005, **119**, 293

[95] L.J. Allamandola, M.P. Bernstein, S.A. Sandford and R.L. Walker, *Space Sci. Rev.*, 1999, **90**, 219

[96] P. Ehrenfreund, A. Boogert, P. Gerakins and A.G.G.M. Tielens, *Faraday Discuss.*, 1998, **109**, 463

[97] K.M. Pontoppidan, H.J. Fraser, E. Dartois, W.-F. Thi, E.F. van Dishoeck, A.C.A. Boogert, L. d'Hendecourt, A.G.G.M. Tielens and S.E. Bisschop, *Astron. Astrophys.*, 2003, **408**, 981

[98] M.P. Collings, V.L. Frankland, J. Lasne, D. Marchione, A. Rosu-Finsen and M.R.S. McCoustra, *Mon. Not. Roy. Astron. Soc.*, 2015, **449**, 1826

[99] H.M. Cuppen, E.M. Penteado, K. Isokoski, N. van der Marel, H. Linnartz, *Mon. Not. Roy. Astron. Soc.*, 2011, **417**, 2809

[100] D. Marchione, *Ph.D. Thesis* (Heriot-Watt University, Edinburgh, 2015)

[101] D. Field, O. Plekan, A. Cassidy, R. Balog, N.C. Jones and J. Dunger, *Int. Rev. Phys. Chem.*, 2013, **32**, 345

[102] R. Balog, P. Cicman, N. Jones and D. Field, *Phys. Rev. Lett.*, 2009, **102**, 2

[103] D. Field, O. Plekan, A. Cassidy, R. Balog and N. Jones, *Europhys. News*, 2011, **42**, 32

[104] O. Plekan, A. Cassidy, R. Balog, N.C. Jones and D. Field, *Phys. Chem. Chem. Phys.*, 2011, **13**, 21035

[105] O. Plekan, A. Cassidy, R. Balog, N.C. Jones and D. Field, *Phys. Chem. Chem. Phys.*, 2012, **14**, 9972

[106] A. Cassidy, O. Plekan, R. Balog, N.C. Jones and D. Field, *Phys. Chem. Chem. Phys.*, 2012, **15**, 108

[107] A. Cassidy, O. Plekan, R. Balog, J. Dunger, N.C. Jones and D. Field, *J. Phys. Chem. A*, 2014, **118**, 6615

[108] A. Cassidy, O. Plekan, J. Dunger, R. Balog, N.C. Jones, J. Lasne, A. Rosu-Finsen, M.R.S. McCoustra and D. Field, *Phys. Chem. Chem. Phys.*, 2014, **16**, 23843

[109] J. Lasne, A. Rosu-Finsen, A. Cassidy, M.R.S. McCoustra, D. Field, *Phys. Chem. Chem. Phys.*, 2015, **17**, 20971

[110] J. Lasne, A. Rosu-Finsen, A. Cassidy, M.R.S. McCoustra and D. Field, *Phys. Chem. Chem. Phys.*, 2015, **17**, 30177

[111] A. Rosu-Finsen, J. Lasne, A. Cassidy, M.R.S. McCoustra and D. Field, *Phys. Chem. Chem. Phys.*, 2016, **18**, 5159

[112] A. Rosu-Finsen, J. Lasne A. Cassidy, M.R.S. McCoustra and D. Field, submitted to Astrophys. J.

[113] A. Nilsson, L.G.M. Pettersson and J.K. Noerskov (editors), *Chemical Bonding at Surfaces and Interfaces* (Elsevier, Amsterdam, 2008)

[114] M. Sano, Y. Ohno, T. Yamanaka, T. Matsushima, E.B. Quinay and K. Jacobi, *J. Chem. Phys.*, 1998, **108**, 10231

Chapter 2

Experimental Theory, Equipment and Techniques

Contents of this chapter

2.1 Introduction

Following observations from the astronomical community, models have been built to interpret and reproduce the observed abundances of atoms and molecules. The multitude of equations describing the chemistry and physics occurring throughout the Universe, such as those used in UMIST database (University of Manchester Institute of Science and Technology) [1], are only as reliable as the kinetic information fed into them. These values can, to some extent, be supplied from laboratory experiments. The focus in **Chapter 1** was mostly on dark molecular clouds where pressures are higher and temperatures are lower as compared to the diffuse interstellar medium. These surfaces, as explained, play a crucial role with regards to the formation of molecules such as H_2, H_2O, NH_3 *etc.* [2, 3] and for that reason the experiments conducted in this thesis are of a surface science nature using interstellar dust grain analogues as the substrate surface.

2.2 Surface Science

In essence, surface science can be summarised by **Figure 2.1**.

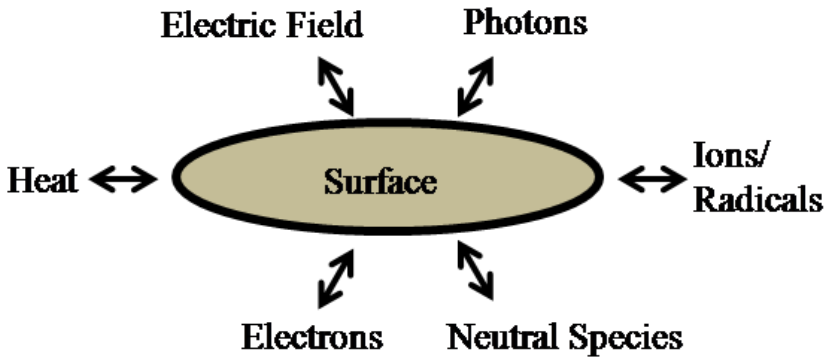

Figure 2.1: The Propst diagram shows what surface science processes are possible and studied in various fields of physical sciences. The main aspects of interest for this work are; electric fields, heat and neutral species.

Figure 2.1 shows a Propst diagram which indicates the fields of interest when conducting experiments on any chosen surface. Chemical species, be they atoms, molecules or radicals, neutral or charged, can be deposited onto a surface. On the surface, the species can be analysed, probed and perturbed before being released to the gas phase. For the sake of this work, the only focus will be on deposition of neutral molecules and atoms, interactions with an electromagnetic field as they are analysed through infrared spectroscopy and thermally heating the species until they desorb where a quadrupole mass spectrometer will detect them in the gas phase above the surface.

In general, surface science experiments are aimed at determining what processes happen on a surface (*e.g.* adsorption mechanisms, reactions, diffusion *etc.*). Analysing the adsorbed molecules can be complemented by the information gathered when molecules desorb in the gas phase due to the microscopic reversibility principle.

Initially, a gas phase species hits a surface where it can either be reflected or accommodated. The rate at which gas phase species collide with a surface, the wall collision rate, Z_w, is given by **Equation 1**.

$$Z_w = \frac{P}{\sqrt{2\pi m k_B T}} \qquad \textbf{Equation 1}$$

where P is the total pressure of the gas, m is the molecular mass of the chemical species, k_B is Boltzmann's constant and T is the absolute temperature of the gas. With **Equation 1**, the time it takes for a complete monolayer equalling 10^{15} molecules cm^{-2} [4] to form covering the entire 6 cm^2 sample surface can be calculated with the results presented in **Table 2.1**. This calculation has been done with N_2 as this is the greatest component of air and by assuming that the temperature of the surface is low enough to allow all incident molecules to stick.

Pressure / mbar	Approximate Time / s
10^{-3}	3.5×10^{-3}
10^{-7}	35
10^{-10} (Experimental Conditions)	3.5×10^{4} (~ 10 Hrs)
10^{-12}	3.5×10^{6} (~1000 Hrs)

Table 2.1: Indicating the approximate times taken for a complete monolayer to be formed at a given pressure. In general, it indicates how long a surface remains clean at a certain pressure. The calculations have been done for N_2 and times will vary depending on the molecule of interest.

The astrochemical surface science experiments that will be described later were done in the ultrahigh vacuum, UHV, region at a base pressure of $1 - 5 \times 10^{-10}$ mbar. **Table 2.1** presents a time of about 10 hours for one ML of N_2 to form on the surface, stressing the importance of using UHV pressures to keep the surface clean throughout an experiment.

The values in **Table 2.1** were calculated with N_2 as this is one of the main contaminant in an ultrahigh vacuum system. H_2 is the most abundant molecule in a UHV due to outgassing from stainless steel surfaces, but as the temperature of the surface is too high for H_2 to stick to it, and as H_2 does not react with the surfaces used or molecules introduced, contamination of H_2 can be disregarded.

The values calculated from **Equation 1** and presented in **Table 2.1** were obtained with an assumed sticking coefficient of unity, meaning that every molecule striking the surface will adsorb on it; however this is not always the case. The sticking coefficient, *S*, can be defined in different ways, one way is as in **Equation 2** and where S_0 is the initial sticking probability of the species incident on a surface and θ is the molecular coverage;

$$S = S_0(1 - \theta). \qquad \textbf{Equation 2}$$

Measuring the sticking coefficient of molecules can be done by the classic King and Wells experiment [5]. These experiments involve directing a beam of gas–phase species towards a surface, obstructing the beam path to the surface is a flag. This flag prevents molecules from sticking to the surface leading to a background pressure of the given molecule which can be measured with a mass spectrometer. When the flag is removed the molecules will bombard the surface onto which they can possibly stick, leading to a drop in the mass spectrometer counting rate. The drop allows the determination of *S*.

Another way of thinking about *S* is one that relates to the rate of adsorption (ν_{ads}) and the rate of collision and can be describe as below in **Equations 3** and **4**:

$$S = \frac{\nu_{ads}}{Z_w}; \qquad \textbf{Equation 3}$$

$$\nu_{ads} = \frac{k_t}{1 + {k_d}/{k_a}}. \qquad \textbf{Equation 4}$$

The variables k_t, k_d and k_a are rate constants for trapping, desorption and adsorption respectively. Trapping refers to the intermediate state of a molecule between the gas phase, desorbed, and being adsorbed to the surface.

Another factor to consider when mentioning molecules adsorbing to a surface is the accommodation coefficient (α). α is concerned with the ability of atoms and molecules effectively transferring their thermal energy to the surface. If the transfer is efficient, the species will not have enough energy to be reflected from the surface, but will instead be adsorbed. The thermal accommodation coefficient is defined as seen in **Equation 5**;

$$\alpha = \frac{T_f - T_i}{T_s - T_i} \qquad \textbf{Equation 5}$$

where T_i is the initial temperature or energy of a molecule before a collision with the surface while T_f is the temperature of the molecule after a surface collision. T_s is the temperature of the surface on which the gas–phase molecules collide. When α = 1, all species are accommodated onto the surface and are adsorbed, whereas when α = 0, no species are accommodated.

Now that molecule have stuck and been accommodated on the surface, two processes with regards to the interaction of the molecule to the surface can happen, chemisorption or physisorption. The two can broadly be regarded as extreme forms of adsorption. Chemisorption is associated with strong, typically in the hundreds of kJ mol^{-1} [6], short range interactions where electrons are shared between adsorbate and surface. In chemisorbed systems, a bond between the surface and adsorbate can be thought to exist as a traditional covalent bond where the electrons are shared between atoms in a molecule. The bond can also be an ionic bond where an electron has been transferred from one molecule to the other. Physisorption does not involve electron sharing or transference between the adsorbate and surface, the interactions are of a van der Waals nature with typical values in the tens of kJ mol^{-1} [6]. Physisorbed species are the types of systems of interest in this work.

2.3 Experimental Equipment

2.3.1 Instrumentation

This section discusses how the theory is put into action to simulate the environment found in a molecular cloud and the surface used as an analogue of interstellar dust grain. Literature regarding of the UHV rig can also be read elsewhere [7, 8]. **Figure 2.2** shows a general picture of the UHV rig and **Figure 2.3** shows the schematic.

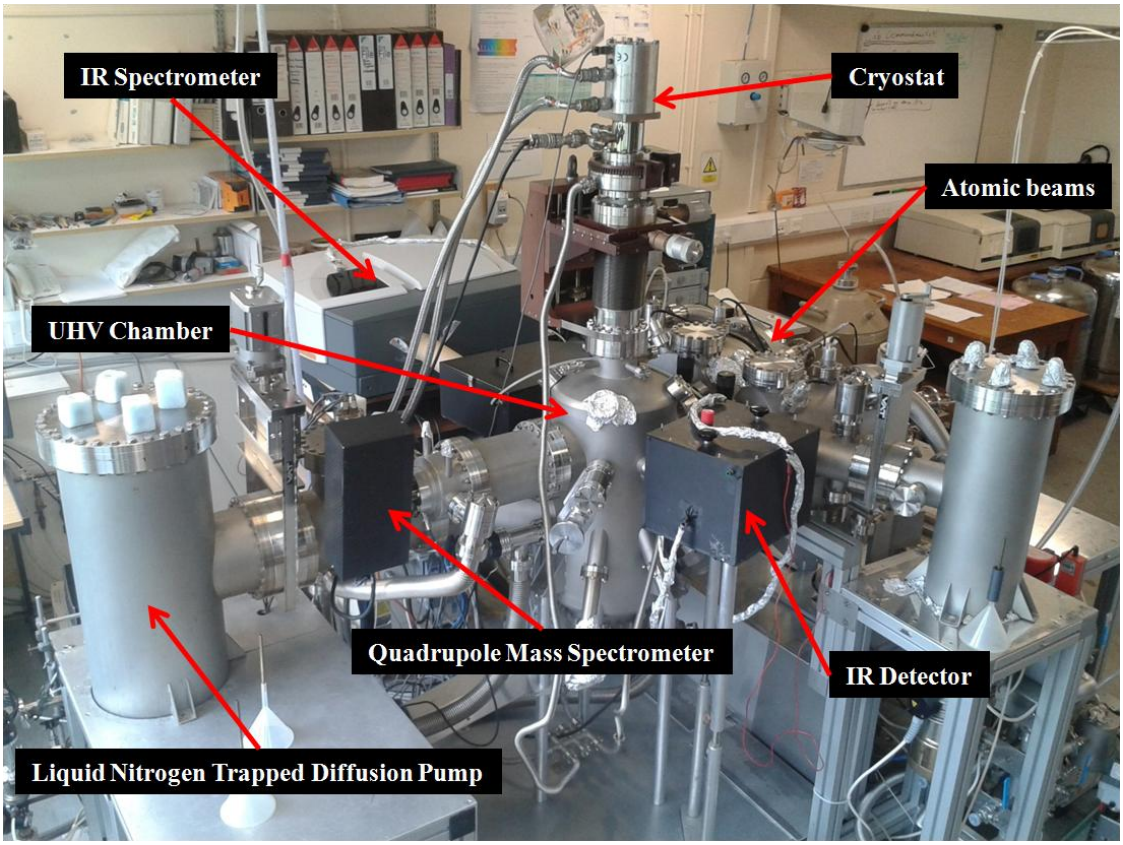

Figure 2.2: A picture of the UHV rig used for this work and the main experimental aspects labelled with red arrows.

In general, the requirements for surface science in a UHV system are few; a chamber is needed with pumps to create the vacuum, a sample is necessary to deposit the desired molecules onto in order to investigate and analyse the surface processes through whichever desired technique.

The central component of the UHV setup is a 30 cm diameter stainless steel chamber (Instrument Technology Ltd.). To evacuate the chamber, three different kinds of pumps are used; A mechanical rotary pump (Edwards High Vacuum International, E2M18) which backs a liquid nitrogen trapped 6" diffusion pump (Edwards High Vacuum International, E06), additionally a liquid nitrogen trapped titanium sublimation pump (AML, TSP2) is used to reduce the residual oxygen–containing species in the gas phase. A gate valve separates the diffusion and sublimation pumps. A nude hot cathode ionization gauge (Instrument Technology Ltd.) with thoria filaments calibrated to N_2, is used to measure the pressure inside the chamber. The operational pressure range of this ion gauge is $10^{-4} – 10^{-11}$ mbar.

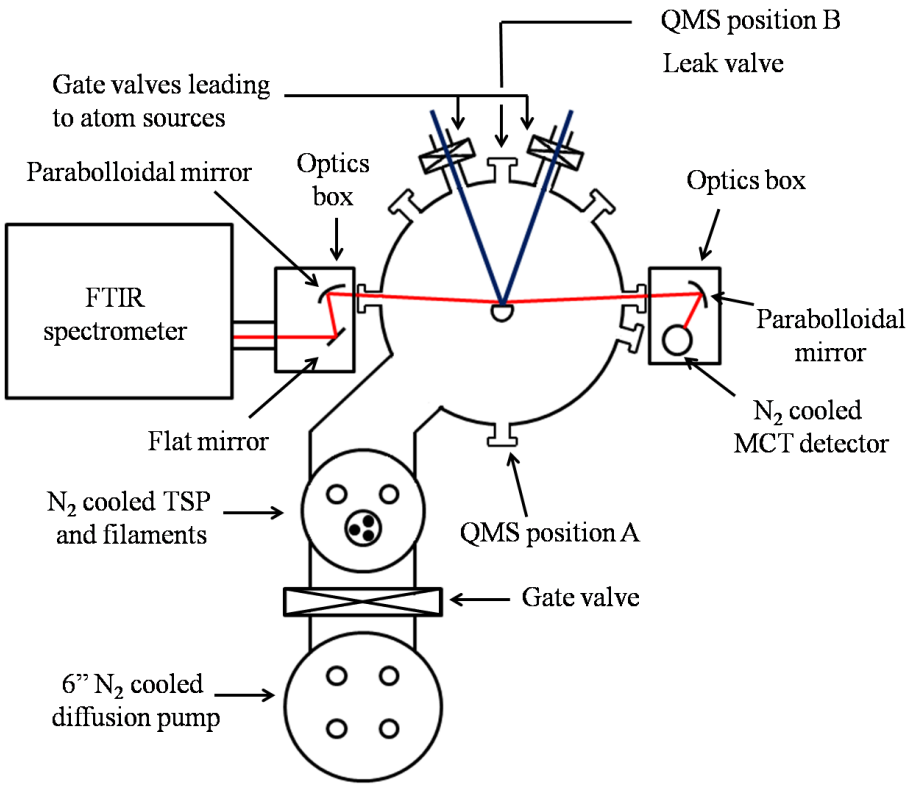

Figure 2.3: A detailed sketch of the UHV rig used for this work. The atomic beams have not been shown, but will be detailed later in **2.3.5**. The sketch is not to scale.

2.3.2 Cryostat and Sample

The sample used until this point in time is a copper substrate coated with a layer of silica. The sample is fixed at the end of a cold finger manipulator with XYZ translations and a virtual rotation of 360° about the Z axis, **Figure 2.4**. The cold finger itself is a 1 m long stainless steel tube connected and cooling the sample through a closed–cycle helium cryostat (APD Cryogenics, HC–2). The cold finger is surrounded by a 1 m long gold coated oxygen free high conductivity copper tube acting as a cryoshield (this is only cooled through the first stage of the cryostat). The reason for the cryoshield is to create a cryogenic microenvironment around the cold finger and sample mount lessening radiative thermal gain from the surrounding environment. The sample, **Figure 2.5**, is regularly cooled to below 20 K. Inside the copper sample block, a cartridge heater (Heatwave Labs Inc., TB–175) is placed which is used to heat the sample surface. To measure the temperature two KP–type thermocouples are used. A KP–type thermocouple is made of two wires, gold and chromel (90% Ni and 10% Cr), with the connecting junction where the temperature needs to be measured. One KP thermocouple is located directly on the sample and the other at the bottom of the cold finger. The reason for the KP thermocouple on the cold finger is to monitor when the sample mount

and cold finger are heated enough to allow desorption which could interfere with the species of interest desorbing from the sample.

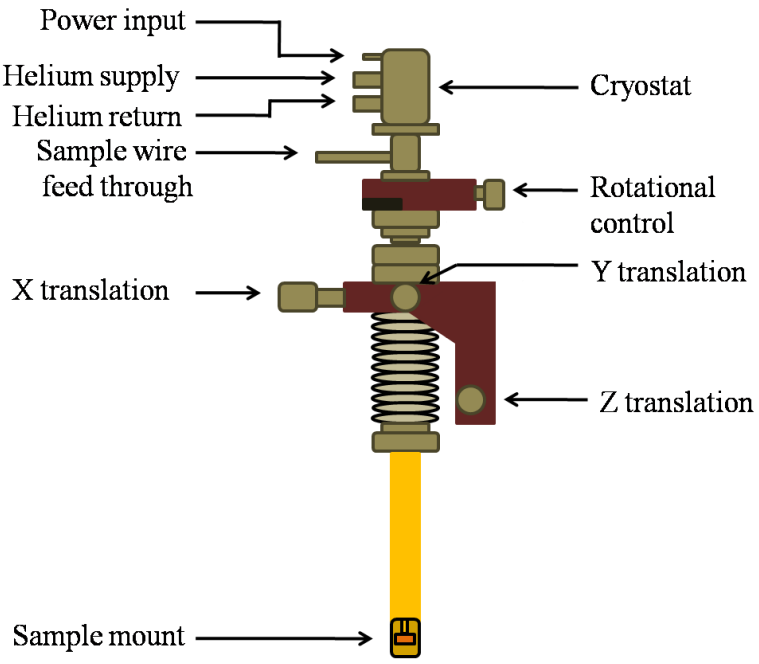

Figure 2.4: A sketch of the entire manipulator with the closed–cycle He cryostat cooling the sample to a minimum base temperature observed for this work of 17 K. The sample has XYZ translations and a virtual 360^{o} rotation.

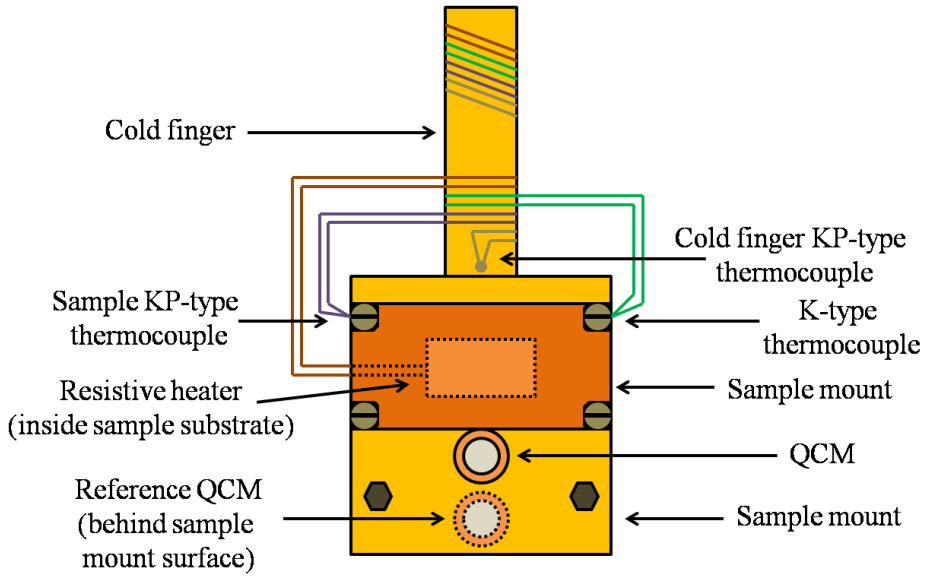

Figure 2.5: The sample itself located at the end of the cryostat. The Cu block is coated with SiO_2 and a cartridge heater selectively heats only the sample block. Two KP–type thermocouples register the temperature throughout experimental work.

2.3.3 Silica Deposition

As will be explained later in this chapter, using a bare metal surface will mean that the metal surface selection rule (MSSR) is in full effect. For this reason, the TO mode of the LO–TO splitting will not be observed; as will also be explained later. Therefore a film of SiO_2 is deposited onto the Cu surface to lessen the MSSR, another reason is for the surface to mimic a bare interstellar dust grain.

Before SiO_2 deposition, the sample has to be cleaned from potential contaminants. This was done by roughly polishing the surface with a 1 μm grain size water/oil emulsion diamond paste (1–KD–C1, Kemet International Ltd.) on a polishing pad, before another 1 μm grain size water based diamond paste was used (1–W–C2, Kemet International Ltd.) on a different polishing pad of the same grain size. At the end of this procedure a mirror finish to the Cu was obtained. Electron beam evaporation of SiO_2 straight onto clean Cu was attempted, however a controlled amount of SiO_2 was difficult to obtain. SiO_2 deposition on stainless steel surfaces is possible and has been done previously in this research group [9–11]. Expecting a stronger interaction with Cu if the surface was not clean, but rather oxidised, meant the clean, polished Cu surface was oxidised with a 1:1 ratio 2 mol dm^{-3} HNO_3 and distilled H_2O. A filter paper was slightly wetted (a couple of drops from a glass pipette) with the mixed solution and the polished Cu surface was placed onto the moist filter paper. This changed the mirror finished Cu surface to an oxidised matt surface. The sample block was then transferred to a different vacuum chamber for the electron beam evaporation of SiO_2 onto the oxidised Cu. A schematic and picture of the chamber can be seen in **Figure 2.6**.

The chamber consists of a liquid nitrogen cooled 6'' diffusion pump (Edwards High Vacuum International, E06) backed by a rotary pump (Edwards High Vacuum International, E2M18) capable of pumping down the chamber to a high vacuum of about 10^{-6} mbar as measured with an ion gauge. The chamber is not baked between transferring samples inside, leaving a background contamination of H_2O. This meant that the surface of the sample is further changed from pure SiO_2 to having a coating surface of silanol, SiOH, groups. Inside the chamber an ingot of SiO_2 quartz was placed in a receptacle with the oxidised Cu surface placed directly above it, a picture of this can be seen in **Figure 2.6**.

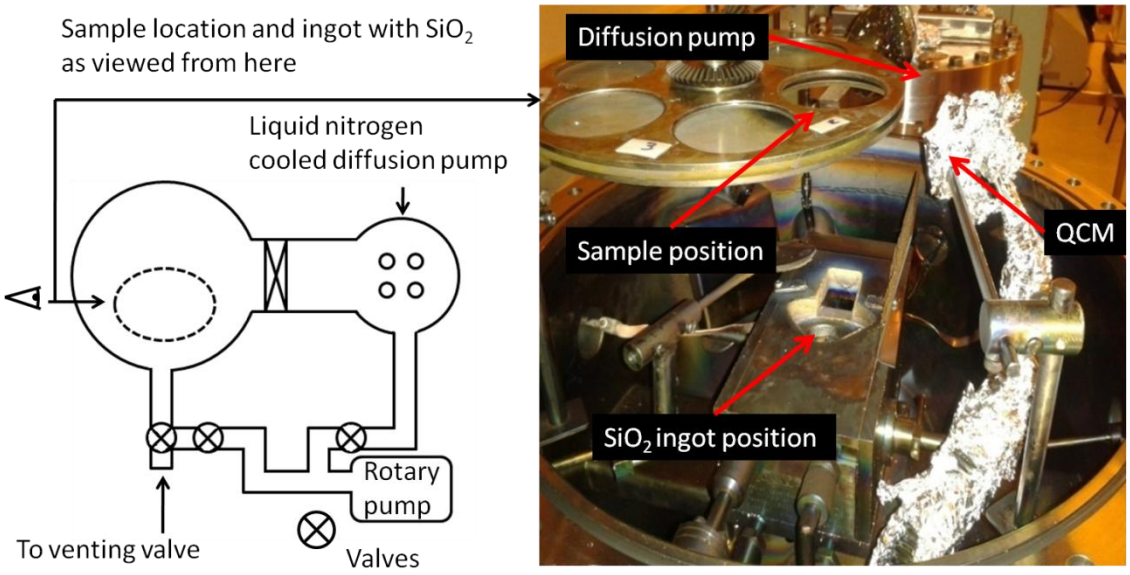

Figure 2.6: To the left is a schematic of the SiO_2 deposition chamber reaching base pressure of 10^{-6} mbar. To the right is a picture of the chamber as viewed from the left side of the rig. The SiO_2 is placed in the path of an electron beam which evaporates it, the sample is positioned directly above the SiO_2 and the rate of deposition is monitored by a QCM.

After reaching a base pressure in the 10^{-6} mbar range, the quartz crystal microbalance, measuring deposition rate, was configured for SiO_2 quartz. Configurations in terms of an impedance factor of 8.25 and a density of 2.2 g cm^{-3} [12] were set before the electron beam evaporation was started. The QCM was placed in close proximity to the sample to ensure a simultaneous and similar growth rate of SiO_2 on both surfaces. Using a mA current, the layer thickness was monitored and a thickness of 300 nm SiO_2 was obtained on the QCM and therefore also on the surface of the oxidised Cu.

The newly coated sample blocks were then transferred to the UHV system described earlier where a RAIRS scan was done in an attempt to observe the longitudinal optical and transverse optical (LO–TO) splitting of SiO_2 (a more detailed description of the LO–TO splitting will follow in **Chapter 5**). The results of this have been shown in **Figure 2.7** where a clear change is observed in the SiO_2 νSiO stretching mode peak position at 1241 cm^{-1} [13] as compared to the spectra of pure Cu (experiments here were done with a resolution of 1 cm^{-1}).

The deposition procedure allows for two samples to be coated with SiO_2 at a time. A simple method to check whether SiO_2 has been deposited onto Cu can be done without

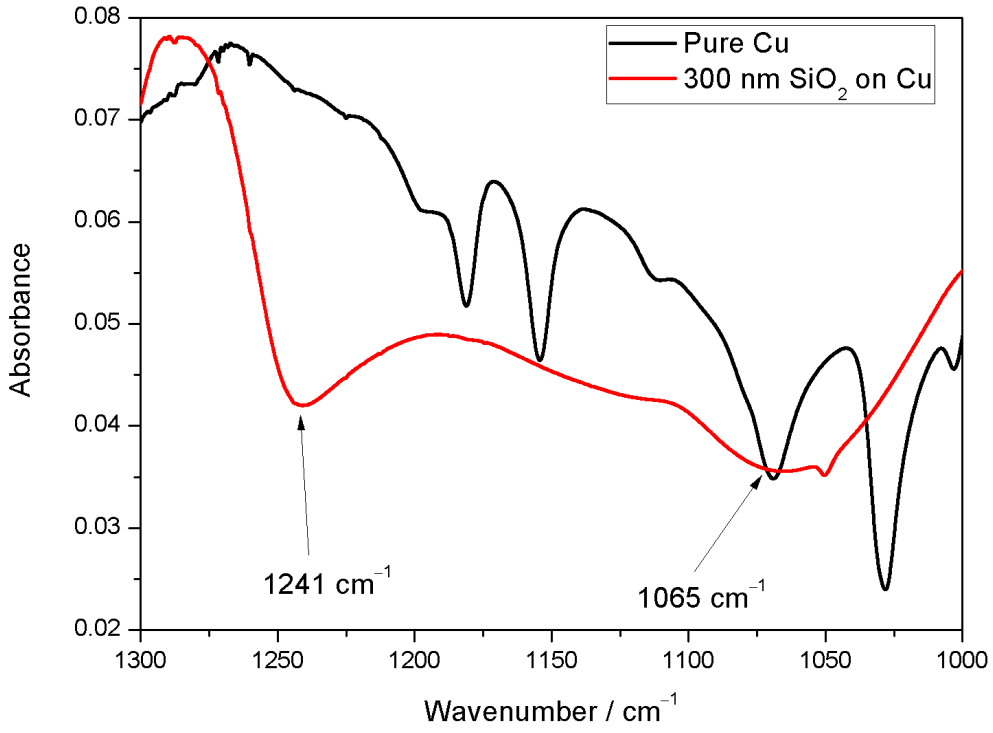

Figure 2.7: Two background spectra showing the difference between a clean Cu sample, black, and one with SiO_2, red, deposited onto it. The 1241 cm^{-1} feature is the LO mode and the 1065 cm^{-1} is the TO optical mode of SiO_2.

the use of an analytical technique such as IR spectroscopy. Droplets of liquid H_2O on SiO_2 will wet the surface, whereas it will form clusters on Cu. The results of this can be seen in **Figure 2.8** where the e^- beam evaporation of SiO_2 onto Cu only managed to coat part of the surface.

Figure 2.8: This shows a simple test to verify if a layer of SiO_2 has been deposited, where droplets of H_2O appear to wet SiO_2 and clusters on Cu. The cloudy material on the left side of the sample is SiO_2 which has not stuck properly to the sample and would not be used in the UHV rig, however for the H_2O test this will suffice.

As can be seen, the gray patch is SiO_2 where the H_2O is barely visible as it has spread over the surface in contrast to the right side of the picture where clusters have formed. This is due to the hydrophilic and hydrophobic nature of SiO_2 and Cu, respectively, with respect to liquid H_2O. This is the macroscopic behaviour of H_2O on Cu and SiO_2, however the microscopic viewpoint of solid H_2O on SiO_2 will be discussed in **Chapter 4**.

2.3.4 Background Deposition

To introduce the desired chemical species into the UHV chamber, two fine–control leak valves (VG Ltd.) are used. Reagents are in glass bulbs or vials linked to the leak valves through a glass gas handling line under rough vacuum, picture in **Figure 2.9.**

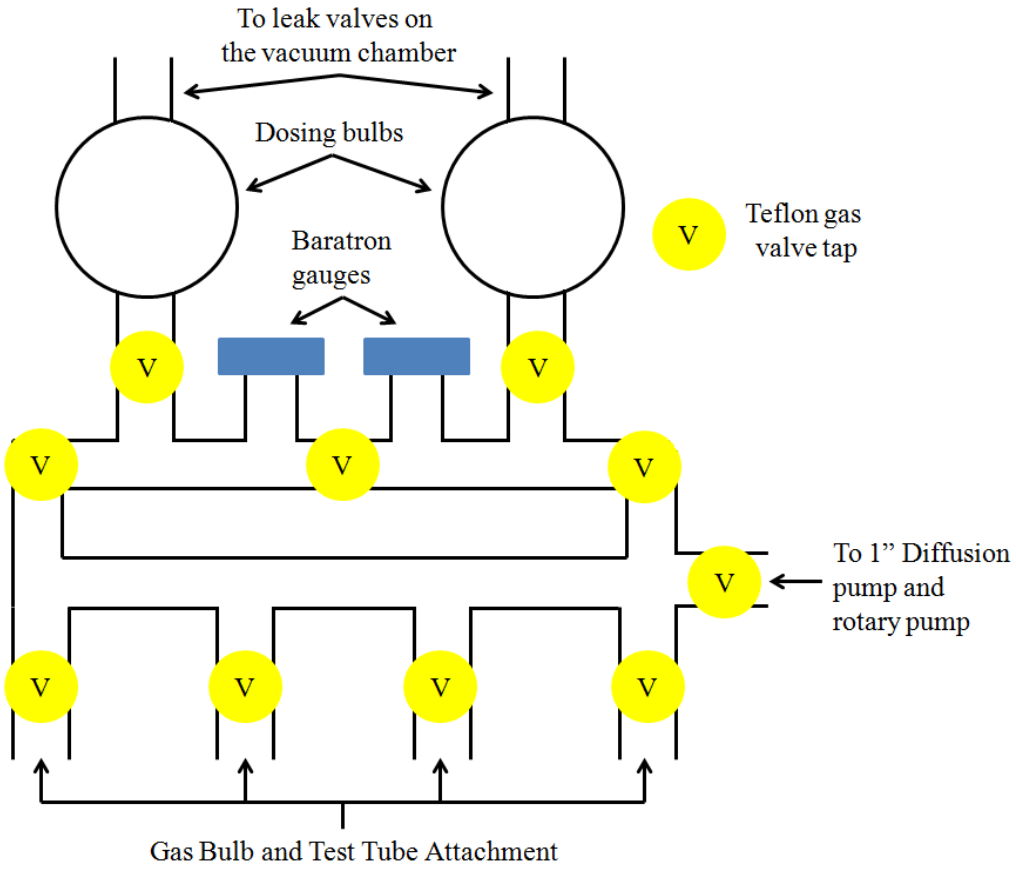

Figure 2.9: A diagram showing the connection of the dosing lines to the leak valves of the UHV chamber. The lines are regularly evacuated and a small volume of gas or vapour containing the molecules of interest is expanded into the dosing bulbs for experimental use.

A general clean of the gas lines is done daily with the species to be used for experiments by expanding a small volume of gas or vapour into the gas handling line before pumping it out again. This procedure is repeated in triplicate. If the compound used is a

liquid, such as H_2O, several freeze–pump–thaw, FPT, cycles may be done prior to the gas clean. FPT cycles are done by freezing the liquid with liquid nitrogen, then opening up for the pump to pump directly on the newly formed solid. As the solid thaws, the pressure slowly increases and more volatile contaminants are pumped away. The solid is then isolated from the pump and left to thaw until becoming a liquid again, this process is also done thrice.

The dosing bulb(s) is(are) then filled with the desired chemical species and deposition can be done through the leak valve(s). When dosing a certain species, the exposure of the surface to the gas needs to be controlled. In surface science, the exposure of a surface to an adsorbant is measured in Langmuir, L. The definition of 1 L is a pressure of 1.33×10^{-6} mbar (10^{-6} Torr) for a period of 1 second. The ionisation coefficient (γ_i) is important when dosing a gas. The ionisation coefficient is the amount of ionised fractions of one molecule of the gas species after it has been ionised by the electrons emitted by the filament of an ion gauge. γ_i has been accounted for in all experiments through the work of Bartmess and Georgiadis [14] and the coverages used are representative of true Langmuir units. Through experimental measurements the exposure in L can be reported in terms of monolayers, ML.

2.3.5 Atomic beams

2.3.5 (a) Introduction

Any molecule can be broken down into its atoms if enough energy is supplied. The easier a molecule is to ionise and the lower the bond dissociation enthalpy is, the lower the energy needed to break it down will be. O_2, as used for the atomic beam in this work, is relatively easy to form even though it has a bond dissociation enthalpy of 497 kJ mol^{-1} [15] due to the double bond. Forming an O atom plasma can not only be done through radio frequency, RF, sources as in this work, but microwave, MW, sources can also be used and a carrier gas, such as He or Ar, can be used if desired [16]. The dissociation fraction of O_2 in MW sources can range from 8 – 12% [17] to 45 – 80% [18] depending on O_2 pressure and power of the source. RF sources can produce a dissociation fraction of O atoms of the order of 25% [19] which is similar to the previously determined cracking fraction of the RF sources used in this thesis (32% ±

9%) [8]. As stated earlier, energy is needed to make the desired atomic fragments from a molecules, **Figure 2.10** shows the potential energy diagram of O_2 and its dissociation.

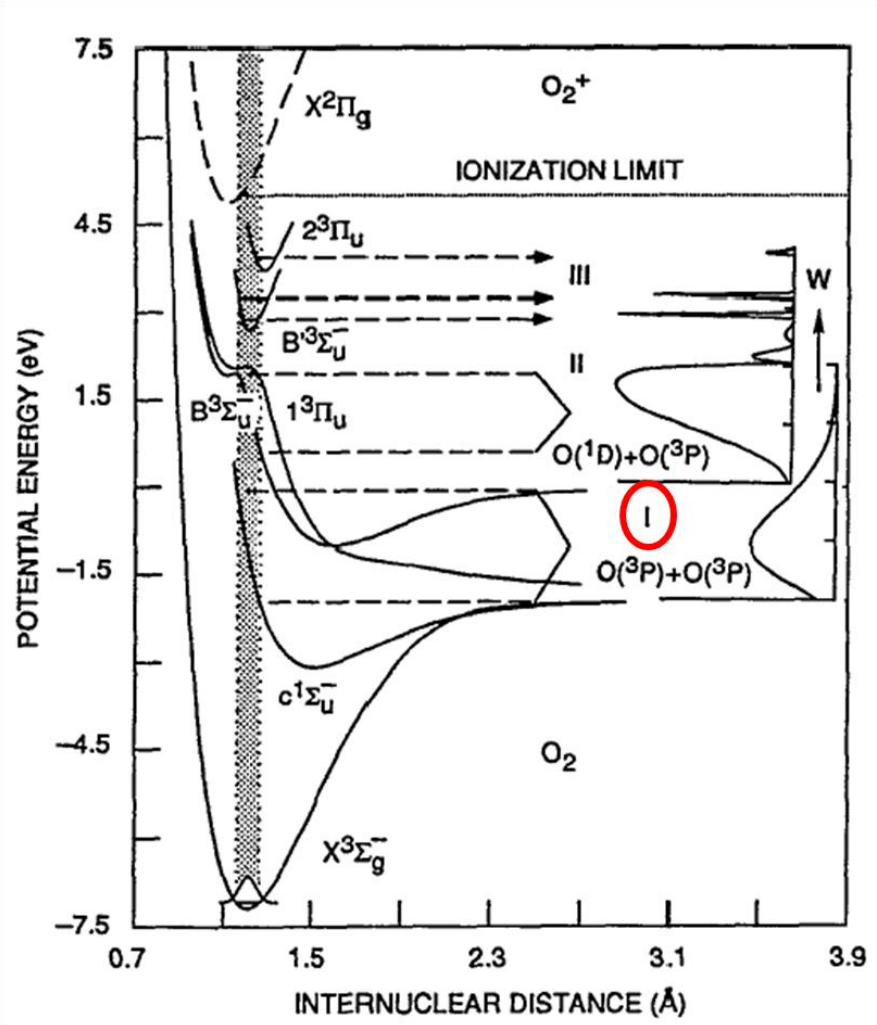

Figure 2.10: This graph shows the potential energy diagram of O_2 and what energy levels are needed to excite, dissociate and ionise O_2. The region labelled l with a red circle is the atoms of interest, $O(^3P)$, for this work.

Looking at **Figure 2.10** above, different excited states can be seen, all originating from the ground state O_2, $X^3\Sigma^-_g$, and rising through the shaded area [20]. The aim of this work is to obtain ground state O atoms, ^3P, through the RF sources with minimal contamination with other species, the region where $O(^3P)$ is formed is labelled I and is marked with a red circle in **Figure 2.10**. The simple solution would be to supply a gas of O_2 with 5.16 eV (497 kJ mol^{-1}) of energy to simply split the molecule, however, this transition is spin forbidden. For this reason O_2 firstly needs to be promoted to the high energy level of the excited state, $c^1\Sigma^-_u$, *via* a 6 eV transition, the system can then relax to the dissociation limit yielding the desired $O(^3P)$. A Grotrian diagram of the electronic

transitions in the O atom [21] can be set up to show all the transitions and the transition observed in this work, **Figure 2.11**.

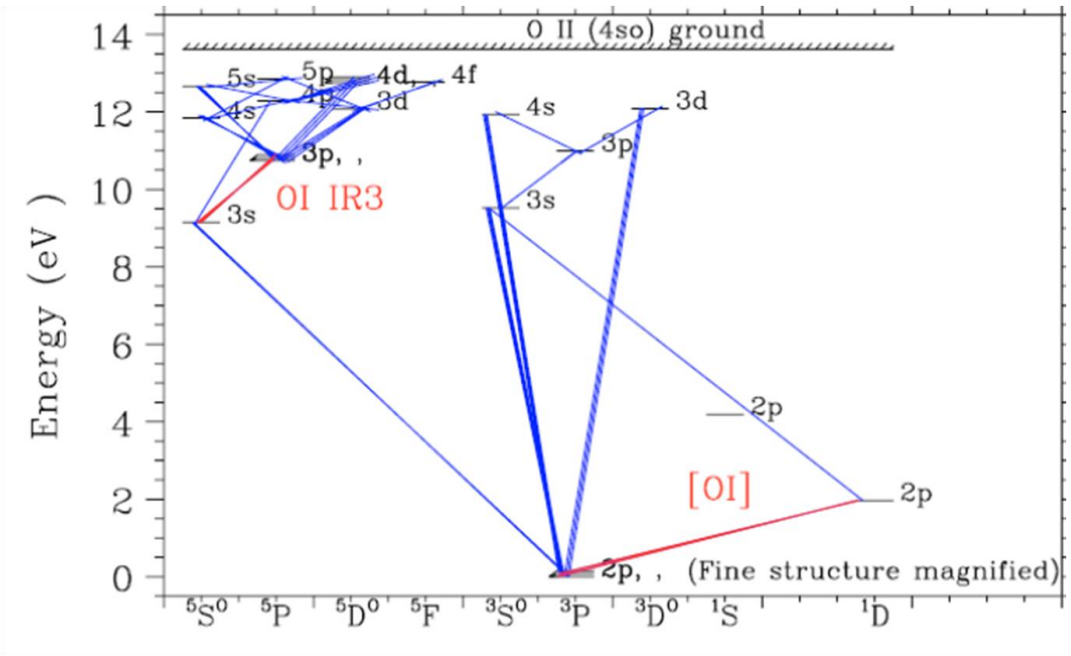

Figure 2.11: Grotrian diagram for O showing all the electronic transitions possible. With the plasma source on, the $^5P \rightarrow {}^5S^0$ transition, labelled as OI IR3 to the left of the diagram, is the strongest.

The x–axis shows the various states of the O atom with the ground state being the ^3P. The transition from ^1D to ^3P is forbidden (marked as [OI] in red), but no evidence of ^1D being formed was observed so this can be disregarded. The other red line, OI IR3, is the transition from ^5P to $^5S^0$ which is the main observed transition with the RF sources used in this work.

2.3.5 (b) Equipment

The plasma source used for this work, radio frequency, RF, plasma source (RF OSPrey, Oxford Scientific, now SPECS) are powered by units (Cesar 136, Dressler) capable of working at an operational frequency of 13.56 MHz and a maximum power of 600 W. A plasma source for H atoms has also been fitted to the UHV rig, however this source was not used for this work and will therefore not be discussed. **Figure 2.12** shows how both beam systems are attached to the rest of the UHV rig.

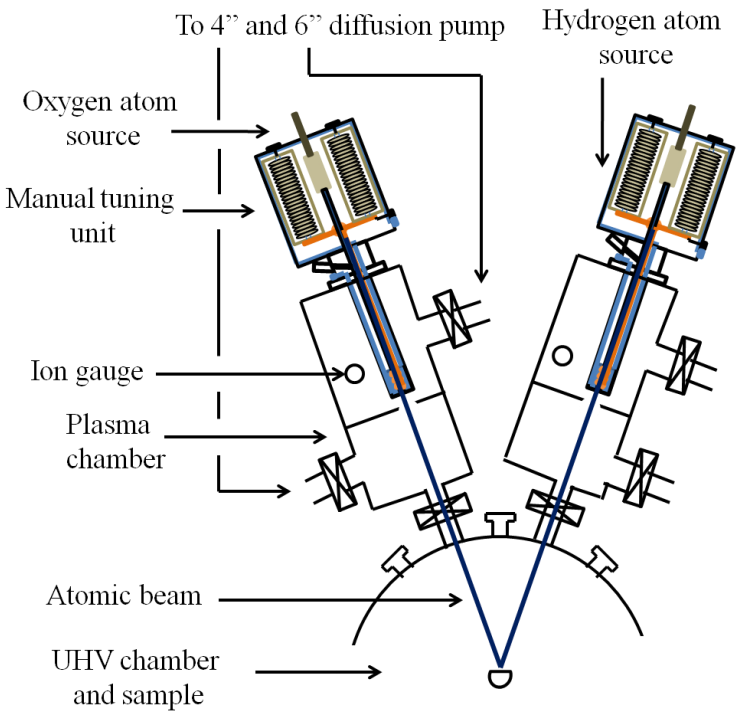

Figure 2.12: A general schematic of the atomic beam sources and their overall construction. The source to the left is for the production of O atoms while the right side is for H atoms (not used in this work). The UHV chamber is as follows from **Figure 2.2**.

Pictures of the plasma tube can be seen in **Figure 2.13** and a closer look at the O atom plasma source itself with the manual tuning unit is shown in **Figure 2.14**.

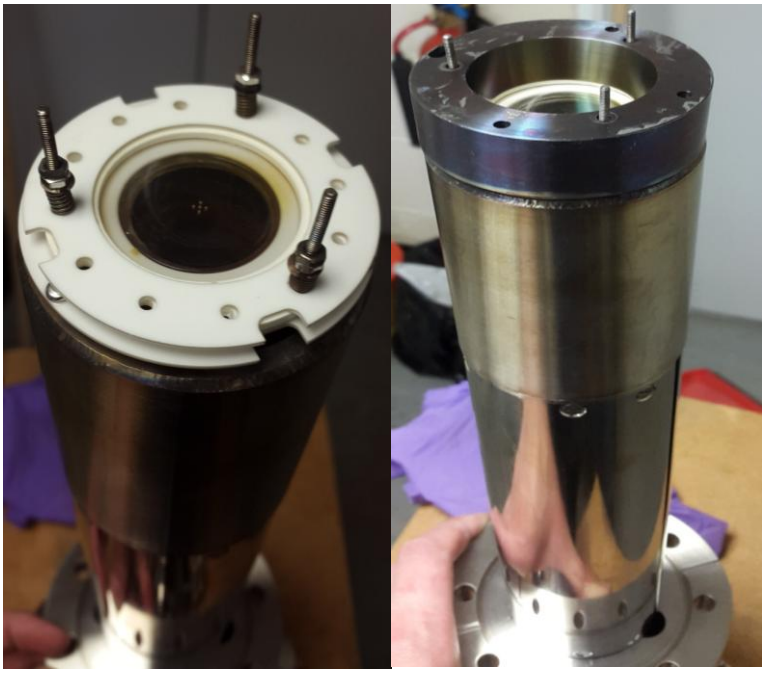

Figure 2.13: To the left is a picture of the plasma tube during reconstruction. The white discs, made of alumina so as to minimise O atom recombination after cracking, hold in place the aperture disc. The 5-hole grid in the centre of the aperture disc allows for the O beam to pass. The right picture is of the fully assembled plasma tube.

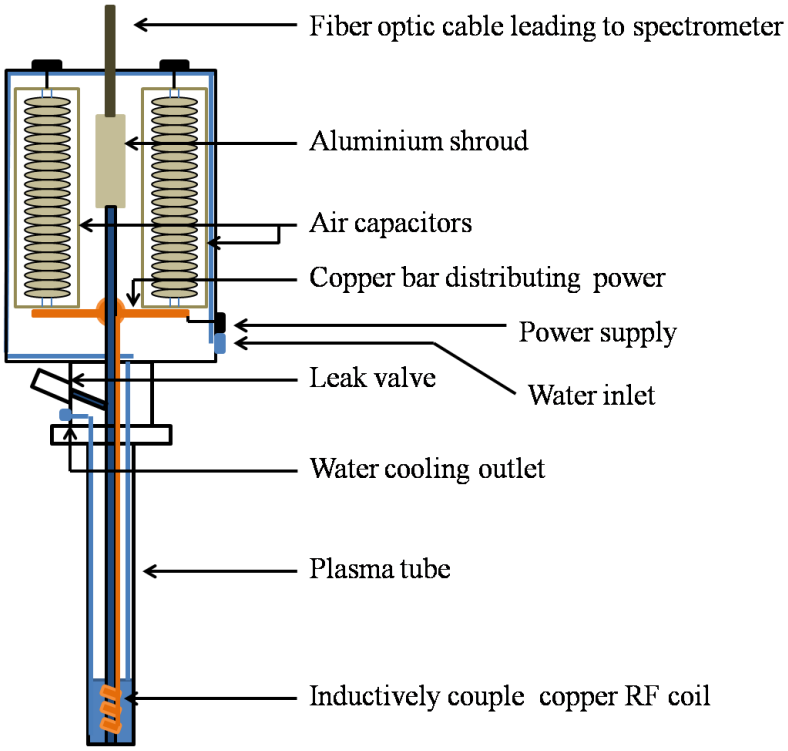

Figure 2.14: A sketch of the entire O atom plasma source. The inductively coupled radio frequency source sparks the O_2 gas when enough power is supplied. The air capacitors are to contain and focus as much power as possible towards the molecular gas. A fiber optic cable records the plasma emission in real time by a spectrometer.

The white rings in **Figure 2.13** are an alumina ceramic and the inside of the plasma tube and chamber has been coated in a similar material to minimise O atom reactions or recombination with surfaces.

The beam is effusive and thermal as there is no adiabatic expansion of the gas or plasma, for that reason the temperature of the gas is believed to be 300 K. The air capacitors in the manual tuning unit in **Figure 2.14** are rotatable by 360°. They are adjusted to reach a minimum of reflected power leading to a desired real power level to spark and maintain the atomic plasma through the inductively coupled RF coil. This in turn means using less "forward" power to obtain a "real" wattage and so reducing the risk of overheating or shorting of the system. A setting of 315° and 90° for the left and right air capacitor, respectively, was found to be optimal. With the real power set to 105 – 110 W, O_2 was leaked into the plasma chamber to a pressure of $1.0 – 1.1 \times 10^{-5}$ mbar as measured by an ion gauge (Edwards High Vacuum International). At this point a gate valve is the only separation between the plasma chamber and the central chamber with the sample in line of sight with the effusive beam. When the gate valve is fully open a certain amount of gas will flow into the main chamber due to the pressure

gradient, the pressure being 10^{-5} mbar in the plasma chamber compared to 10^{-10} mbar in the main chamber.

2.3.5 (c) Beam Flux and Cracking

The flux of the atomic beam can be calculated by pump–down curves. These experiments were conducted at normal experimental pressure conditions with the cryostat at room temperature to cancel the effect of cryopumping. The gate valve was opened for about 30 seconds, then closed and the process was repeated five times with the QMS running continuously monitoring m/z = 32. **Figure 2.15** shows the QMS trace with time.

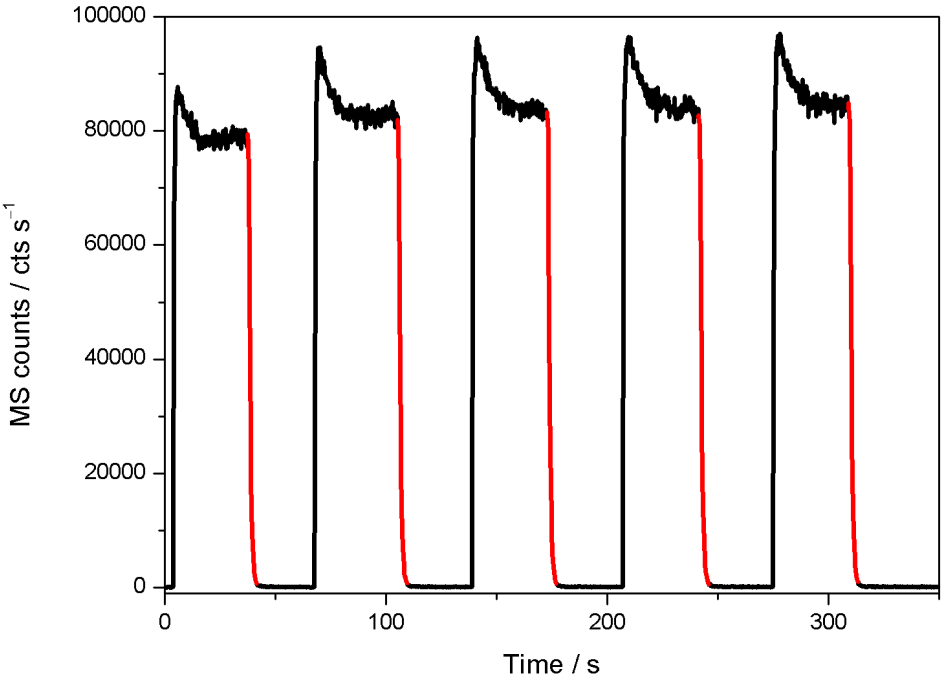

Figure 2.15: The pump–down curve used to assess the beam flux when for O atom experiments. The rise in the MS counts of m/z = 32 is due to the gate valve, separating the plasma chamber and the central UHV chamber, being opened. The count rate is allowed to stabilise and the red line shows the gate valve being closed and the O_2 pumped out of the central UHV chamber. The experiments were done with a room temperature cryostat.

The counts were converted to pressure which was done by background leaking O_2 into the chamber at fixed pressures of 1×10^{-8}, 5×10^{-8}, 1×10^{-7}, 5×10^{-7} and 1×10^{-6} mbar with the QMS monitoring the signal. A linear relationship between pressure and QMS signal leads to a simple conversion of use for the next step in the calculations. Looking at the individual pumping steps, marked in red in **Figure 2.15** above, and setting them to a time of zero leads to **Figure 2.16** (now with pressure instead of MS counts) where

the decrease in signal is due to the gate valve having been shut and molecules evacuated from the chamber by the diffusion pump.

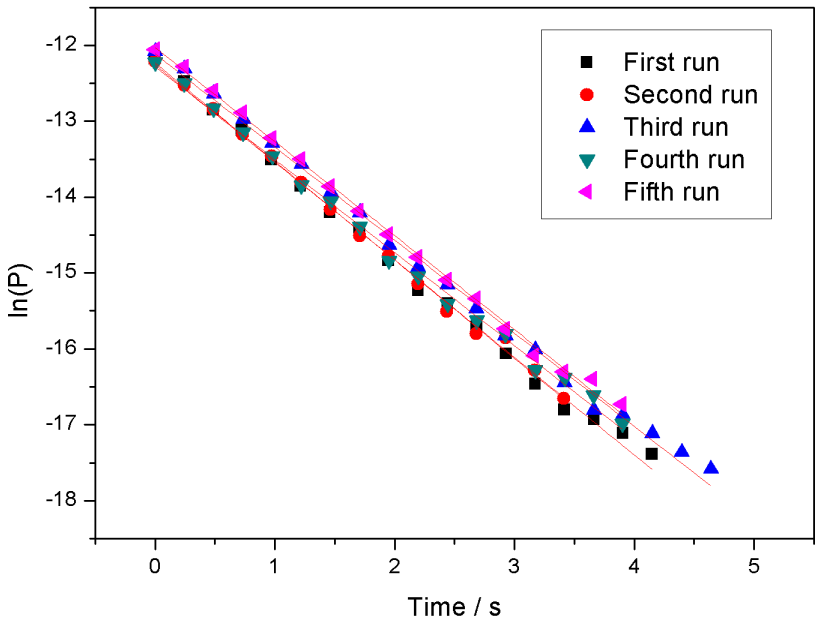

Figure 2.16: The result of the pump down curves form **Figure 2.15** when the MS counts have been converted to pressure, *P*, and each pumping curve has been set to zero to allow for individual and simple analysis.

The linear analysis of the experimental pump down curves is done using **Equation 7**:

$$\ln(P) = -C_m t + \ln(P_0) \qquad \textbf{Equation 7}$$

where P is the pressure, C_m is the pumping coefficient and t is the time. **Table 2.2** has been set up with the values of $\ln(P_0)$ and C_m.

Run number	**ln(P_0)**	**C_m / s^{-1}**
First	–12.26 ± 0.05	–1.28 ± 0.02
Second	–12.23 ± 0.04	–1.29 ± 0.02
Third	–12.11 ± 0.05	–1.23 ± 0.02
Fourth	–12.28 ± 0.04	–1.22 ± 0.02
Fifth	–12.03 ± 0.04	–1.24 ± 0.02
Average	–12.18 ± 0.04	–1.25 ± 0.02

Table 2.2: This table shows the values for the intercept, $\ln(P_0)$, and the gradient, C_m, as obtained from the pump–down curves from **Figure 2.16**.

Using the average values of P and C_m (and considering C_m as being positive due to **Equation 7**), **Equation 8** can be used to calculate the beam flux, F_{Beam}.

$$F_{Beam} = \frac{VC_mP_0}{k_BTA_{beam}} \qquad \textbf{Equation 8}$$

where the volume of the chamber, V, is estimated to be 0.075 m^3 and the area of the beam, A_{beam}, is 2×10^{-5} m^2 [8], k_B is the Boltzmann constant and the temperature, T, as explained earlier is assumed to be 300 K. The flux of the beam is thereby calculated to be about $5.8 \pm 0.4 \times 10^{14}$ molecules cm^{-2} s^{-1}.

From here, the ML formation time can be found by conducting temperature programmed desorption, TPD, experiments as discussed in detail in **section 2.4.1**. An average heating rate of 0.20 K s^{-1} indicates that dosing the molecular oxygen beam for 5 – 10 minutes on a SiO_2 surface held at 17 K yields one ML.

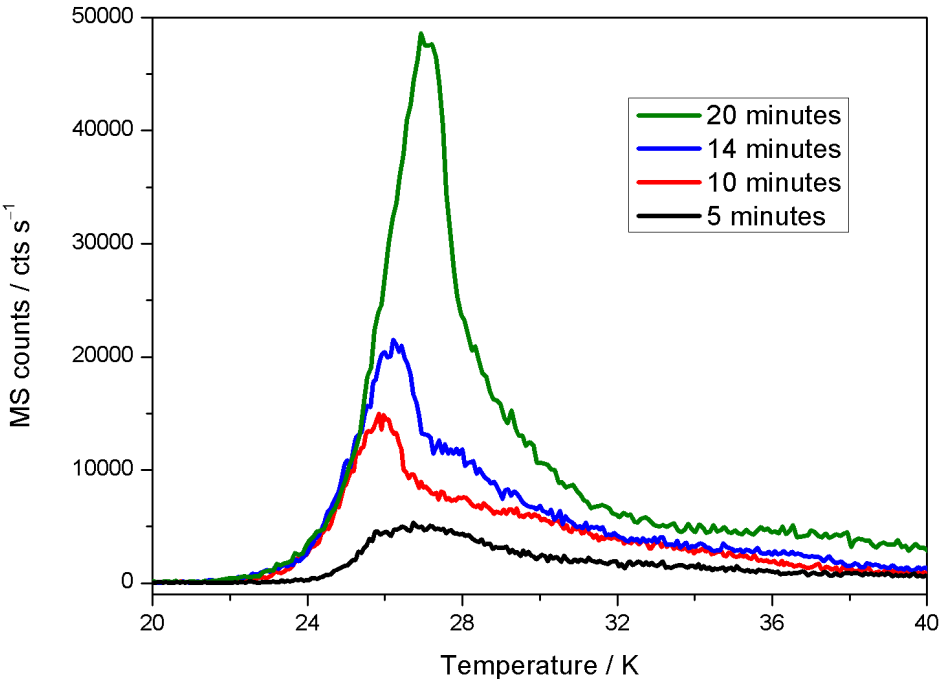

Figure 2.17: The temperature programmed desorption of O_2 beam dosed onto the sample indicate ML formation between 5 – 10 minutes. The beam flux and nature of the surface have effects of the monolayer formation time.

What **Figure 2.17** above shows, as will be detailed later, is that the sub–monolayer grows into a monolayer with increasing coverage as can be seen by the different desorption behaviour when comparing the black trace to the other three traces. The typical behaviour of multilayer desorption can be seen in the 10, 14 and 20 minute

traces where the leading edges begin to align. This is indicative of zero order desorption which is associated with multilayer desorption.

Turning the power units on to 105 – 110 W cracks a certain fraction of the molecular oxygen into the atoms where the main band at 777 nm, **Figure 2.18**, was monitored in real–time by a fiber optic cable linked to a spectrophotometer (USB4000, Ocean Optics) and monitored with SpectraSuite (Ocean Optics). The power and pressure were set as they were to obtain an intensity of the O^3P of 5.5 – 6.0 × 10^4 counts as seen in **Figure 2.18**, counts above this value approach the saturation limit of the spectrophotometer.

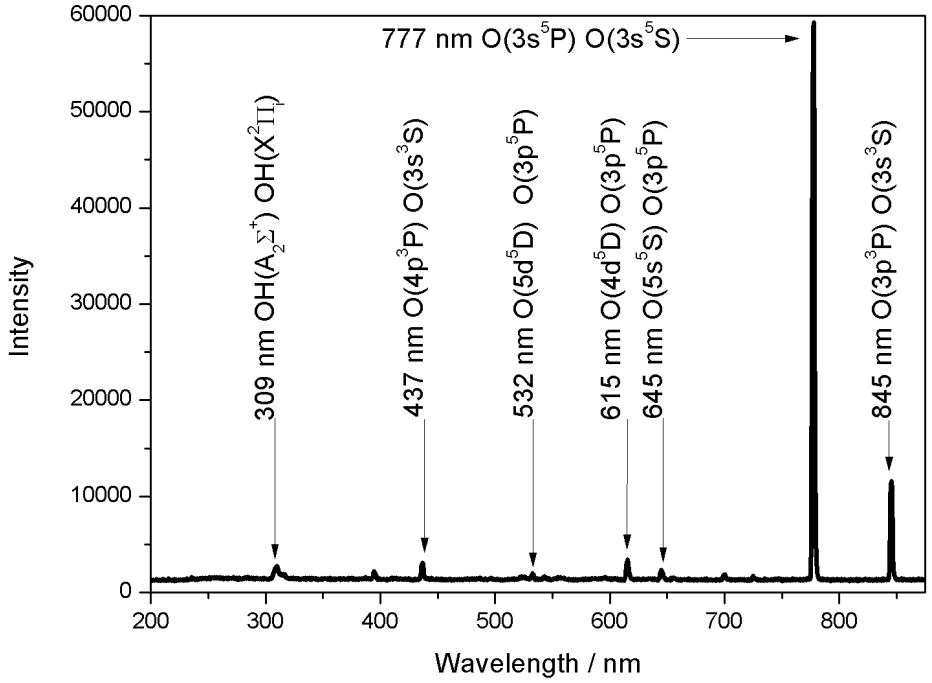

Figure 2.18: This shows the generally obtained spectra of the O atom plasma as monitored through the fiber optic cable linked to the manual tuning unit (see **Figure 2.14**). The minor peaks correspond to various transitions of O atoms, with a slight contamination of OH, but the strongest signal is observed at 777 nm, corresponding to the ($3p\ ^5P$) → ($3s\ ^5S$) transition in the O atom.

The peaks observed in the spectrum above, **Figure 2.18**, can be correlated with the Grotrian diagram, **Figure 2.11**, and the transitions with their wavelength have been summarised in **Table 2.3**. As can be seen, an OH transition is observed indicating a form of contamination with a source of H, possibly H_2O. The fraction of impurity was considered minimal when compared to the main transition observed at 777 nm.

This level of counts, pressures and power is consistent with the high brightness mode of O plasma [23].

O atom transition	Emission Peak / nm (± 1)
OH transitions ($OH(A_2\Sigma^+ \rightarrow X_2\Pi)$)	309
$(4p\ ^3P) \rightarrow (3p\ ^5P)$	437
$(5d\ ^5D) \rightarrow (3p\ ^5P)$	532
$(4d\ ^5D) \rightarrow (3p\ ^5P)$	615
$(5s\ ^5S) \rightarrow (3p\ ^5P)$	645
$(3p\ ^5P) \rightarrow (3s\ ^5S)$	777
$(3p\ ^5P) \rightarrow (3s\ ^5S)$	845

Table 2.3: O atom transitions with the corresponding emission peak from the spectrometer [16, 22]. The 777 nm transition is the strongest signal with the supplied energy as measured by the fiber optic cable linked to the spectrophotometer.

The simplest way to determine the cracking fraction of O_2 into O is by having the QMS in line–of–sight with the beam. This was done when the sources were first installed where a cracking fraction of 32% ± 9% [8] was reached, since then the plasma source has been repaired following a breakdown. Experiments to verify that the cracking fraction is the same were done by a two–fold check; one where the O beam was simply dosed into the chamber to monitor the fraction of $O:O_2$ and another experiment where O_2 and O beams were separately dosed onto the sample.

Looking at the first experiments where the beam was dosed into the chamber; comparing the QMS counts for m/z = 16 and 32 when the O atoms beam on and off, **Figure 2.19**, we get a preliminary cracking fraction of about 20% O to O_2.

As can be seen in **Figure 2.19**, the initial increase in the QMS counts is due to the gate valve being opened. At this stage, indicated by the blue vertical line, the fraction between m/z = 16 and 32 is about 36%. This is the natural cracking pattern for this mass spectrometer with the set multiplier value of 2500 V. The pressure and therefore QMS counts are allowed to stabilize, plateau, before the plasma source is turned on, at which stage the QMS counts increase due to the sudden increase in energy supplied to the O_2 molecules. At this stage, marked with a green vertical line, the percentage has changed to 43%. This means that the plasma source has created what amounts to 7% pure O atoms. As the source warms up and reaches operational conditions after two to three

hours, the percentage has changed to 56%, meaning about 20% of the O_2 molecules have been cracked into O atoms. The decrease observed for both curves of molecular and atomic O is due to adsorption onto cold surfaces and pumping by the diffusion pump.

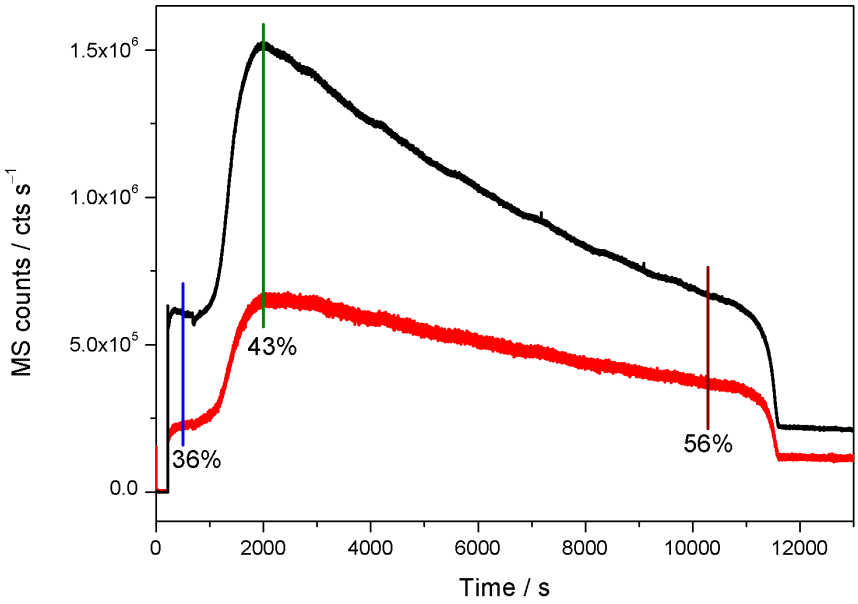

Figure 2.19: The traces here initially indicate only a background of O, m/z = 16, the red trace, and O_2, m/z = 32, the black trace. As the gate valve between the plasma chamber and the central chamber is opened, a sharp rise in the counts happens. As this plateaus an initial measurement of the fragments monitored by the QMS is made (the blue vertical line). The plasma source is then turned on which cracks O_2 into O (the green vertical line). The source is left to stabilise and reach optimum operational conditions and the cracking fraction of the plasma source can be estimated (the brown vertical line).

Looking at the reaction experiments, O and O_2 are monitored during the RAIRS and TPD experiment. From experiments with pure O_2 beams a, so–called, 100% ratio can be estimated. Any change from the 100% in the O_2 count is due to the O atom reactions. Considering the minimal change in the O_3 counts, this can be discounted as a destruction pathway of O_2, purely when considering the cracking fraction and this method of calculating it.

Dosing O_2 and repeating the experiments with O atom dosing will give an idea of the cracking fraction by looking at the creation of O_2 through two O atoms. Dosing both beams for a time of 1, 2, 5 and 10 minutes and looking at the areas under the TPD traces yields **Figure 2.20**.

In **Figure 2.20**, the blue line and symbols are the result of O_2 TPD experiments after the sample has been dosed with the O/O_2 beam, the plasma source was on. The black line and symbols are when pure O_2 is beam dosed and the red lines are linear fits forced through (0,0). The insert is an example TPD trace of the 10 min exposure to show the difference in QMS counts. **Table 2.4** shows the results of the linear regressions.

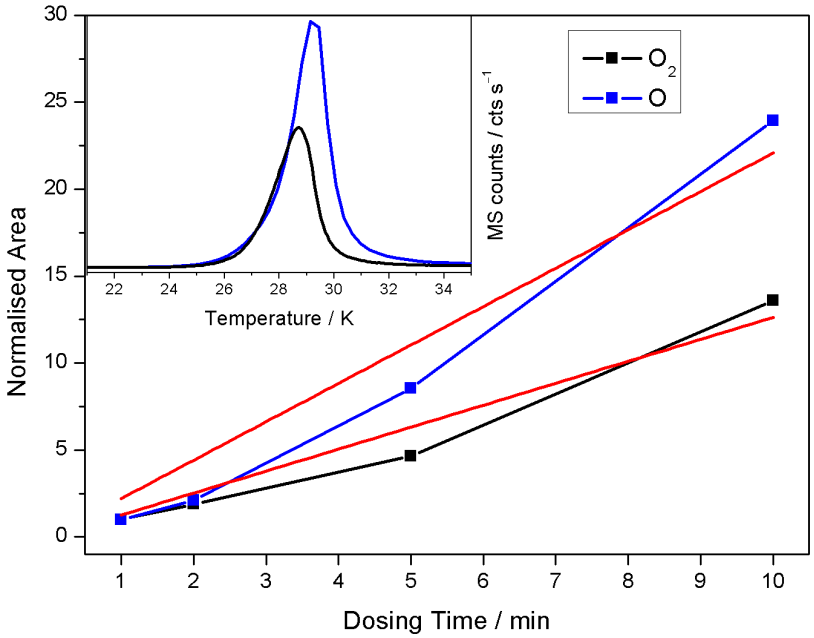

Figure 2.20: This figure shows the integrated and normalised areas of O_2 TPD traces when dosing the O_2 molecular beam (black data set) and atomic O beam (blue data set) for 1, 2, 5 and 10 minutes. The areas have been normalised through integrated area of the 1 minute TPD traces for the O atom beam and the O_2 molecular beam to allow for comparison between the different experiments. The insert shows the difference in the TPD traces when the atomic beam is off or on.

Beam Dosing Method	Gradient	Uncertainty (+/–)
Molecular, O_2	1.26	0.10
Atomic, O	2.18	0.21

Table 2.4: This table indicates the different gradients from **Figure 2.20**. The change in gradient indicates that an increase of about 58% O_2 desorption occurs when the plasma source is on and when every other experimental aspect, flux and time, is kept constant.

Using the initial idea that the pure O_2 experiments are the 100% experiments and any increase being due to formation of O_2 through O + O, leads to an increase in the gradient of about 58%. This percentage also includes the normal fragmentation of O_2 as it is detected by the QMS. As seen in **Figure 2.19** the regular fragmentation pattern of O_2 is about 36%. Accounting for this, the cracking fraction of the plasma source when

comparing TPD experiments from O and O_2 becomes 22% ± 11%. This is similar to the cracking fraction of about 20% when looking at the O_2 beam before turning on the plasma source and letting it warm up. However, the best method for determining the cracking fraction would be to have the QMS in line–of–sight and measuring the fraction directly, which will be done in the future for a more accurate idea of the cracking fraction.

2.4 Experimental Techniques

2.4.1 Temperature programmed desorption (TPD)

Temperature programmed desorption (TPD) is an analytical method which can be used to determine the binding energy between molecules adsorbed onto a surface or bulk molecular interactions, in other words the desorption kinetics. It is one of the fundamental tools in describing surface kinetic processes [24, 25]. The basic idea revolves around heating a surface coated with molecules and observing what desorbs while monitoring the temperature of the surface. As can be understood by the technique's name, it is a destructive analytical method since the originally solid sample is analysed after desorption to the gas phase. To be able to obtain useful information from a TPD experiment certain requirements to the basic idea must be implemented to interpret the data in a simple fashion.

The sample or surface and the chemicals adsorbed must be heated in a controlled fashion. This is done by applying a linear heating rate localised to the sample. With a linear heating ramp one can determine the temperature at various instances through **Equation 9**:

$$T(t) = T_0 + \beta t \qquad \textbf{Equation 9}$$

where *T(t)* is the temperature of the sample as a function of time (*t*), T_0 is the initial temperature and β is the heating ramp, which are both known experimentally.

As the sample heats up, so will the sample mount and cold finger. Analysing the experimental data allows one to determine the desorption of molecules from the sample *versus* non–sample surfaces when relaying the temperature of the sample and the cold finger against the QMS signal.

When the temperature is sufficiently high, the chemical species has received enough thermal energy to break whatever interaction is holding it and desorption takes place. The rate at which molecules and atoms desorb is a function of the surface coverage, this means the desorption rate constant (k_d) is also dependent on the coverage (θ_s). The rate of desorption (v_d) is defined as in **Equation 10**:

$$v_d = k_d \theta_s^m \qquad \textbf{Equation 10}$$

where m is the order of reaction. Desorption of molecules from a surface is activated through heating the sample and follows an Arrhenius law leading to the rate constant (k_d) increasing exponentially as the temperature increases:

$$k_d = \nu \, exp\left(-E_d/_{RT}\right) \qquad \textbf{Equation 11}$$

where ν is the pre–exponential factor, E_d is the desorption energy, R is the ideal gas constant and T is the absolute temperature of the surface. As the temperature is increased, the surface coverage decreases. From the exponential increase of the rate constant and the decrease of surface coverage, a graph (**Figure 2.21**) can be made which yields a prototypical TPD trace.

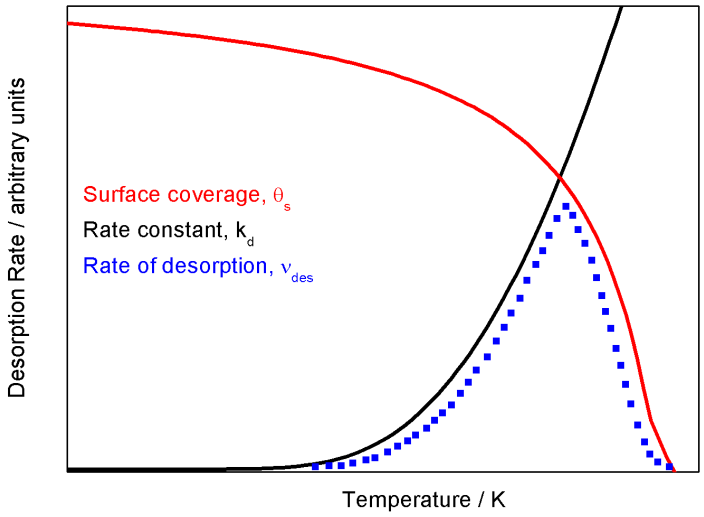

Figure 2.21: This figure show the formation of a TPD trace. Initially molecules are deposited onto a surface of a certain quantity, θ_s, before the sample is heated. As the sample and the film heat up the coverage decreases as the rate constant, k_d increases. The point where the two curve intersect is the peak of desorption and the area under this newly created curve, v_{des}, is proportional to the amount of species deposited.

The point where the surface coverage and rate constant curves meet marks the maximum rate of desorption and the area under the desorption trace will ideally indicate the surface coverage, but contributions from other surfaces or species can prevent this [25].

From a typical rate of desorption trace as in **Figure 2.21** above one can calculate the desorption energy. With the rate constant of desorption, the number of adsorbed molecules, *N*, and the order of the reaction, **Equation 12** can be set up:

$$-\frac{dN}{dt} = k_d N^m. \qquad \textbf{Equation 12}$$

This equation shows how the molecules desorb with respect to time, but the temperature, *T*, is needed to arrive at an expression that matches the experimental procedure and can be introduced as below, **Equation 13**:

$$\frac{dN}{dt} = \frac{dN}{dt} \times \frac{dT}{dT} = \beta \frac{dN}{dT}. \qquad \textbf{Equation 13}$$

The latter part of the equation, *dT/dt*, indicates how the temperature changes with time which is another way of describing the heating rate, *β*, from **Equation 9** above. At this stage we can combine **Equations 12** and **13** to get **Equation 14**:

$$\frac{-dN}{dT} = N^m \frac{k_d}{\beta}. \qquad \textbf{Equation 14}$$

By expanding the rate constant from **Equation 11** one obtains:

$$\frac{-dN}{dT} = \frac{\nu N^m}{\beta} \exp\left(-E_d/_{RT}\right). \qquad \textbf{Equation 15}$$

To obtain the temperature at the maximum of desorption, differentiating **Equation 15** and setting it to zero for m ≠ 0 leads to the general expression of **Equation 16**:

$$\frac{E_d}{RT^2} = \frac{\nu}{\beta} m N^{m-1} \exp\left(-E_d/_{RT}\right). \qquad \textbf{Equation 16}$$

From this equation the desorption energy can be determined since the heating rate is set experimentally, the temperature is monitored and the ideal gas constant, *R*, is known. The pre–exponential factor, *v*, can be found through analysis of the experimental data, but can be assumed to be of the magnitude of molecular vibrational frequencies, around 10^{13} s^{-1} for $m = 1$ [25]. The order of reaction, *m*, can be determined from experimental data through the analysis of the leading edges of the TPD traces.

Reaction orders are important in determining the desorption energy as seen in **Equation 16**. The typical families of desorption are zero, first and second order reactions. To determine the order of desorption one has to conduct several experiments on the same species with different initial surface coverages. When enough traces have been made a trend should be visible. **Figure 2.22** shows examples of TPD traces, and the observable difference after the experimental data has been analysed.

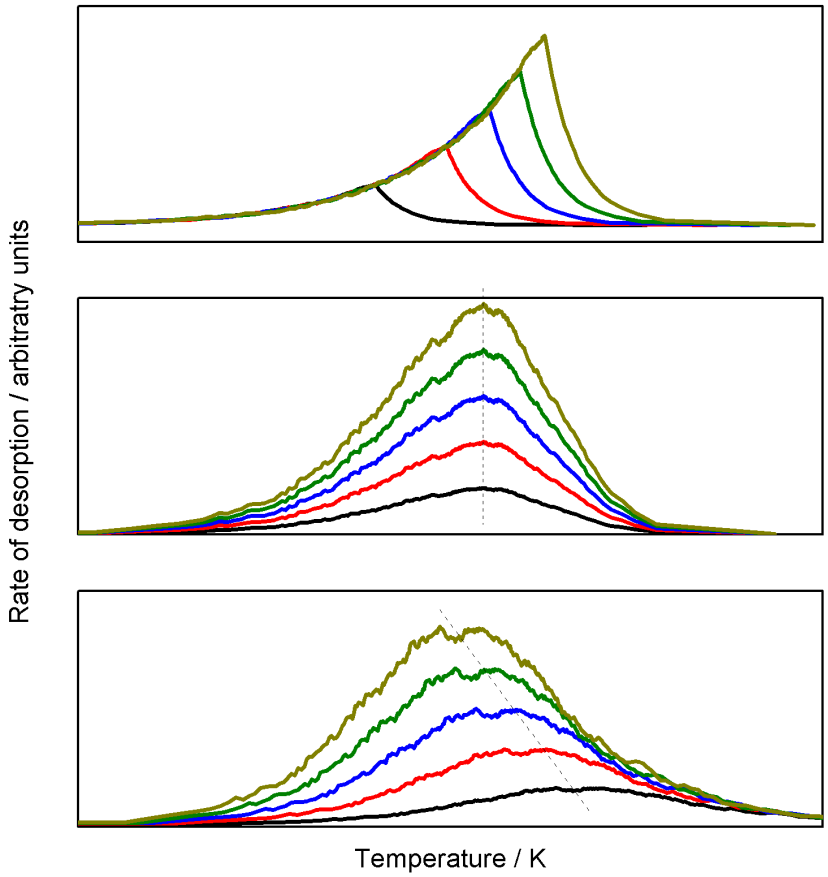

Figure 2.22: The traces above indicate the ideal desorption behaviours of chemical films deposited onto a surface. The top graph shows zero order kinetics where the leading edges align and a bulk material desorbs. The second graph is of 1st order where all the peaks line up to the same peak temperature of desorption which is expected for sub–monolayer desorption. The bottom graph is of 2nd order desorption where the trailing edges align indicative of recombination of molecules on the surface during desorption.

As can be seen in **Figure 2.22**, enough TPD traces lead to different observed tendencies of the peaks and edges. The first graph, zero order, with coincident leading edges is typical of a large coverage leading to multiple molecular or atomic layers, *i.e.* multilayers. The reason for the coincident leading edges is because the main interactions are adsorbate–adsorbate and because *m* is set to zero in **Equation 15**. These interactions are similar throughout a bulk, but the desorption temperature change slightly with coverage purely because the desorption rate increases exponentially as seen in **Figure 2.21**. The second graph, first order desorption, has the peaks lining up at the same desorption temperature which is typical of low coverages when monolayers or sub–monolayers desorb from a surface as seen in **Equation 16**. This is because the main interactions are surface–adsorbate which is constant for the specific molecules adsorbed on a pristine and flat surface. When changing from monolayer to multilayer the desorption kinetics between the surface and adsorbate changes. When low coverages are dosed the molecules can possibly diffuse, depending on the surface temperature, and find the optimal binding sites which leads to slightly higher amounts of energy needed to break the interaction and make the molecule desorb. As more molecules are dosed the interaction between adsorbate–adsorbate interactions become dominant for the desorption kinetics as compared to the lower percentage of molecules involved in the adsorbate–surface interactions. The last graph has coincident trailing edges which is the regime of second order desorption reactions, this occurs when adsorbates recombine before desorption.

These are the ideal behaviours of desorbing molecular layers, but more complex interactions, such as fractional desorption orders and pseudo desorption orders also exist. Fractional desorption orders have been observed for TPD experiments of CH_3OH in various cases [26–28] as H–bonding becomes an important factor in desorbing such molecules. Pseudo–order desorption can be explained as being due to the surface. A surface such as amorphous SiO_2 surface is rough, as explained previously, which offers a wide range of binding sites for the sub–monolayer coverages of molecules. Depending on the temperature, molecules on SiO_2 diffuse and obtain their most energetically favoured binding site before forming a monolayer. This leads to a collection of TPD traces appearing more as second order as compared to the expected first order desorption, termed pseudo–first order. However, the molecules observed to undergo pseudo–first order desorption do not recombine on SiO_2 and, therefore second order desorption kinetics can be ruled out.

2.4.2 Reflection–Absorption Infrared Spectroscopy (RAIRS)

Unlike TPD, infrared spectroscopy is a non–destructive analytical tool that yields information about the various molecular vibration modes of the molecules present in the sample probed and their local environment. The type of IR spectroscopy used for this work is reflection-absorption infrared spectroscopy (RAIRS). This method was initially proposed by Greenler [29] for studying thin layers of adsorbates on metal substrates, and has the advantage of being very surface sensitive.

The technique needs the IR beam to be reflected by a substrate, which acts as a mirror, and then directed onto a detector. Adding an adsorbate to this substrate will change the reflectivity, ΔR, of the substrate. This leads to a spectrum of $\Delta R/R$, where R is the total reflected IR beam from a clean surface. A UHV setup is, strictly speaking, not necessary to perform RAIRS, but this is required for other purposes already explained.

Conducting RAIRS experiments in the UHV chamber means the IR beam is directed into the UHV chamber firstly by paraboloidal and ellipsoidal mirrors located in an optics box. The beam then goes through a KBr window and onto the sample at a grazing incidence of 75^{o} before being directed out through another KBr window. The use of KBr windows is due to their IR transparency in the detection range of the mercury cadmium telluride (MCT) detector [30]. From here the beam is then reverted and re–collimated by another paraboloidal mirror before it reaches the detector in a different optics box. The detector used in is a liquid nitrogen cooled MCT detector which has a detection range from 4000–800 cm^{-1}. Both optics boxes are in a dry air atmosphere to ensure minimal interference from gas phase H_2O and CO_2 from ambient air when conducting an experiment.

When IR radiation is reflected from a surface, the electric field of the incident electromagnetic wave can be considered to comprise two components; one component has the electric field vector parallel to the reflecting surface and the second has the electric field vector perpendicular to the surface. If the electric field of the IR beam is polarised parallel to the surface (*i.e.* in the plane of the surface) the point of reflection will show no reflected electric field. The reason for this is as the incoming beam strikes the surface, mirror electric field vectors are set up in the surface (similar to the concept of a standing wave). In the case of parallel–polarised light, these vectors cancel each

other as depicted on **Figure 2.23**. When the beam is polarised perpendicular to the surface, these same electric field vectors enhance each other [31].

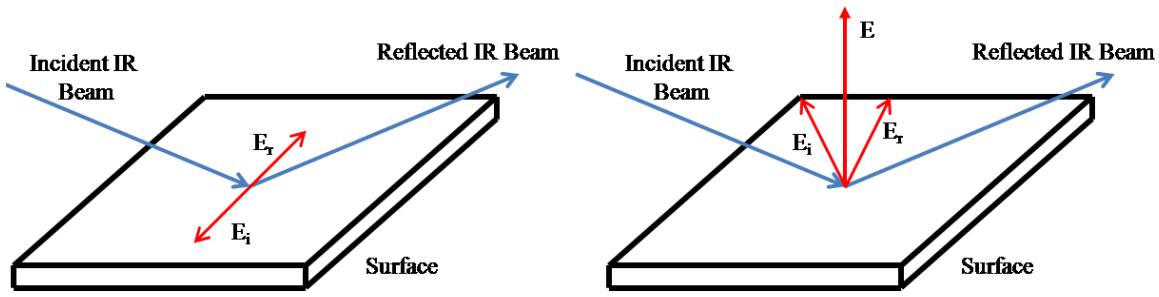

Figure 2.23: A schematic of the electric field vectors on a surface from parallel polarised light (to the left) and perpendicular polarised light (on the right). As can be seen, the electric field is cancelled in the left diagram and enhanced in the right.

Another way of considering the effect of polarised light incident on a surface is shown in **Figure 2.24**. This figure illustrates the phase change of incident polarised light perpendicular (**a**) and parallel polarised light (**b**) to a surface. As can be seen in **Figure 2.24**, parallel polarised light has a phase change of about 180^o at all angles of incident light as it is reflected from the surface. This, combined with the left part of **Figure 2.23** leads to a negligible amount of expected absorbance when a molecular film is deposited onto the surface. Conversely, having a light source that is polarised perpendicular to the surface leads to a more gradual phase change as the incidence angle changes. When investigating thin molecular films, incidence angles of light polarised perpendicular to the surface of about 72^o have previously been used [29] The grazing angle at these values can lead to an increase in the perpendicular component of the electric field and is enhanced nearly twice at a grazing angle of about 75^o.

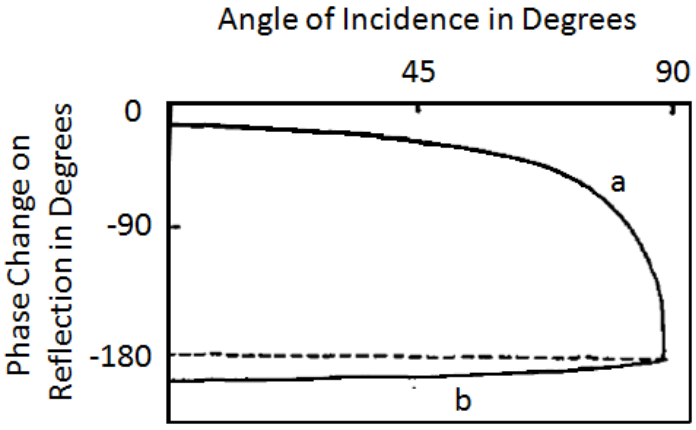

Figure 2.24: This graph shows how the phase changes as polarised light perpendicular (**a**) and parallel polarised (**b**) is incident on a metal surface at a given angle. As can be seen, (**b**) has a greater phase change as the angle of incidence changes. Figure is adapted from [29].

A further advantage of having a beam at grazing incidence is the elliptical spot produced on the surface of the sample. At normal incidence the beam would produce a circular spot which changes into an ellipsis as the incidence angle changes thereby changing the surface area covered by the IR beam. This, in turn, means more molecular oscillators are probed and interact with the radiation. When referring to IR spectroscopy on a metal surface, the metal surface selection rule (MSSR) [31] has to be mentioned and **Figure 2.25** has been made to illustrate the origin of this rule.

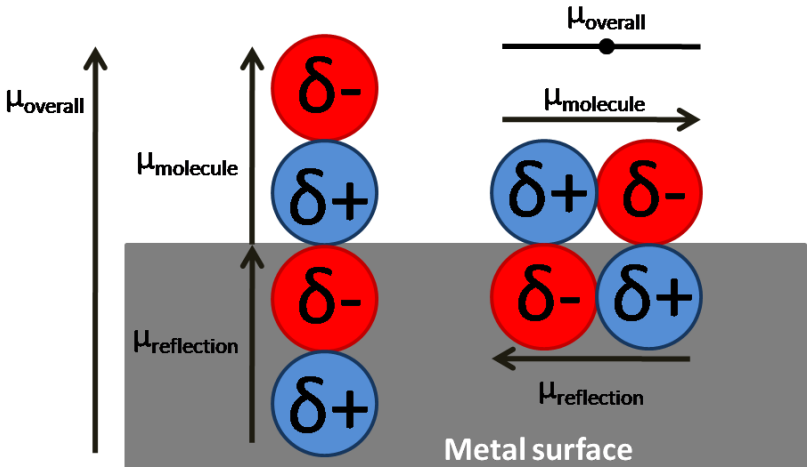

Figure 2.25: The MSSR is important when conducting IR experiments on a pure metal surface. As can be seen, the molecules oriented perpendicular to the surface will have an overall enhanced dipole moment due to the image dipole arising in the metal surface. This effect is cancelled out when the molecules are aligned parallel to the surface.

The MSSR regulates what is observed with respect to the orientation of IR active molecules adsorbed on a surface, in order to maximise their IR absorption. An image dynamic dipole of the dynamic dipole is created in the metal substrate which is either enhanced or cancelled. This rule is very important when molecules are adsorbed directly onto a flat metal substrate, but the irregular and rough layer of silica covering the metal substrate leads to molecules adsorbed with random orientations with respect to the metallic mirror plane. This means the MSSR is effectively circumvented allowing modes that would be otherwise inactive in an orientated sample directly adsorbed on the metal surface to be observed. The inactive modes increase in intensity with respect to the distance they are from the pure metal surface due to the SiO_2 spacer.

2.4.2 (a) Longitudinal Optical – Transverse Optical (LO–TO) Splitting

The effect of the SiO_2 on the MSSR is crucial for the observation of the longitudinal optical–transverse optical (LO–TO) splitting. Without the SiO_2 layer, the TO mode

would be silent as can be seen in **Figure 2.26**, as this mode arises from a collective vibration mode parallel to the metal surface.

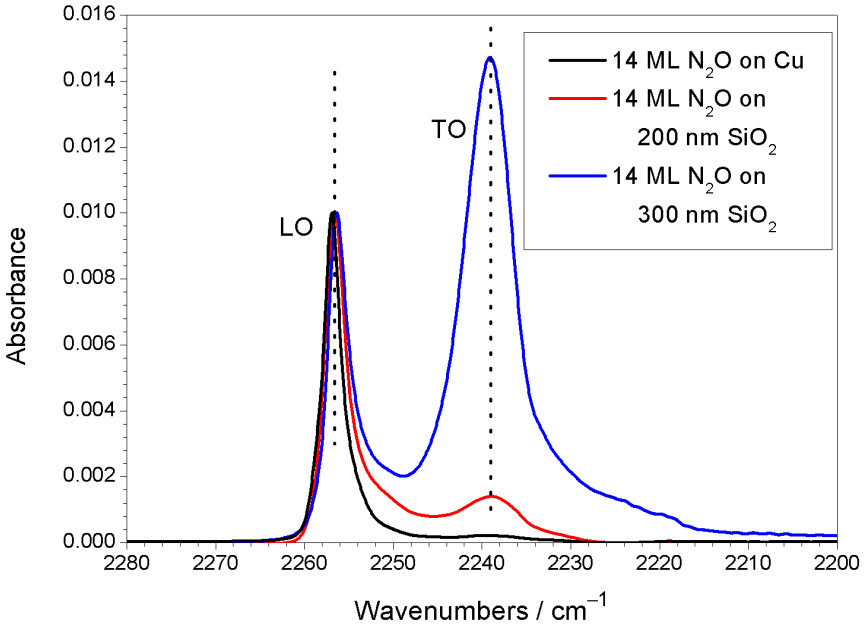

Figure 2.26: RAIRS spectra of the νNN mode of 14 ML N_2O on Cu, blue, 200 nm SiO_2, red, and 300 nm SiO_2, black. As can be seen the TO mode of N_2O is silent when deposited directly on Cu. This mode then activates as it is physically removed from the surface of the Cu by SiO_2 spacers.

The TO mode is silent on a flat metal surface and builds up as the increasing amount of SiO_2 physically removes it from the effect of the image dipole. The immediate effect of the above, **Figure 2.26**, tells us that the extremes of the LO–TO splitting means that the LO mode relates to vibrations perpendicular to the surface and the TO mode parallel to the surface, **Figure 2.27**.

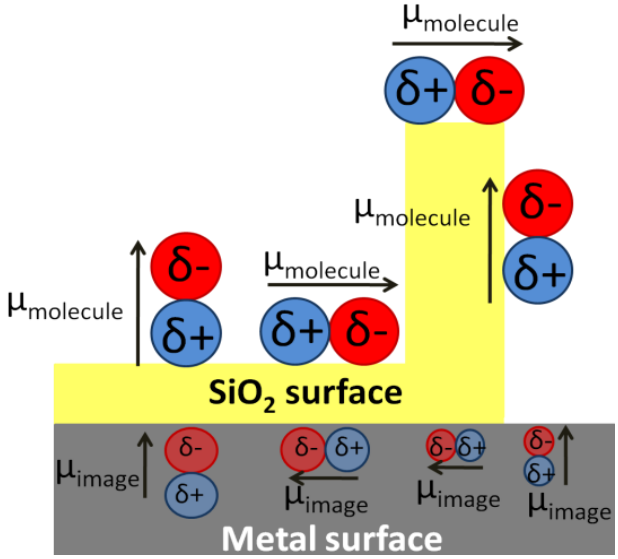

Figure 2.27: A similar diagram to that describing the MSSR in **Figure 2.25**. However, a SiO_2 layer has been placed between the metal and the adsorbed dipolar molecular film illustrating how the roughness can circumvent the MSSR.

The MSSR still applies since there is a metal surface, however the rough SiO_2 spacing layer gives molecules extra possible binding sites leading to an ‘evasion’ of the MSSR.

An IR beam incident to the surface and through the molecular film will carry its inherent electric field. The LO–TO splitting occurs as phonons propagate throughout a dipolar film. A phonon is a unit of vibrational energy occurring when a molecular solid oscillates [32]. The TO mode phonons had long been known to interact with IR beams; indeed it was the work of Berreman [33–35] that showed how the LO mode could be investigated by changing the angle of incidence. According to the Berreman effect, the TO mode is visible and active when the incident IR beam, with electric field components both parallel and perpendicular to the normal of the surface, interacts with a deposited dipolar film if this film is considered infinite in the plane of the film. At this condition, only the TO mode is active. However, changing from an infinite film to a finite film will change what is observed dependent on what surface is used. For experiments like RAIRS, with a metal surface acting as a mirror, if the adsorbate was deposited directly on the metal, the MSSR would become dominant at low coverages and no IR signal would be seen at the frequency of TO modes. If, however, transmission IR spectroscopy was used, the TO mode would still be visible at low film coverages [36].

The LO mode activates as the thickness of the film approaches a comparable value of the wavelength of the IR beam and the angle of incidence changes. Increasing the film thickness brings around another way of thinking about the LO–TO splitting as a 3D network of molecules being essential. In such a 3D network, the neighbouring electrostatic effects needed for the LO mode becomes possible as a neighbouring counterpart appreciates the physical displacement. As this network builds up, the phonon propagation through a dipolar film leads to further displacement of charges, thereby leading to the split when an IR beam interrogates one, usually, degenerate vibrational component of a molecule. An additional effect impacting on the double–peaked nature of the LO–TO splitting is the Vibrational Stark Effect (VSE). This effect arises when degenerate vibrational energy levels are subjected to an external electric field which results in shifts in the vibrational features (such as LO–TO peaks) as the electric field changes [36]. In the case of this work, such an electric field comes from the spontelectric field present through the entirety of the molecular film. This field, as explained, changes with temperature and therefore should lead to changes in the LO–TO

splitting. **Figure 2.28** has been created to visually show what happens as the IR beam investigates a film of N_2O.

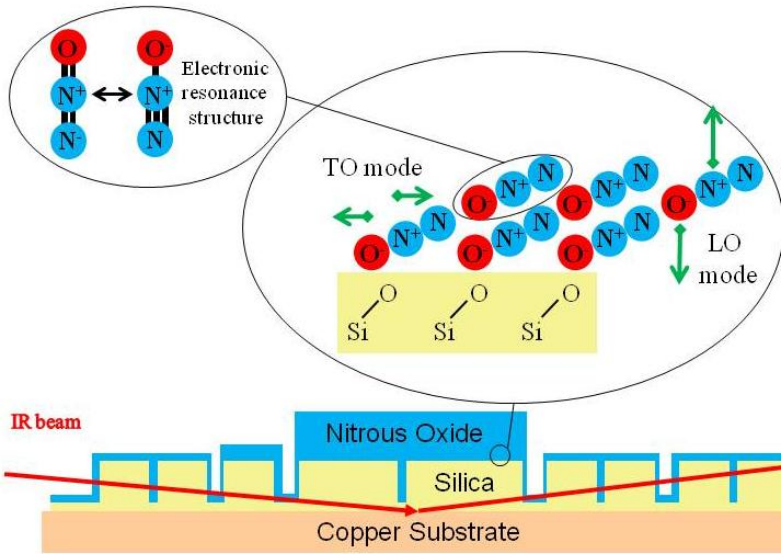

Figure 2.28: This cartoon shows how the LO and TO modes behave in a solid. The LO mode arises as the phonons in the solid interact longitudinally, or along, the electric field when the IR beam hits the surface of the Cu substrate. The TO mode behaves oppositely and interacts transversely with the electric field.

2.5 The Spontelectric Effect

The introduction mentioned the spontelectric effect which will be investigated in detail in **Chapter 5** through the use of RAIRS. However, RAIRS is an indirect method of investigation and a short description of what the spontelectric effect is and how it is directly measured will follow here, but can also be read about in references [37–44].

The term "spontelectric" effect is derived from the production of a spontaneous electric (spontelectric) field leading to a measureable surface potential during the deposition of certain dipolar molecules. The molecules exhibiting the spontelectric effect range from chlorofluorocarbons to nitrous oxide to methyl formate and many more [37]. For the time being, the only similarity between the studied molecules is that they all have a permanent dipole leading to a positive or negative surface potential depending on the how the molecules are oriented in the film.

The experiments directly measuring the surface potential have been conducted at Aarhus University in Denmark by David Field and his group. The equipment used by the group involves the use of a ultrahigh vacuum chamber (~10^{-10} mbar) with a cryostat

cooling a gold coated sample to 38 K connected to a femto–ammeter. Leak valves allow for gaseous molecules to be introduced and a mass spectrometer is used for temperature programmed desorption experiments to determine the monolayer (ML) coverage. A probe is necessary to determine whether the deposited dipolar molecules exhibit a spontelectric effect, and hence a surface potential. This probe comes in the form of synchrotron radiation (from the SGM2 beam line on the ASTRID storage ring) photo–ionising argon gas at a pressure of about 10^{-4} mbar (S1–3 in **Figure 2.29**) yielding near zero kinetic energy photoelectrons with an energy speed of 1.5 meV. The produced photoelectrons are focussed onto the sample surface by a series of electrostatic lenses (L1–4) and a further focussing element (V_{CC}) where the current is measured by the ammeter. The electron source can be offset by a variable potential which can be zeroed with respect to the sample. The chamber also consists of a shield to prevent external magnetic fields from interfering with experimental results. A diagram of the experimental setup has been shown in **Figure 2.29** [37].

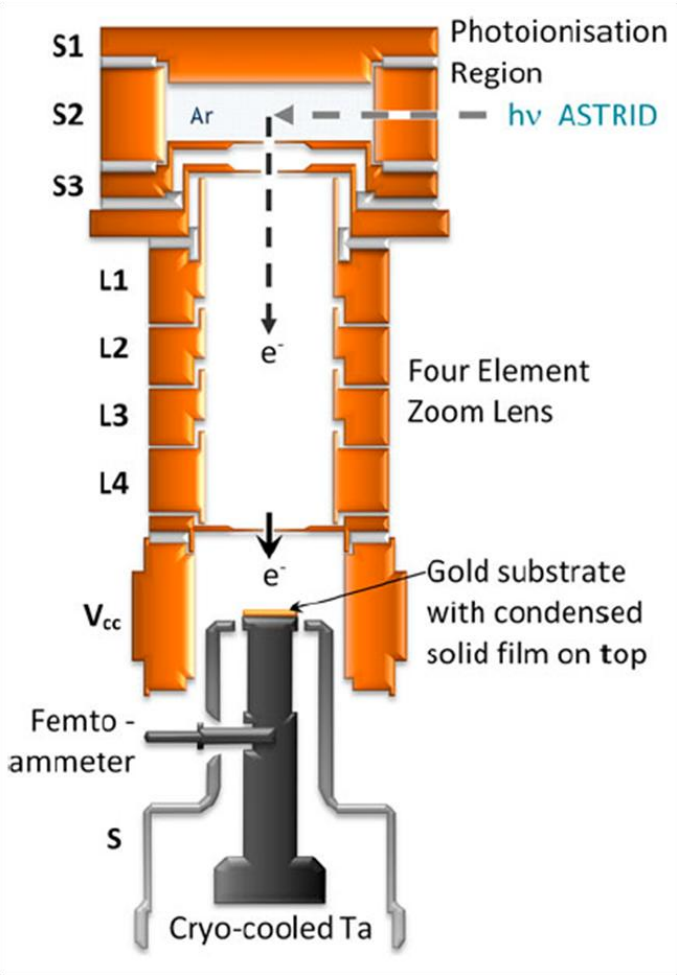

Figure 2.29: This figure illustrates the experimental setup in Aarhus for measuring the surface potential of spontelectric molecules. Photo–ionisation of argon gas (S1–3) produces near–zero kinetic energy electrons which are focussed (L1–4) onto the sample [37].

When the potential at the electron source has been zeroed with respect to the Au sample, the electrons are just able to reach the sample. Introducing molecules into the chamber which deposit as a film will change the measured current. The sample can then be zeroed again by biasing, or correcting the sample potential, and this bias leads to the surface potential measurement of the molecular film as the surface potential arises through the entirety of the bulk molecular film. In essence, this means that as if a molecular film on the Au substrate lead to a +1 V surface potential, the sample would have to be corrected by –1 V for the electrons to just reach the sample to bring the measureable current of the sample back to a relative zero fA value, usually at about 2 – 3 fA. The accuracy with which the surface potential is measured is 2 – 3 meV while the electron beam current is measured at 100 – 200 fA. Such currents do not affect the surface potential measurement [37].

A model has been built by David Field which is fully described in reference [37] to explain experimental data collected from the apparatus as depicted in **Figure 2.29**. A brief description of the mean–field model will be explained here which has been used to successfully describe the surface potential experiments. The initial factor to consider is that the spontelectric effect is a bulk effect starting from the sample–film interface, running through the molecular film normal to the surface and ending at the film–vacuum interface. In other words it can be described as running along the z–axis, if x and y refer to the sample surface plane. The electric field along the z–axis (E_z) is composed of two parts, a local symmetrical part (E_{sym}) and an asymmetric part (E_{asym}).

The symmetrical part, E_{sym}, being local, refers to the interactions holding molecular layers together and determines the intermolecular force field. Dipole alignment causes a surface potential to be measured, so this part is said to contain a constant term and a dipole–dipole term. This dipole–dipole term is proportional to the $(<\mu_Z>/\mu)^2$ and represents the average intermolecular dipole–dipole interaction where $<\mu_Z>/\mu$ is the degree of dipole orientation as a ratio of dipoles oriented along the z–axis direction to the total dipole moment in a solid. The squaring of this term describing the dipole–dipole interaction is followed by all similar interaction involving dipole–image charge, extended dipoles and arrays of dipoles [45–47].

The second part describing E_z is the asymmetrical part (E_{asym}). This non–local component travels through the film and describes long–range interactions. This is the

part of E_z that leads to the observation of a surface potential as measured in the experiments. This model cannot be directly compared to the literature as it is a newly discovered phenomenon, however it is similar to the Weiss field in ferromagnetism [48]. The Weiss field (which in terms of spontelectrics can be thought of as the polarisation field) is proportional to the magnetisation (which in terms of spontelectrics can be thought of as dipole orientation). The long–range part of this term comes from the orientation of the dipoles leading to an overall polarisation felt by other dipoles throughout the spontelectric molecular film. This polarisation occurs spontaneously upon film deposition and acts in a fashion to oppose the local E_{sym} term. The overall mathematical picture of the two opposing terms is shown through **Equation 17**;

$$E_Z = E_{sym} \times \left(1 + \zeta \left({< \mu_Z >}/{\mu} \right)^2 \right) - E_{asym} \times \frac{< \mu_Z >}{\mu} \qquad \textbf{Equation 17}$$

where the $\zeta(<\mu_Z>/\mu)^2$ term can be thought of as a "locking" or frustration term, restricting angular movement of one molecule with respect to another. Mean field theory leads on to an expression for the $<\mu_Z>/\mu$ term which can be described through the Langevin function as seen in **Equation 18**;

$$\frac{< \mu_Z >}{\mu} = \coth\left(\frac{E_Z \mu}{T}\right) - \left(\frac{E_Z \mu}{T}\right)^{-1} \qquad \textbf{Equation 18}$$

where T is the deposition temperature of the molecular film. The dipole moment of molecules, as referred to through its orientation and alignment, will be different from gas–phase species and solid state species due to different and depolarising environments. Solid state dipole moments (μ) can be calculated through **Equation 19**;

$$\mu = \frac{\mu_0}{1 + {\alpha k}/{s^3}} \qquad \textbf{Equation 19}$$

where μ_0 is the gas–phase dipole moment, α is the molecular polarisability, k is the force constant and s is the average spacing between molecular layers. If the model spontelectric molecule, N_2O, is considered, then a solid state dipole moment of 0.08 D is found by using a μ_0 of 0.166 D [49], α of 3.03×10^{-30} m^3, k of 11.034 [50] and s of 0.32 nm. For CO, the solid state dipole moment is found to be 0.076 D with k = 11.034 and α = 13.159 au and s = 0.34 nm (or 6.425 au).

2.6 Kinetic Simulations

Low level and simple models can be built to compare the experimental results to the theoretical predictions. The software used in this work is the Chemical Kinetics Simulator (CKS) developed by IBM [51]. The theory behind the software is the probability theory which attempt to describe the probability of finding a system without obtaining a precise result. This can also be thought of as a stochastic method. Monte Carlo level simulations are commonly used for the probability theory which samples a system at random in order to balance a fundamental condition set by the simulation at each integration. In order for the integration to begin initial differential equations are given as input to describe the system of interest, *i.e.* a TPD experiment and the associated chemical equations [52]. Besides the equations, other values are needed as input such as the initial concentration of a species and how it behaves with the described chemical equations of the system. The temperature can be fixed or varied as required for the specific simulation. When using CKS to simulate a TPD experiment these values have to be supplied to the software along with the energy of desorption and the associated pre–exponential factor. These two values can be extracted from the experimental results as an initial estimate of the values and then optimised to fit the experimental data.

2.6 References

[1] J. Woodall, M. Agundez, A.J. Markwick–Kemper and T.J. Millar, *Astron. Astrophys.*, 2007, **466**, 1197

[2] A.G.G.M. Tielens, *Rev. Mod. Phys.*, 2013, **85**, 1021

[3] H.J. Fraser, M.R.S. McCoustra and D.A. Williams, *Astron. Geophys.*, 2002, **43**, 10

[4] R.I. Maisel, *Principles of Adsorption and Reactions on Solid Surfaces* (Wiley, New York, 1996)

[5] D. King and M.G. Wells, *Surf. Sci.*, 1972, **29**, 454

[6] P. Atkins and J. de Paula, *The Elements of Physical Chemistry*, *4th Edition* (Oxford University Press, Oxford, 1992)

[7] H.J. Fraser, M.P. Collings and M.R.S. McCoustra, *Rev. Sci. Instrum.*, 2002, **73**, 2161

[8] V.L. Frankland, A. Rosu–Finsen, J. Lasne, M.P. Collings and M.R.S. McCoustra, *Rev. Sci. Instrum.*, 2015, **86**, 055103

[9] J.D. Thrower, *Ph.D. Thesis* (Heriot–Watt University, Edinburgh, 2009)

[10] A.G.M.A. Abdulgalil, *Ph.D. Thesis* (Heriot–Watt University, Edinburgh, 2013)

[11] D. Marchione, *Ph.D. Thesis* (Heriot–Watt University, Edinburgh, 2015)

[12] AZO Materials, http://www.azom.com/article.aspx?ArticleID=1114#_Fused_Silica

[13] C.Z. Tan and J. Arndt, *J. Chem. Phys.*, 2000, **112**, 5970

[14] J.E. Bartmess and R.M. Georgiadis, *Vacuum*, 1983, **33**, 149

[15] P. Atkins and J. de Paula, *Atkins' Physical Chemistry*, 7th E*dition* (Oxford University Press, Oxford, 2002)

[16] A.M. Al–Jalal and M.A. Khan, *Plasma Chem. Plasma Process.*, 2010, **30**, 173

[17] S. Ioppolo, G. Fedoseev, T. Lamberts, C. Romanzin and H. Linnartz, *Rev. Sci. Instrum.*, 2013, **84**, 073112.1

[18] M. Minissale, *Ph.D. Thesis* (University of Cergy Pontoise, Paris, 2014)

[19] J. He, D. Jing and G. Vidali, *Phys. Chem. Chem. Phys.*, 2014, **16**, 3493

[20] P.C. Cosby, *J. Chem. Phys.*, 1993, **98**, 9560

[21] M. Asplund, N. Grevesse, A.J. Sauval, C. Allende Prieto and D. Kiselman, *Astron. Astrophys.*, 2004, **417**, 751

[22] A. Sasso, M.I. Schisano, G.M. Tino and M. Inguscio, *J. Chem. Phys.*, 1990, **93**, 7774

[23] Oxford Scientific (now SPECS), RF OSPrey, RF Plasma Source Operating Manual, 2003

[24] J.T. Yates, Jr., *Experimental Innovations in Surface Science* (Springer, New York, 1998)

[25] G. Attard and C. Barnes, *Surfaces* (Oxford University Press, Oxford, 1993)

[26] K. Christmann and J.E. Demuth, *J. Chem. Phys.*, 1982, **76**, 6308

[27] M. Wu, C.M. Truong and D.W. Goodman, *J. Phys. Chem.*, 1993, **97**, 9425

[28] A.S. Bolina, A.J. Wolff and W.A. Brown, *J. Chem. Phys.*, 2005, **122**, 044713

[29] R.G. Greenler, *J. Chem. Phys.*, 1966, **44**, 310

[30] E.M. McCash, *Surface Chemistry* (Oxford University Press, Oxford, 2001)

[31] R. Aroca, *Surface–Enhanced Vibrational Spectroscopy* (Wiley, West Sussex, 2006)

[32] *Dictionary of Physics* (Oxford University Press, Oxford, 2015)

[33] D. Berreman, *Phys. Rev.*, 1963, **130**, 2193

[34] K. Hubner, L. Schumann, A. Lehmann, H.H. Vajen and G. Zuther, *Phys. Status Solidi B*, 1981, **104**, K1

[35] Sol Nudelman and S.S. Mitra, *Optical Properties of Solids* (Plenum Press, New York, 1969)

[36] M. Fox, *Optical Properties of Solids, 2nd Edition*, (Oxford University Press, Oxford, 2010)

[37] D. Field, O. Plekan, A. Cassidy, R. Balog, N.C. Jones and J. Dunger, *Int. Rev. Phys. Chem.*, 2013, **32**, 345

[38] R. Balog, P. Cicman, N. Jones and D. Field, *Phys. Rev. Lett.*, 2009, **102**, 2

[39] D. Field, O. Plekan, A. Cassidy, R. Balog and N. Jones, *Europhys. News*, 2011, **42**, 32

[40] O. Plekan, A. Cassidy, R. Balog, N.C. Jones and D. Field, *Phys. Chem. Chem. Phys.*, 2011, **13**, 21035

[41] O. Plekan, A. Cassidy, R. Balog, N.C. Jones and D. Field, *Phys. Chem. Chem. Phys.*, 2012, **14**, 9972

[42] A. Cassidy, O. Plekan, R. Balog, N.C. Jones and D. Field, *Phys. Chem. Chem. Phys.*, 2012, **15**, 108

[43] A. Cassidy, O. Plekan, R. Balog, J. Dunger, N.C. Jones and D. Field, *J. Phys. Chem. A*, 2014, **118**, 6615

[44] A. Cassidy, O. Plekan, J. Dunger, R. Balog, N.C. Jones, J. Lasne, A. Rosu–Finsen, M.R.S. McCoustra and D. Field, *Phys. Chem. Chem. Phys.*, 2014, **16**, 23843

[45] E. Cohen de Lara and J. Vincent–Geisse, *J. Phys. Chem.*, 1976, **80**, 1922

[46] B.L. Maschhoff and J.P. Cowin, *J. Chem. Phys.*, 1994, **101**, 8138

[47] D. Fernandez–Torre, O. Kupiainen, P. Pyykko and L. Halonen, *Chem. Phys. Lett.*, 2009, **471**, 239

[48] H. Kliem, M. Kuehn and B. Martin, *Ferroelectrics*, 2010, **400**, 41

[49] National Institute of Standards and Technology (NIST), http://webbook.nist.gov/chemistry

[50] J. Topping, *Proc. R. Soc. London, Ser. A*, 1927, **114**, 67

[51] IBM Almaden Research Centre, CKS, IBM corporation, 1995

[52] F.A. Houle and W.D. Hinsberg, *Surf. Sci.*, 1995, **338**, 329

Chapter 3

Oxygen Atom Chemistry

Contents of this chapter

3.1 Introduction

In **Chapter 1**, the importance of dust grains and formation routes of H_2O were introduced. As expressed, the main method of formation on dust grains is through reactive accretion which has been studied from different points of view by many research groups over the years; see for instance [1–4 and references therein].

In this chapter, the formation routes of H_2O as outlined in **Figure 3.1** will be studied, with particular emphasis on the initial line of O leading to O_2 and on to O_3, *i.e.* the O atom chemistry. The initial steps of O atom chemistry, ultimately leading to H_2O have in particular been investigated by the groups of Vidali and Dulieu. Both groups use atomic O beams, but on differing surfaces. An important note to consider is that the results of this chapter are preliminary and will therefore, to a certain degree, lean on the work published by these research groups to show the application of the atomic beam sources as discussed in **Chapter 2**.

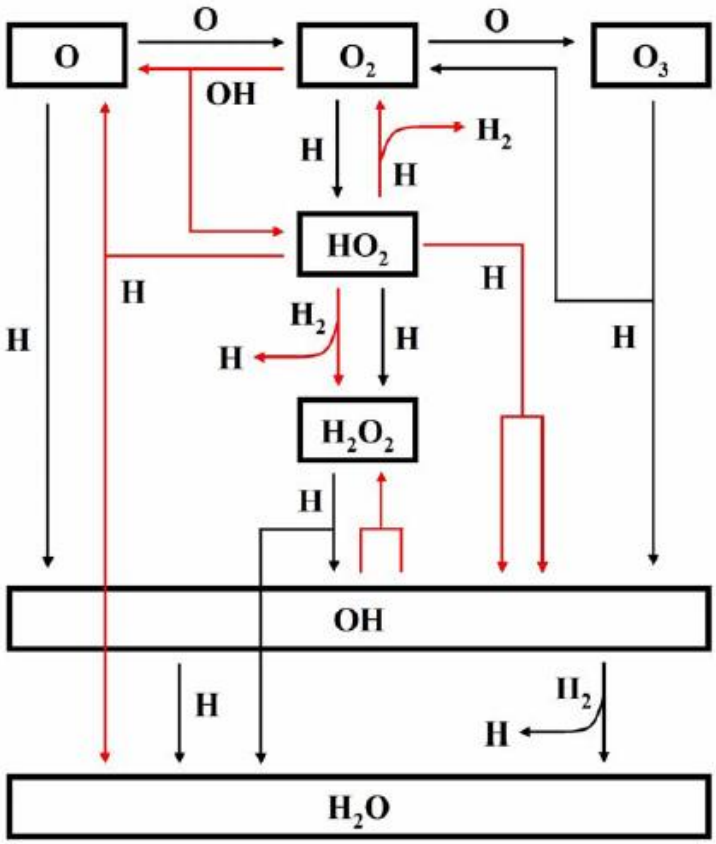

Figure 3.1: This figure indicates a variety of routes of H_2O in the solid phase on interstellar dust grains. The focus point of this chapter will be in the top line where O atoms lead to O_2 which can lead to O_3. This figure is taken from [3].

3.2 Experimental

The equipment and general method of working have been described in **Chapter 2**, but the specific steps taken in looking at the oxygen chemistry will be discussed here. Prior to an experiment the sample was heated to 220 K for 10 minutes to clean the sample and cold finger, then left to cool to a base temperature of 17 K while the separate gas dosing lines were purged with O_2 and H_2O. With a clean O_2 gas line, the plasma source was turned on to a power of 150 W before O_2 was leaked into the plasma chamber to a final value of $1.0 - 1.1 \times 10^{-5}$ mbar, the plasma chamber was then left to warm up. This pressure corresponds to a beam flux of 5×10^{14} molecules cm^{-2} when the gate valve between the plasma and main chamber is opened. After two to three hours the plasma source reached operational conditions and the power was turned down to 110 W. The plasma emission was monitored with the fiber optic cable linked to an Ocean Optics spectrophotometer leading to a typical intensity of 5.5×10^4 counts. At this value of counts the beam is composed of about 20% O atoms as explained in **Chapter 2.3.5**. RAIRS backgrounds were taken after optimization of the IR spectrometer, 512 scans were taken per experiment with a resolution of 1 cm^{-1}. For the experiments involving H_2O an ionisation coefficient of unity was assumed in depositing 50 ML of p–ASW (at base temperature), of c–ASW (at 110 K) or of CSW (at 140 K). During the testing phase, the maximum time for atomic oxygen bombardment was determined to be 50 minutes. Beam dosing for a longer time will lead to greater desorption from the cold finger, thereby increasing the pressure to beyond the safe operational conditions of the QMS. TPD experiments were also conducted following the RAIR measurement with a average heating ramp of 0.24 K s^{-1} for O_2 desorption and 0.17 K s^{-1} for O_3 desorption.

3.3 Results and Discussion

In this section the results of the beam dosing experiments relevant to oxygen and water chemistry relevant to the interstellar medium will be presented. Initially, experiments with the molecular beam were done to be able to directly compare any differences when the plasma source was turned on. Reflection–absorption infrared spectroscopy (RAIRS) and temperature programmed desorption (TPD) are the analytical techniques that will be used to investigate any potential reactions occurring.

3.3.1 O_2 molecular beam dosing

Before the atomic oxygen experiments were conducted, molecular oxygen experiments were performed. This was done with a beam flux (as described in **Chapter 2**) of 5×10^{14} molecules cm^{-2} and dosing for 1, 2, 5, 10, 20 and 50 minutes. TPD experiments were conducted with m/z = 16 and 32 only as no O_3 is formed; RAIR spectra were not measured as O_2 is in principle IR inactive as it is electrically dipole forbidden, however IR bands of solid O_2 have been detected in the 1580 – 1630 cm^{-1} region [5] which are not observed in this work.

The results of the TPD experiment can be seen in **Figure 3.2**. At higher temperature O_2 begins to desorb from the cold finger which has not be included in this figure.

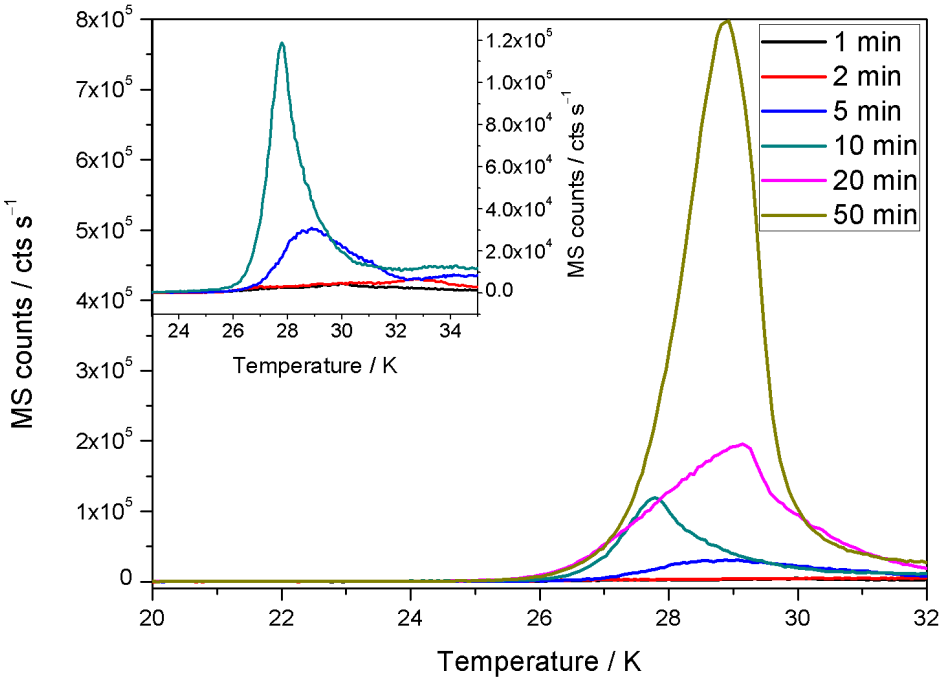

Figure 3.2: This figure shows the results of the TPD experiments of molecular oxygen beam dosed onto SiO_2 for 1, 2, 5, 10, 20 and 50 minutes. A clear change can be seen between 5 and 10 minute dosing, this is due to the change from sub–monolayer to multilayers of O_2. This change is more clearly shown in the insert of 1, 2, 5 and 10 minute dosages.

As can be seen in **Figure 3.2**, the traces of 10, 20 and 50 minute dosing all have somewhat aligned leading edges which is indicative of multilayer desorption as explained in **Chapter 2**. A difference between the 10 minute and 20/50 minutes TPD traces can be seen in **Figure 3.2**. The heating rates are similar (only differing by 0.01 K s^{-1}) and are not expected to be the cause of the shift in this temperature range. The work

of Collings *et al.* [6] showed that a difference in O_2 TPD traces is observed between 2.5 and 3.7 ML when background dosing O_2 using the same experimental set–up. This shift in the TPD traces is possibly the $\alpha \rightarrow \beta$ crystalline phase transition of O_2 as noted by Cairns and Pimentel [7] and Freimann and Jodl [8] and it could possibly be the same reason for the shift observed between the multilayer O_2 TPD traces of **Figure 3.2**. Dosing O_2 for shorter time leads to sub–monolayer quantities of O_2 where the desorption peaks move to lower temperatures as the exposure increase from 1 to 2 to 5 minutes. This is shown with the insert in **Figure 3.2** which includes the 10 minutes trace for reference. Considering the change between the 5 and 10 minute dosing, one can estimate that 1 ML of O_2 is formed after 10 minutes, therefore the maximum dosing time of 50 minutes corresponds to about 5 ML of O_2.

Typical first order desorption, as is expected from sub–monolayer amounts of material, should show the same peak temperature as the coverage increases. This is not seen in the insert of **Figure 3.2** for O_2 sub–monolayer desorption, however that is not unusual due to the array of binding sites rough surfaces such as an amorphous SiO_2 film offers [6, 9, 10].

With the context of atomic oxygen deposition onto various surfaces in this work, the longer the dosing time, the more O_2 and O_3 will be formed. Considering this, only the greatest exposure will be analysed, however an interesting trait can be seen between the multilayers when O_2 desorbs. Dosing times above 50 minutes leads to pressure increases too great for the QMS to handle, for that reason the remainder of the chapter will focus on these regions where about 5 ML of O_2 has been deposited after 50 minute dosing.

With this in mind, this thick layer corresponding to 5 ML O_2 desorbing from SiO_2 will be analysed and the kinetic parameters extracted. Firstly, a leading edge analysis (LEA) will be done to show that desorption is zero order as befitting the theory behind multilayer desorption where the leading edges are aligned. This is done by comparing the rate of desorption (r_{des}) with the number of molecules (N) leaving the surface at a specific temperature. The relationship between these variables can be described through **Equation 1**,

$$r_{des} = N \times 6\ cm^2 \times 10^{15}\ molecules\ cm^{-2} \qquad \textbf{Equation 1}$$

where *N* is calculated through the total number of molecules in the TPD spectrum minus the molecules in the gas phase at a chosen temperature with respect to the number of monolayer TPD trace. The value of 6 cm^2 corresponds to the surface area of the sample used in this work and 10^{15} molecules cm^{-2} is the typical number of molecules found in a monolayer [11]. The results of this analysis can be seen in **Figure 3.3**.

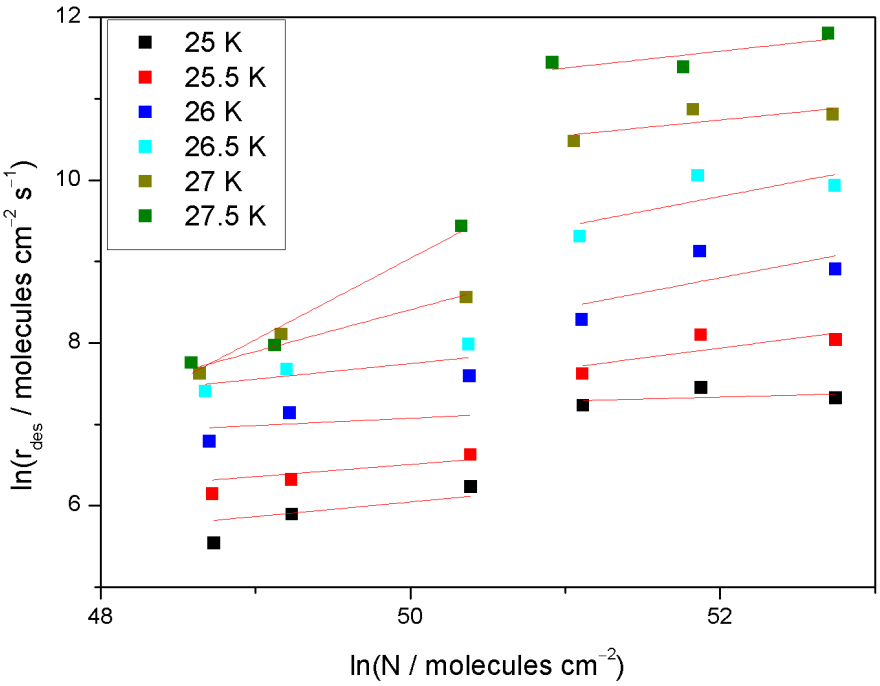

Figure 3.3: This figure shows the results of the leading edge analysis of the pure O_2 molecular beam dosing TPD experiment. Two separate regions can be distinguished where the lower three points relate to the coverages of 1, 2 and 5 minute beam dosing and the latter three points are of the 10, 20 and 50 minute dosing. These two regions are the sub–monolayer and multilayer respectively.

As can be seen in **Figure 3.3**, two regions exist when desorbing O_2 dosed at a range of molecular thicknesses. The first three points lead to an average gradient of 0.49 ± 0.20 which is the desorption order for the low coverages of 1, 2 and 5 minute beam dosing. A value closer to unity was expected as this is considered the sub–monolayer regime for O_2 desorption, however with more data points the gradient is expected to change to approach a value of one. This can be seen when background dosing O_2 on SiO_2 as in Collings *et al.* [6]. The plateau has an average gradient of 0.23 ± 0.21 and is the region of interest as multilayers will be studied in this chapter, and an order of zero is indicative of such layers. As can also be seen, the plateau is not completely zero, even when considering the uncertainty. A possible reason for this is linked to the difference in the leading edges of the TPD trace with the α → β phase transition explained earlier in this section. If more data points were studied, an ideal behaviour of two separate

regions with zero order desorption kinetics is expected. Zero order kinetics is therefore assumed to be involved in the desorption process when an amount of >10 minute O_2 beam dosing is desorbed. Considering that desorption of this molecular film follows zero order kinetics, **Figure 3.2** can be inverted to shows **Figure 3.4** which is the natural logarithm *versus* the inverted temperature of the molecules leaving the surface.

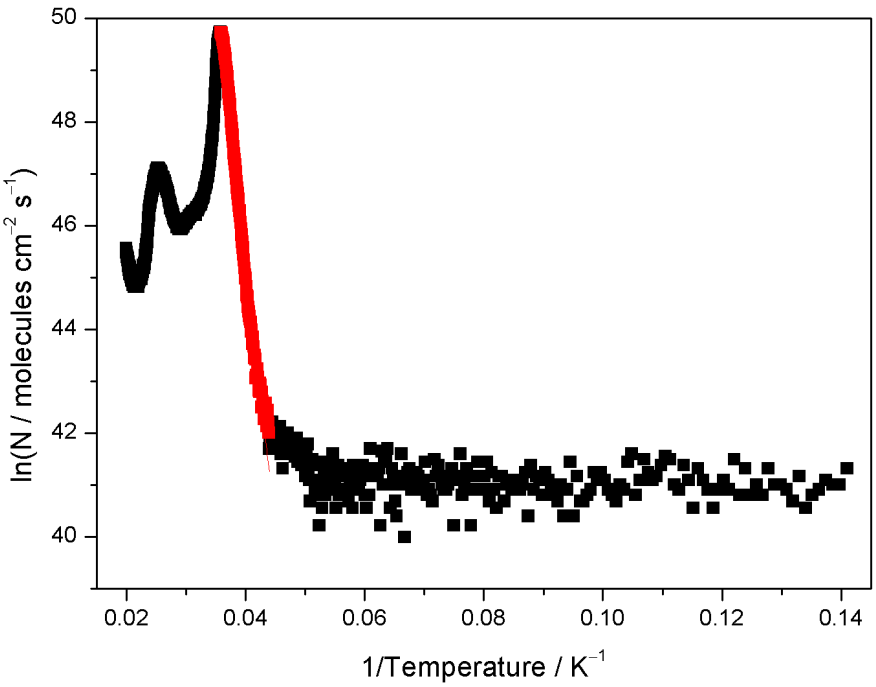

Figure 3.4: This figure shows the Arrhenius plot of the TPD trace after the molecular oxygen beam has dosed the bare SiO_2 surface for 50 minutes. The black dots correspond to the experimental data and the red dots highlight the leading edge of the TPD profile from the same 50 minute TPD trace in **Figure 3.2**.

The red line in **Figure 3.4** corresponds to the leading edge as O_2 desorbs in **Figure 3.2** which can be described by the Arrhenius equation (**Equation 2**) as mentioned in **Chapter 2**,

$$\ln(k) = \ln(\nu) - \frac{E_a}{RT} \qquad \textbf{Equation 2}$$

where E_a is the activation energy for desorption which is determined through the gradient of the red line, R is the gas constant, T is the temperature on the sample, ν is the pre–exponential factor which can be determined through the intercept with the Y–axis and k is the rate constant. As can be seen from **Figure 3.4**, and with the use of **Equation 2**, the desorption energy can initially be estimated as being 8.7 kJ mol^{-1} and the pre–exponential factor can be estimated as being about 10^{32} molecules cm^{-2} s^{-1}. These values, along with an estimated concentration of O_2 on the surface being 5×10^{15}

molecules cm^{-2}, (as 10^{15} molecules cm^{-2} is typically assumed as one ML [11]) leads to a simple CKS model being built. This model will only consider the multilayer desorption process following the model set up in **Equation 3**:

$$O_2\,(s) \rightarrow O_2\,(g) \qquad \textbf{Equation 3 (A)}$$

$$O_2\,(g) \rightarrow O_2\,(pump) \qquad \textbf{(B)}$$

where the bracketed terms refer to O_2 being in the solid form on the surface (s), in the gas phase (g) and as it is pumped away (pump). The rate constant for the last step where gas–phase O_2 is pumped away is temperature independent and has an associated rate constant of 0.03 s^{-1} to model the pumping speed of the diffusion pump (this rate constant is not associated with the rate determining step meaning it has to be relatively high in value). The results of the model when compared to the experimental data can be seen in **Figure 3.5** where the solid line shows the model and scatter plot indicates the experimental data.

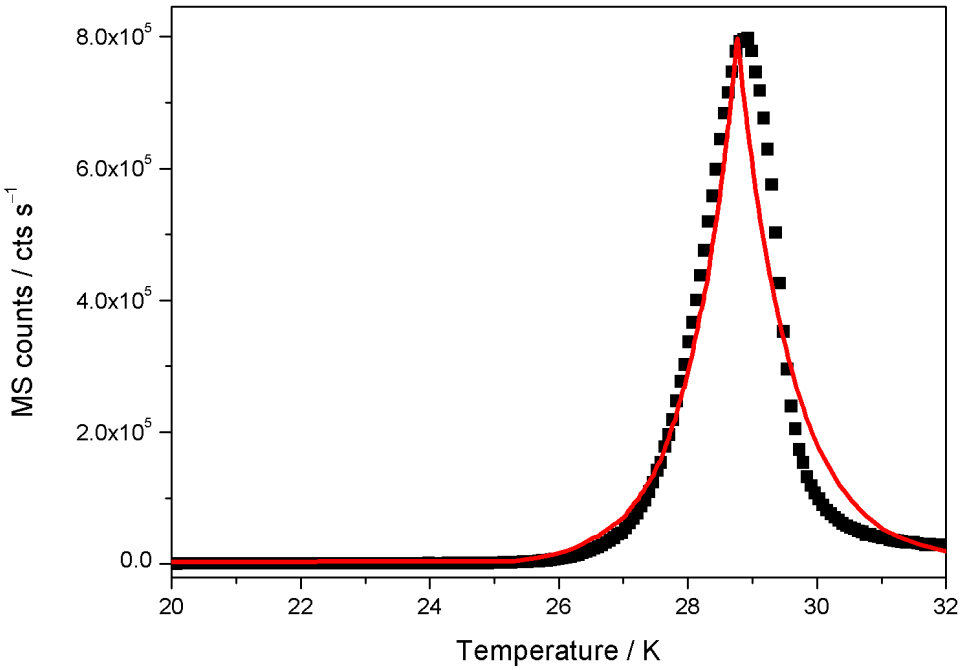

Figure 3.5: This figure shows the TPD results of 50 min molecular oxygen dosing onto SiO_2 (black scatter) with the CKS model as a red solid line.

From **Figure 3.5** and the CKS model used to fit the data, a closer approximation of the kinetic parameters can be extracted. For the desorption process of about 5 ML O_2 leaving the SiO_2 surface an associated energy is found to be 8.5 ± 0.1 kJ mol^{-1} with a pre–exponential factor of $4 \times 10^{30\pm1}$. Background dosing of O_2 and its TPD spectrum has been studied to a great extent from such as the work from Collings *et al.* [6] where

O_2 was desorbed from the same surface as described in this thesis. In that work an E_{des} of 7.5 ± 0.2 kJ mol^{-1} and $\nu = 10^{28\pm1}$ molecules cm^{-2} s^{-1} was determined as being the kinetic parameters needed for O_2 to desorb. Another example is in the work on Acharyya *et al.* [12] and Fuchs *et al.* [13] where an E_{des} of 7.6 ± 0.2 kJ mol^{-1} was determined as required energy for multilayer desorption of O_2. As can be seen, a discrepancy between the literature data and the data of this work exists. A possible reason for this could be in the deposition method. A TPD study regarding different deposition method of H_2O, background dosing and beam dosing, by Kimmel *et al.* [14] has shown a similar difference as noted here. Background dosing, or background filling of the chamber leads to a slower deposition rate and a more inflated solid structure, possibly due to 'hit–and–stick' ballistic deposition. Beam dosing is more direct with a lower pressure in a UHV chamber, this leads to a more compact solid film. In other words, the morphology of molecular films changes depending on dosing technique.

3.3.2 O Atoms on Silica

Having categorised how beam dosed O_2 molecules behave on SiO_2, the plasma sources can now be turned on and the O/O_2 beam can be studied on different surfaces. To be able to compare the results directly, the beam flux was kept constant at 5×10^{14} molecules cm^{-2} and a clean SiO_2 sample was initially used. The specific reaction steps involving oxygen chemistry that will be studied are shown in **Equation 4**.

$$O \xrightarrow{O} O_2 \underset{O}{\overset{O}{\rightleftarrows}} O_3 \qquad \textbf{Equation 4}$$

This simple reaction scheme indicates the reactions that are possible when the $O:O_2$ beam is dosed onto bare SiO_2. O_3 degradation with another oxygen atom leading to $2O_2$ molecules is naturally also possible, but the extent to which this happens cannot be determined through these experiments. This sort of chemistry can be considered as the solid state version of the Chapman mechanism known in atmospheric chemistry [15].

3.3.2 (a) Reflection–Absorption Infrared Spectroscopy

Similar to the TPD experiments explained earlier, the maximum O atoms dosing time was set to 50 minutes. However, an experiment where the dosing time was increased as in the O_2 beam experiment was also done. The results of dosing O atoms onto SiO_2 for times of 1, 2, 5, 10, 20 and 50 minutes can be seen in **Figure 3.6**.

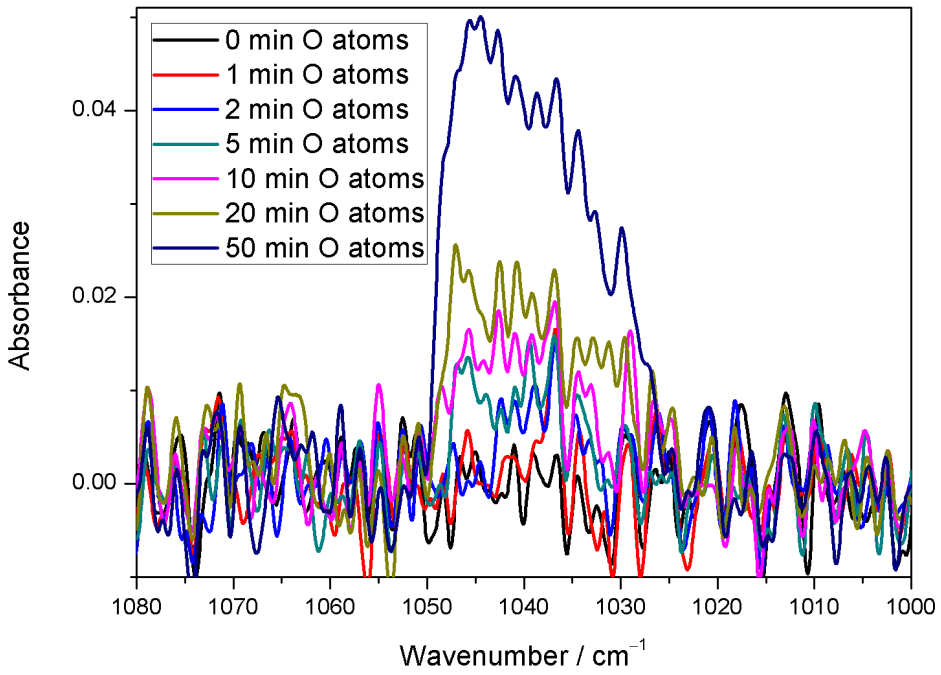

Figure 3.6: As can be seen in this figure, O_3 is produced as the O atom beam bombards the bare SiO_2. As the dosing time is increased a peak at about 1045 cm^{-1} is seen to grow as dosing time is increased.

As is naturally expected, and as can be seen in **Figure 3.6**, the longer time the O atoms bombard the SiO_2 surface, the more O_3 is formed. Therefore, the limiting the discussion to the 50 minute O atom dosing time remains the focus of the chapter. A peak is seen to form at about 1045 cm^{-1} which can be fitted with three Gaussians leading to **Figure 3.7** for a better understanding of the band. The three Gaussians as shown in blue in **Figure 3.7** were compiled to reduce the residual difference between the experimental data (red) and the overall fit as shown in red. This can be seen in the top of **Figure 3.7** where the difference between the observed absorbance (A_{Obs}) and the fitted abundance (A_{Fit}) is shown over the region of the O_3 peak which indicates that the fit is appropriate considering the signal–to–noise level. The three Gaussians involved in creating the O_3 peak fit have been listed in **Table 3.1**.

Wavenumber / cm^{-1} (± 1)	**Assignment**	**Literature / cm^{-1} (± 2)**
1031	$[O_3...O]$	1032
1036	O_3 (ν_3) O–O asymmetric stretch	1037
1045	$[O_3...O_3]$	1042

Table 3.1: This table shows the IR frequencies composing the O_3 band displayed in **Figure 3.7** which have been compared to literature values.

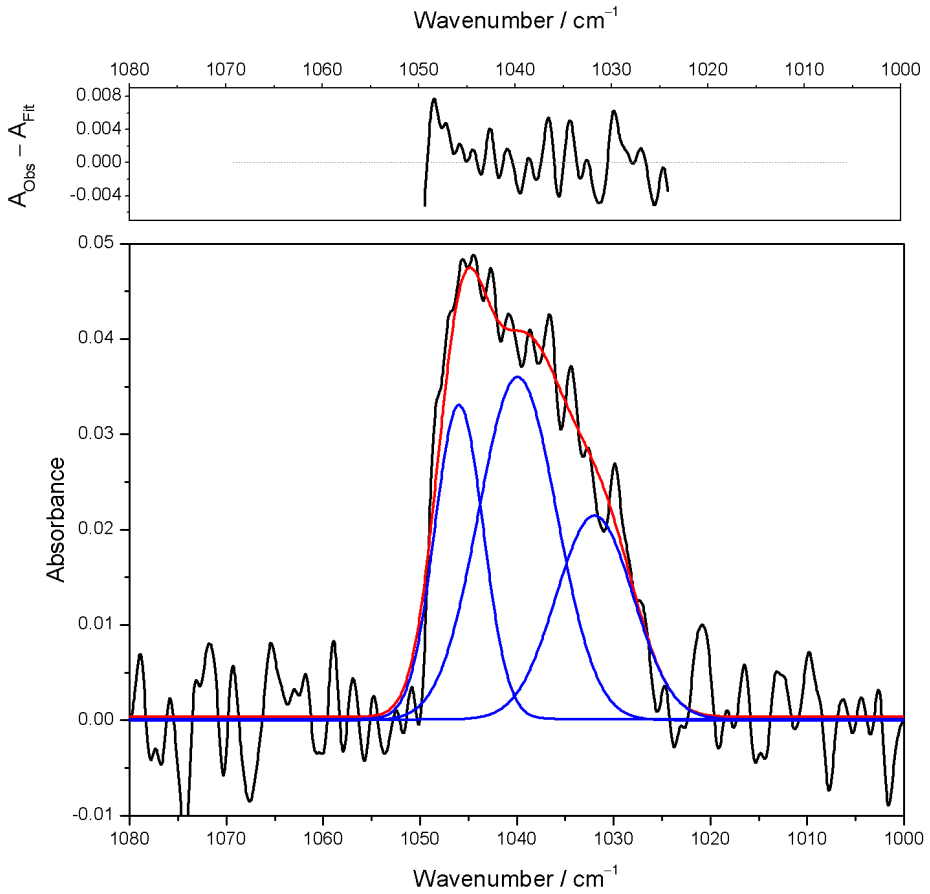

Figure 3.7: This figure shows the fit between the RAIRS data (black) and the fit (red) which is made by three Gaussians in blue. The result of the fit has been listed in **Table 3.1**. Further to this, the top of the figure shows the residuals from the experimental data and the overall fit.

As can be seen in **Figure 3.7** and **Table 3.1**, O_3 features have been found after O atom bombardment of the bare SiO_2 sample. Other features of O_3 such as O–O symmetric stretching vibration at 1104 cm^{-1} or the O–O–O bending vibration at 702 cm^{-1} [16] were not detected in any of the experiments due to low signal or being outside of the MCT detection range [17].

3.3.2 (b) Temperature Programmed Desorption

The results of what happens in **Equation 4** can be also seen through the TPD experiment subsequent to dosing the $O:O_2$ beam onto SiO_2 for 50 minutes as illustrated in **Figure 3.8**.

In **Figure 3.8** O_2 desorption is observed to begin at about 23.8 K and peak at about 29.1 K while O_3 shows no clear TPD trace, only a slightly higher count rate in the 50–60 K

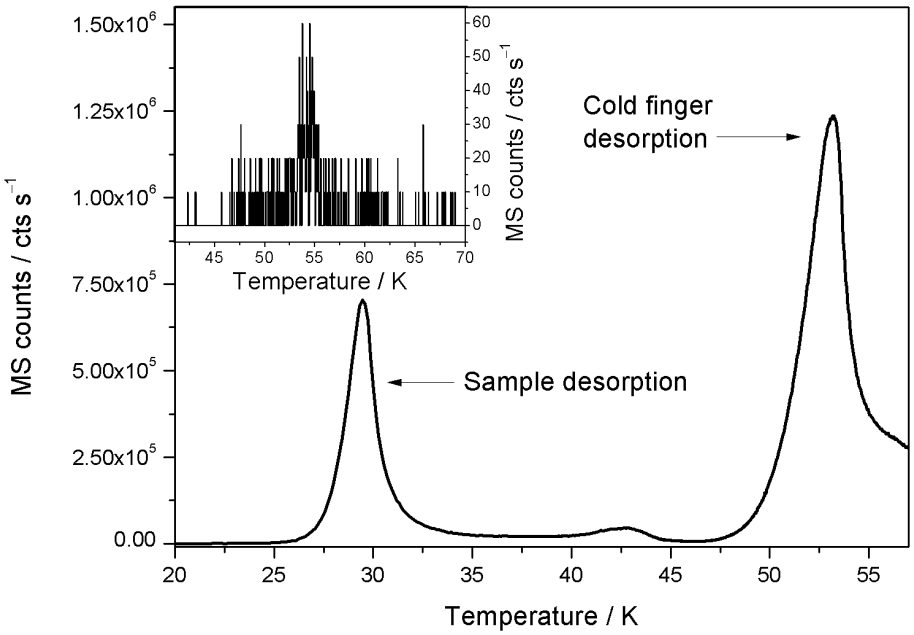

Figure 3.8: This figure shows the results when the O atomic beam is dosed onto SiO_2 for a duration of 50 minutes. The O_2 TPD trace, measured through m/z = 32 shows two main peaks, the low temperature peak corresponds to sample desorption while at higher temperatures O_2 is released from the cold finger. The insert shows O_3 desorption, m/z = 48, as measured simultaneously with O_2 cold–finger desorption.

range. As can be seen in **Figure 3.8** between the main figure and the insert, O_3 desorption occurs in the same temperature range as O_2 desorption from the cold finger.Due to the larger quantity of O_2 sticking to the colder surfaces of the cold finger, distinction between regular O_2 and decomposed O_3, into O and O_2, does not follow a simple procedure. However, an analysis of O_3 desorption will follow later in this chapter, in **section 3.3.6**. Monitoring m/z = 16 (O^+ atoms alone) leads to no deviation from the O_2 signal meaning that single oxygen atoms are not observed during the experiments which has also been the case for other research projects [18]. However, O atom desorption has been noted by various sources as leaving SiO_2 and H_2O surfaces with energies ranging from about 10 – 15 kJ mol^{-1} [9, 19] and other values such as 12.1 kJ mol^{-1} [20, 21] from C_2H_2 and 11.2 kJ mol^{-1} from pyrene [22].

Considering how these and the following O atom beam dosing experiments were only done for the maximum possible time to obtain the highest levels of O_3 formation, LEA was not done. However, this was done for O_2 beam dosing as discussed earlier and for that reason the O_2 TPD traces can be analysed by assuming zero order desorption kinetics as discussed earlier. Inverting **Figure 3.8** to find the kinetic parameters for O_2 desorption when dosing O atoms, similar to the O_2 beam analysis, leads to the Arrhenius plot of **Figure 3.9**.

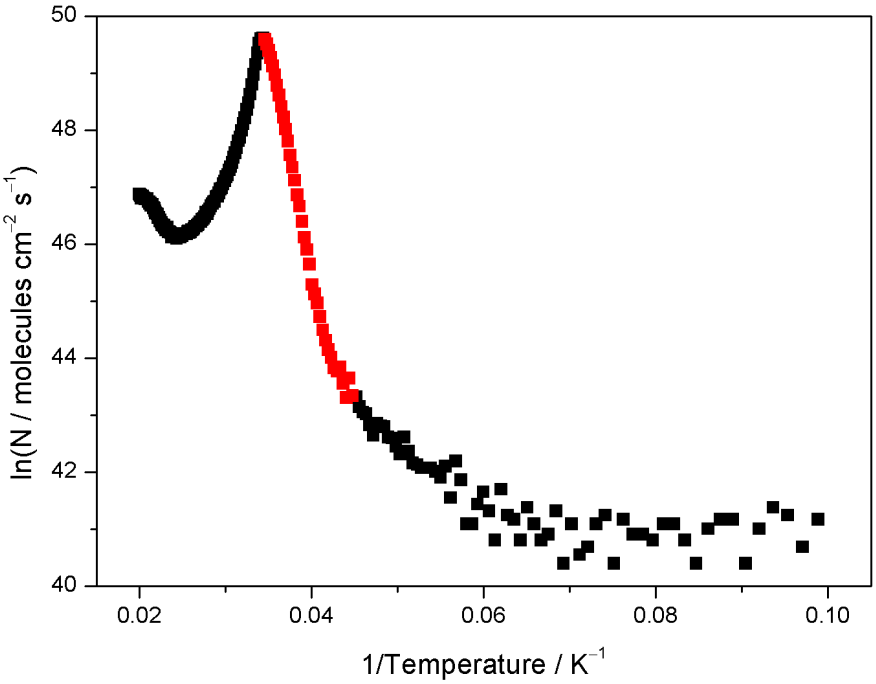

Figure 3.9: This is the Arrhenius plot of the desorption profile from the TPD trace in **Figure 3.8**. The black scatter is representative of the inverted TPD trace after the atomic beam has bombarded the bare SiO_2 for 50 minutes with the red points being the leading edge of the TPD trace.

From **Figure 3.9** we can estimate the activation energy for desorption, E_{des}, and the pre–exponential factor, v, for desorption of O_2 molecules through the gradient and the intercept, respectively, through the red linear scatter points as stated in **Equation 2**. As

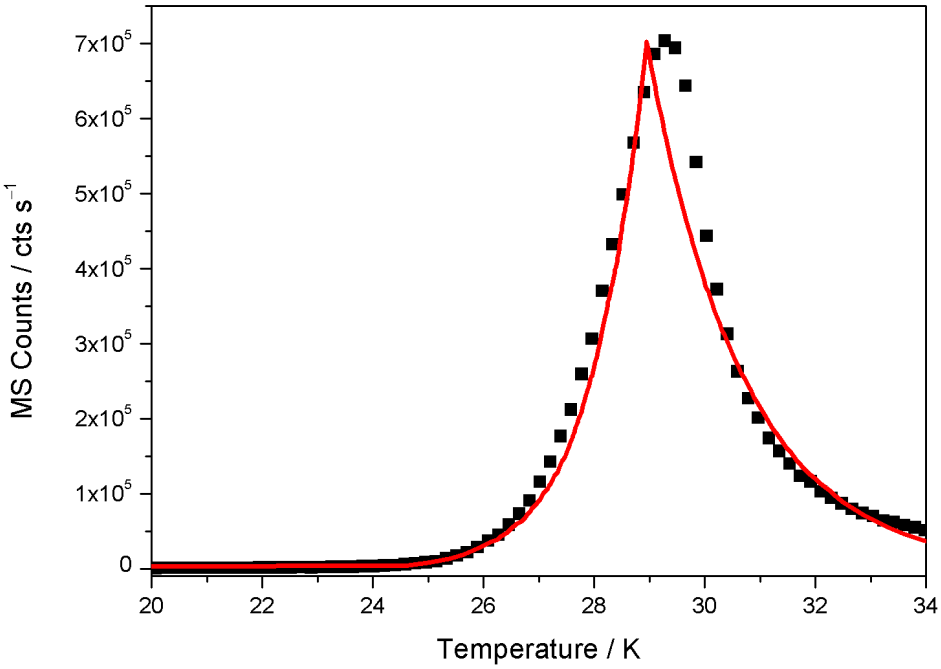

Figure 3.10: This figure shows the comparison between the experimental data (black scatter) and the CKS model (red solid line). This fit has been created with an E_{des} of 6.7 kJ mol^{-1} and 5 × 10^{27} molecules cm^{-2} s^{-1}.

a first estimate **Figure 3.9** yields a value for E_{des} of 6.5 kJ mol^{-1} and ν of 2 × 10^{33} molecules cm^{-2} s^{-1}. These values can be used in a similar set of CKS equation as **Equation 3** earlier. With this model arranged and considering an initial [O_2] corresponding to 5 ML the graph in **Figure 3.10** can be produced.

Figure 3.10 shows the experimental data in circles with the simulated spectra as a line. When the E_{des} and ν are set to 6.7 kJ mol^{-1} and 5 × 10^{27} molecules cm^{-2} s^{-1} the agreement between the two curves is good. Initial thoughts when comparing the desorption energy of molecular O_2 dosing (8.5 kJ mol^{-1}) and atomic beam dosing (6.4 kJ mol^{-1}) could be that the values should be the same. O atoms and O_2 molecules are deposited at the same time, leading to more O_2 molecules and O_3 formation. As further O atoms bombard the O_2 molecules on the surface, a change in the morphology is possible, due to O_2 and O_3 formation. The energy released as the molecules are formed has to be dissipated in order for the reaction product to remain on the ice surface. This reaction enthalpy release promotes the morphological change. When this reaction occurs on SiO_2, the energy is dissipated into the surface of the sample, however an O_2 layer is continually being made during O beam deposition. As more O_2 molecules are deposited and formed, new O_2 reaction will begin to take place on O_2 rather than SiO_2. The formation energy is now dissipated into the O_2 film which could lead to changes in the morphology and structure of the film. If this is the case, a more fluffy ice could begin to be formed, an O_2 film that is partially amorphous. Amorphous solids generally have a lower E_{des} as compared to its crystalline counterpart [24 and references therein]. Similar amorphisation mechanisms have been observed in other experiments where energy is in a thin film, *e.g.* electron bombardment of benzene films [25] and exposure of H_2O ices to ionising sources, both protons and electrons [26].

3.3.3 O Atoms on Porous Amorphous Solid Water

Having investigated what happens as the O:O_2 beam bombards a naked SiO_2 surface, the focus will turn to the more realistic scenario where H_2O is already present on a dust grain. The same beam flux as for the previous experiments is used, but a 20 ML film of H_2O is now pre–deposited onto the SiO_2 surface before O atom bombardment. To begin with the H_2O film will be deposited as porous amorphous solid water (p–ASW).

With the presence of H_2O already on the surface, the same O_3 formation pathway is possible, however H_2O_2 formation could possibly become important [27] through **Equation 5**:

$$O + H_2O \rightarrow H_2O_2 \qquad \textbf{Equation 5 (A)}$$

or possibly more accurately

$$O + H_2O \rightarrow 2OH \qquad \textbf{(B)}$$

$$2OH \rightarrow H_2O_2 \qquad \textbf{(C)}$$

The formation of H_2O_2 in **Equation 5** proceeds through O^1D and as stated in **Chapter 2**, only O^3P is believed to be present in the atomic beam. Therefore, formation of H_2O_2 would mean that the atomic beam is not pure as expected. Formation of H_2O_2 has also been studied through ion irradiation of H_2O surfaces [28], the HO_2 + HO_2 reaction [29] and by hydrogenation of O_2 through the intermediary molecules of 2OH [30] as depicted in **Figure 3.1**.

3.3.3 (a) Reflection–Absorption Infrared Spectroscopy (RAIRS)

Any formation of H_2O_2 and O_3 can be observed as the H_2O is bombarded through RAIRS. As has been discussed previously; O_3 shows a peak in the IR spectrum at about 1140 cm^{-1}, this peak can be seen in **Figure 3.11**.

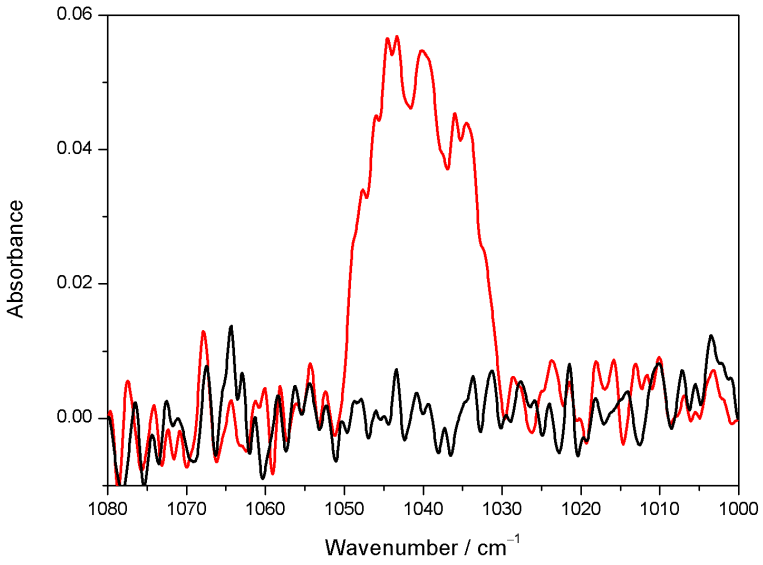

Figure 3.11: This figure shows the formation of O_3 when the O atom beam bombards 20 ML p–ASW. As can be seen, the shape and character of the feature is similar to when O atoms probe the bare SiO_2 surface.

Figure 3.11 can be fitted similar to **Figure 3.7** to show what components make up the O_3 band. From the previous analysis of O_3 on SiO_2, the same vibrational characteristics can be seen to make to the ~1145 cm^{-1} feature, **Table 3.2**.

Wavenumber / cm^{-1}	Assignment	Literature / cm^{-1}
1031 ± 1	[O_3...O]	1032 ± 2
1037 ± 1	O_3 (ν_3) O–O asymmetric stretch	1037 ± 2
1045 ± 1	[O_3...O_3]	1042 ± 2

Table 3.2: This table shows the result of resolving the components of the O_3 band when fitted with Gaussians and their comparison with literature values.

As can be seen in **Table 3.2**, the feature in **Figure 3.11** corresponds to O_3 in different environments and matches the literature frequencies nicely. Having confirmed that O_3 is produced on different surfaces, the focus will shift towards H_2O_2 formation. The infrared spectrum of H_2O_2 has been studied extensively, as for example by looking at the 3700 and 1601 cm^{-1} features [27], the 2850 cm^{-1} feature [28], and small clusters and monomers isolated in different matrices [31, 32], making it simple to follow any formation of this molecule in the IR spectrum, **Figure 3.12** shows these regions.

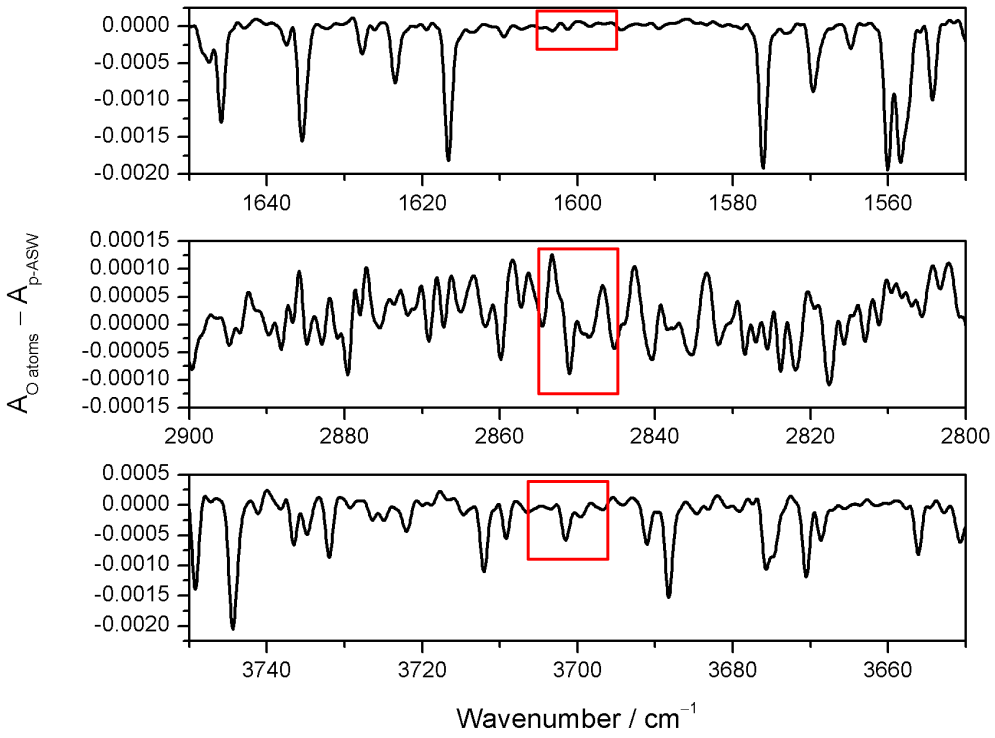

Figure 3.12: This figure shows the three regions of interest in the IR spectrum. These are difference spectra showing the difference in absorption of the p–ASW film (A_{p-ASW}) after O atom bombardment ($A_{O\ atoms}$). The red boxes indicate the specific regions where H_2O_2 features are expected if formed, however no such features are observed.

Figure 3.12 is of three difference spectra of the p–ASW film (A_{p-ASW}) and the same film after 50 minute O atom bombardment ($A_{O\ atoms}$). The red boxes indicate the regions of interest where H_2O_2 features are expected if the molecules has been formed during O atom bombardment, however no features are observed. The sharp peaks from 3600 cm^{-1} and greater and about 1500 – 2000 cm^{-1} are of gas–phase water in the optics boxes outside of the UHV chamber. Considering the entire detection range of the MCT detector used 4000 – 800 cm^{-1}, the only change observed is at about 1045 cm^{-1} as O_3 is formed as seen in, for example, **Figure 3.11**.

3.3.3 (b) Temperature Programmed Desorption

As with the studies of O atom beam irradiation of SiO_2, the initial molecule studied will be O_2, however as the procedure has been explained in the previous chapter, **Section 3.3.2**, only a brief summary will be given here before the general results.

Monitoring m/z = 32 as the temperature is raised, post–atom beam bombardment, leads to **Figure 3.13**.

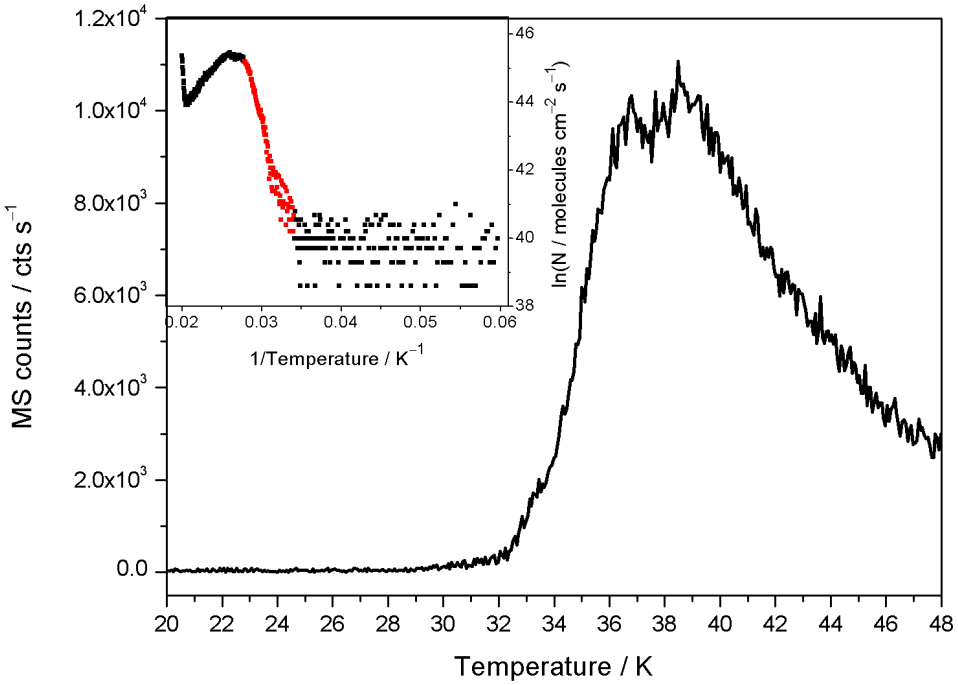

Figure 3.13: This figure is of the 20 ML p–ASW film after 50 minute O atom bombardment as it desorbs. The species of interest in this figure is O_2 as it leaves the surface, the shape and temperature at which it leaves the surface is due to the porosity of H_2O. The insert is an Arrhenius plot where the red dots (the leading edge of desorption) are used to extract the kinetic information of the desorption process.

Figure 3.13 shows the desorption process of O_2 from 20 ML p–ASW. At first glance, the temperature at which O_2 begins to leave the surface, about 32 K, is greater than observed when O_2 leaves bare SiO_2 as shown in **Figures 3.2** and **3.8**. A change can also be seen in the shape of the peak. The reasons for these new features are put down to the change in the surface. The porous nature of the H_2O underlayer leads to a varying and different surface as compared to SiO_2. Dangling bonds are present at a much greater concentration on p–ASW as compared to other types of H_2O films [33, 34] which could be a contributing factor to the observed differences. The insert in **Figure 3.13** is of the Arrhenius plot of the TPD data. This plot leads to an approximate E_{des} (6.6 kJ mol^{-1}) and pre–exponential factor (6×10^{29} molecules cm^{-1} s^{-1}) as previously demonstrated. A similar CKS model can be built, including only the same two steps as earlier of solid O_2 becoming gas phase and the gas leading to the pumping stage as seen in **Equation 3** above. With this model and the various parameters included, **Figure 3.14** has been created.

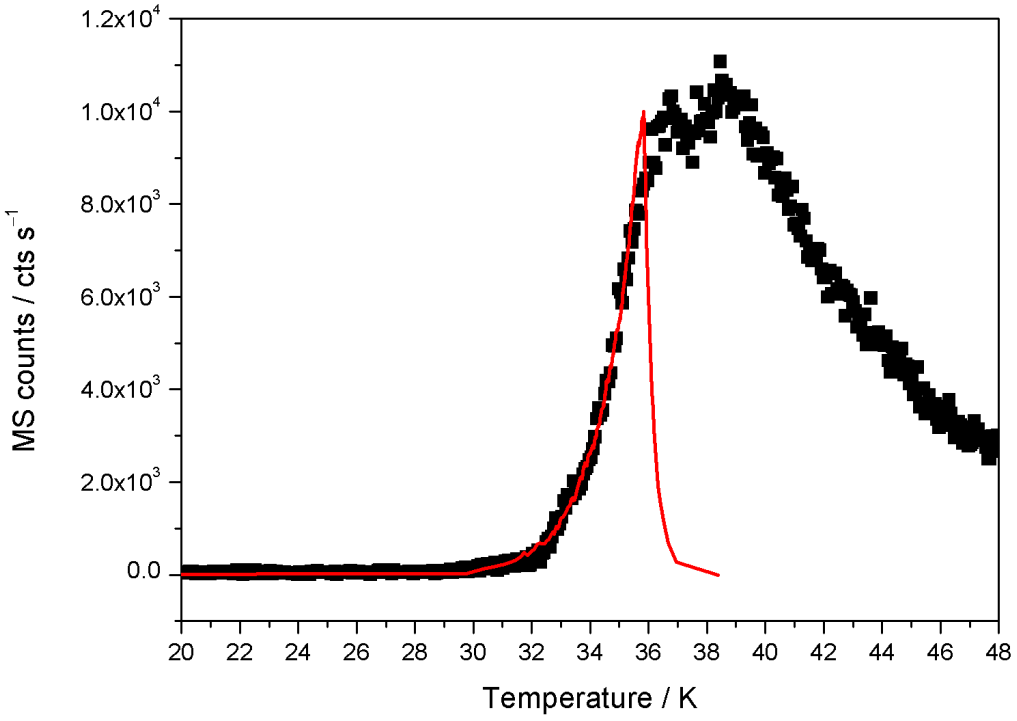

Figure 3.14: This figure shows the comparison between the experimental data (black) of O_2 desorption from 20 ML p–ASW and the model (red).

Figure 3.14 shows the fit of the CKS model to the experimental results. A perfect fit was not obtained due to the peculiar line–shape of the TPD trace which could possibly be due to both multi– and monolayer desorption from p–ASW. The long trailing edge after the second peak is indicative of sub–monolayer desorption from rough surfaces [6]

and pores of p–ASW films [35, 36]. The E_{des} as modelled through CKS is still lower than the literature, and even though there are pores and O_2 does diffuse, O_2 formation could still possibly occur on a pre–existing O_2 layer. This would explain why an E_{des} = 7.4 kJ mol^{-1} is found for this desorption process.

Formation and desorption of O_3 is also investigated from p–ASW and is as limited as when the O_3 is observed to leave the bare SiO_2 surface. **Figure 3.15** shows the observed QMS count rate as the temperature increases showing a slight change above the noise level as O_3 desorbs.

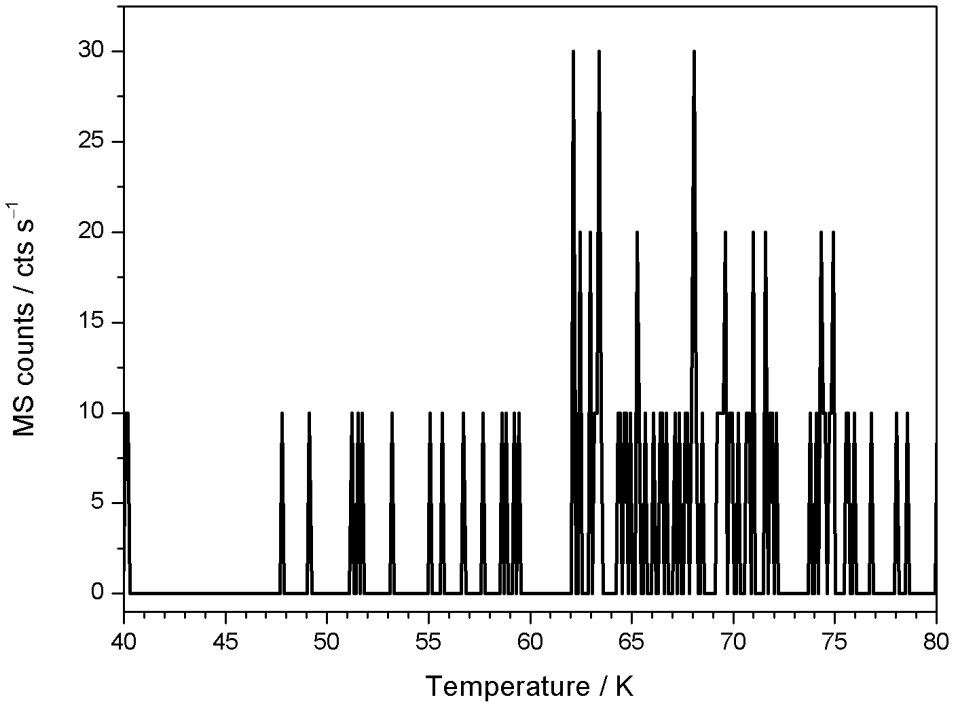

Figure 3.15: This figure shows the desorption of O_3 after 20 ML p–ASW has been bombarded by O atoms for 50 minutes. A change is observed in the temperature region above 62 K as O_3 begins to leave the surface.

A full analysis of the kind of TPD as seen in **Figure 3.15** is not possible, however a discussion of the TPD spectra of O_3 will follow at the end of this chapter.

Recollecting that the RAIR spectra gave no positive indication of H_2O_2 being present on the surface or in the molecular film, does not necessarily imply that no H_2O_2 formation occurs at all. Therefore, a second test is needed to verify this using a different technique, such as mass spectrometry. The fragmentation pattern for this species comprises of mass fractions at m/z = 34, 32, 17 and 16. The masses monitored so far in this chapter

have mainly been m/z = 32 and 16 for O_2 desorption with m/z = 18 and 17 intended for H_2O desorption, formation and therefore desorption of H_2O_2 will therefore lead to differences in the TPD profiles when comparing the various masses. These comparisons can be seen in **Figure 3.16** where the addition of m/z = 34 has been shown together with m/z = 32 and 16 in panel **(A)** and m/z = 17 and 18 are shown in panel **(B)** against experimental time.

Figure 3.16 shows what happens as a 20 ML p–ASW bombarded with O atoms for 50 minutes, is desorbed from the SiO_2 surface. Previously in this section, O_2 and H_2O desorption experiments were analysed. Through those results it can be said that the peaks in panel **(A)** correspond to O_2 desorption, initially from the sample and then the

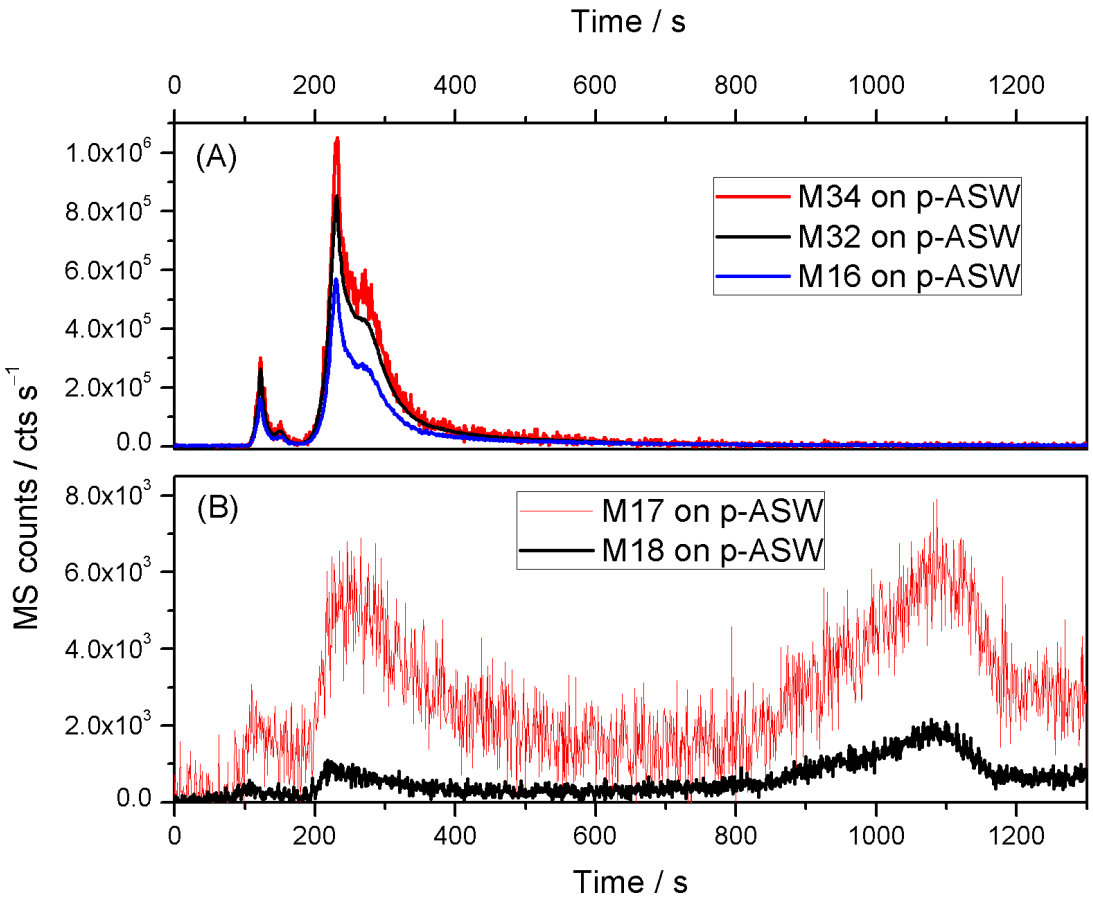

Figure 3.16: The two panels in this figure illustrate the lack of H_2O_2 during the experiments. Panel **(A)** shows the desorption of O_2 which **(B)** is of H_2O as followed through different mass fragments. The two spectra are expected to be more similar in the high time end if H_2O_2 is desorbed.

broad peak being from the cold finger. As is typically expected, and also discussed in **Chapter 2**, the O_2 to O (m/z = 32 to 16) ratio is constant and invariant as the experiment progresses. A m/z = 34 is also expected when monitoring O_2, however at a much smaller intensity, usually at about 0.04% of the O_2 signal [37, 38]. If this

anomaly, which could be due to a mass spectrometer calibration issue, is ignored, then the overall trend of m/z = 16, 32 and 34 should follow each other exactly if the mass spectrometer is monitoring the same molecule, such as O_2 in this case. **Figure 3.16 (A)** shows no change in any of the three masses throughout the TPD experiment. H_2O_2 will desorb at a temperature similar to H_2O desorption at about 165 K [28]. However, no change in the profile of m/z = 32 and 34 is observed. Thereby H_2O_2 is not observed in the TPD data and has not been formed during the experiment. Further verification comes from panel **(B)** in **Figure 3.16** where m/z = 17 and 18 are monitored. A m/z = 18 obviously represent H_2O desorbing from p–ASW. However, m/z = 17 should also be present at a level of 23%. [37, 38]. The m/z = 17 mass fragment is also formed from H_2O_2 as it desorbs and decomposes in the ion source of the QMS. Panel **(B)** point towards no change being observed in the TPD profiles of m/z = 17 and 18 during the experiment. The relative signal of m/z = 17 compared to 18 is as unusual as when comparing m/z = 32 and 34. However, if only the profiles are compared, no change is observed. The initial sets of peaks correspond to co–desorption of H_2O as O_2 desorbs. At later stages of the experiment, the m/z = 17 signal is expected to diverge from the 18 signal if H_2O_2 were to desorb. This does not seem to occur.

Following various masses with the QMS related to the mass of H_2O_2 and attempting to observe the specific frequencies with RAIRS expected from thin films of H_2O_2, it can be said that H_2O_2 production is not possible under these experimental conditions.

3.3.4 O Atoms on Compact Amorphous Solid Water

Having studied what happens as the O atom beam bombards bare SiO_2 and a multilayer of p–ASW, the focus will now shift towards changing the surface further to compact amorphous solid water (c–ASW). The main difference between porous and compact amorphous solid water is that pores are now closed and O/O_2 will not be as free to thermally diffuse into them. The compact form of H_2O is believed to be the dominant form on the surface of an icy dust grain in the ISM [39]. The focus will remain the same, O_2 and O_3 observation and desorption; however H_2O_2 is still not observed in any of the experiments and as such, spectra similar to **Figures 3.12** and **3.16** have been excluded from this section.

3.3.4 (a) Reflection–Absorption Infrared Spectroscopy

After the 20 ML c–ASW have been deposited, the ground state O atoms will bombard the surface for 50 minutes. Before and after the bombardment RAIR spectra were obtained at every step of the experiment, yielding **Figure 3.17**.

As can be seen from **Figure 3.17**, the general shape, position and character of the band is very similar to the previous O_3 spectra shown above in **Figures 3.7** and **3.11**. This might be indicative of the surface not being of immense importance for the adsorption of O_3 as the amount of H dangling bonds have changed drastically with the surfaces already investigated. The O_3 band in **Figure 3.17** is made up of the same contributions as the above O_3 bands, namely an [O...O_3], [O_3...O_3] and the O_3 asymmetric stretching mode. These modes are found are 1032, 1045 and 1037 cm^{-1} respectively, similar to the former experiments.

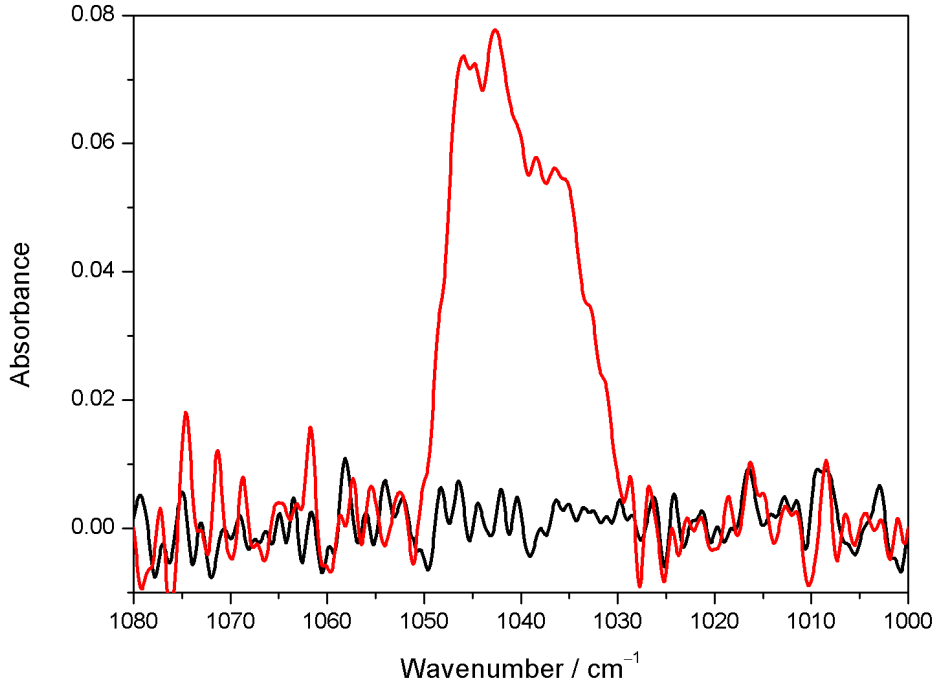

Figure 3.17: This figure shows the O_3 peak after the O atom beam has bombarded a multilayer surface of c–ASW for 50 minutes. There are no other observed differences in the IR spectrum.

3.3.4 (b) Temperature Programmed Desorption

Similar to the previous experiments, O_2 desorption can be studied by looking at m/z = 32 as the sample temperature increases as can be seen in **Figure 3.18**.

The main differences between O_2 desorption from p–ASW in **Figure 3.14** and from c–ASW as in **Figure 3.18** is the temperature at which desorption initiates and the shape of the TPD profile. The amount of O_2 should in theory be the same, however the difference in porosity of the two surfaces is significant. Pores are still present in this type of ASW, however pores collapse from about 30 K [35] leading to less of a variety

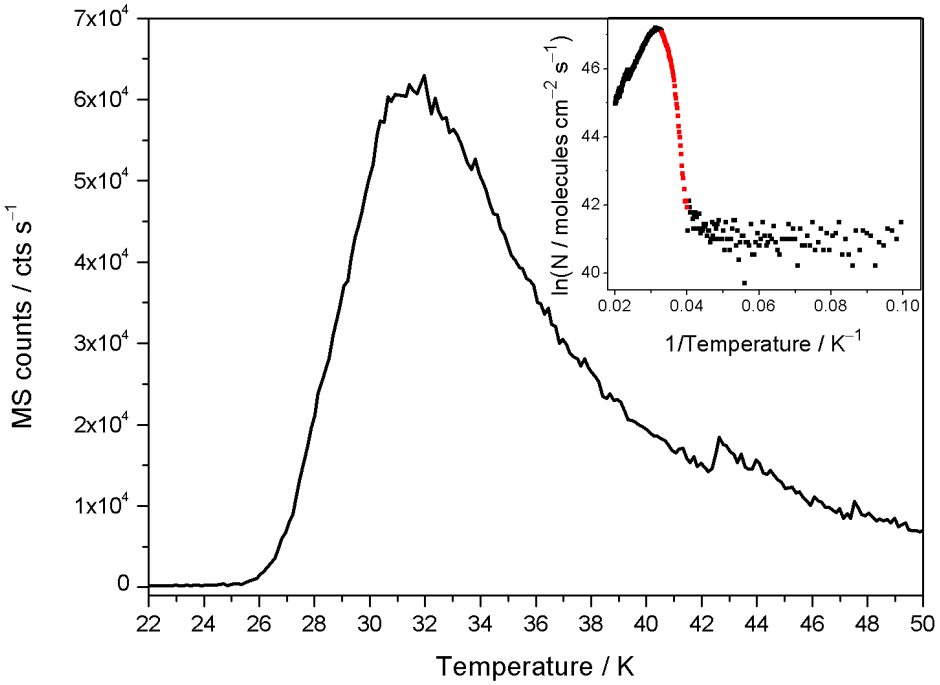

Figure 3.18: This figure illustrates what happens after the O atoms have bombarded a multilayer surface of c–ASW for 50 minutes. Desorption is seen to initiate at about 25 K and a more clear peak is observed as compared to a similar amounts of O_2 desorbing from p–ASW. The insert shows the Arrhenius plot of the desorption from which kinetic parameters can be extracted.

of binding sites in c–ASW as compared to p–ASW and a reduced surface area. This trend is expected to continue in the next section with O_2 desorption from CSW. The insert in **Figure 3.18** is of the Arrhenius plot, which has been constructed the same way as previously described, to yield an initial estimate of the kinetic parameters involved in O_2 desorption from c–ASW. With a CKS model being set up as follows **Equation 3** above, **Figure 3.19** can be made to show the fit of the model in red with experimental data in black.

The fit between the experimental data and the CKS model in **Figure 3.19** is not perfect. However, the Arrhenius analysis and the knowledge that the pores in the H_2O film are closed means that O_2 can be considered as following zero order desorption during the experiment. With this being said, a fit with an E_{des} of 6.3 ± 0.4 kJ mol^{-1} and a ν of $10^{26\pm2}$ molecules cm^{-2} s^{-1} is not great. The leading edges do not line up and the entire TPD

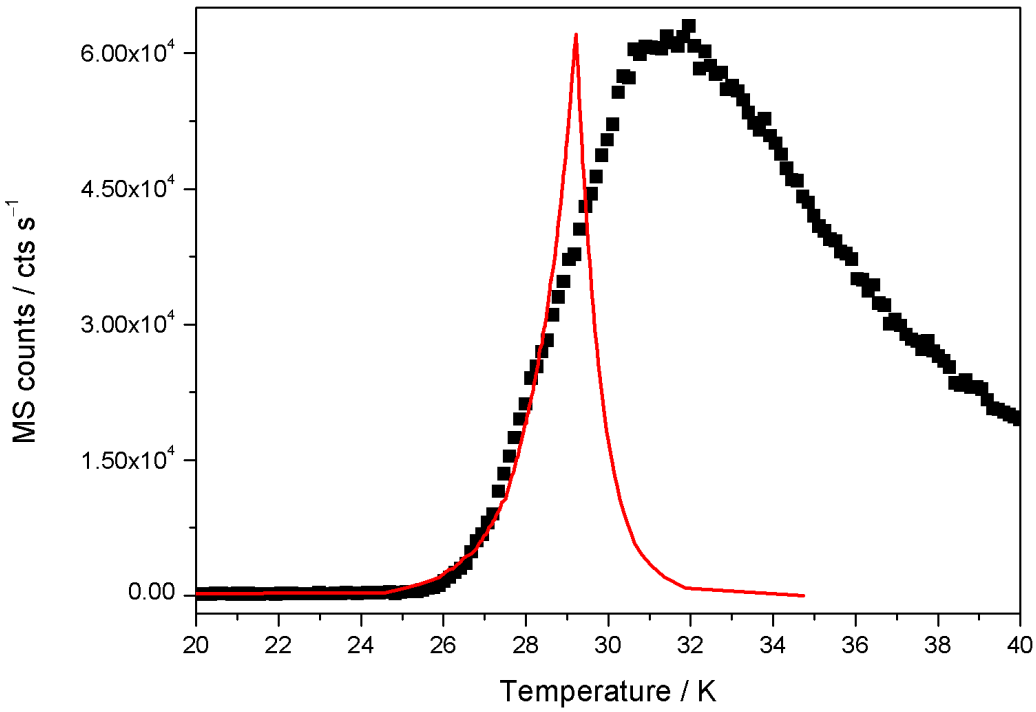

Figure 3.19: This figure shows the attempt at fitting O_2 desorption from c–ASW (black scatter) with a CKS model (red solid line). The O atoms beam is believed to alter the morphology of the molecular film leading to the experimental data appearing as presented.

trace spans a greater temperature range than expected for multilayers, however this has also been observed when desorbing a pre–deposited CO multilayer on a c–ASW substrate [36]. The fit of the model in **Figure 3.19** leads to an E_{des} which is similar to the value of E_{des} found for the O beam on SiO_2 experiments. The same reason for a lower energy for c–ASW applies as when analysing the O atom on SiO_2 experiment as there are no pores in the H_2O film. Formation of O_2 molecules leads to excess energy which is dissipated into the O_2 layer leading to amorphisation. The desorption trace in **Figure 3.19** is broad spanning a range greater than 10 K which is however unusual.

Following this analysis of the O_2 desorption, a quick glance will also be taken at the O_3 desorption. The experiment yielded results which are very similar to the previous TPD experiments of O_3 desorption from SiO_2 and p–ASW and the TPD profile has not been shown as examples are shown in **Figures 3.8** and **3.15** previously. As for the other O_3 TPD experiments, an analysis involving an Arrhenius plot is not possible from the data obtained when monitoring O_3 desorption from c–ASW. Extraction of E_{des} and ν will follow in the last section of this chapter after O atom bombardment of CSW has been reported.

3.3.5 O atoms on Crystalline Solid Water

The final surface to be studied is the crystalline solid water (CSW) surface where the experimental procedure will be the same as for the previously discussed experiments. The difference between the CSW and the ASW surface is that now there are no pores, a greater surface area and a more rigid and long–range ordered structure is found in the molecular film. H_2O_2, and the lack of observable data for H_2O_2, has also been excluded in this section as no evidence for its formation was observed.

3.3.5 (a) Reflection–Absorption Infrared Spectroscopy

Once again, only the O_3 peak was observed to be the region with any change, this peak, which is similar to the previous experiments, is shown in **Figure 3.20**. This peak can be seen to span from about 1050 – 1030 cm^{-1} exactly as when studying the O_3 feature of SiO_2, p–ASW and c–ASW considering the uncertainty of 1 cm^{-1}. For this reason, fitting **Figure 3.20** with Gaussians leads to the overall feature being broken down into a O_3 asymmetric stretching vibration at about 1037 cm^{-1}, a [O...O_3] (1032 cm^{-1}) and a [O_3...O_3] part (1045 cm^{-1}).

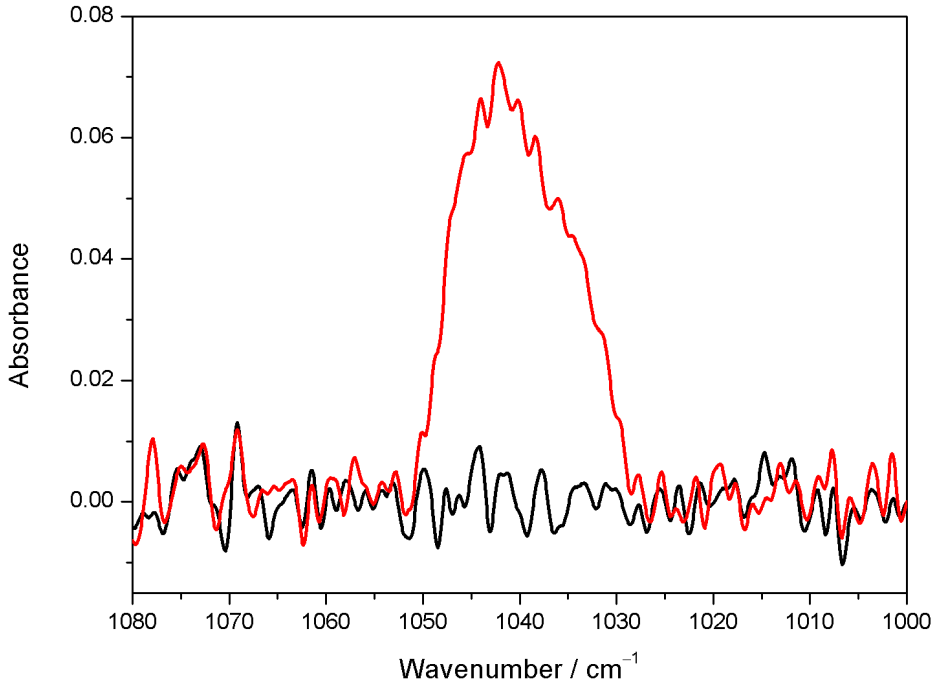

Figure 3.20: This figure shows the result, when looking at O_3, when a 20 ML CSW film has been bombarded with O atoms for 50 minutes. No other change in the 800 – 4000 cm^{-1} region was observed.

The difference in the experiment now is that H–dangling bonds are not present to the same extent of the previous ASW films. In essence, the CSW surface is similar to the

bare SiO_2 surface, and should therefore show similar RAIR spectra. However, all four experiments show the same span of wavenumbers for the O_3 peak. This could be due to O_3 being formed and embedded in an O_2 matrix. Another option is that 20 ML H_2O does not cover the entire sample leaving bare SiO_2 for O_2 and O_3 to adsorb to.

3.3.5 (b) Temperature Programmed Desorption

Focussing on O_2 desorption once again, and excluding a figure for O_3 desorption as any simple TPD profile of O_3 is, in itself, unrevealing, **Figure 3.21** can be analysed of O_2 desorption from a multilayer of CSW.

Figure 3.21 has yielded a sharp leading edge at a temperature similar to that seen when O_2 desorbs from SiO_2 (**Figure 3.8**). The insert in **Figure 3.21** is of the Arrhenius plot for this TPD profile and the clear leading edge in the TPD spectrum is noticeable in the insert. This insert is used to extract the kinetic information regarding this desorption process which will be used in a CKS model similar to the analysis and models previously described. The model and reaction steps used can be seen in **Equation 3**, following the fitting of the model to the experimental data, **Figure 3.22** can be made.

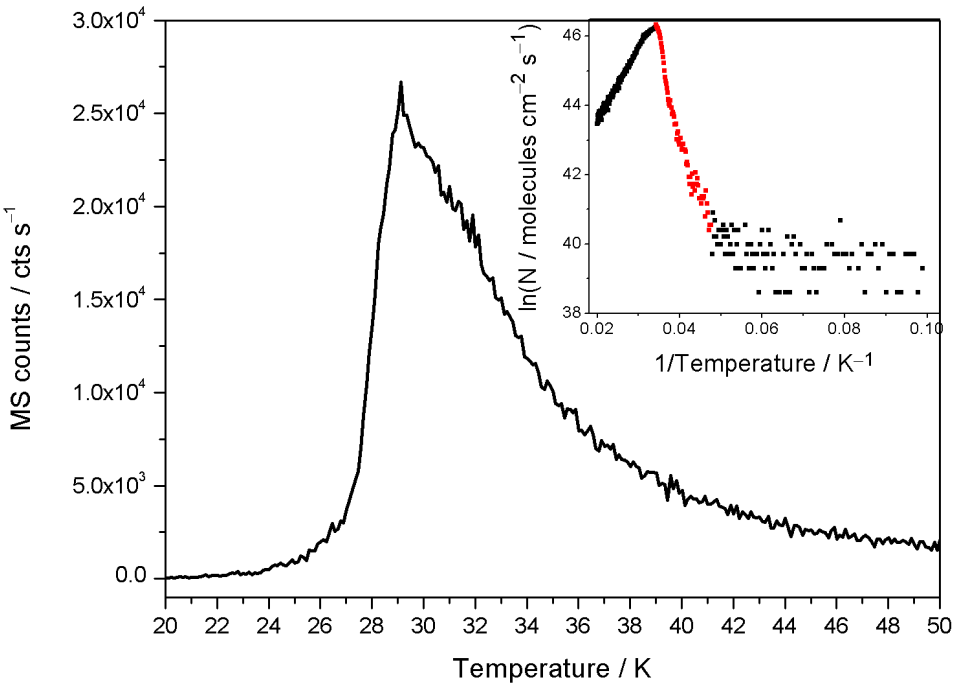

Figure 3.21: The figure illustrates the shape as O_2 is desorbed from SiO_2 after a 50 minute atomic beam dose. The reason for the long trailing edge of this multilayer desorption spectra is believed to be due to the O atom beam affecting the morphology of the CSW surface. The insert sheds light on the desorption kinetics through linear analysis of the red points.

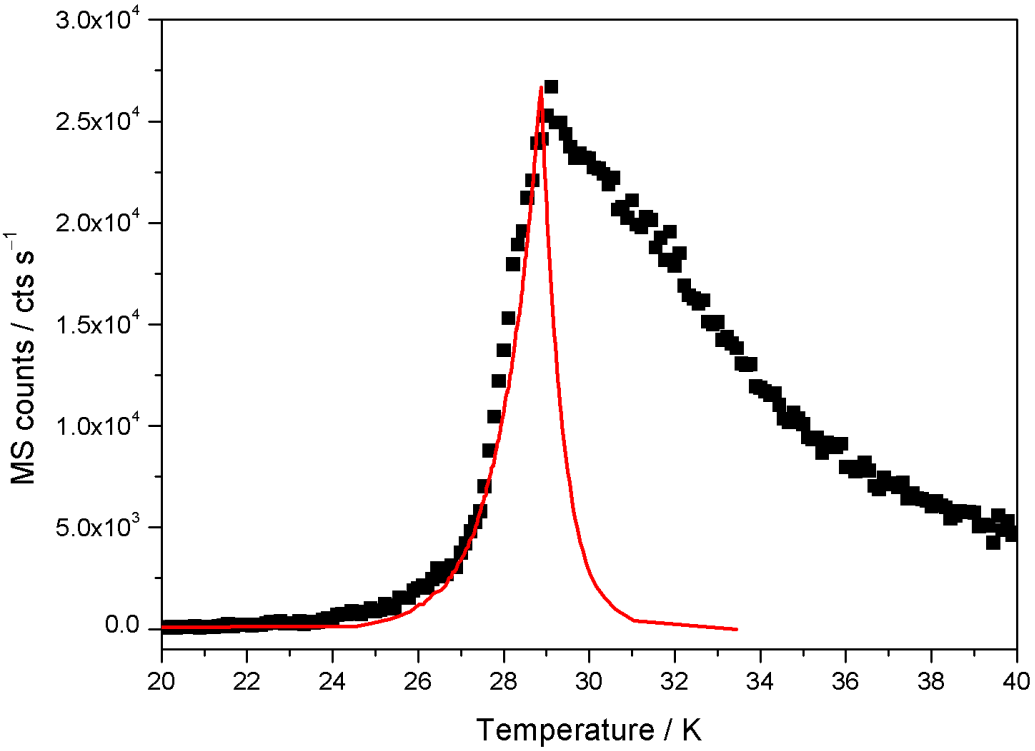

Figure 3.22: This figure shows the similarity in the leading edge of the experimental data and the CKS model of O_2 desorption from CSW after 50 minute O atoms beam dosing.

From the CKS model as compared to the experimental data (**Figure 3.22**) the final kinetic parameters of 6.7 ± 0.2 kJ mol^{-1} and 5 × $10^{27\pm1}$ molecules cm^{-2} s^{-1} can be evaluated against the other experiments. Again the value of E_{des} is seen to be below the literature of about 7.5 kJ mol^{-1}, which can be explained as in the previous cases.

3.3.6 O_3 Characterisation

As can be seen from the individual O_3 TPD experiments, the peaks are not particularly intense. Furthermore, O_3 desorption unfortunately occurs in the same temperature range as O_2 desorption from the cold finger. Hence as O_3 desorption is monitored through the m/z = 32 fragment TPD traces are mixtures of O_2 and O_3 and not pure O_3. Co–adding each O_3 TPD spectra at m/z = 48 can be done and a more defined peak can be obtained as seen in **Figure 3.23**.

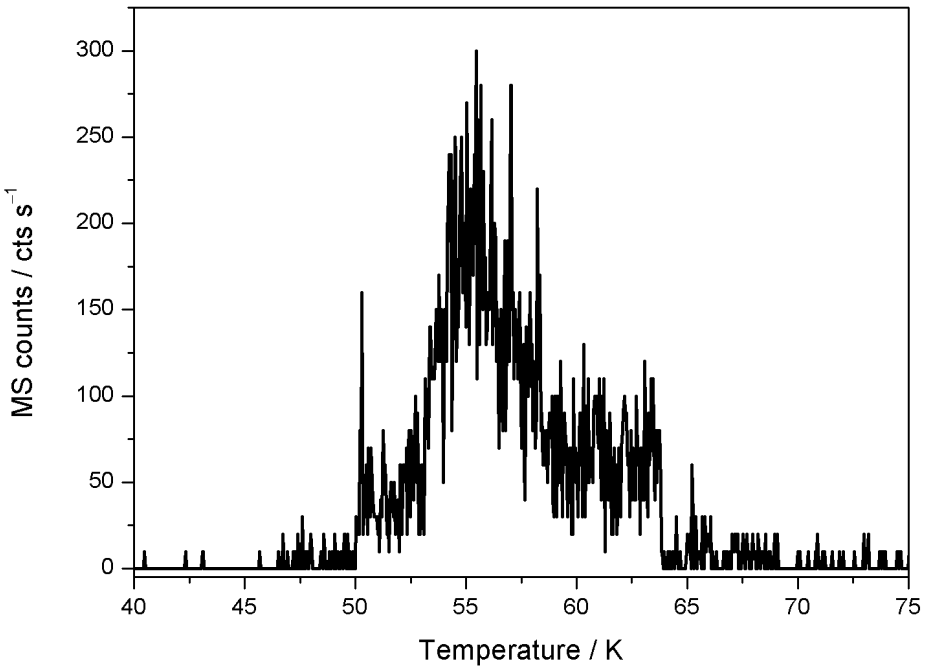

Figure 3.23: This figure shows the result of adding all the TPD spectra into one graph. A clearly defined peak is observed which can be used for further analysis.

The heating rates for all the O_3 desorption experiments are similar and only vary by 0.07 K s^{-1}, allowing the simple co–addition to work successfully, however, great care was still used when lining up the peaks of desorption leading to the co–addition. The initial stage of O_3 desorption can be seen at about 50 K with a peak at about 55 K. No other evidence of O_3 desorption is apparent at other temperatures, such as volcano desorption when 50 ML ASW crystallises or co–desorption with H_2O. These temperature values are consistent with the literature of 55 K [41]. However, the double peak observed by Minissale *et al.* [42] was not clearly observed due to less resolved spectra and possibly as a result of co–adding all the spectra. The double peak in the work of Minissale *et al.* [42] corresponds to multilayer desorption at a lower temperature and monolayer desorption at higher temperatures. However, the shoulder forming at higher temperatures of about 62 K could possibly be the monolayer, but more experimental data would be needed to confirm this assignment.

Inverting **Figure 3.23** means the Arrhenius parameters can be extracted. The inversion has been shown in **Figure 3.24** where the red points corresponds to the leading edge of desorption.

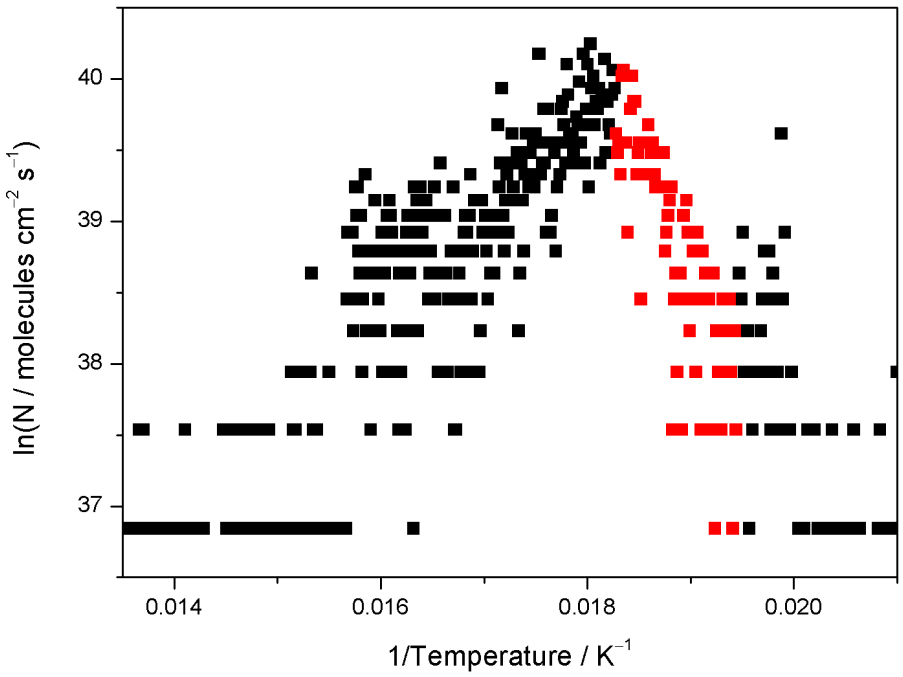

Figure 3.24: This inverted figure leads to the desorption energy through the gradient of the red line while the intercept gives an indication of the pre–exponential factor.

Fitting the red region in **Figure 3.24** with a straight line gives an estimate of the desorption energy from the gradient and the pre–exponential factor from the intercept. These initial values are about 15.4 kJ mol^{-1} for the desorption energy and 10^{33} molecules cm^{-2} s^{-1} for the pre–exponential factor. From here, a simple CKS analysis can be used to obtain better kinetic values for the desorption of O_3 from a SiO_2 surface. The simple steps are shown in **Equation 6** for O_3 on the surface (s), in the gas phase (g) and when it is being pumped out of the chamber (pump).

$$O_3\,(s) \rightarrow O_3\,(g) \qquad \textbf{Equation 6 (A)}$$

$$O_3\,(g) \rightarrow O_3\,(pump) \qquad \textbf{(B)}$$

The pumping stage is temperature independent and has an associated rate constant of 0.03 cm^2 mol^{-1} s^{-1} to model the pumping speed of the diffusion pump. With these steps and experimental results in mind, remembering that the heating rate was 0.17 K s^{-1}, the CKS model was optimised and the simulated spectra can be compared to the experimental as seen in **Figure 3.25**.

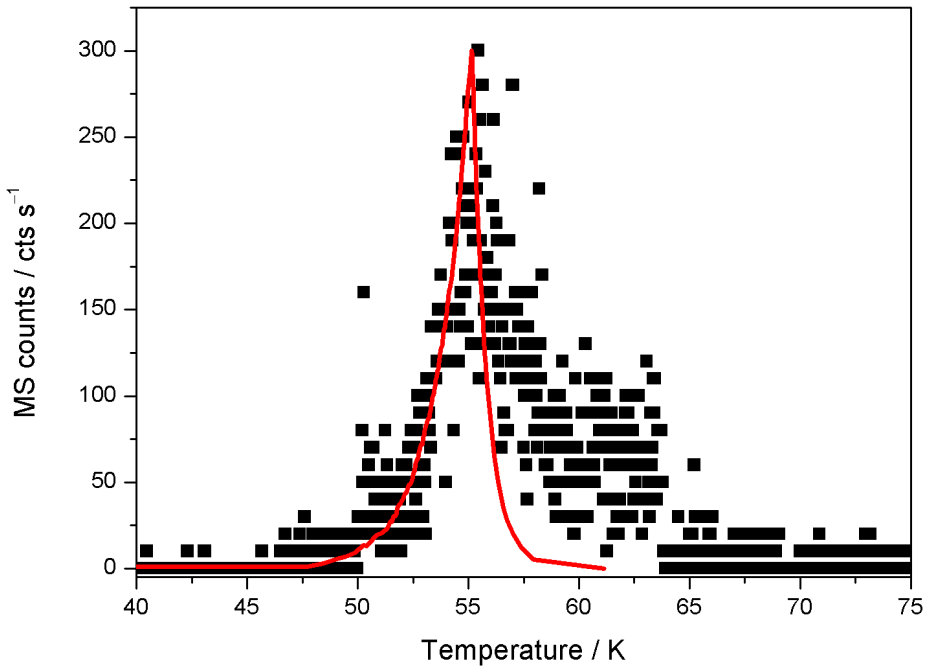

Figure 3.25: This figure shows the correlation between the experimental data (black scatter) and the model (red solid line) of O_3 desorption.

As can be seen in **Figure 3.25**, the model fits the experimental data. The model was generated using a desorption energy of 14.7 ± 0.5 kJ mol^{-1} which is similar to He *et al.* and Jing *et al.* [9, 43] who reported a value of 15.2 ± 0.5 kJ mol^{-1}.

3.3.7 O_3 Formation and Destruction

Looking at the combined TPD traces of O_3 (for instance **Figure 3.23**) one can see the total MS count rate being minor as compared to a general O_2 TPD spectra. Considering the MS counts as being directly proportional to the molecular concentration on the surface it can be said that the TPD experiments show a ratio of 0:1 for O_3 to O_2 when integrating the desorption peak of O_3 (**Figure 3.23**) and O_2 (*e.g.* **Figure 3.10**). As has also been said in this report, issues with measuring O_3 desorption due to cold finger desorption of O_2, along with O_3 dissociating in the MS head, meant that this O_3:O_2 ratio is not precise. Further to this, O_3 can be destroyed by addition of O atoms as seen in **Equation 4**.

The work of Minissale *et al.* [18, 44] has shown that O and O_2 diffuse with an activation energy as low as 2.4 kJ mol^{-1} on silicate surfaces. Minessale *et al.* have also considered O_2 and O_3 formation pathways as occurring with no reaction barrier. With this in mind the reaction steps in **Equation 7** can be setup to study O_3 formation and destruction.

$$O\,(g) \rightarrow O\,(surf)$$ **Equation 7 (A)**

$$O_2\,(g) \rightarrow O_2\,(surf)$$ **(B)**

$$O\,(surf) \rightarrow O\,(diff)$$ **(C)**

$$O\,(surf) + O\,(diff) \rightarrow O_2\,(surf)$$ **(D)**

$$O\,(diff) + O\,(diff) \rightarrow O_2\,(surf)$$ **(E)**

$$O_2\,(surf) \rightarrow O_2\,(diff)$$ **(F)**

$$O\,(diff) + O_2\,(surf) \rightarrow O_3$$ **(G)**

$$O\,(surf) + O_2\,(diff) \rightarrow O_3$$ **(H)**

$$O\,(diff) + O_2\,(diff) \rightarrow O_3$$ **(I)**

$$O\,(diff) + O_3 \rightarrow 2O_2$$ **(J)**

The bracketed terms of g, surf and diff refer to atoms and molecules either in the gas–phase, on the surface or diffusing on the surface, respectively. The gas phase concentration of O atoms and O_2 molecules are taken from the estimated beam flux of about 5.8×10^{14} molecules cm^{-2} s^{-1} and cracking fraction of about 20%. A sticking coefficient of unity has been considered for steps **(A)** and **(B)**, while diffusion parameters are taken from Minessale *et al.* as mentioned previously. The destruction of O_3 by addition of another O atom has not been discussed to a great extent in this chapter, however such a step has been included in this model. Parameters for this destruction reaction are not easily come by, however it has been mentioned in similar experiments as being negligible [18, 41]. Since no values for the energy or pre–exponential factor are available, a variety of values will be used to show the possible extent of O_3 destruction.

- Chapman type chemistry: With a reaction barrier of about 17 kJ mol^{-1}, O_3 and O combine to form $2O_2$ in the gas–phase in the atmosphere of the Earth. For this reaction to occur in the solid state, the dependency on the diffusion or hopping rate of O atoms is needed. This hopping rate becomes the pre–exponential factor for the destruction mechanism of O_3.
- Barrierless reaction: All chemical reactions are considered as proceeding with no activation barrier.

The hopping rate, Γ, can be calculated through an Arrhenius–type equation, **Equation 8**,

$$\Gamma = \nu \times \exp\left(-\frac{E_{diff}}{RT}\right). \qquad \textbf{Equation 8}$$

Initially, with a temperature of 17 K, **Equation 8** gives a value of 4.22×10^4 s^{-1}, but is naturally dependent on temperature, *T*. With this estimate of the pre–exponential factor and with the two limits discussed in the bulleted list above, the CKS model can be setup as seen in **Table 3.3** and depicted in **Figure 3.26**. As can be seen, the models have been computed over a variety of deposition temperatures ranging from 7 K to 52 K. Also, the pre–exponential factor has been varied by $\pm 10^5$ s^{-1} due to its unknown nature which lead to no change in the O_3:O_2 ratio. The lower–end of the uncertainty leading to a pre–exponential factor of 10^{-1} s^{-1} has not been shows as this lead to all O_3 remaining intact. Further to this, the high–end uncertainty level leads to negligible level of O_3 destruction.

Temperature / K	**Barrierless**		**E_A = 17 kJ mol^{-1} and ν = 4.22 × 10^4**	
	O_2:O_3	**O_3:O_2**	**O_2:O_3**	**O_3:O_2**
7	1:0.16	1:0.09	1:0.25	1:0.00
12	1:0.16	1:20	1:0.25	1:0.00
17	1:0.16	1:21	1:0.25	1:0.00
22	1:0.16	1:20	1:0.25	1:0.00
27	1:0.16	1:20	1:0.25	1:0.00
32	1:0	1:20	1:0	1: 0.00
37	1:0	1: 21	1:0	1: 0.00
42	1:0	1: 20	1:0	1: 0.00
47	1:0	1: 20	1:0	1: 0.00
52	1:0	1: 21	1:0	1: 0.00

Table 3.3: This table shows the results of the different limits put onto the CKS model for investigating the O_2 and O_3 formations in columns two and four (labelled O_2:O_3) and O_3 destruction (labelled O_3:O_2) in columns three and five. As can be seen, a greater extent of O_3 is produced than observed in the TPD experiments with negligible destruction.

What can be seen in **Table 3.3** and **Figure 3.26** is O_3 formation and destruction leading to $2O_2$ molecules. The barrierless reaction does show O_3 decomposition while the reactions with a barrier show negligible destruction. Further to this, leaving the reaction energy as 17 kJ mol^{-1} and increasing the pre–exponential factor to a value of 10^{50} leads to an O_3:O_2 ratio of 1:0.06. With this simple CKS model, it can be said that O_3

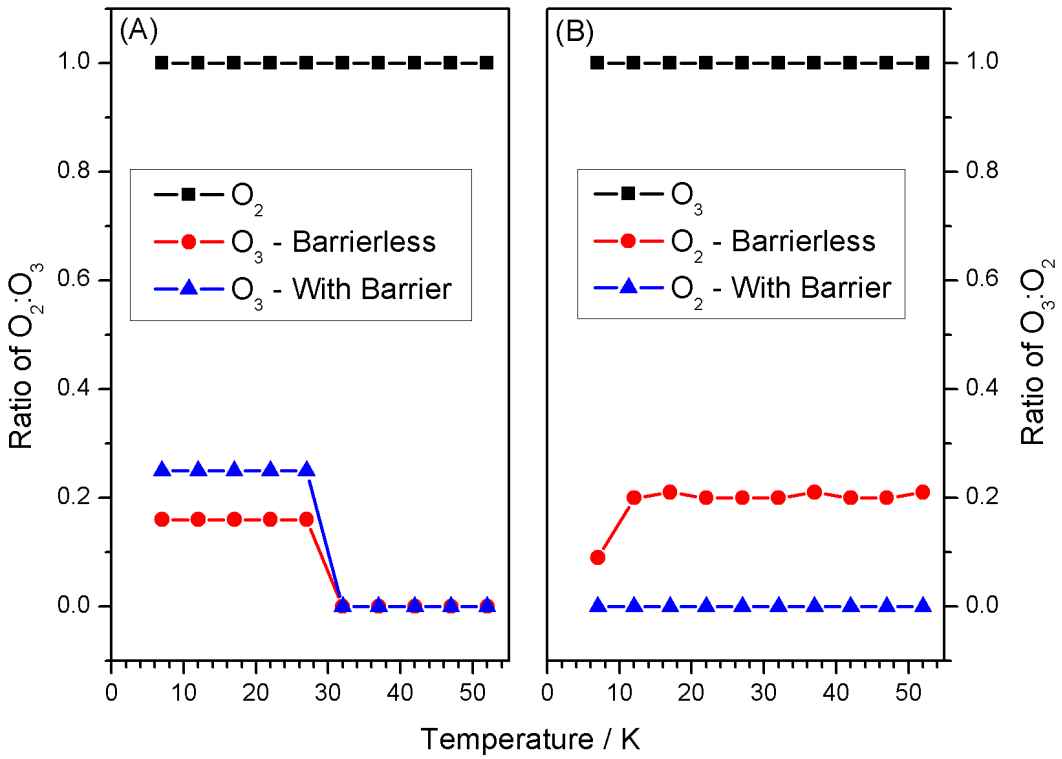

Figure 3.26: This figure shows the results as gathered from the CKS model and presented in **Table 3.3**. Formation of O_3 **(A)** occurs as expected, however to a greater extent than shown in the experimental TPD data. O_3 destruction **(B)** has also been shown in this figure and is considered not to be the cause for the lack of O_3 signal during desorption in the TPD experiments.

destruction by reactions of diffusing O atoms is negligible which has also been the conclusion of Minissale *et al.* [18]. Sivaramen *et al.* [41] have stated that O atoms prefer to react with other O atoms to form O_2 as compared to reacting with O_2 molecules to form O_3. This, by extension, could mean that O atoms are even less likely to react with O_3 molecules, which is what this simple CKS model indicates. Overall the CKS model shows that O_3 is created to a greater degree than what is observed experimentally through the TPD experiments. Also, the O_2:O_3 ratio cannot be determined through IR as O_2 is not observed in these experiments.

The simulated data presented in **Table 3.3** and **Figure 3.26** range from 7 K to 52 K. At temperatures above 37 K O_2 is not expected to reside on a SiO_2 surface for long and will naturally not yield an experimental TPD trace, however these simulations were done without the TPD model as they were done in the previous sections. The fundamental reason for including these values was to examine what effect the temperature has on O_3 formation and destruction. As seen, for temperatures above 32 K the O_2:O_3 ratio shows only O_2 which would not be expected in experimental TPD experiments. However, O_3

destruction is only observed for barrierless reactions, but the extent of simulated destruction when no barrier is present (around 20%) does not fully explain the lack of O_3 signal during TPD experiments. This, therefore, leads back to the previous idea that O_2 contamination from cold finger desorption is the cause of lack of O_3 signal along with a great extent of O_3 decomposition with the QMS filaments. Also, experiments with different deposition temperatures were not conducted, however a lesser amount of O_3 would be expected as the temperature is raised as there will be less O_2 molecules present on the SiO_2 surface as explained by the TPD experiments.

3.4 Conclusion

This chapter has discussed one of the steps in the H_2O formation pathway in the interstellar environment. To do this O_2 molecules were initially beam dosed onto a bare SiO_2 surface and subsequently desorbed through temperature programmed desorption (TPD). This lead to higher values of E_{des} as compared to background dosed O_2; 8.5 kJ mol^{-1} and 7.5 kJ mol^{-1} respectively. Atomic beam dosing of O onto SiO_2 leads to a significant reduction in the E_{des} which further changed as the SiO_2 was covered in different forms of H_2O. The experimental values have been summarised in **Table 3.4**.

	O_2 beam	**O atomic beam**			
	SiO_2	**SiO_2**	**p–ASW**	**c–ASW**	**CSW**
E_{des} / kJ mol^{-1}	8.5 ± 0.1	6.7 ± 0.2	7.4 ± 0.6	6.3 ± 0.4	6.7 ± 0.2
ν / molecules cm^{-2} s^{-1}	$4 \times 10^{30\pm1}$	$4 \times 10^{27\pm1}$	$1 \times 10^{25\pm2}$	$1 \times 10^{26\pm2}$	$5 \times 10^{27\pm1}$

Table 3.4: This table shows the TPD results of O_2 desorption. The first column of values is of O_2 desorption after having been beam dosed onto the bare SiO_2 sample. The other columns are of O_2 having been dosed with the atomic beam onto the different surfaces.

As can be seen in **Table 3.4**, the overall results vary in a significant fashion as the underlayer changes. The reasons for this have been discussed throughout this chapter, where the deposition method has been argued to be the main reason for the changes in the O_2 beam dosing experiment as compared to background dosing. Also, amorphisation during the reactions has been indicated as possibly being the reason for the changes when different H_2O multilayers are deposited prior to O atom dosing. Further to the desorption experiments, no reactive desorption of any species was observed during

beam dosing. This does not mean that reactive desorption does not occur, however more experiments will be needed to further study this.

O_3 has been observed to be formed no matter the surface and with no relative change in amount of formation. Individual TPD traces of O_3 do not lead to much information as seen. The reason for this is that O_3 decomposes as it interacts with the QMS during the experiments leading to part of m/z = 32 and 16. These masses were recorded in all experiments, however O_3 desorption has been shown to occur at the same time as O_2 desorption from the cold finger. With a considerable O_2 desorption from the cold finger also contributing to the increase in m/z = 16, O_3 desorption could not be determined through the O or O_2 TPD traces. However, co–addition of the O_3 TPD experiments did lead to an overall desorption peak. This peak has a considerable amount of uncertainty. However, an E_{des} value of 14.7 ± 0.5 kJ mol^{-1} was estimated through CKS which is very similar to the literature. To summarise the overall results of the O_3 band on the different surfaces as studied through RAIRS, **Table 3.5** has been constructed.

	SiO_2 (± 1)	**p–ASW (± 1)**	**c–ASW (± 1)**	**CSW (± 1)**	**Literature (± 2)**
$[O_3...O]$ / cm^{-1}	1031	1031	1032	1032	1032
O_3 O–O asymmetric stretch / cm^{-1}	1036	1037	1037	1037	1037
$[O_3...O_3]$ / cm^{-1}	1045	1045	1045	1045	1042

Table 3.5: This table summarises all the values of the O_3 band from the different surfaces after they have been fitted with Gaussians as compared to the literature values [16].

Table 3.5 shows the component of the O_3 band and their frequencies as H_2O is added and changed in the different experiments discussed in this chapter. As can be seen, the values of the O_3 components do not change as the substrate changes and are similar to the literature values [16] when considering the uncertainties. The invariance in the RAIRS band of O_3 could indicate that the formed molecules are imbedded in an O_2 matrix, O_3 islands on the differing surfaces or 20 ML does not cover the entire SiO_2 surface on where O_3 would then prefer to be adsorbed directly onto SiO_2. From this stage, hydrogenation of O_3 has been shown to lead to H_2O [45].

3.5 References

[1] A.G.G.M. Tielens and W. Hagen, *Astron. Astrophys.*, 1982, **114**, 245

[2] S. Ioppolo, H.M. Cuppen, C. Romazin and H. Linnartz, *Phys. Chem. Chem. Phys.*, 2010, **12**, 084504

[3] H.M. Cuppen, S. Ioppolo, C. Romanzin and H. Linnartz, *Phys. Chem. Chem. Phys.*, 2010, **12**, 12077

[4] H. Linnartz, S. Ioppolo and G. Fedoseev, *Int. Rev. Phys. Chem.*, 2015, **34**, 205

[5] H.J. Jodl, W. Loewen and D. Griffith, *Solid State Commun.*, 1987, **61**, 503

[6] M.P. Collings, V.L. Frankland, J. Lasne, D. Marchione, A. Rosu–Finsen and M.R.S. McCoustra, *Mon. Not. Roy. Astron. Soc.*, 2015, **449**, 1826

[7] B.R. Cairns and G.C. Pimentel, *J. Chem. Phys.*, 1965, **43**, 3432

[8] Y.A. Freiman and H.J. Jodl, *Phys. Rep.*, 2004, **401**, 1

[9] J. He, D. Jing and G. Vidali, *Phys. Chem. Chem. Phys.*, 2014, **16**, 3493

[10] Noble, E. Congiu, F. Dulieu and H.J. Fraser, *Mon. Not. R. Astron. Soc.*, 2012, **421**, 768

[11] G. Attard and C. Barnes, *Surfaces* (Oxford University Press, Oxford, 1993)

[12] K. Acharyya, G.W. Fuchs, H.J. Fraser, E.F. van Dishoeck and H. Linnartz, *Atrophys. Astron.*, 2007, **466**, 1005

[13] G.W. Fuchs, K. Acharyya, S.E. Bisschop, K.I. Oberg, F.A. van Broekhuizen, H.J. Fraser, S. Schlemmer, E.F. van Dishoeck and H. Linnartz, *Faraday Discus.*, 2006, **133**, 331

[14] G.A. Kimmel, K.P. Stevenson, Z. Donhalek, R.S. Smith and B.D. Kay, *J. Phys. Chem.*, 2001, **114**, 5284

[15] S. Chapman, *Philos. Mag.*, 1930, **10**, 345

[16] C.J. Bennett and R.I. Kaiser, *Astrophys. J.*, 2005, **635**, 1362

[17] E.M. McCash, *Surface Chemistry* (Oxford University Press, Oxford, 2001)

[18] Marco Minessale, *Ph.D. Thesis* (University of Cergy Pontoise, Paris, 2014)

[19] M. Minissale, E. Congiu, G. Manico, V. Pirronello and F. Dulieu, *Astron. Astrophys.*, 2013, **559**, A49

[20] H.J. Kimber, C.P. Ennis, S.D. Price, *Faraday Disc.*, 2014, **168**, 571

[21] M.D. Ward and S.D. Price, *Astrophys. J.*, 2011, **741**, 121

[22] H. Bergeron, N. Rougeau, V. Sidis, M. Sizun, D. Teillet–Billy and F. Aguillon, *J. Chem. Phys. A*, 2008, **112**, 11921

[23] P.C. Cosby, *J. Chem. Phys.*, 1993, **98**, 9560

[24] A.G.M.A. Abdulgalil, *Ph.D. Thesis* (Heriot–Watt University, Edinburgh, 2013)

[25] D. Marchione, J.D. Thrower and M.R.S. McCoustra, *Phys. Chem. Chem. Phys.*, 2016, **18**, 4026

[26] M.S. Gudipati and J. Castillo–Rogez, *The Science of Solar System Ices (Astrophysics and Space Science Library)* (Springer, New York, 2012) page 383

[27] R.L. Hudson and M.H. Moore, *Astrobiology*, 2006, **6**, 483

[28] M.J. Loeffler, U. Raut, R.A. Vidal, R.A. Baragiola and R.W. Carlson, *Icarus*, 2006, **180**, 265

[29] L.E. Christensen, M. Okumura, S.P. Sander, R.J. Salawitch, G.C. Toon, B. Sen, J.–F. Blavier and K.W. Jucks, *Geophys. Research Lett.*, 2002, **29**, 1299

[30] T. Lamberts, H. Cuppen, S. Ioppolo and H. Linnartz, *Phys. Chem. Chem. Phys.*, 2013, **15**, 8287

[31] J.A. Lannon, F.D. Verderame and R.W. Anderson, *J. Chem., Phys.*, 1971, **54**, 2212

[32] M. Pettersson, S. Touminen and M. Rasanen, *J. Phys., Chem.*, 1997, **101**, 1166

[33] J.E. Schaff and J.T. Roberts, *J. Phys. Chem.*, 1996, **100**, 14151

[34] J.E. Schaff and J.T. Roberts, *Langmuir*, 1999, **15**, 7232

[35] M.P. Collings, J.W. Dever, H.J. Fraser, M.R.S. McCoustra and D.A. Williams, *Astrophys. J.*, 2003, **583**, 1058

[36] M.P. Collings, J.W. Dever, H.J. Fraser and M.R.S. McCoustra *Astron. and Space Sci.*, 2003, **285**, 633

[37] Hiden Analytical Ltd., http://www.hidenanalytical.com/en/tech–data/fundamental–data/cracking–patterns

[38] N. Yoshimura, *Vacuum Technology – Practice for Scientific Instruments* (Springer, Berlin Heidelberg, 2007)

[39] A.G.G.M Tielens, *Rev. Mod. Phys.*, 2013, **85**, 1021

[40] M.P. Collings, J.W. Dever, H.J. Fraser and M.R.S. McCoustra, *Astron. and Space Sci.*, 2003, **285**, 633

[41] B. Sivaramen, C.S. Jamieson, N.J. Mason and R.I. Kaiser, *Astrophys. J.*, 2007, **669**, 1414

[42] M. Minissale, E. Congiu and F. Dulieu, *J. Chem. Phys.*, 2014, **140**, 074705.1

[43] D. Jing, J. He, J.R. Brucato, G. Vidali, L. Tozzetti and A. De Sio, *Astrophys J.*, 2012, **756**, 98

[44] E. Congiu, M. Minissale, S. Baouche, S. Cazaux, H. Chaabouni, G. Manico, A. Moudens, V. Pirronello and F. Dulieu, *Faraday Discuss.*, 2014, **168**, 151

[45] H. Mokrane, H. Chaabouni, M. Accolla, E. Congiu, F. Dulieu, M. Chehrouri, and J.L. Lemaire, *Astrophys. J.*, 2009, **705**, L195

Chapter 4

Towards a more Realistic Icy Grain Mantle Model

Contents of this chapter

4.1 Introduction

Having investigated one of the key sequences of reactions in the H_2O formation cycle, the thesis will now turn to look at how such multilayers begin to form on interstellar dust grains. H_2O has recently been of interest again with the Rosetta mission as it was found in the solid state on the comet 67P / Churyumov–Gerasimenko [1]. Reactive accretion is the dominant formation route of H_2O, however adsorption of H_2O from the gas–phase also occurs to a minor extent. In the early stages of mantle formation on a dust grain only small coverages of H_2O will be formed on the bare surface before it builds a coat. Temperature programmed desorption, TPD, experiments of H_2O have consistently shown zero order desorption kinetics on SiO_2 [2], on Au [3], Sapphire [4] and Ru (000)/Al(001) [5]. As explained in **Chapter 2**, TPD probes the surface–adsorbate and adsorbate–adsorbate interactions through analysis of the leading edges and the maximum temperature of desorption. The results of this kind of analysis allow one to say that the H_2O–H_2O interaction is favoured over the H_2O–SiO_2 interaction. The H_2O–H_2O interaction being dominant is indicative of multilayer desorption with ballistic deposition [6] (hit–and–stick adsorption) as likely occurs at cryogenic temperatures of the ISM [7], a mixture of isolated monomers or random sized groups of H_2O is produced on the grain surface. This would mean that H_2O begins to become mobile at some temperature, leading to cluster formation, before desorption ensues. So, when does a sub–monolayer coverage of H_2O become a multilayer? One way of observing how H_2O behaves on a SiO_2 surface is by using RAIR spectroscopy. This chapter illustrates what happens on the grain surface in the initial conditions of low H_2O coverage.

Preliminary experimental results can be found in the literature where 0.5 ML H_2O was deposited on SiO_2 at 20 K and progressively annealed in 20 K steps [2]. These results show a marked change in the intensity profile of the νO–H stretching region of RAIRS as H_2O is annealed as seen in **Figure 4.1**.

Similar IR based techniques have been used to study the movement of, for instance, CH_3OH and $(CH_3CH_2)_2O$ (diethyl ether) on SiO_2 [9] and HCl on H_2O surfaces [10].

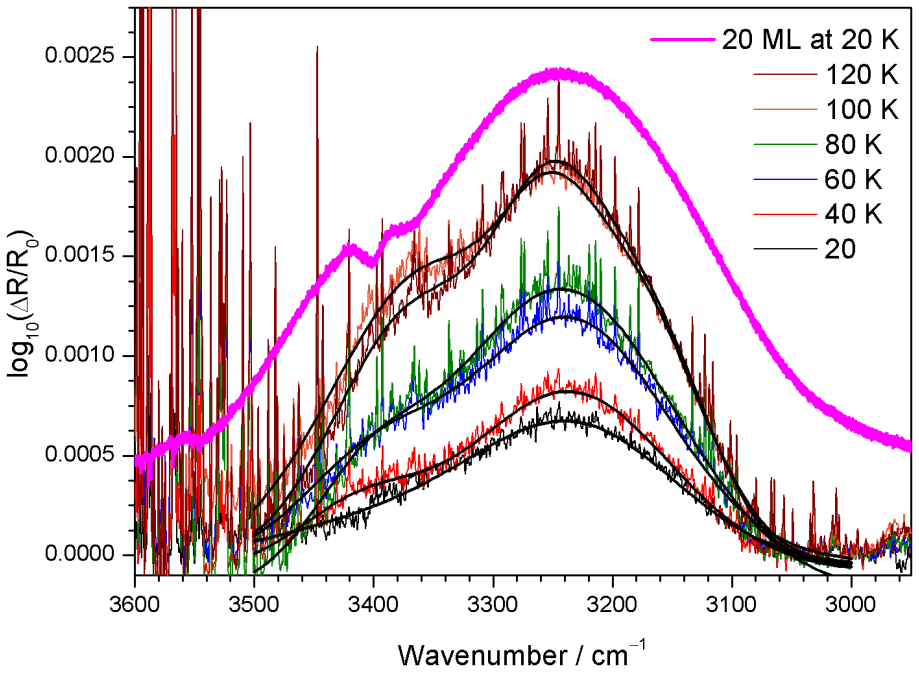

Figure 4.1: Temperature programmed RAIRS of 0.5 ML H_2O on SiO_2 showing an increasing intensity of the νOH band as the temperature increases. The magenta band shows a 20 ML spectrum of H_2O, as can be seen, the annealed appear similar to the multilayer. The sharp features are due to gas–phase water in the optics boxes on the air side of the UHV apparatus. This figure is taken from [2] and [8].

One interesting aspect of looking at the movement of H_2O on a dust grain analogue surface has to do with the Onion model [11, 12] as discussed in **Chapter 1**. The model describes how the polar H_2O layer forms and a layer of apolar CO covers it being a large consituent of the icy mantle [13]. Another way of thinking of the layer formation is in terms of H–bond capability. Naturally, since H_2O is the dominant part, a multilayer is expected, but a precise description of the construction of the polar layer is not available. The idea of a H_2O multilayer shielding the dust grain from other molecules is proposed through the Onion model, however if water is mobile at cryogenic temperatures, the whole grain might not be shielded by the H_2O. This would lead to a mixture of binding sites where other icy mantle molecules will find the optimum binding site on H_2O clusters or bare dust grain surfaces.

4.2 Experimental

The general equipment and experimental method were detailed in **Chapter 2**. The specific steps used to obtain the results for this chapter are, however, briefly explained here. Before any results were obtained the sample was cleaned by heating the sample to 220 K for a variable time. The heating time was dependent on the level of H_2O in the

chamber as determined by the QMS, when a quantity of H_2O amounting to 2×10^{-10} mbar or lower was reached the cleaning process was stopped and the sample was left to cool to base temperature. H_2O was prepared by three freeze–pump–thaw, FPT, cycles and the glass gas handling line was purged with water vapour to ensure a high purity of H_2O. Background dosing of 0.5 ML H_2O was done after the initial set of background and bare sample RAIR spectra. The H_2O film was annealed from base temperature of 17 K to the specified temperatures of 18, 21, 24, 27, 30, 40, 50, 60 and 100 K as stated in the results in **Section 4.3.1** at 100 s steps for a total of 500 s. After this stage a final annealing step was conducted at 100 K for 20 min. RAIR spectra were collected on these H_2O coverages and temperatures with a resolution of 1 cm^{-1} and a total of 512 scans per experiments and all data was collected by the liquid nitrogen cooled mercury cadmium telluride, MCT, detector. Initial testing of the time between RAIR scans at temperature >18 K was on average 1 hr. For that reason, the time taken between RAIRS spectra collected at ≤18 K was also 1 hr. To minimise the effect of gas–phase water re–adsorbing on the sample and biasing the experimental results, only one experiment was done per day.

4.3 Results and Discussion

4.3.1 H_2O De–Wetting

Due to repairs on the UHV apparatus, as briefly mentioned in **Chapter 2**, the system was baked before the H_2O de–wetting experiments were initiated. This helped to reduce the background contamination of H_2O However, additional measurements and tests were conducted to look at H_2O partial pressure effects and the effect of re–adsorption of H_2O after a temperature programmed desorption experiment.

Measuring the background levels of H_2O vapour in the UHV chamber is important as any extra adsorption of H_2O will inevitably lead to an increase of the νOH stretch in a RAIR spectrum. The partial pressure of H_2O was measured by background filling the chamber with H_2O at certain pressures, 1×10^{-8}, 5×10^{-8}, 1×10^{-7}, 5×10^{-7} and 1×10^{-6} mbar, with the QMS measuring the counts of m/z = 18. The pressure reading was allowed to stabilise and left at said pressures for one minute at a time. The results are shown in **Figure 4.2**.

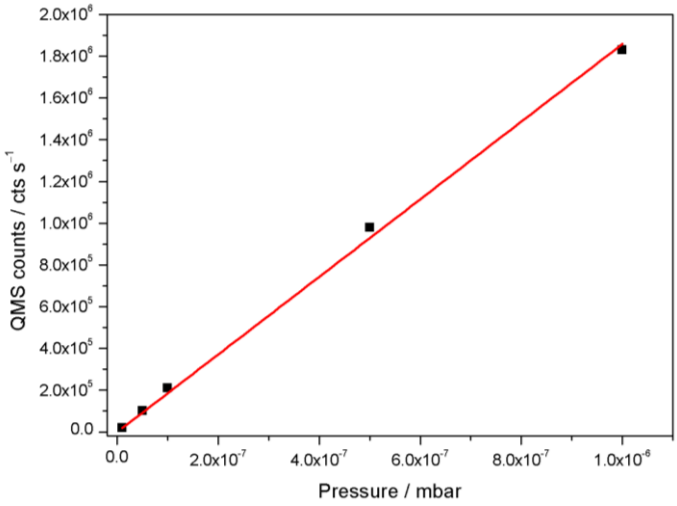

Figure 4.2: This plot shows the correlation between pressure in mbar and counts of m/z = 18 as monitored by the QMS. This linear relationship between pressure and counts was used throughout to note the background H_2O pressure during an experiment.

The test concerning the TPD experiments were done by depositing 0.5 ML H_2O onto the sample and collecting an IR spectrum. The film was then desorbed by heating the sample with a 0.04 K s^{-1} heating ramp, after desorption from the sample the temperature was kept at 170 K. The QMS monitored this process and when the counts reached a plateau equivalent to 2×10^{-10} mbar of H_2O, the sample was cooled to 17 K where another IR scan was collected. The results of this test are shown in **Figure 4.3** below.

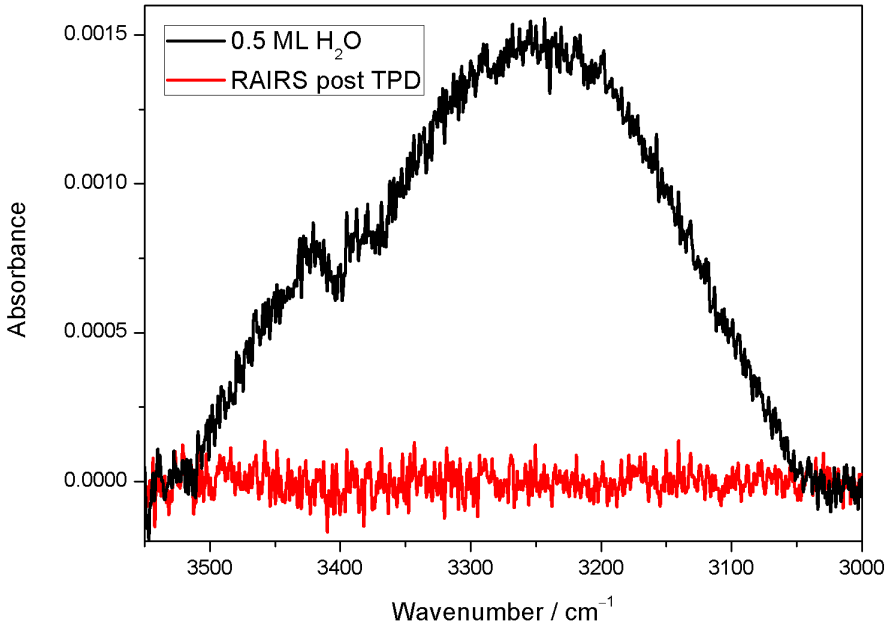

Figure 4.3: These spectra show the deposition of 0.5 ML H_2O (black) on SiO_2 followed by TPD of that film. After the partial pressure of H_2O has decreased to $<2 \times 10^{-10}$ mbar the sample was cooled and another spectrum was taken (red). Re–adsorption of H_2O on the timescale of the experiment is not significant due to the low H_2O partial pressure.

The red spectrum in **Figure 4.3** displays a clear absence of H_2O. Maintaining a surface temperature greater than the desorption temperature of H_2O on SiO_2 until the QMS indicates a low partial pressure means re–adsorption of H_2O is negligible. Following the knowledge that a partial pressure of H_2O $<2 \times 10^{-10}$ mbar leads to no H_2O RAIRS observable adsorption, all IR scans reported in this work have been conducted in this low partial pressure regime. The QMS was continuously used to verify this, and following background filling the chamber with 0.5 ML H_2O, the first RAIR spectrum was only taken when the QMS counts were deemed sufficiently low to reflect these observations.

With these constraints in mind, dosing 0.5 ML H_2O at base temperature and conducting the time dependent experiment, yields **Figure 4.4** below. From here on the initial spectra of 0.5 ML H_2O deposited on SiO_2 will be referred to as A_0 while the final annealing step at 100 K for 20 minutes will be referred to as $A_{infinity}$ or A_∞.

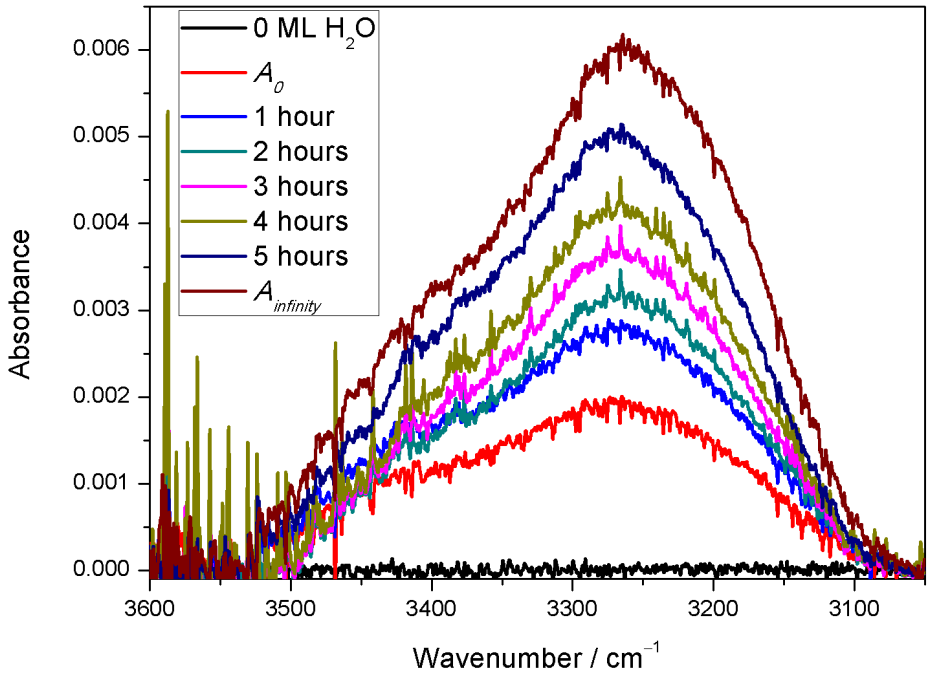

Figure 4.4: The result of depositing 0.5 ML H_2O onto SiO_2 at 18 K. The time between each RAIR spectrum was one hour as this was determined to be the average time between scans when H_2O is annealed at the other temperatures investigated. The sharp peaks are due to gas–phase H_2O in the optics boxes on the air side of the UHV apparatus.

What is observed in **Figure 4.4** is initially only the red trace. This was collected when the background partial pressure of H_2O was in $<2 \times 10^{-10}$ mbar. The film was then left for one hour before the next spectrum was collected giving the blue broad band of νOH.

The increase in absorbance throughout of 0.5 ML H_2O continues for the next spectra before the film is annealed at 100 K to get the $A_{infinity}$, or A_∞, spectrum. The same experiments were done for annealing temperatures of 18, 21, 24, 27, 30, 40, 50, 60 and 100 K which all show the same trend in increasing absorbance with temperature. **Figure 4.5** shows the result of annealing 0.5 ML H_2O at 100 K for a total of 500 seconds.

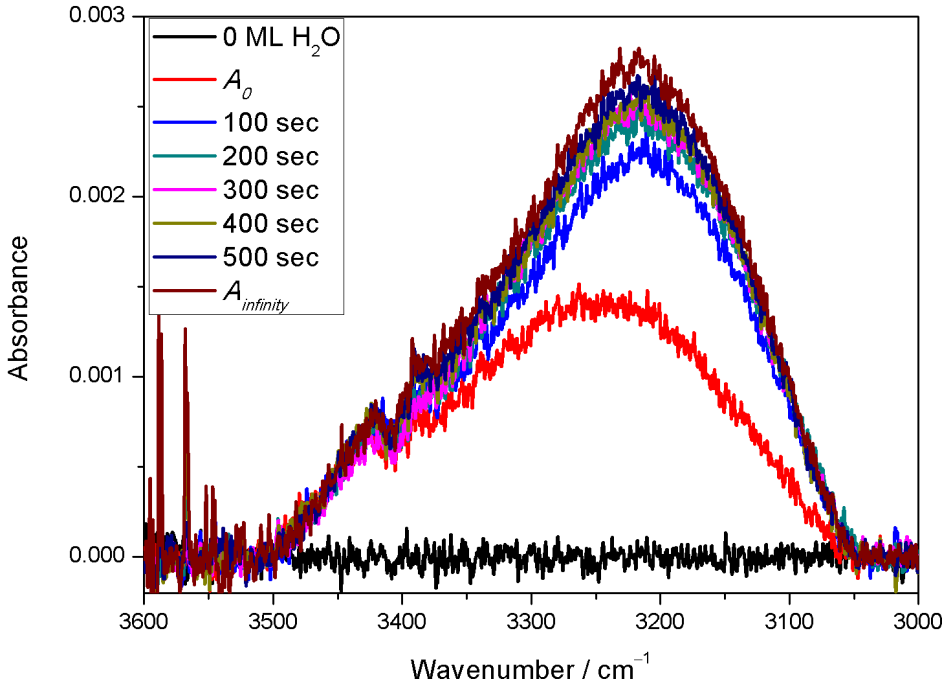

Figure 4.5: The result of depositing 0.5 ML H_2O onto SiO_2 at 100 K for a total of 500 sec before annealing to the $A_{infinity}$ times, A_∞, factor. The sharp peaks at 3500 – 3600 cm^{-1} are due to gas–phase H_2O in the optics boxes on the air side of the UHV rig.

In **Figure 4.5**, the same trend can be seen as that of **Figure 4.4** with an increase of absorbance as a function of annealing time at 100 K, albeit a greater change from the A_0 spectrum to the first of the annealing times of 100 s. H_2O molecules accommodate on the SiO_2 surface *via* a hit–and–stick mechanism at the cryogenic temperatures. However, as the partial pressure of H_2O is negligible, meaning further adsorption of H_2O after the A_0 trace is close to zero, another process must cause the increases in the observed absorbencies. De–wetting of H_2O molecules forming H–bonded islands and clusters would explain this. This can be seen in **Figure 4.5** where the main νOH band centred at roughly 3250 cm^{-1} for the A_0 spectra (the red trace) and the minor peak at just above 3400 cm^{-1}. These are the TO and LO modes of amorphous solid water [14]. As has been explained in **Chapter 2**, the LO–TO modes only occur in a 3–D network indicating that the 17 K spectra have enough of a bulk network to create this optical effect at sub–monolayer coverages. The dangling bond of H_2O at about 3692 cm^{-1} [15–

17] cannot be observed in these experiments due to gas–phase H_2O interference in the optics boxes. Smaller clusters such as dimers, trimers and tetramers [18, 19] also appear in the regions of the spectra where gas–phase H_2O is dominant and were not observed either. However, as H_2O is mobile at the base temperature of these experiments such observations were not expected.

The band profiles between **Figure 4.4** and **4.5** are the same, and as can be seen in **Figure 4.5**, annealing at 100 K still shows increases in the absorbance. The increase in absorbance means the de–wetting process still occurs and that H_2O is still forming clusters at this high temperature. For all the experiments below 100 K, the A_∞ factor has been estimated by annealing the 0.5 ML H_2O coverage at 100 K, however as **Figure 4.5** still shows absorbance increases A_∞ must be an underestimate. A correction for all A_∞ spectra has to be made which is done by depositing 0.5 ML H_2O at 17 K, annealing this to 100 K for 20 minutes (the usual A_∞ spectra) before taking a spectrum and then annealing it further for 120 minutes. The results of this can be seen in **Figure 4.6** below.

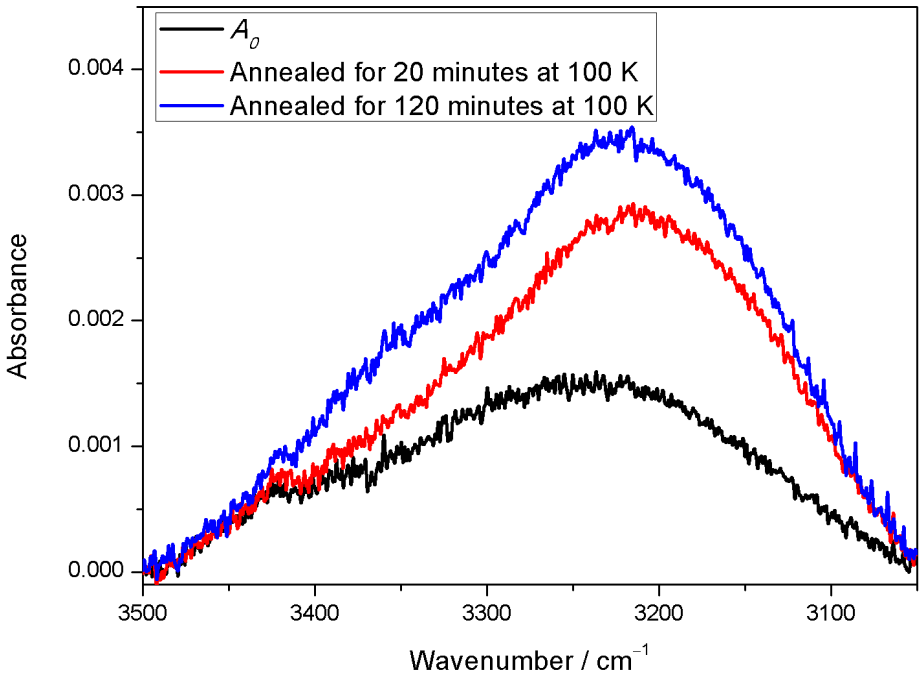

Figure 4.6: These spectra show the change when depositing 0.5 ML H_2O at 17 K before annealing to 100 K for 20 minutes and again for 120 minutes.

A change in the absorbance in **Figure 4.6** is still observed, albeit a slight change of a factor of 1.25, and the difference in the area of the νOH band between the two 100 K spectra is used to scale all A_∞ spectra. The reason for this correction is to approach a closer and more accurate value of A_∞ used for calculating the activation energy for de–

wetting of H_2O from SiO_2 where all H_2O molecules have formed a bulk solid, *i.e.* a multilayer of H_2O. A further increase is expected if the annealing time is increased to a greater value, however this was not done as only a relatively small change is observed in **Figure 4.6** after increasing the annealing time six–fold.

An example of the values obtained can be seen in **Table 4.1** for the 24 K annealing experiment (not shown).

Time / s	Integrated Absorbance	Corrected Integrated Absorbance
0	0.480	–
100	0.566	–
200	0.603	–
300	0.663	–
400	0.748	–
500	0.793	–
1200	1.340	1.678

Table 4.1: This table shows the areas of the νOH band after the spectra have been baseline corrected and smoothed. The correction of the A_∞ value comes as a result of **Figure 4.6**.

The values seen in **Table 4.1** are the results for the integrated smoothed spectra in the region of 3050 – 3500 cm^{-1}. The reason for this range and the smoothening is to minimise the additional area added to the experimental results from gas–phase H_2O observed as sharp peaks at higher wavenumbers in **Figure 4.4**.

If we assume that the de–wetting process:

$$H_2O_{\text{isolated}} \rightarrow H_2O_{\text{clustered}} \qquad \textbf{Equation 1}$$

follows first order kinetics with time, *t*:

$$[H_2O_{isolate}]_t = [H_2O_{isolate}]_0 e^{-kt} \qquad \textbf{Equation 2}$$

with a rate constant, *k*, then a simple kinetic analysis of the spectroscopic data gives **Equation 3** [20]

$$\ln\left(\frac{A_\infty - A_0}{A_\infty - A_t}\right) = kt$$ **Equation 3**

where *t* is the annealing time at a set temperature. This leads to **Table 4.2**:

Time / s	Area under spectra	Corrected area for A_∞	$\ln\left(\frac{A_\infty - A_0}{A_\infty - A_t}\right)$
0	0.480	–	0
100	0.566	–	0.105
200	0.603	–	0.154
300	0.663	–	0.239
400	0.748	–	0.373
500	0.793	–	0.452
1200	1.340	1.678	—

Table 4.2: This table shows the next step in the analysis using **Equation 3**. The areas used come from smoothing of the spectra for the 24 K de–wetting experiment.

Constructing a graph, **Figure 4.7**, from **Table 4.2** leads to the value of *k* in the linear relationship, **Equation 3**, as expected from a first order process.

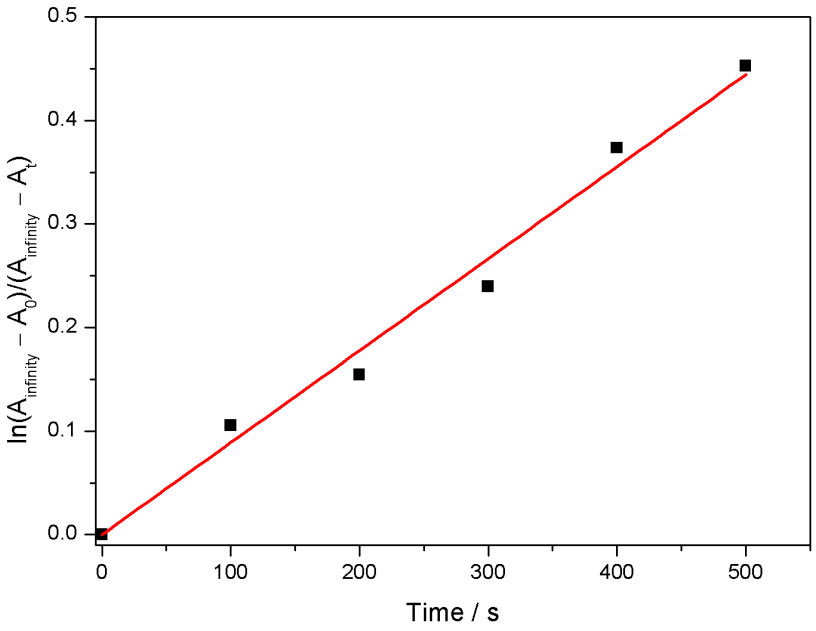

Figure 4.7: This figure shows the linear relationship of **Equation 3**. The slope is the rate constant, *k*, for the isolated H_2O to a bulk process. The values for this figure are obtained from **Table 4.2**.

With a value of *k* for the experiment involving an annealing temperature of 24 K, and doing the same analysis for the other experiments leads to **Table 4.3**.

T_{anneal} / K (± 0.3 K)	$1/T_{anneal}$ / K^{-1}	k / s^{-1} (± 3%)	ln(k / s^{-1})
17	0.059	2.432×10^{-5}	–10.624
18	0.056	3.640×10^{-5}	–10.221
21	0.048	5.188×10^{-4}	–7.564
24	0.042	8.894×10^{-4}	–7.025
27	0.037	8.788×10^{-4}	–7.037
30	0.033	1.508×10^{-3}	–6.497
40	0.025	2.046×10^{-3}	–6.192
50	0.020	1.392×10^{-3}	–6.577
60	0.0167	1.300×10^{-3}	–6.645
100	0.1	1.400×10^{-3}	–6.571

Table 4.3: This table shows the individual values of the rate constant, *k*, with respect to its annealing temperature. Plotting the inverse temperature and the ln(*k*) will lead to the associated energy through **Equation 4**.

The results of **Table 4.3** lead to the Arrhenius plot which is shown in **Figure 4.8** below.

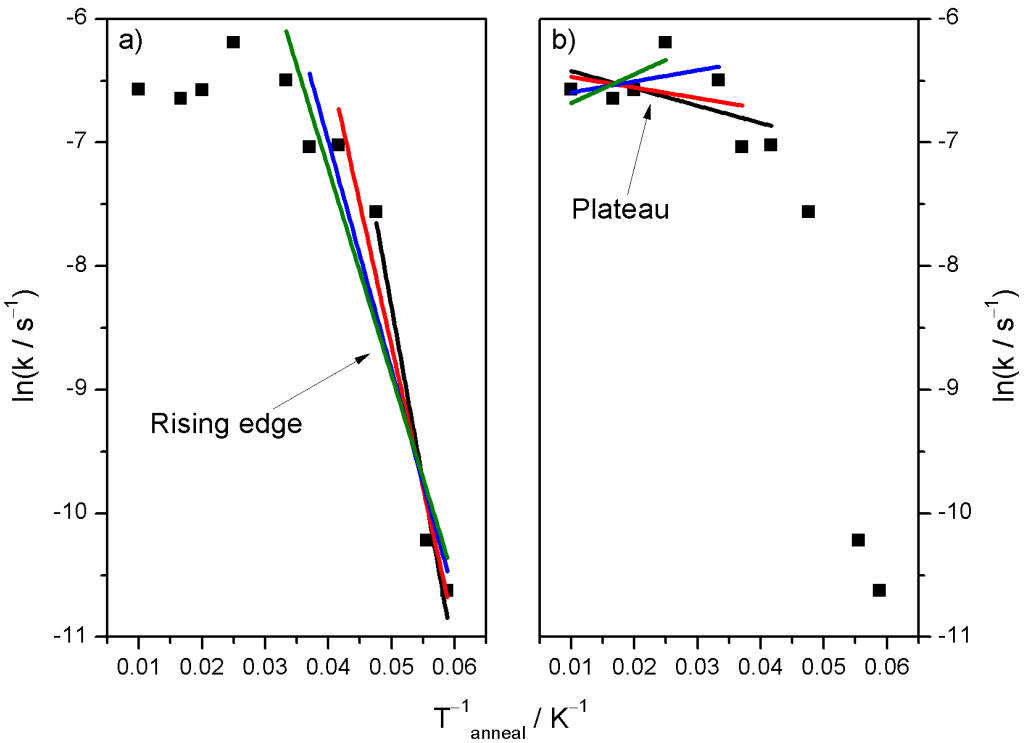

Figure 4.8: This figure shows the Arrhenius plot where two regimes can be observed. The first regime, **a)**, illustrates a rising edge while **b)** indicates a plateau. A series of fits have been done to estimate an average gradient for each **a)** and **b)** in order to obtain an activation energy, however a clear change is apparent as the temperature increases. The figures have been shown in two parts for clarity with matching colours for the linear fits.

As can be seen in **Figure 4.8**, two clear regions are presented. The initial region, **Figure 4.8a**, represents the value of ln(*k*) as the annealing temperature is increased. A clear rise is apparent which leads to a plateau region as shown in **Figure 4.8b**. The exact temperature separating the regions can be argued and for that reason linear fits have been done to various points as seen in **Figure 4.8** where the colour coding matches each **a** and **b** sections. **Table 4.4** states the values of the gradient for each linear fit plotted in **Figure 4.8a** and **4.8b** above.

Linear fit	Rising edge / K^{-1}	Plateau / K^{-1}
Black	–284.595 (± 47.709)	–14.022 (± 9.709)
Red	–229.971 (± 35.877)	–8.526 (± 12.591)
Blue	–184.503 (± 35.636)	8.928 (± 10.496)
Green	–166.972 (± 27.509)	23.285 (± 16.199)
Average	–216.510 (± 36.683)	2.416 (± 12.249)

Table 4.4: This table shows the gradients for the linear fits of **Figure 4.8a** and **4.8b**.

Taking the average values for the slopes from **Figure 4.8** leads to a simpler graph as seen below, **Figure 4.9**.

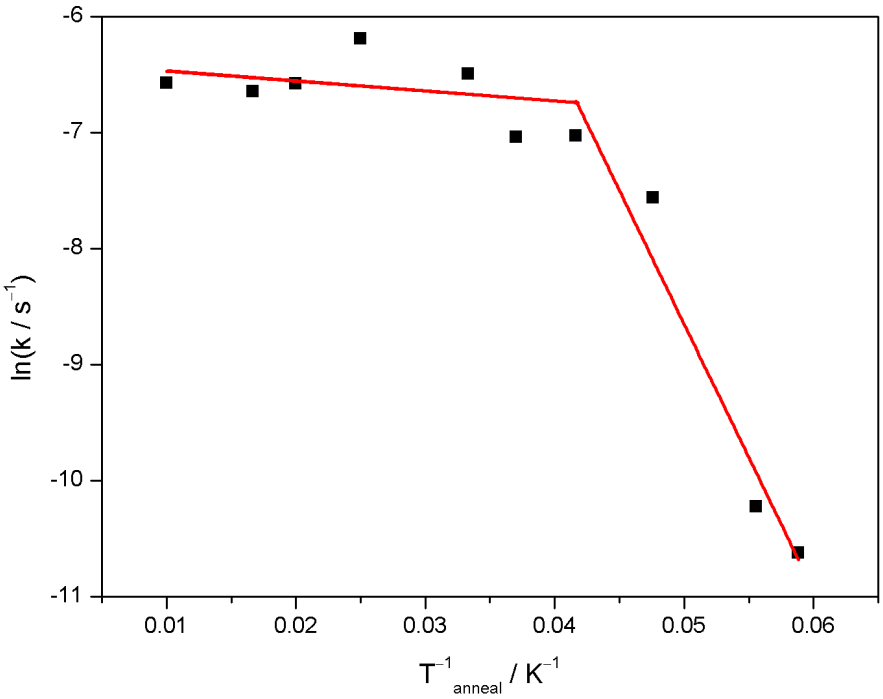

Figure 4.9: This figure shows the final step after analysis with an indication of the best linear fits to the two data regions in the experimental results.

This method of analysis has been used for finding activation energies, E_{act} for various purposes such as desorption energy from temperature programmed desorption [21].

$$\ln(k) = \ln(A) - \frac{E_{act}}{RT} \qquad \textbf{Equation 4}$$

where A is the pre–exponential factor, R is the ideal gas constant and T is the temperature. The associated values for the energies from **Figure 4.9** can be calculated by considering **Equation 4** and a value for R of 8.314 J K^{-1} mol^{-1}. This has been shown in **Table 4.5**.

E_{act} / kJ mol^{-1}	
Rising edge	**Plateau**
1.8 ± 0.3	0.0 ± 0.1

Table 4.5: This table reports the activation energy values associated with the de–wetting process of H_2O (rising edge) and the subsequent region (plateau) where isolated H_2O molecules have formed a greater bulk.

From **Table 4.5**, the rising edge has an associated energy of about 1.8 kJ mol^{-1} ± 0.3 kJ mol^{-1} which changes to the plateau with what amounts to 0.0 ± 0.1 kJ mol^{-1} at 24 K. The plateau seems to have a negative gradient, however the error associated with the data outweighs this gradient, suggesting a value of 0.0 kJ mol^{-1}. This means that a sub–monolayer coverage of H_2O of 0.5 ML will have formed a bulk multilayer after being heated to about 24 K when considering **Figure 4.9**. The implication of this means that a coverage of 0.5 ML H_2O on SiO_2 has formed an island or cluster as observed when conducting TPD experiments of a sub–monolayer coverage of H_2O on SiO_2.

An assumption about diffusion of molecules on surfaces is that in general 10 – 15% of the binding energy approximates the activation energy of diffusion [22] or, in the case of this work, the energy required for H_2O to de–wet from SiO_2. This assumption holds true for C, N, O, H, S, CO and NO on metal surfaces [22 and references therein]. With this assumption in mind and knowing that H_2O has a desorption energy of 43.9 kJ mol^{-1} [2] for the two H–bonds breaking one H–bond in water has an associated energy of about 22 kJ mol^{-1}. This value of a H–bond corresponds well with the known values of 8 – 40 kJ mol^{-1} [23] or more generally described as 20 kJ mol^{-1} [24]. Considering the diffusion energy assumption of 10% of the binding energy leads to an energy for H_2O

diffusion of about 2.2 kJ mol^{-1}, which is very similar to the 1.8 kJ mol^{-1} determined in this work.

An important note to consider, however, is that reorganisation of H_2O molecules at the temperature used in these experiments can also occur. As stated in the introduction, **Section 4.1**, H_2O undergoes a phase change from p–ASW to c–ASW starting at a temperature of about 38 K [25] and a further phase change from c–ASW to CSW at above 130 K [26, 27]. When purely looking at the temperature profile of the experiments, the rising edge leads to a plateau at about 24 K. Recent work regarding the amorphous H_2O has shown the porous to compact amorphous H_2O phase change to possibly begin at temperatures of 25 K [28]. However, phase changes between amorphous states of H_2O cannot be detected with IR in these experiments presented in this thesis due to the lack of observable H–dangling bonds. Other techniques can be used to investigate this phase transition such as co–deposition of CO onto H_2O films at different temperatures followed by TPD experiments to look at CO entrapment [25, 29, 30]. That is not to say that re–organisation of the bulk H_2O molecules cannot happen at these low temperatures before a phase change occurs. Experiments looking at the de–wetting of H_2O at temperatures approaching the compact to crystalline phase change were not possible due to a change in the νOH band sharpening up as the onset of crystallisation occurs and at higher temperatures due to the initial stages of desorption.

4.3.2 O Atom Bombardment of H_2O Films

Considering the work discussed in **Chapter 3**, a question could be; what happens as such a sub–monolayer coverage of H_2O is bombarded by O atoms? When looking at the experiment where H_2O moves on the SiO_2 surface at 18 K one can see that the de–wetting process is relatively slow and only picks up when thermal energy is supplied to the molecular film. De–wetting is observed within the first hour of the experiment, as seen in **Figure 4.4**, however the rate constant associated with the entire de–wetting experiment at 18 K is comparatively low and therefore should be a slow process. Starting from this basis, depositing 0.5 ML H_2O at 18 K and bombarding with O atoms leads to **Figure 4.10**.

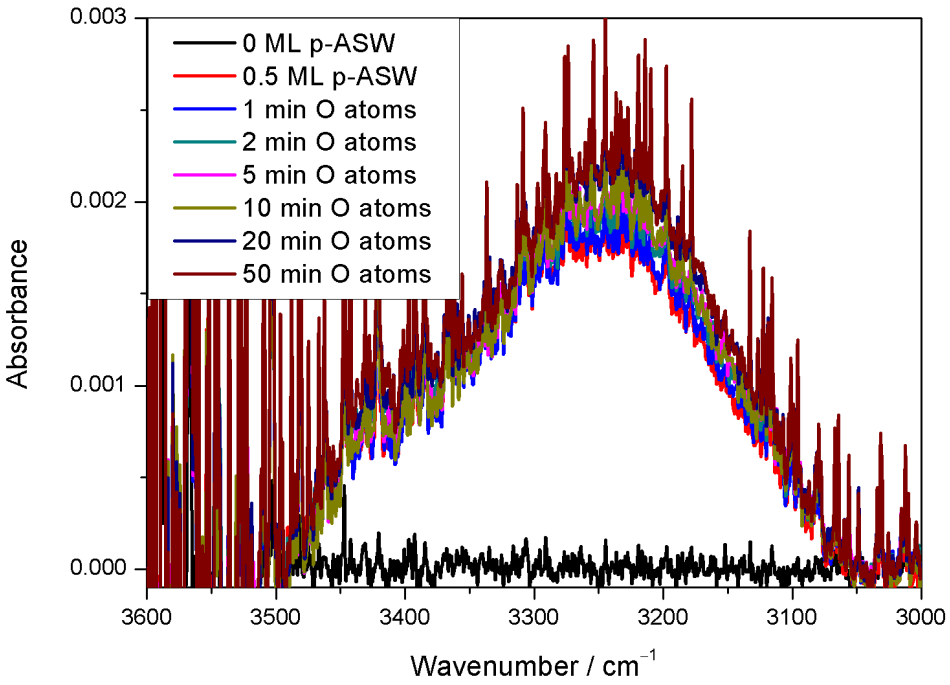

Figure 4.10: This figure shows the effect of O atom bombardment on 0.5 ML H_2O. The large sharp peaks are due to gas phase H_2O in the optics boxes outside of the UHV chamber.

From **Figure 4.10** one can see that the general trend is still observed; the intensity of the main band centred at about 3250 cm^{-1} increases as atomic O beam dosing time increases. The features in the spectrum at about 3400 cm^{-1}, corresponding to smaller clusters of H_2O, seem invariant throughout the experiment. This is an indication that the diffusion process is slow and barely active at this time scale. The main band is seen to increase though leading to a different process occurring when O atoms bombard the surface. A possible process is network reconnection of the hydrogen bonds in small H_2O clusters. Analysis of **Figure 4.10** was done as previously explained with smoothed spectra in the 3500 – 3000 cm^{-1} range (not shown here) and yields a rate constant of 1.8 $\times 10^{-3} \pm 0.2 \times 10^{-3}$ s^{-1} which is about 2 orders of magnitude greater than the 18 K de–wetting of **Figure 4.4**.

Increasing the H_2O coverage will inevitably lead to greater clusters on the SiO_2 surface, and thereby a greater chance for O atoms to strike H_2O instead of SiO_2. Deposition of 1 ML p–ASW will not create a monolayer and clusters are expected considering TPD data and the work presented in this chapter. For that reason a change in intensity of the main O–H stretch remains expected. This is indeed what is observed in **Figure 4.11**.

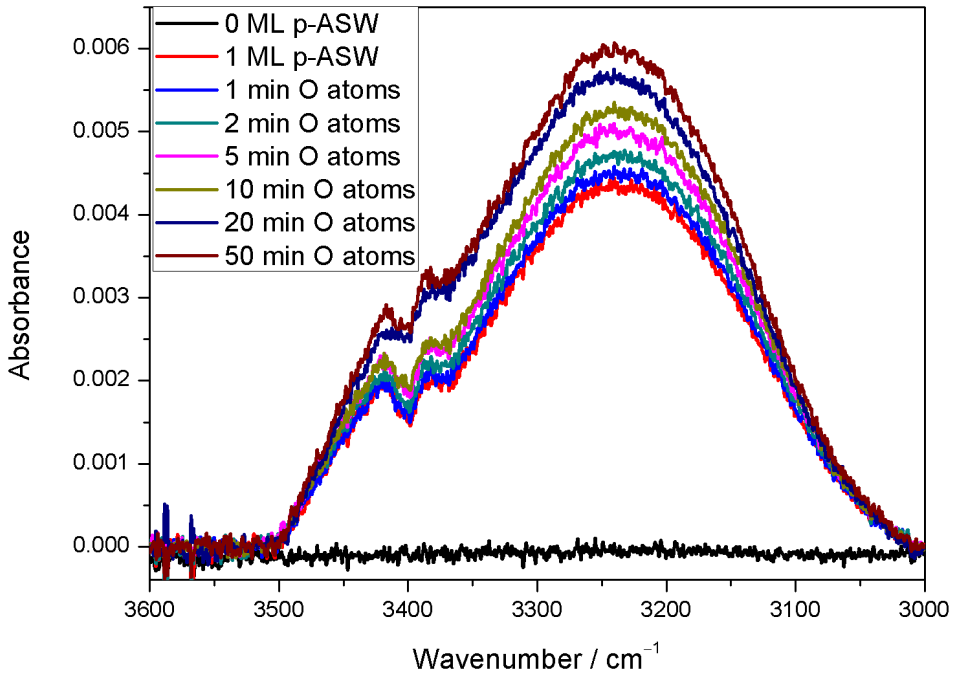

Figure 4.11: This figure is of 1 ML p–ASW as O atoms bombard the sample for a total of 50 minutes. The same trend is seen here, however to a greater extent, as is seen in **Figure 4.10**.

Deposition of 1 ML H_2O, as in **Figure 4.11**, still shows increases in the main band at about 3250 cm^{-1}, however the features at about 3400 cm^{-1} seem to remain unaltered throughout the experiment. In general, the behaviour observed in **Figure 4.10** is also observed in **Figure 4.11**, a difference is observed when calculating the rate constant. The value for k is $1.2 \times 10^{-3} \pm 0.2 \times 10^{-3}$ s^{-1}, having fallen when increasing the H_2O coverage. If O atom bombardment were to aid in the de–wetting process, a greater rate constant would be expected; this is not observed. However, O_2 formation releases about 580 kJ mol^{-1} [31] which has to be dissipated into the film for molecular formation to take place. A greater concentration of H_2O would be able to dissipate this energy more efficiently than a lesser concentration leading to the observed difference in the rate constants.

With no H_2O present on the film, O_2 formation would take place and the energy dissipated in to the SiO_2 underlayer with no change to the SiO_2 network. This was the basis of **Chapter 3**. However, O atomic bombardment could induce a change in the H_2O H–bonded network. Altering the H_2O film before O atomic bombardment will give information regarding the H_2O H–bonded network.

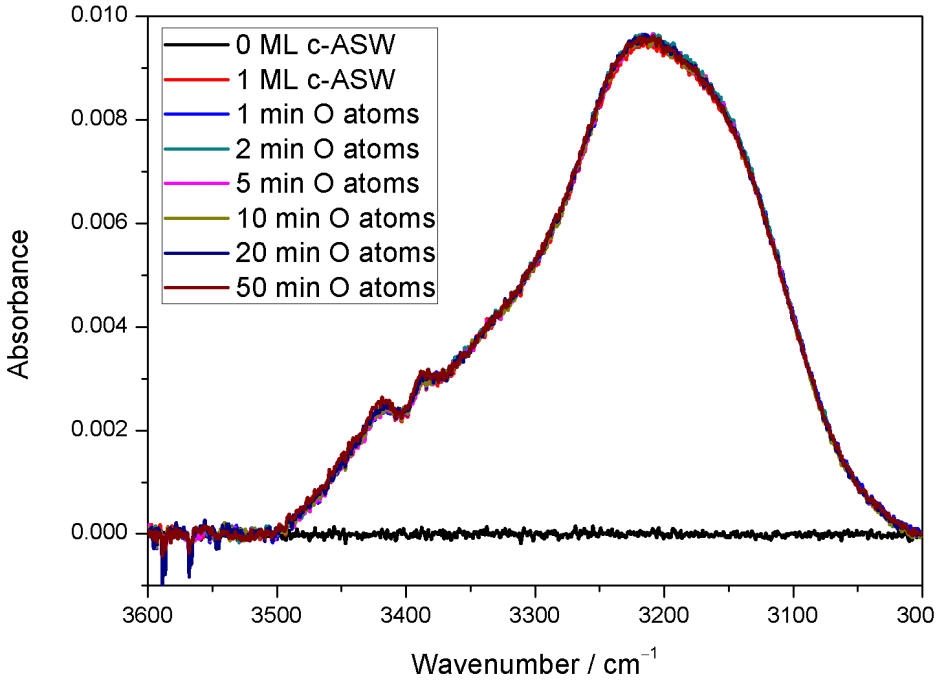

Figure 4.12: As can be seen in this figure, 1 ML of c–ASW does not behave as the p–ASW films. Throughout O atom irradiation for 50 minutes, the band is invariant, however has the same shape as the p–ASW spectra presented in this work.

Firstly, looking at the 1 ML coverage of compact amorphous solid water (c–ASW) and bombarding it with O atoms for 50 minutes gives **Figure 4.12**. As can be seen, the band shape is similar to other H_2O spectra presented, however the main 3250 cm^{-1} band is not observed to vary with time or atomic O bombardment. The integrated areas do no differ by a substantial amount, leading to the rate constant nearly equalling zero considering the uncertainty ($8.6 \times 10^{-4} \pm 7.9 \times 10^{-4}$ s^{-1}). The rate constant is not fully equal to zero as re–connection of the H–bonded network is still a possibility. At the deposition temperature of 100 K, the H_2O molecules will have enough thermal energy to de–wet instantly meaning the de–wetting process is not believed to occur and be the reason for the value of the rate constant.

Further changing the H_2O to produce a crystalline solid water (CSW) film can be seen in **Figure 4.13**.

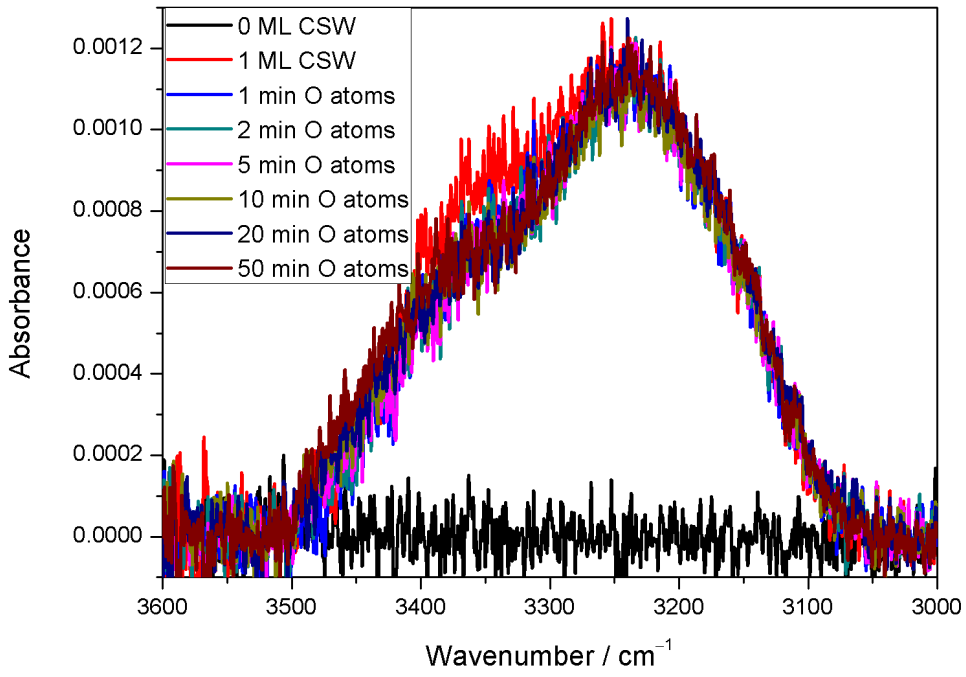

Figure 4.13: This figure shows the effect of O atoms bombarding a 1 ML CSW film. The atomic beam was dosed in steps for a total of 50 minutes. The bump seen in the 1 ML CSW spectrum (red spectra) at about 3350 cm^{-1} disappears during O atom bombardment.

The red spectrum in **Figure 4.13** shows the initial 1 ML CSW film prior to O atom irradiation. A bump can be seen in the 3300 – 3400 cm^{-1} range which has previously been described as a feature of crystalline H_2O films [32]. This feature disappears as O atoms bombard the surface leaving the final spectrum (after 50 minute O atom dosing) similar in shape to the spectra shown in **Figure 4.12**. There is no information regarding the rate constant because of this disappearance of the 3350 cm^{-1} feature leaving the area of the A_0 spectra greater than all A_t spectra rendering **Equation 3** of no mathematical use. Disregarding the rate constant of the CSW experiment, **Table 4.6** has been produced to directly compare the results.

Water type and coverage	***k* / s^{-1}**
0.5 ML p–ASW	$1.8 \times 10^{-3} \pm 0.2 \times 10^{-3}$
1 ML p–ASW	$1.2 \times 10^{-3} \pm 0.2 \times 10^{-3}$
1 ML c–ASW	$8.6 \times 10^{-4} \pm 7.9 \times 10^{-4}$
1 ML CSW	–

Table 4.6: This table has been made to show the difference in the rate constant (*k*) as the coverage changes in p–ASW films and the film itself is changed to c–ASW and CSW.

O atom bombardment of a H_2O will produce O_2 as discussed in **Chapter 3**, and as previously said, the energy of fusion has to be dissipated by surrounding molecules for the reaction product to remain. In the p–ASW and CSW films, this excess energy is possibly used to form a c–ASW film through the breaking of H–bonds from the dissipated fusion energy [27]. This would explain why the RAIR spectra of CSW after O atoms irradiation (**Figure 4.13**) begin to become similar to the c–ASW spectra in **Figure 4.12**. A simple way of looking at this has been described in **Equation 5**.

$$\mathrm{p-ASW} \xrightarrow{\mathrm{O}} \mathrm{c-ASW} \xleftarrow{\mathrm{O}} \mathrm{CSW} \qquad \textbf{Equation 5}$$

This idea and equation could also be part of the reason why the main constituent of an interstellar grain's icy mantle is c–ASW and not p–ASW or CSW.

4.4 Astrophysical Implications of H_2O de–wetting

Returning to the H_2O de–wetting results and looking at these from an astrochemical stand–point one should consider the cooling environments of the ISM, *i.e.* a diffuse cloud collapsing into a dense one. Initially, however, the focus will be on a dust grain already in the core of a dark cloud and following the dust grain as the cloud warms up. The heating rate in these environments of the ISM is estimated to be 1 K century^{-1} [33].

Using the results obtained for the de–wetting experiments, a simple picture can be drawn to compare the data with the H_2O monolayer formation time through **Equation 6** where *i* refers to isolated H_2O and *c* is clustered H_2O.

$$\mathrm{H_2O\ (i)} \xrightarrow{\mathrm{k}} \mathrm{H_2O(c)} \qquad \textbf{Equation 6}$$

The result of this equation and the associated simulation can be seen in **Figure 4.14** below. **Figure 4.14** indicates that isolated H_2O moves to a clustered environment on a timescale of about 400 years at a temperature of about 5 K which is considerably less than the typical temperatures of 10 K in a dark cloud [34]. The results therefore indicate that H_2O will have the mobility to form clusters even in the coldest parts of the ISM. This will also mean that the time for H_2O to complete an entire film on interstellar dust grains might be higher than the estimated 10,000 years [35] as cluster formation at these early times and low temperatures will delay this time.

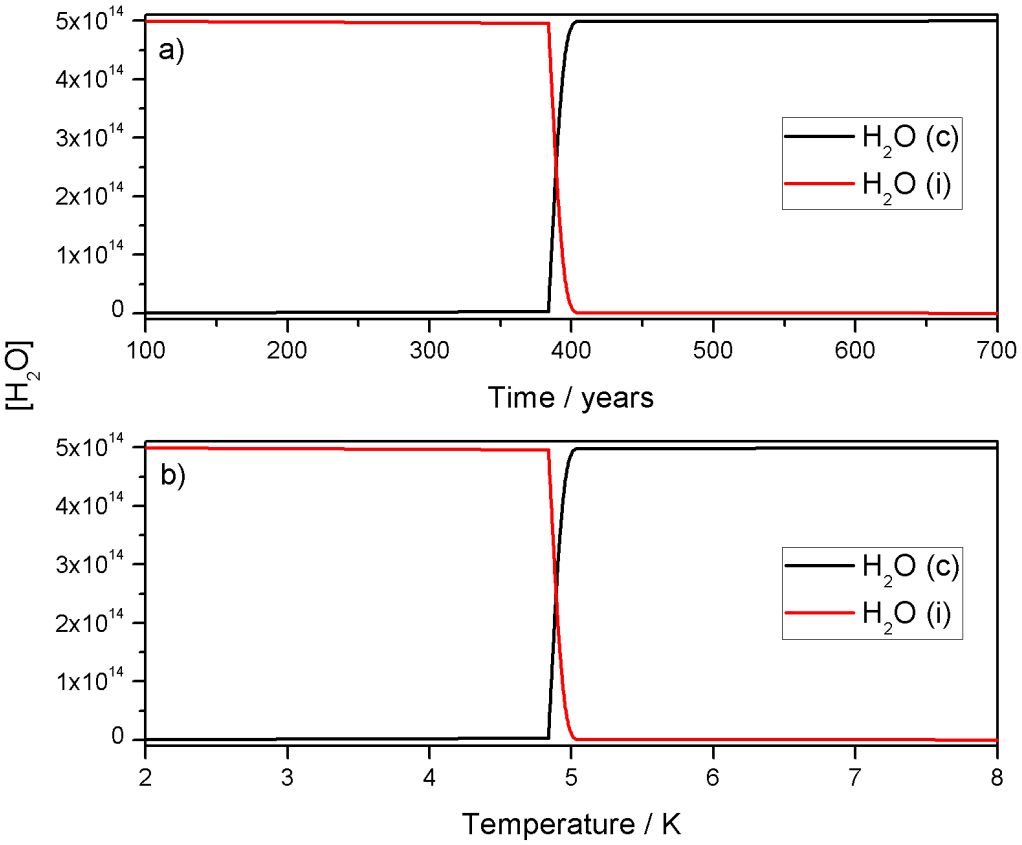

Figure 4.14: This figure shows the H_2O as isolated (i) converting into clusters (c) with time through a heating rate of 1 K century^{-1} **(a)** and the corresponding temperature for the cluster formation **(b)**. The simulation has been done for 0.5 ML H_2O with an E_{act} of 1.8 kJ mol^{-1} and a pre–exponential factor of 10^{12} s^{-1}.

The results of the simulation in **Figure 4.14** come from taking a bare dust grain and plunging it into the depths of the cold core of a molecular cloud to look at the mobility of H_2O. However, a bare grain will build an icy mantle as a cloud collapses and the environment cools. As stated in the introduction, the time for a cloud to collapse has been estimated to be at least in the order of 10^6 years [36, 37] and as this happens the temperature will gradually fall from about 100 K in diffuse clouds [38] to 10 K in the core of dark molecular clouds [34]. As this occurs molecules will adsorb onto dust grains, this freeze–out process occurs on a time scale of 10^6 years [39]. Therefore, the cooling rate can be estimated as being about 1 K per 10^4 years when cooling from about 100 K to 10 K. As this happens, accreted H_2O will naturally find itself in different structural states such as crystalline (CSW) and compact amorphous (c–ASW). For that reason a second CKS model can be built to show the effect of this, more natural, process while knowing that H_2O prefers to be in its clustered c–ASW or CSW state. The steps used are as follows:

$$H_2O\ (g) \rightarrow\ H_2O_{isolated}\ (s) \qquad \textbf{Equation 7 (A)}$$

$$H_2O\ (g) \rightarrow\ c-ASW\ (s) \qquad \textbf{(B)}$$

$$H_2O_{isolated}\ (s) \rightarrow c-ASW\ (s) \qquad \textbf{(C)}$$

$$c-ASW\ (s) \rightarrow H_2O_{isolated}\ (s) \qquad \textbf{(D)}$$

$$c-ASW\ (s) \rightarrow CSW\ (s) \qquad \textbf{(E)}$$

$$H_2O_{isolated}\ (s) \rightarrow H_2O\ (g) \qquad \textbf{(F)}$$

$$c-ASW\ (s) \rightarrow H_2O\ (g) \qquad \textbf{(G)}$$

$$CSW\ (s) \rightarrow H_2O\ (g) \qquad \textbf{(H)}$$

The adsorption processes in **Equation 7 (A)** and **(B)** have an assumed sticking coefficient of unity. Further to the adsorption steps; it is assumed that H_2O will adsorb at random and in equal proportion of isolated and clustered states. The de–wetting step in **(C)** follows the values supplied in this chapter. The reverse (step **(D)**) proceeds *via* H–bond breaking similar to the desorption processes in **(F–G)** with energies ranging from 45 – 47 kJ mol^{-1} [2, 40]. With the data in **Figure 4.14**, a likely result will be to see H_2O only in the clustered or bulk phase on the surface. This is indeed what **Equation 7** leading to **Figure 4.15** below indicates.

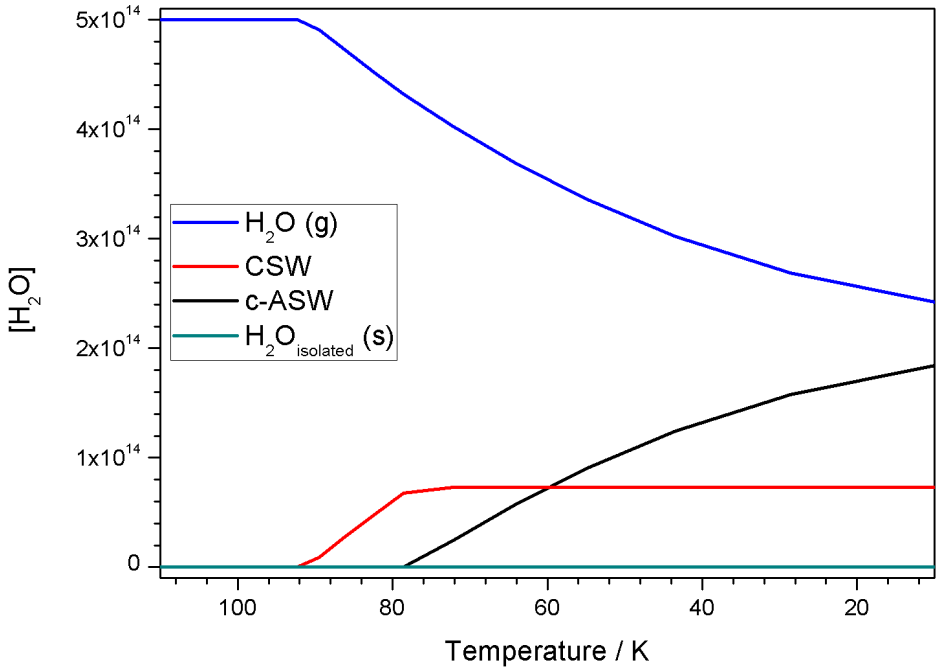

Figure 4.15: This figure shows what happens as H_2O adsorbs onto an interstellar dust grain as during cloud collapse and freeze–out as the temperature falls from 110 K to 10 K. Gas phase molecules (g) will either adsorb as isolated or clustered H_2O. As the temperature is above the energy needed for de–wetting, isolated molecules instantly become crystalline or clustered depending on temperature. The simulation has been done for 0.5 ML H_2O with an E_{act} for de–wetting of 1.8 kJ mol^{-1} and a pre–exponential factor of 10^{12} s^{-1} with a cooling rate of 1 K century^{-1}.

Figure 4.15 shows H_2O initially in the gas phase, (g), before adsorbing to the surface as either isolated or clustered H_2O. As the temperature falls and H_2O is adsorbed, no isolated molecules are found on the surface as seen in the $H_2O_{isolated}$ (s) trace, this means H_2O is found in a clustered form from the initial stages. As the temperature is great enough to give H_2O the thermal energy needed to construct the crystalline form, the red trace ($H_2O_{crystalline}$ (s)) grows until the temperature reaches 80 K. At this stage, H_2O can only form the compact amorphous solid structure while isolated molecules are still not expected to form. The cooling rate used for **Figure 4.15** was only 1 K century^{-1} due to restrictions with the CKS software. Changing the cooling rate to 1 K per ten millennia (which is a better estimate of the astrophysical cooling rate) will shift the temperature scale so that adsorption occurs at a higher temperature, however the general and overall trend regarding isolated H_2O moving to clusters will remain consistent.

All the experiments and simulations have been done considering a pure SiO_2 surface, since H_2O is mobile at low temperatures one large cluster can be expected to form. However, silicate dust grains in the ISM, as explained in **Chapter 1**, are highly amorphous and comprised of metal centres scattered throughout. These metal centres, such as iron are initially thought to be cationic leading to iron nanoparticles due to space weathering [41]. At low coverages H_2O will dissociate on a polycrystalline Fe surface [42] however, the interstellar dust grains would have a variety of binding sites leading to preferred sites of H_2O adsorption. Therefore, the possibility of H_2O forming more than one cluster is possible. However many clusters are formed, bare grain surfaces could be expected, due to the de–wetting process, for other molecules to adsorb to. As stated earlier, CO is a large component of the icy mantle coating dust grains. If a simple dust grain model is assumed where only H_2O is present and CO adsorbs at a later stage, onto what surface would CO adsorb? Once again, TPD experiments can provide the answer. Firstly, CO will form a monolayer on a SiO_2 surface [2, 21] and also on a H_2O surface [43] before it binds to another CO molecule to form a multilayer. Further to this, at a very low coverage of CO, 0.1 ML, the binding energy of CO to SiO_2 is greater by about 1 kJ mol^{-1} than for compact amorphous H_2O, at monolayer and greater thicknesses the CO–CO interaction becomes dominant and the energies of desorption become similar for the SiO_2 and H_2O surfaces mentioned [21]. Pontoppidan *et al.* [44] investigated CO in various H_2O poor environments in the ISM. Three features linked to CO were found at 2143.7 cm^{-1}, 2139.9 cm^{-1} and 2136.5 cm^{-1}, where the first two features were assigned to multilayers of CO. The latter feature was left unidentified.

Experiments conducted by Collings *et al.* [2] with 0.5 ML CO deposited onto an amorphous SiO_2 surface lead to a peak at 2137 ±1 cm^{-1} which could correspond to the unassigned feature detected by Pontoppidan *et al*. This would therefore mean that CO can possibly be found to interact directly with the dust grains and that H_2O will not cover the entire grain as it will rather form clusters or islands. However, this same feature at 2136.5 cm^{-1} can also be assigned to CO in a CH_3OH matrix as this alcohol is the final hydrogenation product of CO [45]. If the 2136.5 cm^{-1} feature is considered to be CO on SiO_2, then another simple CKS model can be created while considering the difference in CO–SiO_2 and CO–H_2O interaction energy leading to CO preferably interacting with SiO_2. Once again running the model in a cooling environment where 0.5 ML H_2O, in its c–ASW form, is already on the dust grain surface and letting one ML CO adsorb from the gas–phase onto the dust grain leads to **Figure 4.16**.

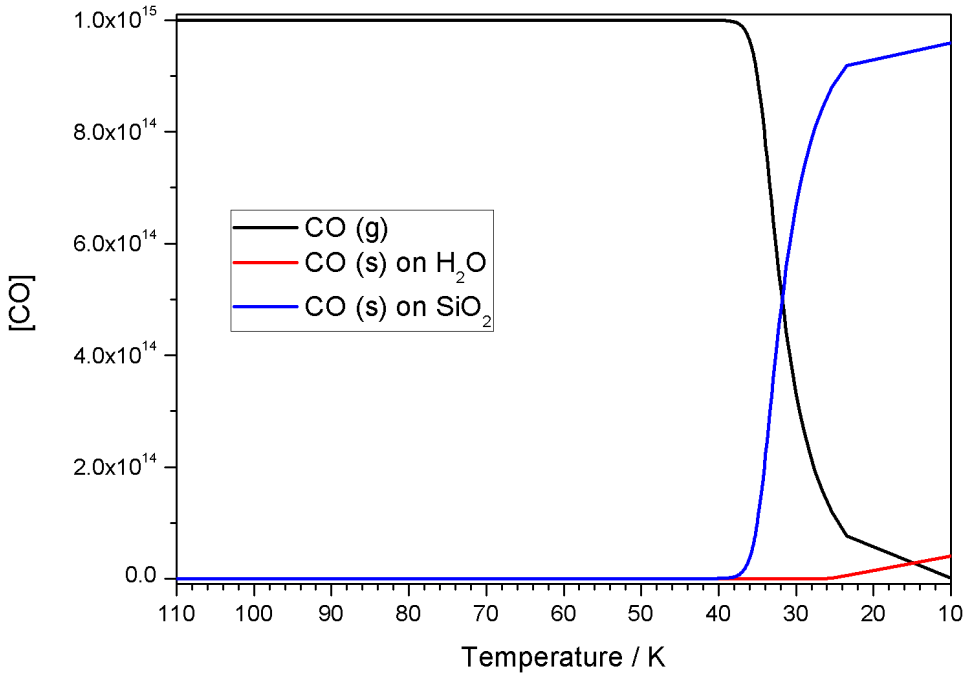

Figure 4.16: This figure shows the behaviour of CO as it adsorbs onto an interstellar dust grain with H_2O already present. Assuming an equal probability of CO initially adsorbing onto H_2O or SiO_2, CO then migrates to the preferred SiO_2 sites until all SiO_2 sites are inhabited leaving H_2O sites open for interactions as compared to the less favoured CO multilayer formation.

Shown in **Figure 4.16** is the adsorption of CO onto SiO_2 and c–ASW. There is no preference for where CO adsorbs, but the molecules do migrate to the SiO_2 surface leading to almost all CO adsorbed onto SiO_2. When the CO coverage approaches the full monolayer, CO will have to adsorb onto the H_2O as this interaction is still favoured

over CO multilayer formation. This model has been constructed with energies for CO–SiO_2 interaction being favoured over CO–H_2O as has been shown experimentally [21]. Also, the same steps for H_2O adsorption were used as described in **Equation 7**, with the extra steps shown in **Equation 8** leading to CO adsorption.

$$\mathrm{CO\ (g)} \rightarrow \mathrm{CO_{H_2O}\ (s)} \qquad \textbf{Equation 8 (A)}$$

$$\mathrm{CO\ (g)} \rightarrow \mathrm{CO_{SiO_2}\ (s)} \qquad \textbf{(B)}$$

$$\mathrm{CO_{H_2O}\ (s)} \rightarrow \mathrm{CO_{SiO_2}\ (s)} \qquad \textbf{(C)}$$

The step in **Equation 8 (C)** illustrates the preferred interaction of CO with SiO_2 as compared to H_2O. This simple model therefore shows that regions of CO directly adsorbed onto dust grains are possible.

4.5 Conclusion

This chapter has focused on the initial stages of the icy mantle covering an interstellar dust grain as H_2O is formed as studied through the use of RAIRS. As explained in the introduction of this chapter, **Section 4.1**, TPD experiments show zero order desorption which explains that the H_2O–H_2O interaction is favoured over the H_2O–SiO_2 interaction even at a sub–monolayer coverage. Therefore, if a hit–and–stick mechanism of H_2O adsorption is applied at cryogenic temperatures, H_2O will need an amount of energy to begin to move from isolated to clustered regions. According to this work, the mobility of H_2O has an activation energy of about 2 kJ mol^{-1} forming clusters at very low temperatures on a SiO_2 surface. H_2O does therefore not hit and stick as is typically thought. Further to this, when bombarding H_2O cluster with O atoms a general shift from p–ASW and CSW to c–ASW films is observed. H_2O ice covering interstellar dust grains is thought mainly to be in the c–ASW form due to a lack of the dangling H–bond. These O atom bombardment experiment could be one mechanism for the transformation of different H_2O structures leading to the observable evidence of c–ASW ices in the ISM.

The simulations of this process indicate that, even at temperatures experienced by grains at the very core of molecular clouds H_2O will form clusters before a complete monolayer is formed. **Figure 4.17** is a simple cartoon of the H_2O cluster formation as a diffuse interstellar clouds collapses to become a dense molecular cloud. **Figure 4.17**

displays CO as binding with only one end of the molecule to the surface. This is because of the work done by Collings *et al.* [46] showing that a so–called sigma binding of CO occurs through the C end of the molecule leaving the positive O end protruding to the vacuum.

As a cloud collapses the temperature decreases and the gas becomes mainly molecular, leaving the dust grains covered with a mantle of ice. During the cooling process all H_2O molecules reactively accreted and adsorbed onto a dust grain will have sufficient energy to agglomerate. The warmer the grain, the faster the de–wetting process. The dust grains will continue to cool and more H_2O will be formed still able to cluster leaving relatively pure H_2O environments and bare regions of dust grain surfaces. These experiments

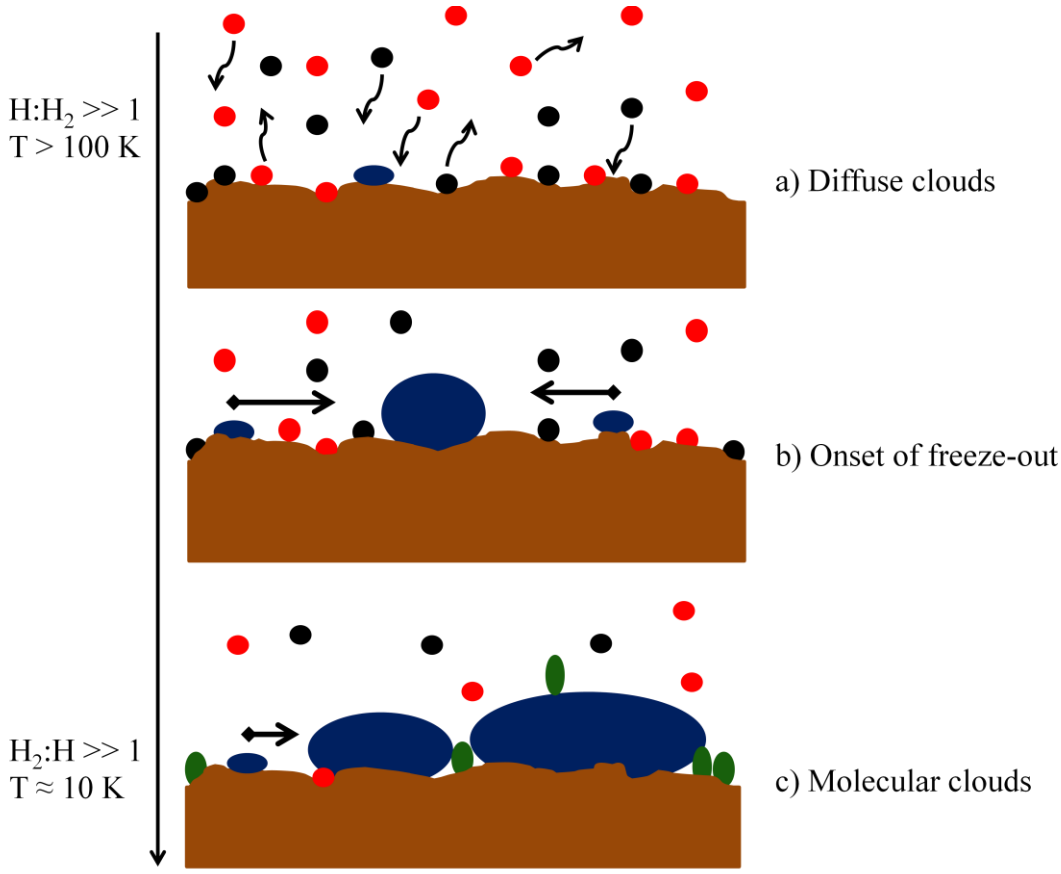

Figure 4.17: This cartoon represents the onset of H_2O cluster formation and the de–wetting process even at temperatures of 10 K on dust grains, brown substrate, in the cores of molecular clouds. The red circles are representative of O atoms, black circles are H atoms, blue ovals are H_2O molecules and green ovals are molecules of CO. This figure draws inspiration from [8].

therefore demonstrate that the Onion model will have to be revised. The typical idea of a dust grain coated with H_2O, sometimes estimated as about 100 ML [35] followed by

CO does not match the experimental data in this work. Bare dust grain surfaces will be available for other molecules, such as CO, to interact with, this interaction can be stronger and therefore CO could be desorbed less efficiently from bare dust grain surfaces. Astronomical models will also need to reflect this as the binding energies of other molecules can be different when adsorbing to the dust grain surface, SiO_2, as compared to H_2O.

4.6 References

[1] G. Filacchione, M.C. De Sanctis, F. Capaccioni, A. Raponi, F. Tosi, M. Ciarniello, P. Cerroni, G. Piccioni, M.T. Capria, E. Palomba, G. Bellucci, S. Erard, D. Bockelee–Morvan, C. Leyrat, G. Arnold, M.A. Barucci, M. Fulchignoni, B. Schmitt, E. Quirico, R. Jaumann, K. Stephan, A. Longobardo, V. Mennella, A. Migliorini, E. Ammannito, J. Benkhoff, J.P. Bibring, A. Blanco, M.I. Blecka, R. Carlson, U. Carsenty, L. Colangeli, M. Combes, M. Combi, J. Crovisier, P. Drossart, T. Encrenaz, C. Federico, U. Fink, S. Fonti, W.H. Ip, P. Irwin, E. Kuehrt, Y. Langevin, G. Magni, T. McCord, L. Moroz, S. Mottola, V. Orofino, U. Schade, F. Taylor, D. Tiphene, G.P. Tozzi, P. Beck, N. Biver, L. Bonal, J–Ph. Combe, D. Despan, E. Flamini, M. Formisano, S. Fornasier, A. Frigeri, D. Grassi, M.S. Gudipati, D. Kappel, F. Mancarella, K. Markus, F. Merlin, R. Orosei, G. Rinaldi, M. Cartacci, A. Cicchetti, S. Giuppi, Y. Hello, F. Henry, S. Jacquinod, J.M. Reess, R. Noschese, R. Politi and G. Peter, *Nature*, 2016, **529**, 368

[2] M.P. Collings, V.L. Frankland, J. Lasne, D. Marchione, A. Rosu–Finsen and M.R.S. McCoustra, *Mon. Not. Roy. Astron. Soc.*, 2015, **449**, 1826

[3] H.J. Fraser, M.P. Collings and M.R.S. McCoustra, *Mon. Not. Roy. Soc.*, 2001, **327**, 1165

[4] D.R. Haynes, N.J. Tro and S.M. George, *J. Chem. Phys.*, 1992, **96**, 8502

[5] R.J. Speedy, P.G. Debenedetti, R.S. Smith, C. Huang and B.D. Kay, *J. Chem. Phys.*, 1996, **105**, 240

[6] G.A. Kimmel, K.P. Stevenson, Z. Donhalek, R.S. Smith and B.D. Kay, *J. Phys., Chem.*, 2001, **114**, 5284

[7] T.W. Hartquist and D.A. Williams, *The Chemically Controlled Cosmos* (Cambridge University Press, Cambridge, 1995)

[8] D. Marchione, *Ph.D. Thesis* (Heriot–Watt University, Edinburgh, 2015)

[9] D. Marchione, A.G.M. Abdulgalil, A. Rosu–Finsen, and M.R.S. McCoustra, In Preparation

[10] A.B Horn and J. Sully, *J. Chem. Soc. Faraday Trans.*, 1997, **93**, 2741

[11] P. Ehrenfreund, A. Boogert, P. Gerakins and A.G.G.M. Tielens, *Faraday Discuss.*, 1998, **109**, 463

[12] L.J. Allamandola, M.P. Bernstein, S.A. Sandford and R.L. Walker, *Space Sci. Rev.*, 1999, **90**, 219

[13] E. Dartois, *Space Sci. Rev.*, 2005, **119**, 293

[14] W. Hagen, A.G.G.M. Tielens and J.M. Greenberg, *Chem. Phys.*, 1981, **56**, 367

[15] J.P. Devlin and V. Buch, *J. Phys. Chem.*, 1991, **94**, 4091

[16] J.P. Devlin and V. Buch, *J. Phys. Chem.*, 1995, **99**, 16534

[17] J.A. Noble, C. Martin, H.J. Fraser, P. Roubin and S. Coussan, *J. Phys. Chem. C*, 2014, **118**, 20488

[18] P. Ehrenfreund, P.A. Gerakines, W.A. Schutte, M.C. van Hemert and E. F. van Dischoeck, *Astron. Astrophys.*, 1996, **312**, 263

[19] S.S. Xantheas and T.H. Dunning Jr., *J. Chem. Phys.*, 1993, **99**, 8774

[20] H.E. Avery and D.J. Shaw, *Basic Physical Chemistry Calculations, 2nd Edition* (Butterworth–Heinemann Ltd., Oxford, 1980)

[21] J.A. Noble, E. Congiu, F. Dulieu and H.J. Fraser, *Mon. Not. R. Astron. Soc.*, 2012, **421**, 768

[22] J.K. Nørskov, F. Studt, F. Abild–Pedersen and Thomas Bligaard, *Fundamental Concepts in Heterogenous Catalysis* (Wiley, Hoboken, 2014)

[23] L. Pauling, *The Nature of the Chemical Bond and the Structure of Molecules and Crystals: An Introduction to Modern Structural Chemistry, 3rd edition* (Cornell University Press, Cornell, 1960)

[24] P. Atkins and J. de Paula, *Atkins' Physical Chemistry*, 7th E*dition* (Oxford University Press, Oxford, 2002)

[25] P. Jenniskens and D.F. Blake, *Science*, 1994, **265**, 753

[26] R.S. Smith, C. Huang, E.K.L. Wong and B.D. Kay, *Phys. Rev. Lett.*, 1997, **79**, 909

[27] P. Jenniskens, D.F. Blake, M.A. Wilson and A. Pohorille, *Astrophys. J.*, 1995, **455**, 389

[28] U. Raut, B.D. Teolis, M.J. Loeffler, R.A. Vidal, M. Fama and R.A. Baragiola, *J. Chem. Phys.*, 2007, **126**, 244511

[29] A.H. Narten, C.G. Venkatesh and S.A. Rice, *J. Chem. Phys.*, 1976, **64**, 1106

[30] Q.–B. Lu, T.U. Madey, L. Parenteau, F. Weik and L. Sanche, *Chem. Phys. Lett.*, 2001, **342**, 1

[31] P.C. Cosby, *J. Chem. Phys.*, 1993, **98**, 9560

[32] A.S. Bolina, A.J. Wolff and W.A. Brown, *J. Phys. Chem. B*, 2005, **109**, 16836

[33] S. Viti and D.A. Williams, *Mon. Not. Roy. Astron. Soc.*, 1999, **305**, 755

[34] A.G.G.M Tielens, *Rev. Mod. Phys.*, 2013, **85**, 1021

[35] H.M. Cuppen and E. Herbst, *Astrophys. J.*, 2007, **668**, 294

[36] T.J. Millar and D.A. Williams, *Astrophys. Space Sci.*, 1977, **48**, 379

[37] R.B. Larsson, *The Structure and Content of Molecular Clouds – 25 Years of Molecular Radioastronomy* (Springer, Berlin Heidelberg, 1994)

[38] D.H. Wooden, S.B. Charnley and P. Ehrenfreund, *Comets II* (University of Arizona, Tucson, 2004)

[39] T.J. Millar and D.A. Williams, *Dust and Chemistry in Astronomy* (Institute of Physics Publishing Bristol and Philadelphia, 1993)

[40] A.G.M.A. Abdulgalil, *Ph.D. Thesis* (Heriot–Watt University, Edinburgh, 2013)

[41] S. Sasaki, K. Nakamura, Y. Hamabe, E. Kurahashi and T. Hiroi, *Nature*, 2001, **410**, 555

[42] E. Murray, J. Prasad, H. Cabibil and J.A. Kelber, *Surf. Sci.*, 1994, **319**, 1

[43] M.P. Collings, J.W. Dever, H.J. Fraser and M.R.S. McCoustra, *Astron. Space Sci.*, 2003, **285**, 633

[44] K.M. Pontoppidan, H.J. Fraser, E. Dartois, W.–F. Thi, E.F. van Dishoeck, A.C.A. Boogert, L. d'Hendecourt, A.G.G.M. Tielens, S.E. Bisschop, *Astron. & Astrophys.*, 2003, **408**, 981

[45] H.M. Cuppen, E.M. Penteado, K. Isokoski, N. van der Marel and H. Linnartz, *Mon. Not. Roy. Astron. Soc.*, 2011, **417**, 2809

[46] M.P. Collings, J.W. Dever and M.R.S. McCoustra, *Phys. Chem. Chem. Phys.*, 2014, **16**, 3479

Chapter 5

The Spontelectric Effect

Contents of this chapter

5.1 Introduction

5.1.1 The Spontelectric Effect

The introduction mentioned interstellar dust grain charging and, in brief, the spontelectric effect of dipolar molecules. **Chapter 2** delved further into how direct measurements of the spontelectric effect are carried out at Aarhus University and the model developed by David Field explaining the experimental results. This chapter will describe the characteristics of the spontelectric effect as also found in references [1–8] and its relevance to this thesis and the astronomical community.

The study of the surface potential created by spontelectric molecules and the spontelectric effect itself is a new area of research, for that reason there are some outstanding questions. One of these questions regards the origin of the effect. This is not yet known, however what is known is that it is a bulk effect arising after a certain number of ML of material is deposited onto a surface [1]. The specific number of ML depends on the molecule investigated. The characteristics of spontelectric films as determined through experimental observations have been listed below [1];

- Deposition of certain dipolar molecules leads to a spontaneous and measureable surface potential which can reach several volts;
- The surface potential increases linearly with increasing film thickness. This potential will be positive or negative depending on the end of the dipolar molecule at the film–to–vacuum interface;
- Long–range (or non–local) interactions between spontelectric molecules lead to a measured surface potential;
- The measured surface potential is independent of the substrate;
- However, the spontelectric effect is dependent on the nature of the spontelectric molecule and temperature of the sample;
- Warming (or annealing) a typical spontelectric film leads to a irreversible decrease in the measured surface potential. Changing the temperature at which the film is deposited brings a greater irreversible reduction to the surface potential as compared to annealing;
- Above a certain temperature, termed the Curie point, the surface potential drops to zero;

These observations lead to the idea that the surface potential arises from the bulk effect of the spontelectric molecules from the sample–to–film interface to the film–to–vacuum interface. An example of effect of the molecular film thickness and deposition temperature has been shown in **Figure 5.1** [1].

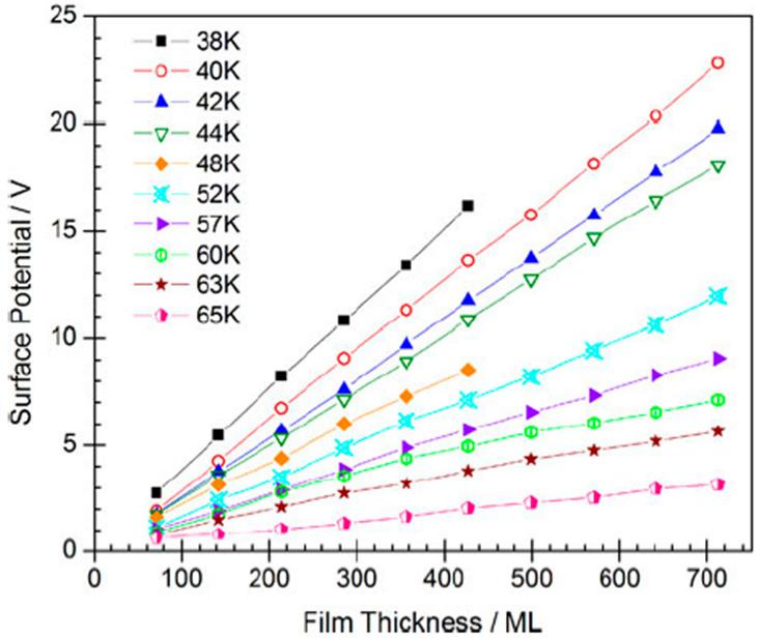

Figure 5.1: This figure shows how the surface potential varies proportionately with amount of N_2O. A decrease in the potential is observed as the deposition temperature rises. At temperatures above 65 K, N_2O does not stick effectively to the gold surface under UHV conditions and no measurements are made [1].

As the molecules are deposited, the species are believed to spontaneously adjust their orientation to adopt more thermodynamically unfavoured positions as illustrated in **Figure 5.2 (B)**. However, if intermolecular forces are too great for the spontelectric state to cope with, no surface potential is observed.

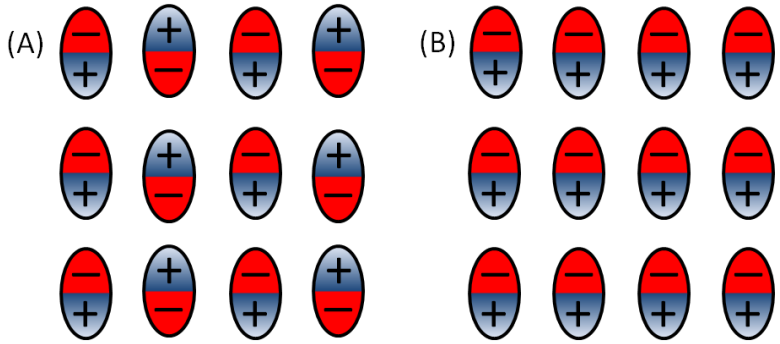

Figure 5.2: This cartoon illustrates the thermodynamically most favoured structure for a dipolar molecular solid **(A)** and the likely molecular orientation in the spontelectric phase **(B)**.

As the temperature of the dipolar films is increased the potential decreases [1]. This is likely caused by thermal perturbation of the dipolar alignment in the films. This supply of thermal energy could lead to the thermodynamically favoured structure as seen in **Figure 5.2 (A)** as compared to the believed molecular orientation as seen in **(B)**. This is the case for all molecules save the anomalous case of methyl formate where the surface potential has been observed to increase with increasing temperature until its Curie point is reached [5].

5.1.2 RAIRS and the Spontelectric Effect

One way to investigate molecules in a solid film is to employ the technique of infrared (IR) spectroscopy, in the case of this work, specifically reflection–absorption infrared spectroscopy (RAIRS). For the time being, only dipolar molecules have been investigated with regards to the spontelectric effect, meaning molecules investigated will not be IR inactive.

If we consider thermal perturbation of dipole orientation leading from the spontelectric structure seen in **Figure 5.2 (B)** to a non–spontelectric state and more favoured structure of **(A)**, then changes in the IR bands must become visible. Such orientational changes have been studied by other research groups, for instance the work of Jones and Swanson [9] which has yielded **Equation 1**;

$$\nu_{LO}^2 - \nu_{TO}^2 = \frac{4\pi}{\varepsilon V} \times \left(\frac{\partial \mu}{\partial q}\right)^2 . \qquad \textbf{Equation 1}$$

This equation correlates the frequencies of the longitudinal optical (ν_{LO}) and transverse optical (ν_{TO}) modes to the degree of dipole alignment ($\partial\mu/\partial q$) through a factor of the unit cell volume (V) and the relative permittivity (ε).

As discussed in **Chapter 2**, RAIRS is one of the analytical techniques which can be employed to study molecular films on the SiO_2 surface. **Chapter 2** also discussed the LO–TO splitting which is presented in **Equation 1** where the splitting is related to the dipole alignment which itself is related to the spontelectric effect. Therefore, RAIRS can be used as an indirect probe to study the dipole alignment of spontelectric molecules through the LO–TO splitting. This splitting has also been observed for a

variety of molecules both with a permanent dipole moment, such as N_2O [9–11] and CO [12], and molecules with induced dipoles moments such as CO_2 [13], CF_4 [14].

Up until this point of this thesis, an investigation into one of the H_2O formation pathways has been studied. H_2O will slowly build up on a dust grain, however initially only small quantities will be found on the surface. Isolated H_2O molecules and small clusters have been shown to move at cryogenic temperature as shown in this thesis. As the icy mantle covering a dust grain grows, sub–monolayer amounts of ice become multilayer amounts. Now, light will be cast upon these solid films of multilayer ice as found in the dark clouds of interstellar clouds. As already observed in **Chapter 4**, the H_2O band is very broad and even though an LO–TO splitting has been discussed as being present in H_2O films [15–17], these films are not analysed here since observations of the splitting is difficult. However, the second most abundant molecule in interstellar ice is CO which has a permanent dipole. Initially, though, a study of N_2O must be conducted to illustrate how the spontelectric effect of molecules can be studied without direct surface potential measurements. Therefore, this chapter will outline how reflection–absorption infrared spectroscopy (RAIRS) can be used as an indirect measure of the spontelectric effect.

5.2 Experimental

The overall capabilities of the UHV equipment have been explained in **Chapter 2**, however, a brief outline of the steps taken to produce the results shown in this chapter will be supplied here. Temperature programmed desorption (TPD) was used to a small extent to determine the number of monolayers (ML) deposited onto the 300 nm SiO_2 layer coating the Cu sample block. These experiments were done with an average heating rate of 0.6 K s^{-1} for N_2O (Sigma–Aldrich, purity ≥ 99.998%) and 0.3 K s^{-1} for CO (BOC, purity ≥ 99.9%) desorption. Ionisation coefficients in the ion gauge head of 1.2, 1 and 1 were taken into account when dosing N_2O, CO and H_2O, respectively [18]. Reflection–absorption infrared spectroscopy (RAIRS) was the main analytical method used to investigate the deposited films with a grazing incidence of 75^o and collected by the liquid nitrogen cooled MCT detector. A total of 512 scans were collected with a resolution of 1 cm^{-1} and 0.1 cm^{-1} for the N_2O and CO experiments, respectively.

5.3 Results and Discussion

In this section, results from experiments of N_2O deposited onto SiO_2 will first be reported. Temperature programmed desorption (TPD) will be employed first to determine when a multilayer is present on the surface. Then 100 L of N_2O (equivalent to 14 monolayer (ML)) will be deposited onto SiO_2 and reflection–absorption infrared spectroscopy (RAIRS) will be used to study the LO–TO splitting of the ν_{NN} feature as the temperature (both annealing and deposition temperatures) is increased. Next the same procedure will be done for CO on SiO_2 where a 5 ML film will be studied with RAIRS. Following this, 20 ML CO on different H_2O surfaces will be studied. The types of H_2O used are porous amorphous solid water (p–ASW), compact amorphous solid water (c–ASW) and crystalline solid water (CSW). As will become apparent throughout this section, the relative ML coverage is not important as long as the LO–TO splitting is observable in the multilayer films.

5.3.1 Multilayer N_2O Films

As explained in the introduction of this chapter, **Section 5.1**, N_2O is the model spontelectric molecule which is the reason for this being the initial test molecule to determine the spontelectric effect as observed through reflection–absorption infrared spectroscopy (RAIRS). The figures in this section can also be found in Lasne *et al.* [19].

Initially, temperature programmed desorption (TPD) experiments were conducted to determine the coverage equivalent to one monolayer (ML) of N_2O, following this a multilayer will be deposited onto the SiO_2 surface for RAIRS studies. The results of the TPD experiment can be seen in **Figure 5.3**.

As can be seen in **Figure 5.3**, the monolayer is formed after depositing 7 L of N_2O. The peak temperature of desorption in the multilayer is 72.7 K to 73.7 K (± 0.3 K) which corresponds well with other experiments on multilayer N_2O desorption where a temperature of 75 K ± 5 K has been stated [20]. The higher temperature bumps relate to the more favourable binding sites of N_2O to SiO_2 in the sub–monolayer regime. Desorption kinetics have not been analysed as the focus of this experiment was to determine when N_2O is found to be a multilayer on SiO_2.

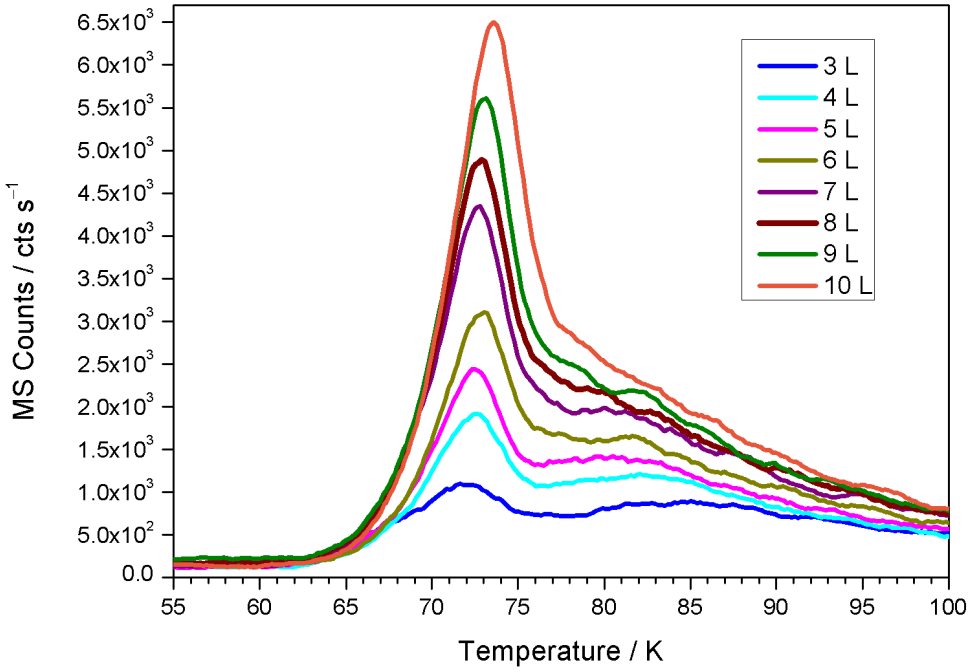

Figure 5.3: This figure shows the TPD results of depositing various amounts of N_2O onto SiO_2 and desorption of the molecular films. N_2O detected as m/z = 44 is recorded as a function of temperature of the substrate. As can be seen, a clear change is observed between 6 L and 7 L which is the change between the sub–monolayer and the multilayer regimes as explained in **Chapter 2**.

As the spontelectric effect is a bulk effect and a multilayer is required for a surface potential to be measured, a film thickness corresponding to 100 L (about 14 ML) will be used for the RAIRS experiments. This means the splitting should be observed at this film thickness. In **Figure 5.4** [19], the LO–TO splitting is indeed apparent.

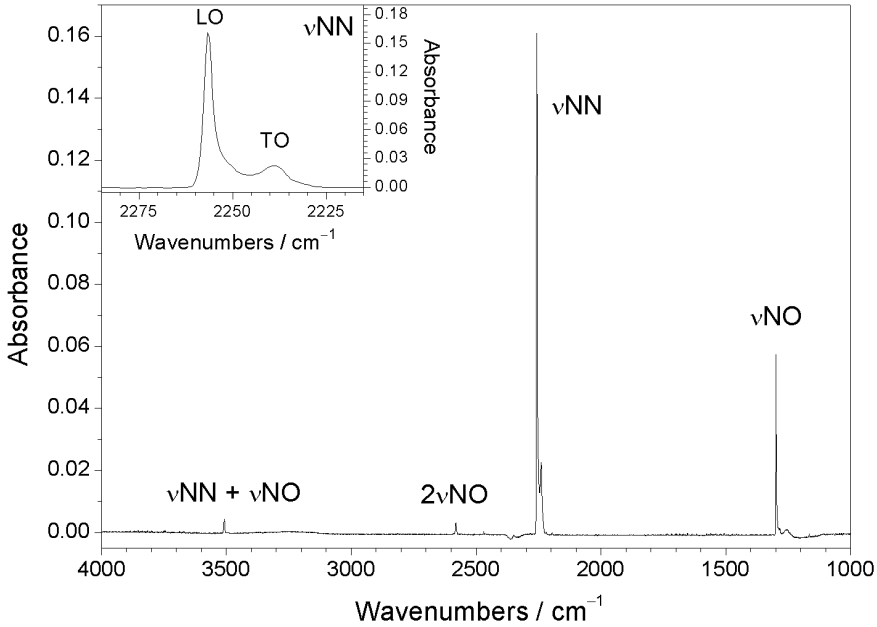

Figure 5.4: This figure shows the full range of the spectrum obtained when having deposited 14 ML N_2O onto SiO_2 at 50 K. The peaks of interest at about 2250 cm^{-1} have been highlighted in the insert [19].

As can be seen in the **Figure 5.4**, the *ν*NN mode is the dominant mode when compared to the other modes observed, such as *ν*NO, in the IR spectrum centred at roughly 2250 cm^{-1}, or more precisely at 2256 ± 1 cm^{-1} and 2239 ± 1 cm^{-1} for the LO and TO modes, respectively. The peak position and its LO–TO splitting has already been of interest for other research groups [10–12] and will also be used in this work due to its clarity and intensity. As explained in **Section 5.1**, the spontelectric effect decreases for N_2O as the temperature increases, be it annealing or deposition temperature. Also, as per **Equation 1**, the degree of LO–TO splitting is proportional to the dipole order in a solid [9]. Thereby, supplying thermal energy to the 14 ML film will lead to thermal disorder of the dipole ordering, meaning less order of the dipoles and a decrease of the LO–TO splitting. The first step is to investigate IR peak position with respect to N_2O amount to ensure any shifts are not caused by the N_2O film thickness. This has been displayed in **Figure 5.5**.

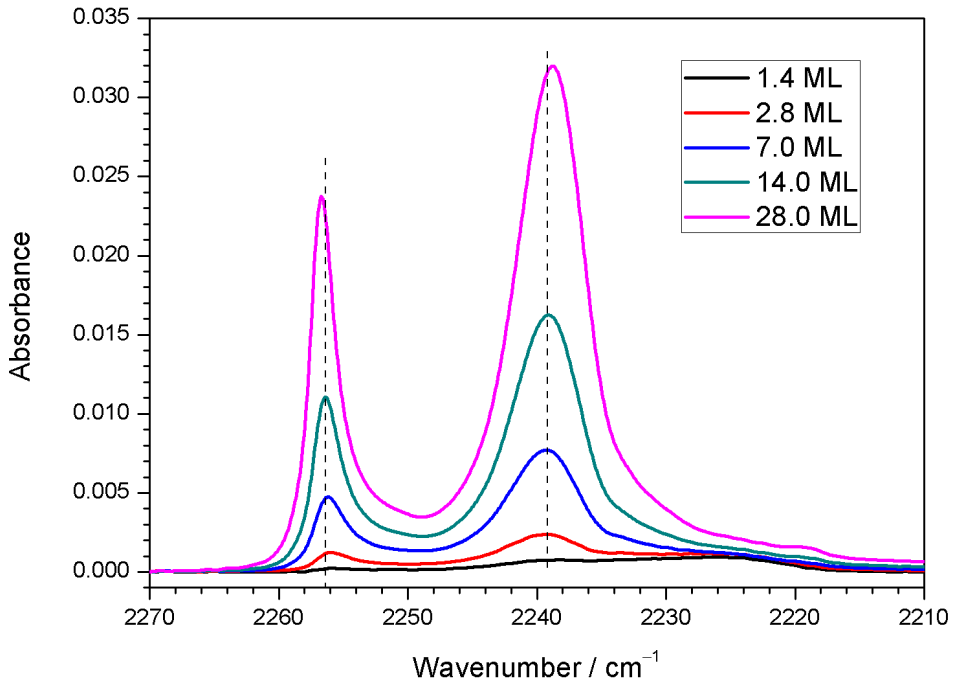

Figure 5.5: This figure indicates that changing the amount of N_2O from 1.4 ML to 28 ML has little bearing on the peak positions. The N_2O films were deposited at 50 K to ensure the sharp features of the LO–TO splitting. The dashed lines are a guide to the eye to show peak shifts as compared to the centre of the peak of the 14 ML N_2O spectrum.

From **Figure 5.5**, one can see that the LO–TO splitting changes slightly with film thickness. The uncertainty of background dosing is large (about 20%) meaning that a film of 7 or 28 ML N_2O is not expected as this would be half or double of 14 ML. The

RAIR spectra of 7 ML N_2O shows LO and TO mode peak positions at 2256 ± 1 cm^{-1} and 2239 ± 1 cm^{-1}, respectively, and 2257 ± 1 cm^{-1} and 2239 ± 1 cm^{-1} for the 28 ML amount. Therefore, considering the resolution of the experiment giving the uncertainty of 1 cm^{-1}, 14 ML of N_2O is used for the experiments described in the next sections can be regarded as not being dependent of film thickness. The effect and implication of molecular amount will be discussed in more detail later on in this chapter. This means change in the frequency of the peaks must be due to changes in the temperature. The effect of this can be seen in **Figure 5.6** for annealing.

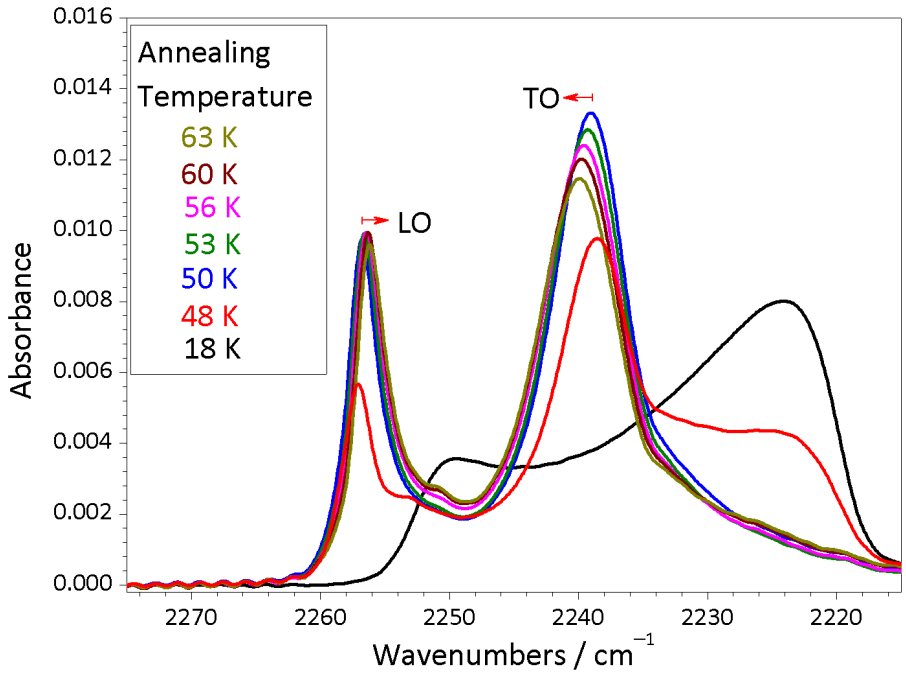

Figure 5.6: This figure shows 14 ML N_2O on SiO_2 being annealed from base temperature. The red arrows indicate the movement of the peaks as they shift with increasing temperature. N_2O deposited at 18 K is believed to be amorphous and the higher temperature spectra (>48 K) are crystalline. When the film is annealed to 48 K characteristics of both structural states can be observed.

As can be seen in **Figure 5.6**, increasing the temperature leads to a contraction of the LO–TO splitting and thereby as explained the dipole ordering decreases too. As this occurs the spontelectric effect diminishes. What can also be seen in **Figure 5.6** is a change in the band profile as the N_2O film is annealed past 48 K. This change is normally, in IR spectroscopy, associated with an amorphous to crystalline phase change in a molecular film as seen in, for instance, films of ethanol [21], vinylacetylene [22] and acetone [23] where peaks become more narrow due to a greater degree of structural order throughout a molecular film. However, as stated in Cassidy *et al.* [24] techniques such as neutron diffraction is a better way of clarifying the nature of the phase change.

Considering the sharp features of the observed N_2O bands and the ease with which a peak positions can be specified, this work will focus on molecular films as studied by RAIRS above 48 K. The surface potential decreases more rapidly if molecules are deposited at higher temperatures as compared to when a molecular film is annealed to the same temperature. For that reason 14 ML films of N_2O have also been deposited at a variety of temperatures as seen in **Figure 5.7** [19].

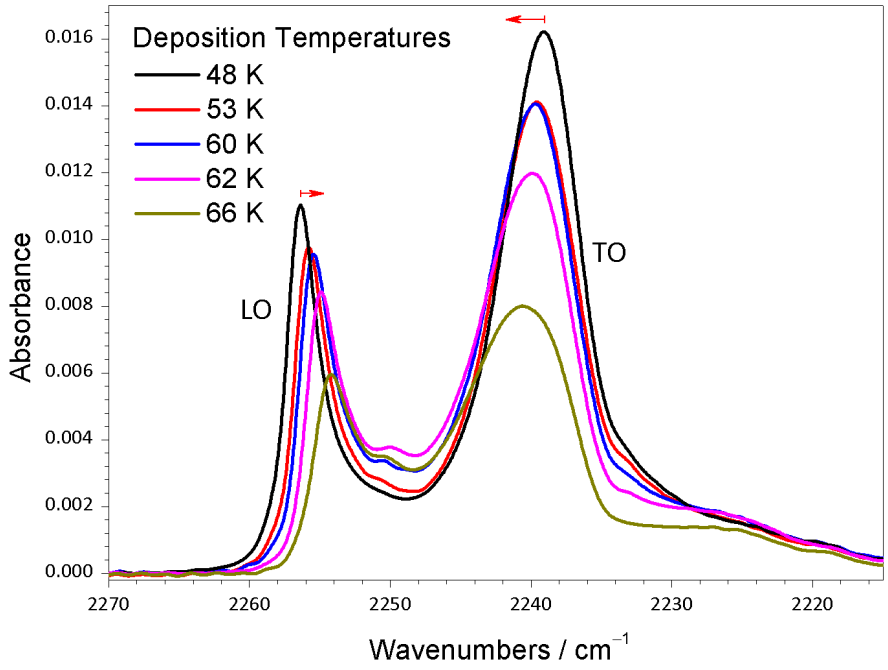

Figure 5.7: This figure shows the effect of changing the deposition temperature of 14 ML of N_2O. A greater contraction of the LO–TO splitting is observed as compared to **Figure 5.6**. To make the figure easier to read, only five experiments have been shown instead of the full range [19].

Figure 5.7 has been shown with only five different deposition temperature experiments (48, 53, 60, 62 and 66 K). However, a total of nine experiments were done also including 51, 52, 55 and 56 K which are not shown for clarity. As can be seen in **Figure 5.7**, the same trend is observed as witnessed in **Figure 5.6** where the LO–TO splitting contracts as the temperature of the sample increases. The LO–TO splitting contracts more as the deposition temperature is increased as compared to when the N_2O film is annealed. As explained earlier, this is also a characteristic of the spontelectric effect. The data in **Figure 5.7**, and the >48 K annealing data from **Figure 5.6**, has been fitted with Gaussians as was also done in **Chapter 3**. As explained in the experimental section of this chapter, the RAIR spectra for the N_2O experiments were conducted with a resolution of 1 cm^{-1}. However, fitting the data with Gaussians leads to a greater

accuracy of the peak positions, and therefore also the LO–TO splitting. The results of such fits can be seen in **Figure 5.8**.

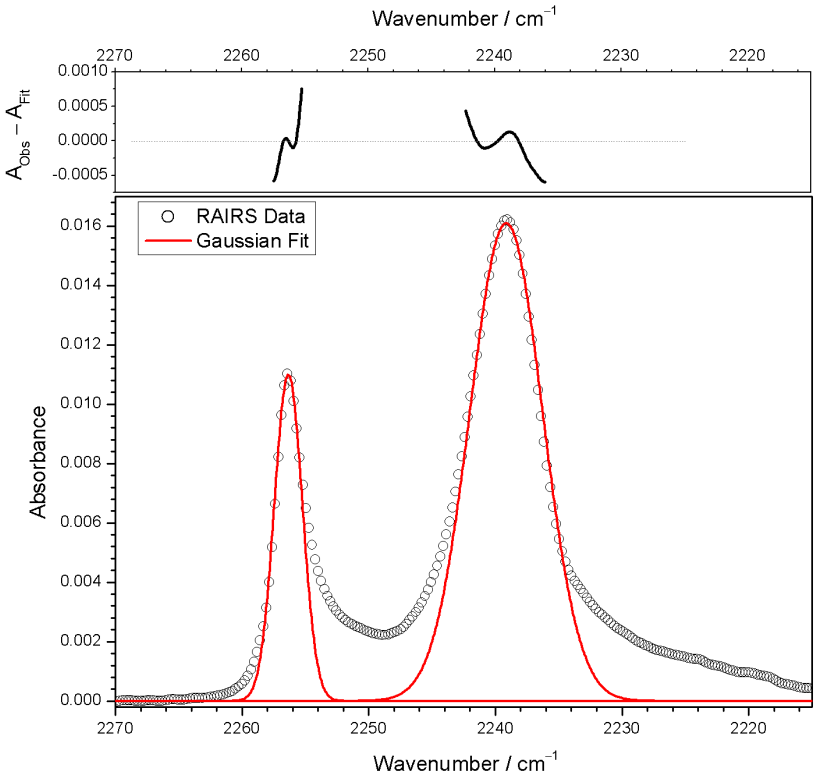

Figure 5.8: This figure shows the comparison between the experimental data (open circles), and the Gaussian fits (solid red line) to the LO–TO splitting of N_2O with the residuals shown in the box above the graph.

The Gaussian fits, as seen in **Figure 5.8**, was done to all >48 K experimental data of N_2O. The result of this means that the peak positions of the LO and TO modes can be stated to a greater degree of certainty, now ±0.1 cm^{-1} for the LO mode and ±0.2 cm^{-1} for the TO mode. The peak positions and LO–TO contractions for all N_2O experimental data shown in **Figure 5.6** and **5.7** have been detailed in **Table 5.1** and further displayed in **Figure 5.9** [19].

Annealing Temperature / K	**Wavenumber / cm^{-1}**		**Δ_{LO-TO} / cm^{-1}**
	LO (± 0.1 cm^{-1})	**TO (± 0.2 cm^{-1})**	
50	2256.8	2239.05	17.75
53	2256.6	2239.3	17.3
56	2256.4	2239.6	16.8
60	2256.3	2239.8	16.5
63	2256.2	2240.0	16.2

Deposition Temperature / K	Wavenumber / cm^{-1}		Δ_{LO-TO} / cm^{-1}
	LO (± 0.1 cm^{-1})	TO (± 0.2 cm^{-1})	
48	2256.35	2239.15	17.2
51	2255.9	2239.6	16.3
52	2255.8	2239.8	16.0
53	2255.8	2239.7	16.1
55	2255.3	2240.05	15.25
56	2255.3	2240.0	15.3
60	2255.4	2239.85	15.55
62	2254.9	2240.1	14.8
66	2254.2	2240.8	13.4

Table 5.1: This table shows the peak positions and the difference in the LO–TO splitting for the annealing data (upper section) and the different deposition temperature data (lower part) from **Figures 5.6** and **5.7**. Only data at ≥48 K have been included due to the more clearly defined peaks.

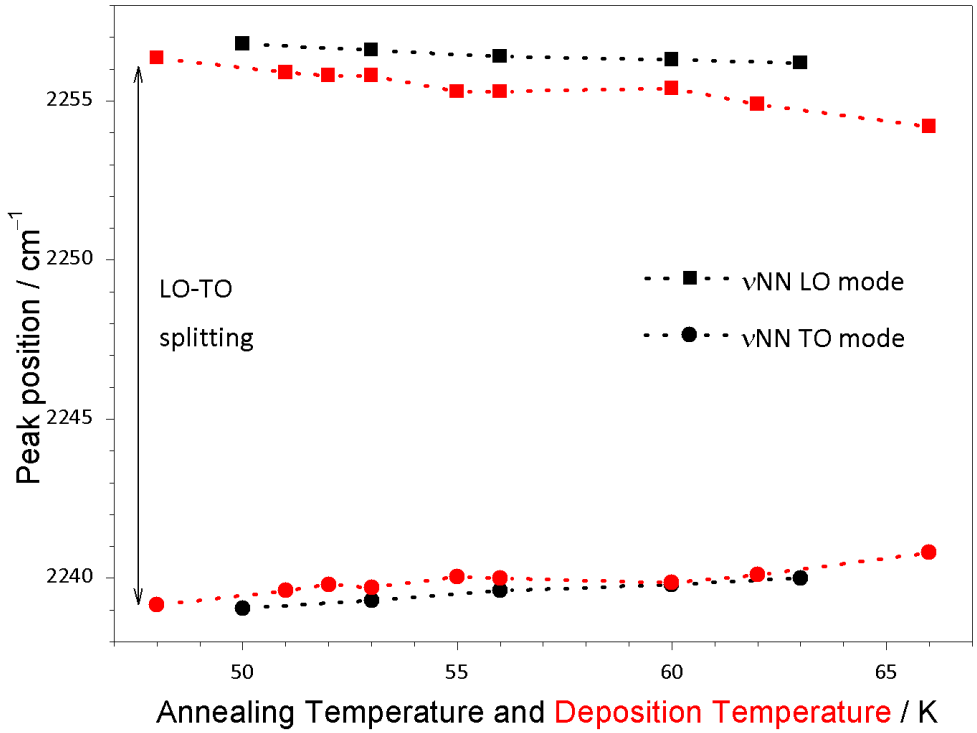

Figure 5.9: This figure shows the result of plotting the data outlined in **Table 5.1** where squares and dots correspond to the LO and TO peaks, respectively. Further to this, the black and red represent the annealing and deposition temperature experiments, respectively. As can be seen, a contraction occurs with increasing temperature, and greater so when the deposition temperature is increased [19].

Figure 5.9 has been created to better illustrate the effect of temperature on the LO–TO splitting. As can be seen, depositing a 14 ML film of N_2O at 18 K and annealing it to higher temperatures the splitting contracts as shown through the black data set. The same can be said for depositing the N_2O at different temperatures leading to a greater contraction which is seen with the red data points. The squares and dots are representative of the LO and TO modes of N_2O. As stated earlier, this is an indication of disorder of dipoles in the molecular film. Another method of look at the dipole alignment with RAIRS is to study the inhomogeneous broadening in a qualitative fashion as this broadening measures the range of environments a molecule finds itself in. To do this, and to be able to compare different experiments, means estimating the intensity at 2150 cm^{-1} (central position of the LO–TO splitting) and normalising by the entire integrated area of the feature. The results of this can be seen in **Figure 5.10** [19].

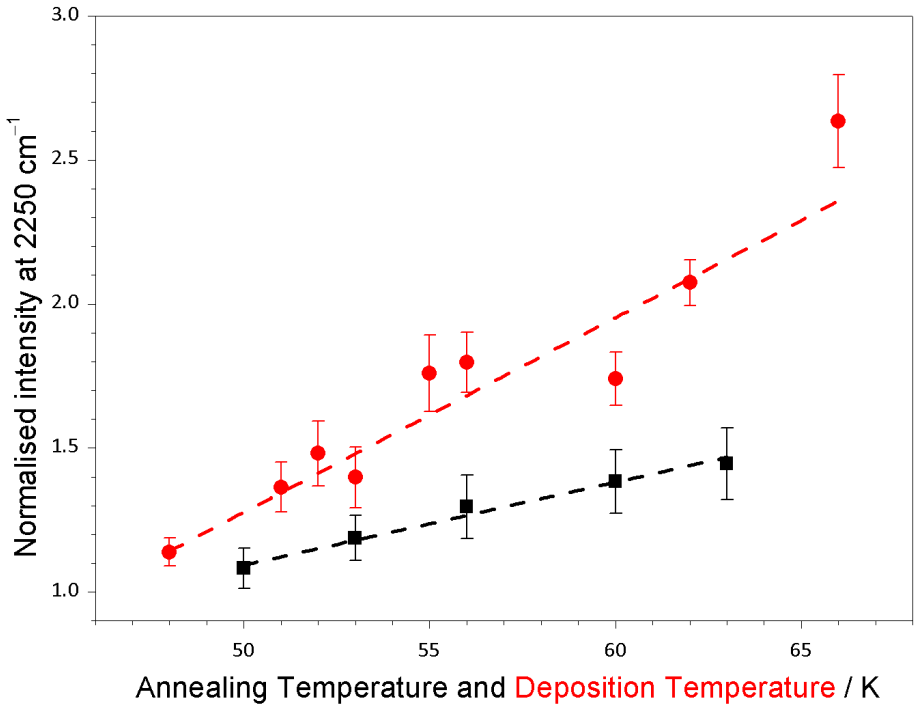

Figure 5.10: This figure shows the change in the inhomogeneous broadening of the LO–TO splitting of N_2O from the annealing experiment (black squares) and the different deposition experiments (red dots) [19]. The data points were calculated by measuring the intensity at 2150 cm^{-1} and normalising the data from **Figures 5.6** and **5.7**.

As the inhomogeneous broadening increases, so does the disorder of dipoles of a molecular film, this is what is observed in **Figure 5.10**. The difference in gradients of **Figure 5.10** is about 50% larger for the deposition temperature data as compared to the

annealing experiments. This is once again the same trend and characteristic of the spontelectric effect with regards to temperature effects on the surface potential.

With the presented data so far one can state that the LO–TO splitting and the inhomogeneous broadening behaves as expected for the prototypical spontelectric molecule of N_2O.

5.3.2 Spontelectric CO Films on SiO_2

Having demonstrated the potential of RAIRS to probe the spontelectric effect of N_2O, the thesis will now focus on the impact of the spontelectric effect in the astronomical environment. As this effect is a solid bulk effect, the nature of the solid state in such environments must be considered and this highlights the importance of interstellar dust grains and their icy mantles. As explained in **Chapter 1**, molecular clouds play host to a wide range of molecules of which H_2O is the dominant solid phase species [25 and references within]. Direct surface potential measurements of H_2O were conducted at Aarhus University, but no spontelectric effect was observed [1]. As a dipolar molecule, a surface potential could be expected to exist, but the strong H–bonding capability in solid H_2O is thought to overpower any spontelectric dipolar ordering. However, surface work function changes has been measured using a Kelvin probe which may indicate that a surface potential could be present on ballistically–deposited H_2O films at very low temperatures [26]. The O–H stretching frequency in the sub–monolayer regime was studied in **Chapter 4** where the LO–TO splitting was difficult to observe even though multilayer thick films were explored. For that reason monitoring shifts in the LO–TO splitting of H_2O multilayer films were not carried out. The attention of this thesis is therefore shifted onto the second most abundant solid state species, CO. The gas–phase dipole moment of CO (0.122 D) is similar to that of N_2O (0.167 D) and the C–O stretching frequency at about 2140 cm^{-1} and its LO–TO splitting [27] lie in a relatively clean part of the IR spectrum as there is no interference from gas–phase H_2O or CO_2. Initially, multilayer CO films directly adsorbed on amorphous SiO_2 will be studied.

As with the N_2O experiment, initial TPD experiments were conducted to convert units of Langmuir (L) to monolayer (ML). The results of this can be seen in **Figure 5.11**.

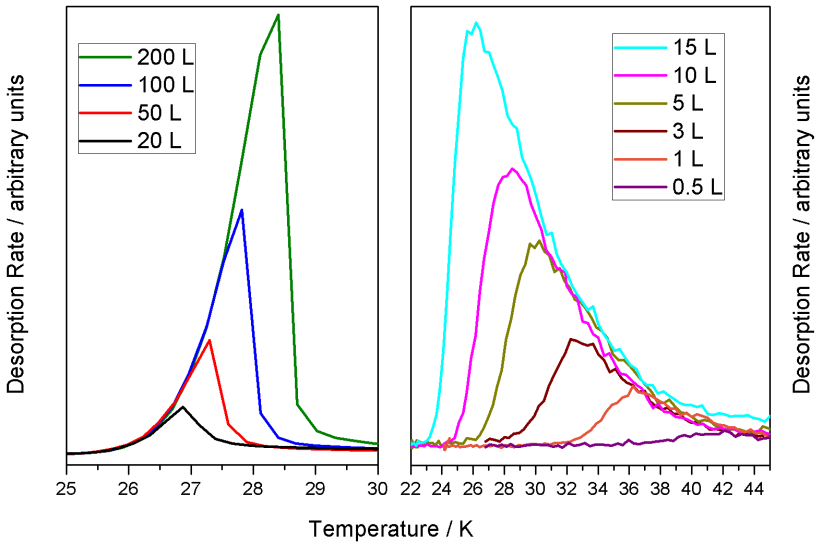

Figure 5.11: This figure shows the desorption of different CO coverages from SiO_2. As can be seen, a clear change in behaviour is observed between 15 L and 20 L indicating that this is the completion of the first monolayer.

As can be seen in **Figure 5.11**, a ML is formed after introducing 20 L of CO into the chamber. Only the monolayer to multilayer transition is of interest in this work and desorption kinetics have therefore not been analysed. However, another indication of

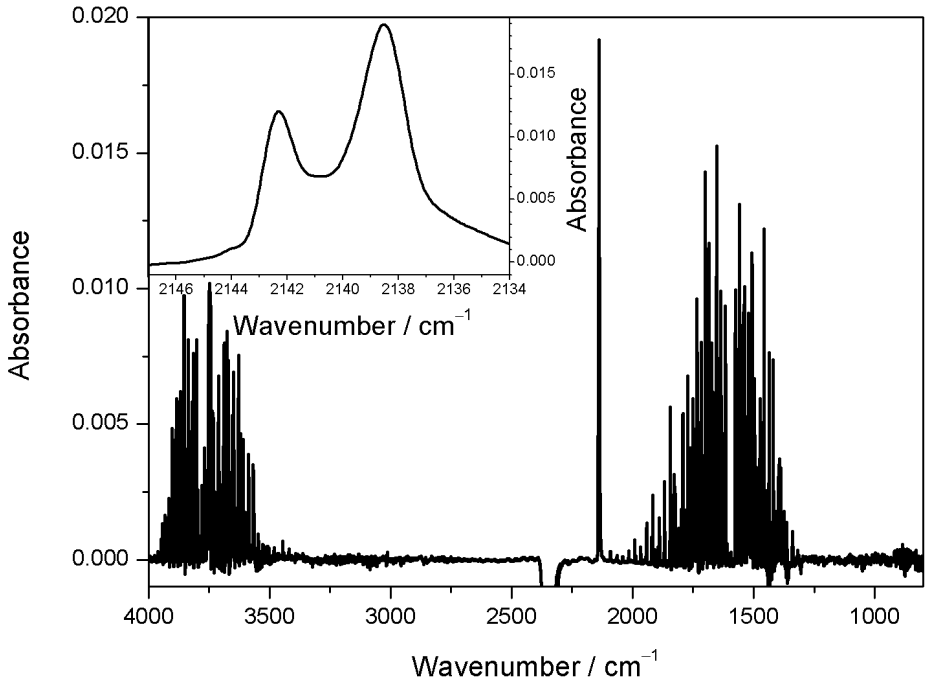

Figure 5.12: This figure shows the whole spectrum when depositing 5 ML of CO onto SiO_2 at 20 K. The feature of interest, the CO stretch, at about 2140 cm^{-1} has been highlighted in the insert to show the LO–TO splitting. The sharp bands at >3500 cm^{-1} and in the 1250–2000 cm^{-1} range are of gas–phase H_2O with the negative bands at about 2300 cm^{-1} being gas–phase CO_2 in the optics boxes outside of the UHV chamber [28].

this is the presence of the LO–TO splitting when studying the molecular film with RAIRS. Depositing 5 ML CO onto SiO_2 gives this LO–TO splitting as can be seen in **Figure 5.12** [28].

As can be seen in **Figure 5.12**, a clear LO–TO splitting is observable with a film thickness of 5 ML, there is also a certain degree of inhomogeneous broadening between the peaks. Once again, the 300 nm SiO_2 layer softens the MSSR and allows both the LO and TO modes to be observed. These peaks will be the focus in this section and the next. From the base temperature of these experiments (20 K) no phase change of the solid CO layer is observed until desorption. The next experiment was to see if the peaks observed in **Figure 5.12** change with film thickness. The results of this are displayed in **Figure 5.13**.

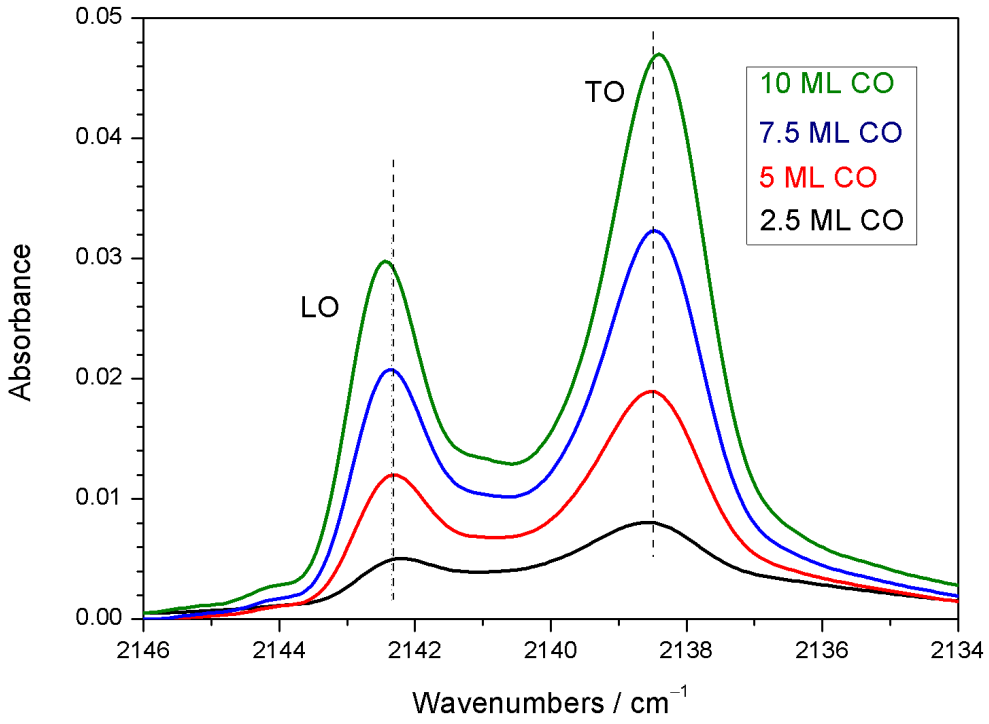

Figure 5.13: This data shows that as the amount of CO is increased from 2.5 ML to 10 ML a slight change above the spectrometer resolution is observed when the film thickness is doubled. However, considering the general uncertainty of background dosing being about 20%, the amount of molecules on the surface can be said to have no impact of the LO–TO peak positions.

Knowing that the thickness of the film has no impact on peak position when considering the uncertainty in background dosing (*i.e.* 5 ML ± 20 %), a 5 ML film of CO was annealed from 20 K to 22 K to 24 K to 26 K leading to the data displayed **Figure 5.14**.

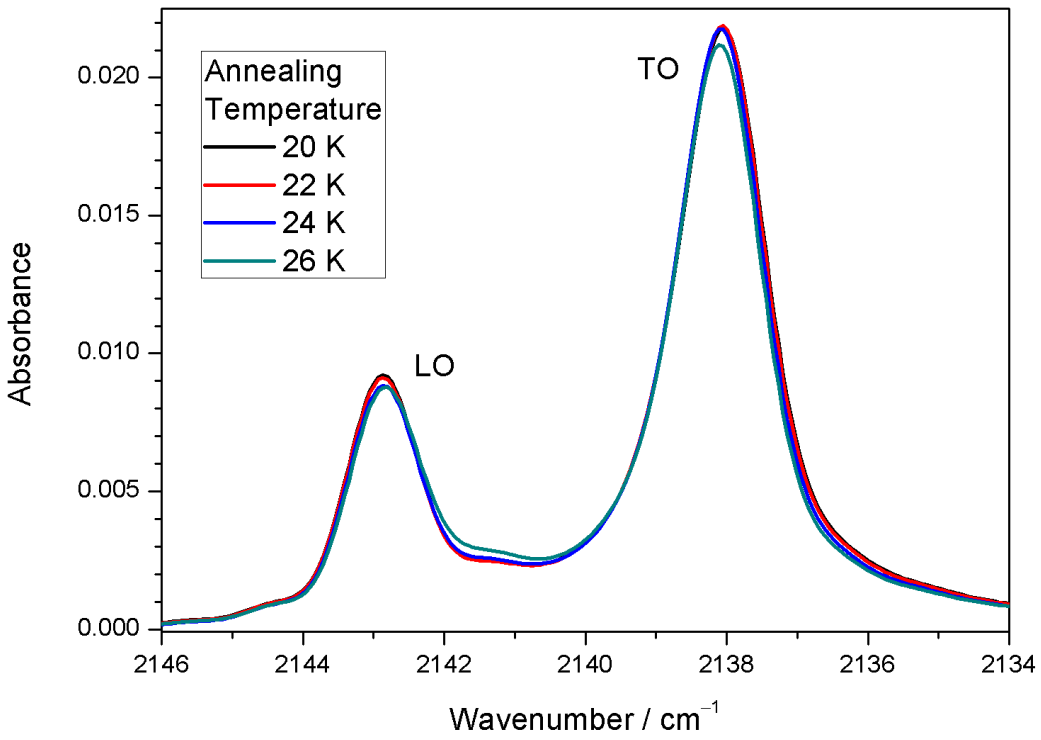

Figure 5.14: This shows the LO–TO splitting as the 5 ML CO film is annealed from 20 K to 26 K. Observing shifts of the peaks over the resolution of the spectrometer is impossible.

No contraction or expansion of the LO–TO splitting is observed in **Figure 5.14** during annealing of a 5 ML CO film at a resolution of 1 cm^{-1}. Due to the lack of observable changes, the spectrometer resolution was increased to 0.1 cm^{-1}, however further annealing experiments of CO films were not conducted. The reason for this is the increased effect of deposition temperature of measured surface potentials, and the following figures will therefore be of 0.1 cm^{-1} RAIR scans with different deposition temperatures. Due to the cooling power of the cryostat, a lower base temperature cannot be obtained, however there seems to be no LO–TO shifts at temperatures below 20 K [29]. Further to the temperature constraints of these experiments, the TPD experiment indicates that 26 K is the highest possible temperature before desorption of the multilayer from SiO_2 ensues. Having said this, a decrease in intensity is observed in **Figure 5.14** when the 5 ML CO film is annealed to 26 K. However, as explained in **Section 5.3.1**, annealing a spontelectric film will lead to less of a change in the IR spectrum as compared to changing the deposition temperature. Therefore CO was deposited at variety of temperatures in order to investigate the possible spontelectric properties of CO films, the results of the deposition temperature experiments can be seen in **Figure 5.15** [28].

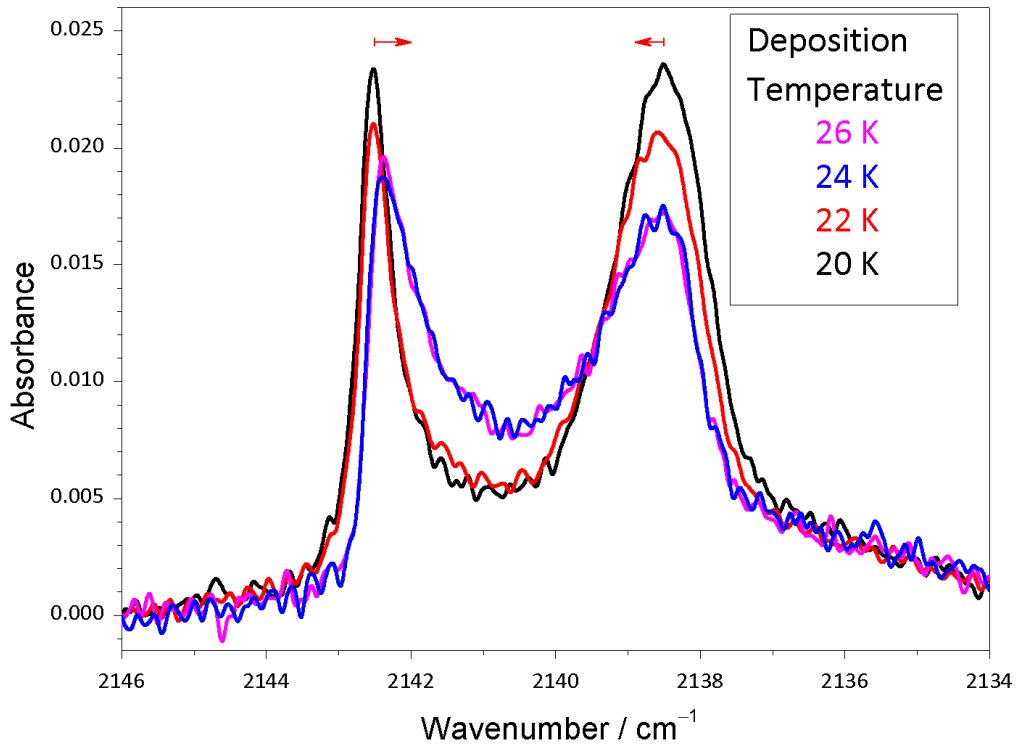

Figure 5.15: This figure shows the results of depositing 5 ML CO onto SiO_2 at different temperatures. A slight shift in the LO–TO splitting of the νCO band is now observed which is greater than the resolution of the spectrometer (0.1 cm^{-1}) [28].

As can be seen in **Figure 5.15**, a contraction of the LO–TO splitting is now observed as the deposition temperature is increased, again showing that the deposition temperature has a greater effect on frequency shifts as compared to annealing. This, as previously explained, is an indication of a spontelectric material as measured through the surface potential in Aarhus and through the use of RAIRS of N_2O as in **Section 5.3.1**. This contraction although slight in the temperature range possible for these experiments is still greater than the 0.1 cm^{-1} resolution of the spectrometer. These spectra were fitted with Gaussians as the N_2O peaks were in **Section 5.3.1** and an example of this has been shown in **Figure 5.16**.

Fitting the other CO spectra with Gaussians means that the peak position can be quoted to a greater degree of certainty. The errors in the peaks can now be estimated as 0.01 cm^{-1} and 0.02 cm^{-1} for the LO and TO mode, respectively, an increased accuracy of an order of magnitude. **Table 5.2** has been constructed to display the data from the deposition experiments (annealing data has not been fitted with Gaussians due to the lack of frequency shifts, and therefore not shown in **Table 5.2**).

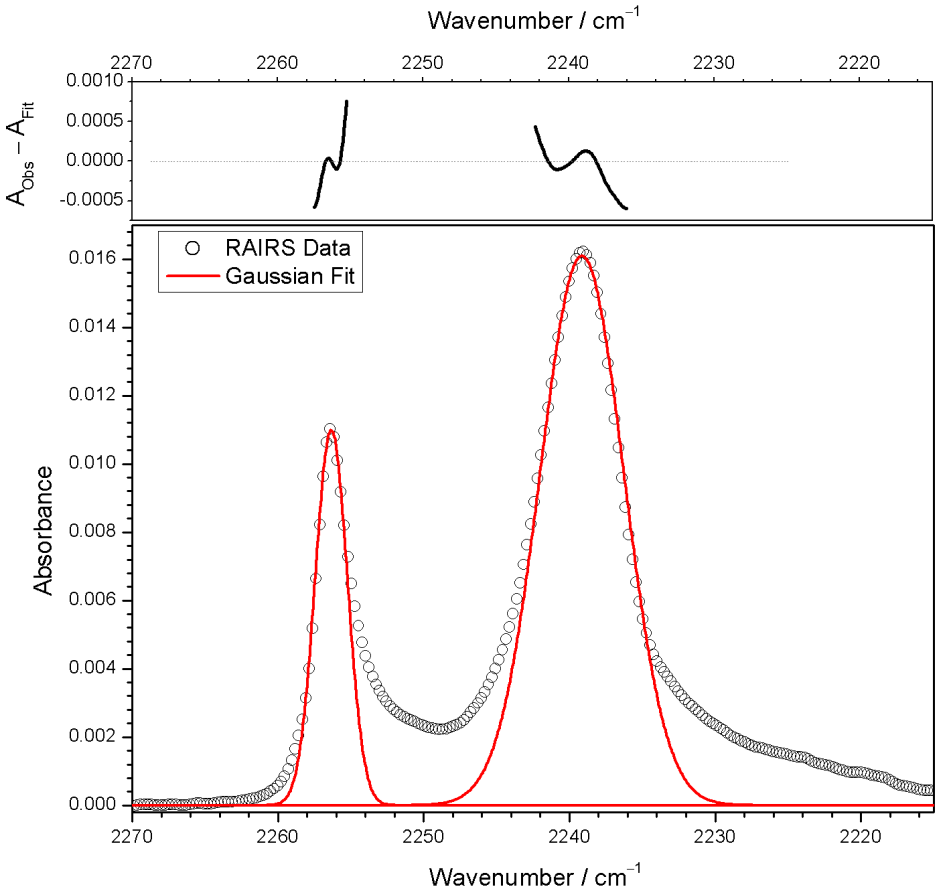

Figure 5.16: This figure shows the comparison between the experimental RAIRS data of the νCO band of 5 ML CO on SiO_2 at 20 K and the fit with Gaussians with the residuals shown above the data and fit.

Deposition Temperature / K	**Wavenumber / cm^{-1}**		**Δ_{LO-TO} / cm^{-1}**
	LO (± 0.01 cm^{-1})	**TO (± 0.02 cm^{-1})**	
20	2142.52	2138.50	4.02
21	2142.51	2138.55	3.96
22	2142.48	2138.58	3.9
24	2142.41	2138.62	3.79
26	2142.38	2138.63	3.75

Table 5.2: This table produces a more clear sight of the peak shifts of CO as the deposition temperature changes. A contraction is observed which is indicative of a spontelectric material.

The data in **Table 5.2** shows a contraction of the LO–TO splitting as calculated in the last column. This contraction has also been graphed in **Figure 5.17** [28] of the LO and TO position with respect to deposition temperature.

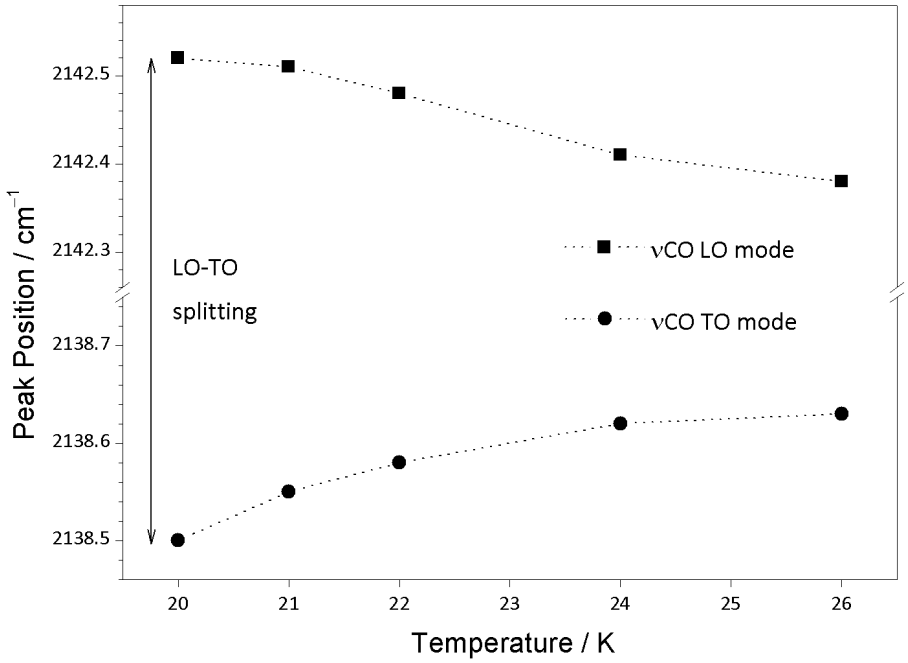

Figure 5.17: This figure shows the position of the LO and TO modes of the νCO band of 5 ML CO on SiO_2 as the deposition temperature changes from 20 K through to 26 K [28].

As is more clearly shown on **Figure 5.17**, the LO–TO splitting contracts with increasing deposition temperature. This leads on to the next determination of dipole disordering in the CO multilayer as temperature increases, the inhomogeneous broadening as shown in **Figure 5.18** [28].

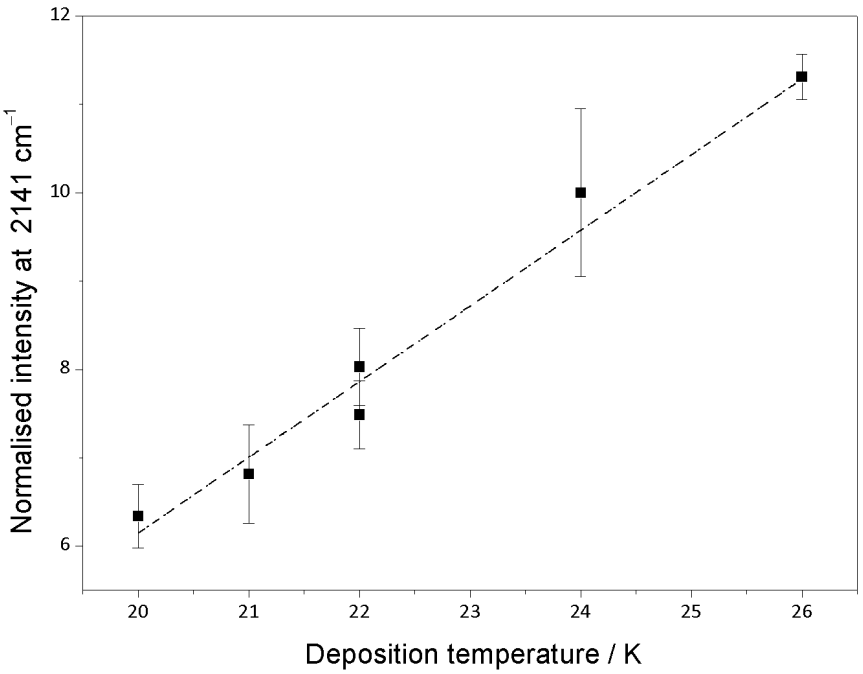

Figure 5.18: This figure shows another way of looking at the order of dipoles in the 5 ML CO film as the temperature of deposition is increased from 20 K through to 26 K [28].

As was observed for N_2O (**Figure 5.10**), the inhomogeneous broadening of CO also increases with temperature. The method for producing this graph is the same as that for N_2O, however now the central point between the LO and TO modes of the νCO band is 2141 cm^{-1}. All the CO on SiO_2 data shown exhibits the same behaviour in the RAIR spectra as seen for N_2O when the temperature is changed. Thereby, these data sets indicate CO to be another molecule exhibiting the spontelectric effect. What cannot be determined from the RAIRS data is if the possible surface potential will be positive or negative. However, the work of Collings *et al.* [30] has shown that CO will bind to SiO_2 through the carbon leaving the positive oxygen protruding into the vacuum. Thereby, this will create a positive surface potential on the surface. The same is said when CO is deposited onto H_2O as will be discussed in the next section.

5.3.3 Spontelectric CO Films on H_2O

In **Section 5.1** a characteristic of the spontelectric effect was stated as being independent of the nature of the surface the spontelectric molecules were deposited on. With this in mind and gearing these experiments towards the astrophysical environment means once again using CO as a probe molecule. In **Chapter 4**, a conclusion of possibly having CO directly bonded to the interstellar grain surface was put forward and this situation with regards to the spontelectric effect was discussed in the previous sub–section. However, CO can still be found on a H_2O layer when the icy mantle is thick enough. The spontelectric effect being a long–range interaction means CO on H_2O should also exhibit a surface potential when CO film is great enough. For that reason, this section will focus on CO on H_2O multilayers with different structures. The H_2O structures under investigation will be porous amorphous solid water (p–ASW), compact amorphous solid water (c–ASW) and crystalline solid water (CSW).

For these experiments TPD, was not conducted to estimate the coverage of CO on the different H_2O surfaces. Instead the procedure as described in **Section 5.3.3** was used leading to 20 ML CO on the H_2O surfaces. An important note regarding the amount of data points with temperature is that once again only data from 20 K have been recorded. But this time, a maximum temperature of 24 K is used because CO desorption from H_2O occurs at lower temperature [13] as compared to SiO_2. As can be seen in **Figure 5.19** [31], CO on the different substrates are indeed multilayers as the bulk optical effect leading to the LO–TO splitting is observed.

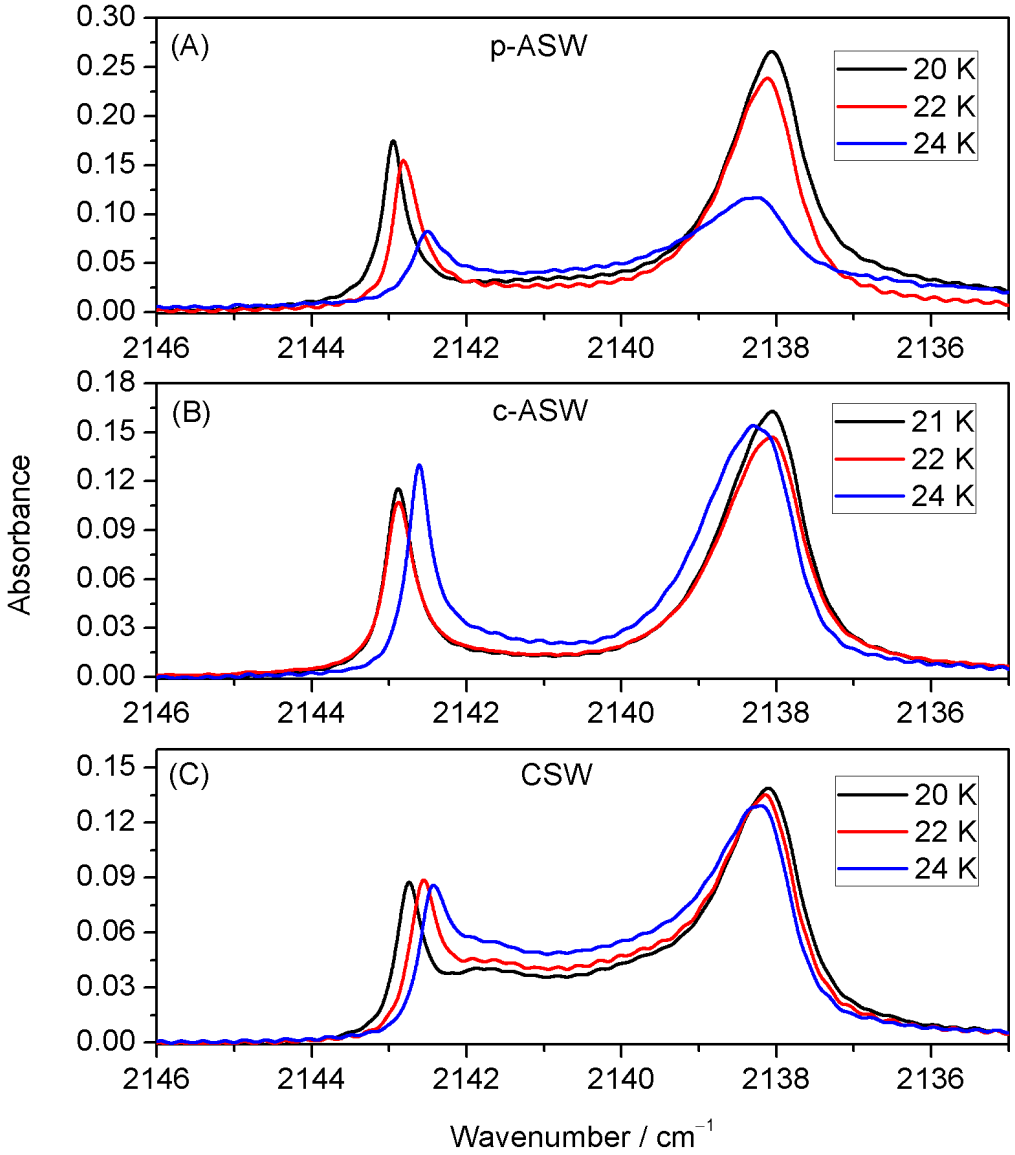

Figure 5.19: This figure shows all the RAIRS data collected when 20 ML CO is deposited onto multilayers of p–ASW (A), c–ASW (B) and CSW (C) at the indicated temperatures in the 20 K to 24 K range. A shift in the LO–TO splitting of *ν*CO is observed as the temperature increases [31].

The LO–TO splitting of the *ν*CO band is observed to contract when on the surface of the different H_2O substrates as the deposition temperature is increased as seen in **Figure 5.19**. Annealing experiments of CO on H_2O were not conducted as the peak shifts were expected to be too small to be seen, as observed when depositing CO on SiO_2. At first sight, the shifts seem to be similar considering the uncertainties, however fitting the peaks with Gaussians leads to a greater estimate of the uncertainties and peak positions as done for N_2O and CO on SiO_2 previously. The uncertainties can once again be quoted as 0.01 cm^{-1} and 0.02 cm^{-1} for the LO and TO modes respectively. The peak positions and their shifts as the deposition temperature is increased have been detailed in **Table 5.3** and graphed in **Figure 5.20**.

p–ASW			
Deposition Temperature / K	**Wavenumber / cm^{-1}**		**Δ_{LO-TO} / cm^{-1}**
	LO (± 0.01 cm^{-1})	**TO (± 0.02 cm^{-1})**	
20	2142.96	2138.08	4.88
22	2142.82	2138.12	4.70
24	2142.43	2138.34	4.09
c–ASW			
Deposition Temperature / K	**Wavenumber / cm^{-1}**		**Δ_{LO-TO} / cm^{-1}**
	LO (± 0.01 cm^{-1})	**TO (± 0.02 cm^{-1})**	
21	2142.89	2138.08	4.81
22	2142.89	2138.10	4.79
24	2142.63	2138.29	4.34
CSW			
Deposition Temperature / K	**Wavenumber / cm^{-1}**		**Δ_{LO-TO} / cm^{-1}**
	LO (± 0.01 cm^{-1})	**TO (± 0.02 cm^{-1})**	
20	2142.75	2138.16	4.59
22	2142.54	2138.19	4.35
24	2142.47	2138.29	4.18

Table 5.3: This table shows the peak positions with respect to deposition temperatures for CO on p–ASW, c–ASW and CSW. The data in this table can also be seen in **Figure 5.24**.

As can be seen from the data presented in **Table 5.3** and **Figure 5.20** [31], changes in the LO–TO splitting occur as the substrate is changed. The differences between the surfaces involves many factors such as density of H–dangling bonds, surface area and porosity [32, 33] and any one of these or a combination could cause the difference in the observed splitting. As will be discussed later, this also has an impact on the calculated surface potential of CO films on H_2O. The LO–TO splitting does not give an idea of the different environments CO finds itself in when deposited on different H_2O substrates. However, such environments can once again be qualitatively investigated through the

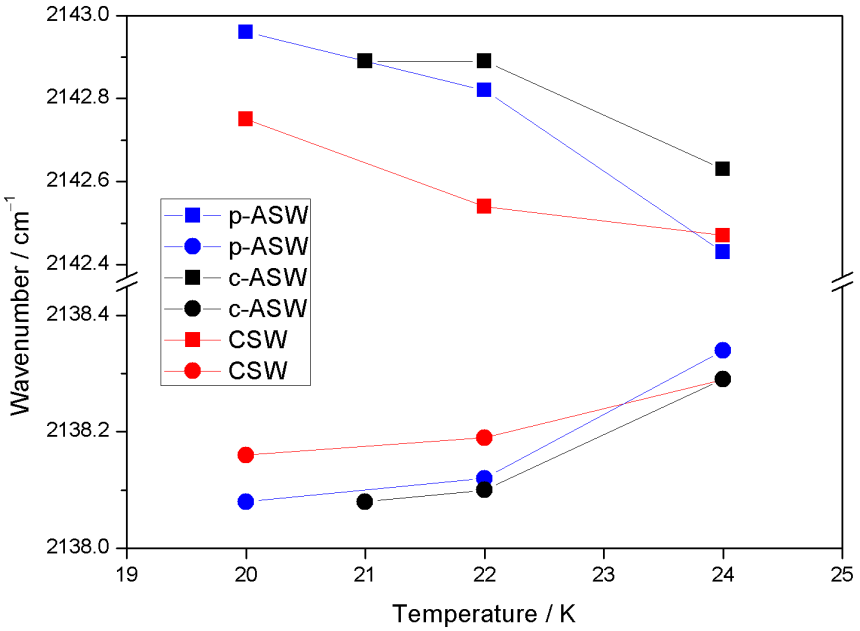

Figure 5.20: This figure displays the data from **Table 5.3** of the LO (squares) and TO (circles) modes of the νCO band contracting with increasing deposition temperature. As can be seen, a greater splitting is observed at 20 K for p–ASW (blue) as compared to the other c–ASW (black) and CSW (red) [31].

idea of the inhomogeneous broadening. The procedure to obtain **Figure 5.21** [31] is exactly the same as that described when looking at CO on SiO_2 in **Section 5.3.3**.

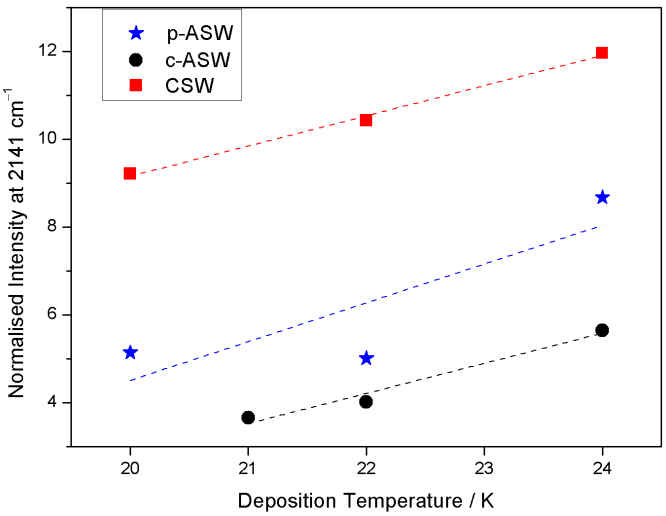

Figure 5.21: This figure shows the inhomogeneous broadening as measured at 2141 cm^{-1} between the LO and TO modes of the νCO band of 20 ML CO on H_2O ice. The blue data points are from CO on p–ASW, black is c–ASW and red is CSW. The linear regressions of the points give an idea of the similarity of environments of CO on H_2O surfaces [31].

From **Figure 5.21** differences or similarities in the environment CO finds itself on the different H_2O surfaces can be extracted. The linear fits between the data points from c–ASW (black data) and CSW (red data) have very similar gradients of 0.68 ± 0.11 K^{-1}

and 0.69 ± 0.05 K^{-1} respectively. In one way, this similarity of CO environments makes sense as there are no open pores in the c–ASW film and the larger uncertainty in the c–ASW can possibly be explained by the H–dangling bonds which are only present at the surface of the ASW film, but not in the bulk. p–ASW films are very different to the other H_2O films, as stated previously, which explains why the gradient of 0.88 K^{-1} in **Figure 5.21** is determined, however this is associated with a large standard deviation of 0.55 K^{-1}. Considering the uncertainties of these gradients, it is possible that CO finds itself in similar environments, no matter the H_2O underlayer. Factors such as porosity, H–dangling bonds and surface area could be irrelevant for these measurements. However, changes in the LO–TO splitting are still observed leading to the surface having some, for the time being, unknown effect on the data and in the end, the possible surface potential of CO in an astronomical environment.

5.4 Modelling RAIRS Data

As has been explained in subsection **5.3.1**, the dipole alignment as seen through the LO–TO splitting changes as the temperature increases. This section will relate RAIRS data obtained in this thesis with the spontelectric experimental results and model from Field and co–workers at Aarhus University in the case of N_2O. Based on the findings presented, and the model used for N_2O, CO will be similarly analysed to determine the parameters associated with the spontelectric effect when deposited on SiO_2 as well as H_2O. The model used to explain the N_2O RAIRS results was created and built by David Field at Aarhus University and further reading material regarding the model can be found in reference [19].

Before the model is introduced a glossary of the different terms has been made in **Table 5.4** for ease of reference.

Symbol	Description
Symbols used for the observed RAIRS data	
ν_{LO}	Longitudinal optical (LO) peak frequency
ν_{TO}	Transverse optical (TO) peak frequency
$\Delta\nu$	Difference in LO and TO peak frequency
$\Delta\nu_S$	Splitting due to spontelectric Stark field
$\Delta\nu_B$	Intrinsic splitting (Berreman effect)

Symbols used for the model	
μ	Dipole moment in the solid state
$<\mu_Z>/\mu$	Degree of dipole orientation
T	Deposition temperature
ζ	Locking term (frustration term)
E_s	Spontelectric field
E_{sym}	Symmetric spontelectric field parameter
E_{asym}	Asymmetric spontelectric field parameter

Table 5.4: This table describes the different terms that the models use to relate the experimental RAIRS data to the surface potential measurements for N_2O and to show the possible extent of the spontelectric effect of solid state CO.

First, consideration of factors which might cause changes in the LO–TO splitting besides the temperature fluctuations with the spontelectric field and the Stark effect must be examined. Two contributions are considered, thermal changes of the unit cell and changes in thickness of the films which will be shown to produce a negligible effect on the LO–TO splitting as the deposition temperature is raised.

Supplying the film with thermal energy, through annealing or changing the deposition temperature will lead to changes in the (unit cell) arrangement, *i.e.* the density can change as for instance is also seen for H_2O [34, 35]. This thermal change can therefore also affect the IR spectrum and LO–TO splitting seen on the bands of solid N_2O. The effect of density changes related to the dipole moment derivative is explained by **Equation 1** [9];

$$\nu_{LO}^2 - \nu_{TO}^2 = \frac{4\pi}{\varepsilon V} \times \left(\frac{\partial \mu}{\partial q}\right)^2. \qquad \textbf{Equation 1}$$

This equation can be rewritten to find the density of the molecular film, *N*, through **Equation 2**;

$$N = 2.307 \times 10^{17} \frac{(\nu_{LO}^2 - \nu_{TO}^2)}{(\partial \mu \,/\, \partial q)^2}. \qquad \textbf{Equation 2}$$

If the data from the 48 K experiment is taken into consideration (where ν_{LO} is 2256.35 ± 0.1 cm^{-1} and ν_{TO} is 2239.15 ± 0.2 cm^{-1}) and $\partial\mu/\partial q$ is 0.292 for the ν_{NN} band a value of

1.848×10^{22} molecules cm^{-3} is found for *N*. This value can be converted to 1.35 g cm^{-3}, which is the density of N_2O [36] at an unknown temperature. By cycling through the data, and using **Equation 2**, it is found that the density changes as the temperature changes. This therefore means that as the density changes the LO–TO splitting can also change through the relationship in **Equation 3**;

$$\Delta\nu \propto \frac{N}{\nu_L + \nu_T}. \qquad \textbf{Equation 3}$$

If the assumption that the average of LO and TO frequencies is not dependent of the density of the film, *N*, and state the LO–TO splitting as $\Delta\nu$. Using the same 48 K data as previously for the LO and TO frequencies, we can then create **Equation 4**;

$$N = 1.074 \times 10^{21} \times \Delta\nu \rightarrow \frac{\partial N}{\partial \Delta\nu} = 1.074 \times 10^{21} cm^{-3} \text{ per } cm^{-1}. \qquad \textbf{Equation 4}$$

When the experimental values from **Table 5.1** are considered, say from 48 to 51 K, the value of $\Delta\nu/\Delta T$ equals 0.3 cm^{-1} K^{-1}. This leads on to the thermal expansion coefficient (dN/dT) of N_2O equalling -3.22×10^{22} cm^{-3} K^{-1} through $dN/d\nu \times d\nu/dT$. The negative sign for this value means that the surface loses 3.22×10^{22} molecules for every degree K. Such a value is equivalent to a volume expansion coefficient of 0.017 K^{-1} as there are 1.848×10^{22} molecules cm^{-3} in solid N_2O when deposited at 48 K. Typical values of volume expansion coefficient lie in the range of 10^{-5} – 10^{-6} K^{-1}, meaning that the volume expansion can be disregarded as having an effect on the LO–TO splitting as it changes with deposition temperature.

Variation in thickness of the films is also a factor to consider which has already been shown to have a slight effect on the LO–TO splitting in **Figure 5.5**. It can be seen that changing the thickness from 7 ML to 28 ML of N_2O changes the difference in the LO–TO splitting by 0.5 cm^{-1} which can be considered negligible when referring the smallest contraction observed in **Table 5.1** of 13.4 cm^{-1}. Further to this, the uncertainty in background dosing is about ±20% meaning films of 7 or 28 ML of N_2O are not expected. The value of 13.4 cm^{-1} is the smallest change in the LO–TO splitting observed and occurs where N_2O is deposited at 66 K. This spectrum, as seen in **Figure 5.7**, shows a marked decrease in intensity as compared to the other deposition temperature experiments. As the amount of material on the surface is proportional to the intensity, then comparing the 66 K spectrum from **Figure 5.7** to the 7 ML N_2O film of

Figure 5.5 shows similar intensities. It can therefore be argued that the 66 K spectrum is actually 7 ML instead of 14 ML as initially dosed. The reason for this decrease is the sticking coefficient as the sample temperature approaches the temperature at which multilayers of N_2O desorb. For that reason the experiments concerning deposition of N_2O at 66 K have been disregarded. Also, the effect of film thickness has been disregarded as having a significant effect on the LO–TO splitting.

Having considered the possible factors affecting the LO–TO splitting (besides the spontelectric effect) and considered them to be negligible, we will move on to the splitting itself. The LO–TO splitting is a fundamental optical effect in the solid state and would occur if there was a spontelectric field affecting a molecular film or not. For that reason, the intrinsic optical effect and the vibrational Stark effect also have to be accounted for to be able to relate the LO–TO splitting to the spontelectric effect. To look at this **Table 5.5** [19] has been created for ease of reference.

Temperature / K (± 0.3 K)	ν_{LO} **/ cm^{-1} (± 0.1 cm^{-1})**	ν_{TO} **/ cm^{-1} (± 0.2 cm^{-1})**	$\Delta\nu$ **/ cm^{-1}**	$\Delta\nu_S$ **/ cm^{-1}**	$\Delta\nu_S/\Delta\nu$	$\langle\mu_Z\rangle/\mu$
48	2256.35	2239.15	17.2	5.2	0.303	0.0813
51	2255.9	2239.6	16.3	4.3	0.265	0.0683
52	2255.8	2239.8	16.0	4.0	0.251	0.0639
53	2255.8	2239.7	16.1	4.1	0.256	0.0614
55	2255.3	2240.05	15.25	3.3	0.214	0.0565
56	2255.3	2240.0	15.3	3.3	0.217	0.0540
60	2255.4	2239.85	15.55	3.4	0.229	0.0449
62	2254.9	2240.1	14.8	2.8	0.191	0.0386
66	2254.2	2240.8	13.4	1.4	0.106	0.0117

Table 5.5: This data is from the experiment where N_2O is deposited at different temperatures [19]. The first four columns are the same as seen in the bottom part of **Table 5.1**.

The first four columns, the same as in **Table 5.1** in **Section 5.3.1**, are of the deposition temperature, the position of the νNN LO and TO modes and the difference in their frequencies, $\Delta\nu$. The fifth column is the change in frequency due to the spontelectric effect, $\Delta\nu_S$, due to the vibrational Stark effect, of the LO–TO splitting with the sixth

column being the ratio between Δv and Δv_S. The last column are values for the dipole ordering ($\langle\mu_Z\rangle/\mu$) of N_2O at their specific temperatures as taken from Field *et al.* [1].

The LO–TO splitting, as stated previously, is an intrinsic optical effect in solid films when observed with infrared spectroscopy in grazing incidence arising from the Berreman effect. However, the Berreman effect is independent of temperature and should therefore not change in these experiments. This means the difference in the LO and TO frequencies (Δv) can be described as being made of two terms, one constant part caused by the Berreman effect (Δv_B) and one variable part caused by the spontelectric effect (Δv_S) which enhances the LO–TO splitting as shown in **Equation 5**;

$$\Delta v = \Delta v_B + \Delta v_S. \qquad \textbf{Equation 5}$$

Having said this, the need to know the value for Δv_B becomes important as the spontelectric contribution of the LO–TO splitting (Δv_S) makes up column five of **Table 5.5**. Firstly, if Δv_S is considered as being due to the Stark effect which in turn is due to the presence of the spontelectric field, **Equation 6** can be written;

$$\Delta v_S = \phi_{LO} \times E_{LO} + \phi_{TO} \times E_{TO} \qquad \textbf{Equation 6}$$

and therefore

$$\frac{\Delta v_S(T_i)}{\Delta v_S(T_j)} = \frac{(\phi_{LO} \times E_{LO} + \phi_{TO} \times E_{TO})_i}{(\phi_{LO} \times E_{LO} + \phi_{TO} \times E_{TO})_j} \qquad \textbf{Equation 7}$$

where ϕ is the Stark tuning due to the spontelectric potential (E) which leads to the Stark shift. **Equation 7** states the same relationship with respect to differing temperature of T_i and T_j. An assumption that the LO and TO modes shift by the same amount with opposite signs has to be made here to simplify the unknowns in this equation. This assumption is sustained by considering the data in **Table 5.1** where the average of the LO–TO splitting at 48 K is 2247.8 cm^{-1} and falls by 0.3 cm^{-1} to 2247.5 cm^{-1} at 66 K while the overall Δv falls by 3.8 cm^{-1} from 48 K to 66 K.

It follows from spontelectric theory that the change in dipole ordering ($\langle\mu_Z\rangle/\mu$) leads to the decrease if the spontelectric field, thereby $\langle\mu_Z\rangle/\mu$ and Δv_S are related. Furthermore, as no other factors affect the LO–TO splitting (save the spontelectric effect), the change

in the splitting as due to the temperature (*i.e.* $\Delta\nu_{Si}/\Delta\nu_{Sj}$) is correlated to the orientation of the dipoles. This means **Equation 8** can be setup;

$$\frac{\Delta\nu_B}{\Delta\nu_{S_j}} = \frac{\left(\langle\mu_Z\rangle/\mu\right)_i \Big/ \left(\langle\mu_Z\rangle/\mu\right)_j - \Delta\nu_i/\Delta\nu_j}{\Delta\nu_i/\Delta\nu_j - 1}. \qquad \textbf{Equation 8}$$

Equation 8 now relates the intrinsic splitting, $\Delta\nu_B$, the spontelectric contribution to the splitting ($\Delta\nu_S$), the dipole orientation ($\langle\mu_Z\rangle/\mu$) and the overall observed LO–TO splitting ($\Delta\nu$) at the deposition temperatures of *i* and *j*. For simplicity, the entire right hand side will be denoted as *A*. Remembering **Equation 5**, **Equation 9** can be derived with slight reordering;

$$\Delta\nu_j = \Delta\nu_B\left(1 + 1/A\right) \rightarrow \Delta\nu_B = \frac{A \times \Delta\nu_j}{(1+A)}. \qquad \textbf{Equation 9}$$

From **Equation 9** the value of $\Delta\nu_B$ can be calculated from the data in **Table 5.5** which yields an average value of 12.0 ± 0.3 cm^{-1} [19]. Given the experimental uncertainties in the values from RAIRS and the determination of the dipole orientation, this value can be considered as being fixed; as expected since the Berreman effect has no dependence on temperature. Once again returning to **Equation 5**, the value for $\Delta\nu_S$ can be calculated as seen in column six of **Table 5.5**.

The vibrational Stark effect is known to behave linearly with changes in the electric field [37–40], such as the spontelectric field generating the surface potential of N_2O. As the spontelectric field arises from the alignment of dipoles along the z–axis ($\langle\mu_Z\rangle/\mu$) the calculated values of $\Delta\nu_S$ can be examined to see if a linear relationship exists with $\langle\mu_Z\rangle/\mu$. This is shown in **Figure 5.22** [19].

As can be seen in **Figure 5.22** [19], a linear relationship does exist between the spontelectric contribution to the LO–TO splitting and the dipole orientation which in itself is proportional to the spontelectric effect. The linear fit goes through the origin as when there is no alignment of the dipole at high temperature a surface potential is not observed. This, as explained earlier, is also the reason for the data point relating to the

66 K data not fitting the trend as the sticking coefficient is less than unity as this temperature is close to the N_2O desorption temperature.

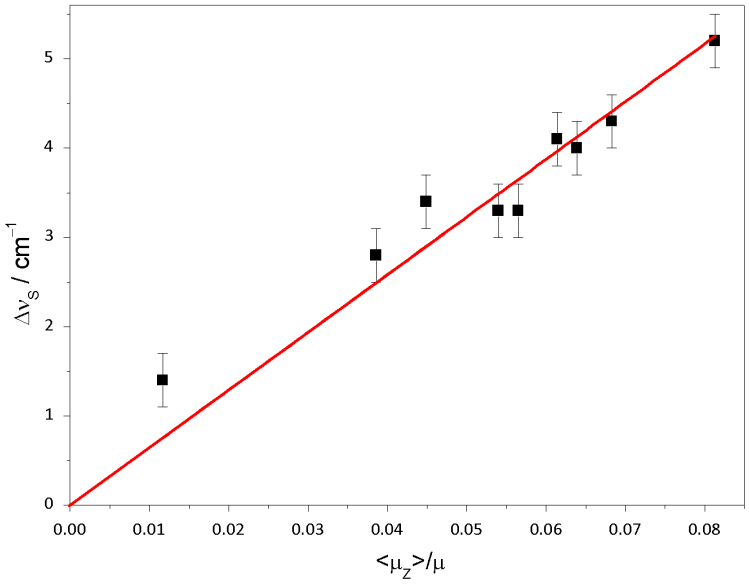

Figure 5.22: This figure shows the relationship with the spontelectric contribution to the LO–TO splitting and the dipole alignment for N_2O. A linear relationship exists as expected except for the 66 K data point due to the decrease in the sticking coefficient when the temperatures approaches the desorption temperature of N_2O [19].

With the different contributions of the Berreman effect and the Stark/spontelectric effect leading to the observed LO–TO splitting characterised, the focus will now change to look at the impact of temperature on the splitting as based on the Stark effect. The goal is to create a model to fit the spontelectric parameters as discussed in the introduction. For clarity, **Equationa 10** and **11** will be shown here which was introduced as **Equations 17** and **18** in **Chapter 2**:

$$E_Z = E_{sym} \times \left(1 + \zeta \left(<\mu_Z>/\mu\right)^2\right) - E_{asym} \times \frac{<\mu_Z>}{\mu}. \qquad \textbf{Equation 10}$$

$$\frac{<\mu_Z>}{\mu} = \coth\left(\frac{E_Z\mu}{T}\right) - \left(\frac{E_Z\mu}{T}\right)^{-1} \qquad \textbf{Equation 11}$$

Both E_{sym} and E_{asym} are related to the Langevin expression (**Equation 11**) through the dipole orientation ($<\mu_Z>/\mu$) as seen in **Equation 10**. Since two different modes are observed in the RAIRS data, the LO and TO modes must have differing force constants. To discuss the differing force constants, the differing frequencies of the LO and TO modes and their associated energies, a brief explanation is required.

Two distinct peaks related to the same vibration mode in RAIR spectra will have different force constants as they appear at different frequencies. Expressions for the high wavenumber peak ($k + \delta_A$) and ($k - \delta_B$) for the low wavenumber peak can be written in terms of a harmonic approximation, $\nu_A \propto (k + \delta_A)^{0.5}$ and $\nu_B \propto (k - \delta_B)^{0.5}$. Once again to simplify the equations to relate them, introducing an *ansatz*, the δ terms are said to be equal to each other and referred to simply as δ (*i.e.* $\delta = \delta_A = \delta_B$). If these expressions are to be related to the LO–TO splitting, then the terms involving A would be for the LO mode as this is always at higher wavenumbers, and B for the TO mode. Also, if the expressions are to be related to the spontelectric effect, then the *ansatz* involves the assumption that the E_{sym}, ζ and $\langle\mu_Z\rangle/\mu$ are the same for both LO and TO modes. **Equation 12** can be set up assuming that $\delta << k$;

$$\nu_A \propto \left[k\left(1 + {}^{\delta}/_{k}\right)\right]^{0.5}/\sqrt{M} \approx \sqrt{k/M} \times \left(1 + \frac{1}{2}\delta/k\right) \qquad \textbf{Equation 12}$$

where M is the molar mass of a molecule. A similar expression for ν_B can be made where the right hand side involves a negative term in the bracketed expression. Therefore, if the ratio of A and B are taken, **Equation 13** is made;

$$\frac{\nu_A}{\nu_B} \approx \left(1 + \frac{1}{2}\delta/k\right)^2 \approx 1 + {}^{\delta}/_{k}. \qquad \textbf{Equation 13}$$

Equation 13 relates to the RAIRS data, where ν_A is ν_{LO} and ν_B is ν_{TO}, and $\Delta\nu$ is equal to $\nu_{LO} - \nu_{TO}$, it can therefore be said that;

$$\frac{\Delta\nu}{\nu_{TO}} = \frac{\delta}{k} \qquad \textbf{Equation 14}$$

where k is 11.034 [41] and therefore $\delta/k \approx 0.008$ in this case, an accuracy of greater than 0.4% is found with these approximations when looking at the data on **Table 5.5**.

Using the result from **Equation 14** including $\delta << k$ and that $\Delta\nu$ is small compared to ν_{LO} or ν_{TO} thereby saying that $\Delta\nu/\nu_{LO} \approx \Delta\nu/\nu_{TO}$, we can look at the energies of the LO and TO modes, U_{LO} and U_{TO} respectively;

$$\frac{U_{LO} - U_{TO}}{U_{TO}} = \frac{\nu_{TO}}{\nu_{LO}} \times \frac{1 + \delta/k}{1 - \delta/k} - 1 \approx \frac{\Delta\nu}{\nu_{TO}}. \qquad \textbf{Equation 15}$$

Using the data from **Table 5.5**, an accuracy of greater than about 0.75% is achieved with the approximations while negligible inaccuracies are found in the differential of $\Delta\nu/\nu_{TO}$ with respect to the dipole orientation ($<\mu_Z>/\mu$). Combining **Equation 14** with the spontelectric parameters discussed earlier, **Equation 16** can be setup;

$$\frac{\Delta\nu}{\nu_{TO}} \approx \frac{\Delta\nu_S}{\Delta\nu} \times \frac{E_{asym} \times (<\mu_z/\mu>)^2}{E_{sym} \times [1 + \zeta \times (<\mu_Z>/\mu)^2]} + \frac{\Delta\nu_B}{\nu_{TO}}. \qquad \textbf{Equation 16}$$

Equation 16 is constructed by considering the entire field relevant to the TO mode. This field introduces both the Berreman effect ($\Delta\nu_B$) and the spontelectric effect ($\Delta\nu_S$) components of the LO–TO splitting which for the surface potential and its model relate to the E_{sym} term from **Equation 10**. Now, the ratio of the total field to the spontelectric part is proportional to $\Delta\nu/\Delta\nu_S$, and remembering that the total LO–TO splitting is the difference between the LO and TO modes means the total spontelectric field must itself also be proportional to the relevant ν_{TO}. This relationship has been described in **Equation 17**;

$$\nu_{TO} \propto \frac{\Delta\nu}{\Delta\nu_S} \times E_{sym} \times [1 + \zeta \times (<\mu_Z>/\mu)^2]. \qquad \textbf{Equation 17}$$

Also, the difference in energies of the LO and TO modes ($U_{LO} - U_{TO}$) is proportional to the spontelectric field multiplied by the degree of dipole orientation ($<\mu_Z>/\mu$). This leads to the effective spontelectric field, however the extra contribution to the LO–TO splitting from the intrinsic Berreman effect has to be accounted for in each RAIR spectrum. Overall, these factors are included to obtain **Equation 16** which can be used to explain the shifts observed in the LO–TO splitting with temperature when using parameters of E_{sym}, ζ and $<\mu_Z>/\mu$ as already discussed. The value of the parameters are taken from the initial work of Field *et al.* [1] where the model was introduced.

However, for **Equation 16** to be used with deposition temperature, we need to initially investigate the LO and TO modes with respect to the dipole orientation.

5.4.1 LO and TO Modes with Dipole Orientation

Determining the degree of dipole orientation ($<\mu_Z>/\mu$) from the value of the LO–TO splitting means having to perform another simplification; that the intrinsic effect in the splitting (Berreman effect, $\Delta\nu_B$) is independent of $<\mu_Z>/\mu$. Having said that, it is

recognised that this may not be true since the LO and TO motions (and associated potentials) are influenced by the degree of dipole alignment. Furthermore, if the potentials are affected in differing manners, the Δv_B will be dependent on the temperature since the spontelectric material is affected with a likewise dependence on temperature. This in turn means that the intrinsic effect could be coupled to the spontelectric effect

As the degree of dipole alignment and the LO–TO splitting has been linked, **Figure 5.9** becomes important again. Once again, focusing on the deposition temperature experiment for N_2O, a linear fit can be applied to the frequency shift per unit temperature of the LO and TO modes leading to –0.1 ± 0.020 cm^{-1} K^{-1} and 0.06 ± 0.022 cm^{-1} K^{-1}, respectively, over the 48 – 62 K range. An assumption has to be made, that the shifts of both LO and TO bands can be said to be of the same amount per degree K which is almost covered by the uncertainty in the fits. This means **Equation 18** can be set up as a simplification. It is important to note that there is no reason as to why these values are the same, it just so happens to almost be the case for N_2O;

$$\left.\frac{dv_{LO}}{dT}\right|_T = -\left.\frac{dv_{TO}}{dT}\right|_T \qquad \textbf{Equation 18}$$

which, when considering how the dipole orientation ($<\mu_Z>/\mu$) is related to the LO–TO splitting, therefore implies that;

$$\left.\frac{dv_{LO}}{d<\mu_Z>/\mu}\right|_T = -\left.\frac{dv_{TO}}{d<\mu_Z>/\mu}\right|_T. \qquad \textbf{Equation 19}$$

After heavy manipulation, **Equation 20** can be created;

$$\frac{dv_{TO}}{d<\mu_Z>/\mu} = -\frac{E_{sym}E_{asym}(<\mu_Z>/\mu)(v_{LO}-\Delta v_B)[2\xi+\eta\xi'(<\mu_Z>/\mu)]}{\left[\eta E_{sym}+\xi E_{asym}(<\mu_Z>/\mu)^2\right]\times\left[2\eta E_{sym}+\xi E_{asym}(<\mu_Z>/\mu)^2\right]}. \qquad \textbf{Equation 20}$$

In **Equation 20** new symbols have been introduced to make the equation more readable, the additions are summarised in **Equation 21**;

$$\xi = \frac{\Delta v_S}{\Delta v}; \qquad \textbf{Equation 21 (A)}$$

$$\eta = E_{sym}\left(1 + \xi\left(<\mu_Z>/\mu\right)^2\right); \quad \textbf{(B)}$$

$$\xi' = \frac{d(\Delta v_S/\Delta v)}{d<\mu_Z>/\mu} \text{ or } = (\Delta v_B/\Delta v^2)\frac{d(\Delta v_S)}{d<\mu_Z>/\mu}. \quad \textbf{(C)}$$

From **Equation 20**, it can be seen that as v_{TO} increases, the dipole orientation ($<\mu_Z>/\mu$) decreases. This means that as the deposition temperature increases, the TO mode increases in frequency as the dipoles become less aligned. The opposite is seen for the LO mode as this decreases with increasing temperature as the dipoles are forced out of alignment. This is also the behaviour seen in the experimental RAIRS data, showing the consistence of the RAIRS results and their interpretation with the physics behind the spontelectric effect.

5.4.2 LO and TO Modes with Temperature

The final step in the modelling of the data is to obtain an expression relating the dipole orientation and the temperature. This is done by combining **Equations 10** and **11** and differentiating this by the temperature (*T*) to give **Equation 22**;

$$\frac{d<\mu_Z>/\mu}{dT} = \frac{(1/\mu E_Z) - (\mu E_Z/T^2)\,\mathrm{cosech}^2(\mu E_Z/T)}{\left((\mu E_{asym} - 2\mu\zeta E_{sym}(<\mu_Z>/\mu))/T\right)\mathrm{cosech}^2(\mu E_Z/T) - \left((E_{asym} - 2\zeta E_{sym}(<\mu_Z>/\mu))T/\mu {E_Z}^2\right) - 1}. \quad \textbf{Equation 22}$$

From **Equation 22**, multiplying this with **Equation 20**, leads to an expression for $\frac{\mathrm{d}v_{LO}}{\mathrm{d}T}$ (and for $\frac{\mathrm{d}v_{TO}}{\mathrm{d}T}$ since both quantities are equal and opposite).

From here, the data from the surface potential experiments is needed to complete the model and compare the observed difference in the LO–TO splitting to that of the model. As previously explained, the RAIRS data covers temperatures to 66 K as the difference in intensity (and thereby film thickness) has been shown to have a negligible effect on the peak positions. However, this is not the case for the surface potential experiments. As the surface potential is dependent on the linear relationship with film thickness, the 66 K data has not been used as the film begins to desorb [1]. Therefore, the data used for the model will range from 48 K to 62 K as seen in **Table 5.5**. To fit the experimental data to the model, the values of E_{sym} (4.57×10^8 V m^{-1} reduced from 5.43×10^8 V m^{-1}), E_{asym} (8.63×10^8 V m^{-1} increased from 7.88×10^8 V m^{-1}) and ζ (75, unitless) [1] are

substituted into the equations to produce the values stated in **Table 5.6** [19]. The increase and decrease in the E_{sym} and E_{asym} give an indication of the uncertainty level as a consequence of the simplifications made throughout the modelling.

Temp. / K	**$-d\nu_{TO}/d\langle\mu_Z\rangle/\mu$ / cm^{-1}**	**$-d(\langle\mu_Z\rangle/\mu)/dT$ / cm^{-1} K^{-1}**	**$d\nu_{TO}/dT$ / cm^{-1} K^{-1}**	**$\Delta\nu$ / cm^{-1} ± 0.8 cm^{-1} (Model)**	**$\Delta\nu$ / cm^{-1} ± 0.3 cm^{-1} (Exp. Data)**
48	76.9	4.30×10^{-3}	0.330	17.8	17.2
51	65.8	2.53×10^{-3}	0.167	16.4	16.3
52	61.3	2.18×10^{-3}	0.129	16.1	16.0
53	60.6	1.97×10^{-3}	0.119	15.8	16.1
55	51.0	1.64×10^{-3}	0.084	15.4	15.25
56	49.8	1.50×10^{-3}	0.075	15.3	15.3
60	44.9	1.11×10^{-3}	0.045	14.75	15.55
62	34.2	1.83×10^{-3}	0.062	14.6	14.8

Table 5.6: This table shows the values as calculated from the model and compared to the observed RAIRS data for N_2O. Explanations for each column can be found in the text [19].

Table 5.6 shows the various values as calculated and finally compared to the observed RAIRS data in column six. The first column is the deposition temperature of the experiments. The values for column two and three are obtained from **Equations 20** and **24**, respectively. Column four are values of the TO mode as it changes with temperature where values for the LO mode are equivalent to the TO mode, but opposite in sign. In essence, column four is the product of column two and three. Column five are the calculated values for the difference in the peak positions of the LO–TO splitting from the model presented. These values and the overall result can be seen in **Figure 5.23**.

As can be seen in **Figure 5.23**, the comparison between the model and the RAIRS data is good, with the exception of the 60 K data. However, the 60 K data point can be considered within the uncertainty limit. The uncertainties in the observed data have been set to 0.3 cm^{-1} as this is the cumulative uncertainty from the Gaussian fits of the experimental data. The uncertainty of the model (red dashed lines) has been set to 0.8 cm^{-1} due to the error propagation during the calculations and estimated from the constants of integration of k_{LO} and k_{TO} and the ζ' term.

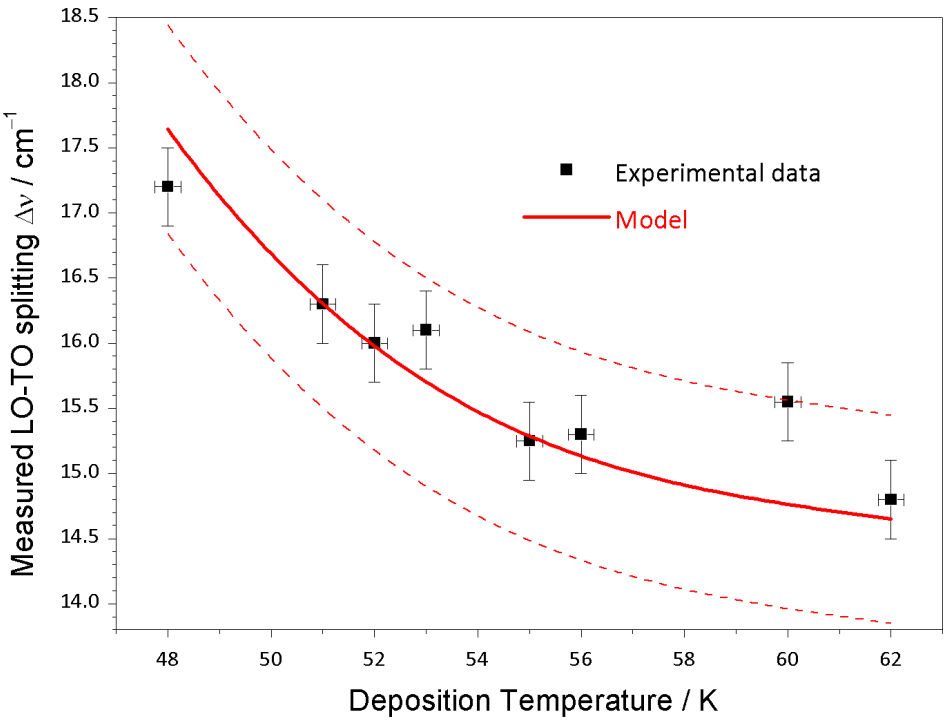

Figure 5.23: This figure shows the final result comparing the observed RAIRS data (black scatter) with the modelled data (red solid line). The dashed red lines indicate the level of uncertainty in the modelled data (± 0.8 cm^{-1}) [19].

5.4.3 Spontelectric CO Films

With the model explained for N_2O in the previous subsection, the same general procedure follows here to indicate what a possible spontelectric field in CO on SiO_2 will be. For that reason, only changes in the analysis and modelling of the CO data will be mentioned. As for the N2O model, these models regarding spontelectric CO films were created by David Field and can also be read about in references [28] and [31]. As previously stated, surface potential measurements have not been done on CO as the base temperature of the UHV apparatus in Aarhus is too high to permit the deposition of solid CO.

To begin with the same considerations as to possible reasons for peak shifts will be outlined. Here the volume expansion is also neglected as having an impact on the splitting as the splitting with respect to temperature as the coefficient for the expansion is between 0.002 to 0.003 K^{-1}. Typical values for the volume expansion coefficient are usually seen to be a factor of about 10^2 – 10^3 times lower than calculated leaving this parameter as being rejected as causing shifts in the LO–TO splitting. Also, the film

thickness is not regarded as having an impact on the splitting for the same reasons as explained for N_2O and as seen in **Figure 5.14**.

For these experiments, the same assumptions are used as explained earlier, this includes that the overall observed LO–TO splitting is composed of an intrinsic part ($\Delta\nu_B$) from the Berreman effect and a spontelectric component ($\Delta\nu_S$) associated with the vibrational Stark effect, as explained in **Equation 5**. Previously, **Equation 9** was used to determine the intrinsic component of the LO–TO splitting, however this requires information on the degree of dipole orientation ($<\mu_Z>/\mu$) which was determined through the experiments conducted in Aarhus. This value is not known experimentally for solid CO and a different approach must be adopted to estimate the value of $\Delta\nu_B$.

Considering what was determined in the previous subsection about $\Delta\nu_B$ not being dependent on the temperature, *i.e.* the peak positions of the LO–TO splitting of non–spontelectric molecules should not change with temperature. This means plotting the value of the LO–TO splitting with the inverse temperature will lead to a value of $\Delta\nu_B$ (intercept) when the effect of $\Delta\nu_S$ is eliminated as the temperature tends to infinity. This is shown in **Figure 5.24** [28].

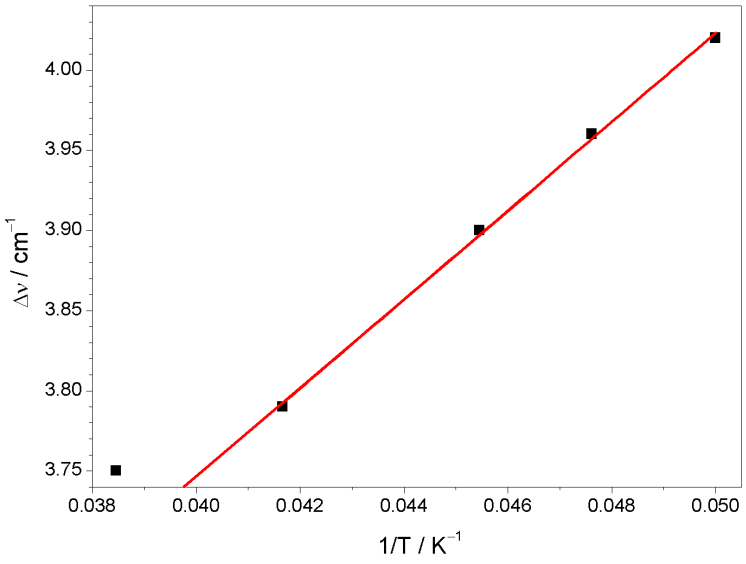

Figure 5.24: This figure shows the linear relationship between the value of the LO–TO splitting of CO on SiO_2 with respect to the inverse temperature. The intercept with the y–axis leads to an approximation for the intrinsic component of the LO–TO splitting of CO [28].

As can be seen in **Figure 5.24**, a near linear relationship exists. The data at 26 K has been ignored in the further analysis below, but is still shown for clarity. The reason for

ignoring it is due to the proximity to the desorption temperature of CO and the inherent issues with deposition of species close to their desorption temperature as also discussed for N_2O. The reason for the plot containing the inverse temperature is because $\Delta\nu_S$ acts to broaden the LO–TO splitting which decreases with temperature as the spontelectric effect diminishes. Excluding the data point at 26 K, the linear fit is accurate to within 0.6% for the slope and 0.3% for the intercept. Extrapolating the linear fit to the intercept leads to a value of 2.59 cm^{-1} as being the intrinsic splitting ($\Delta\nu_B$). This is an *ad hoc* approach. However, with the lack of experimental data for the dipole orientation of CO, this simple, yet highly accurate linear fit, is deemed sufficient for an approximate determination of a potential spontelectric field in CO. With this data, **Table 5.7** [28] can be constructed.

Temperature / K (± 0.3 K)	**ν_{LO} / cm^{-1} (± 0.01 cm^{-1})**	**ν_{TO} / cm^{-1} (± 0.02 cm^{-1})**	**$\Delta\nu$ / cm^{-1}**	**$\Delta\nu_S$ / cm^{-1}**	**$\Delta\nu_S/\Delta\nu$**
20	2138.50	2142.52	4.02	1.43	0.356
21	2138.55	2142.51	3.96	1.37	0.346
22	2138.58	2142.48	3.90	1.31	0.336
24	2138.62	2142.81	3.79	1.20	0.317
26	2138.63	2142.38	3.75	1.16	0.309

Table 5.7: This table shows the data used for the modelling of the CO RAIRS data. The first four columns are taken directly from the experiments with the last two being calculated from the experimental data [28].

From here on a similar approach to before is used to express the $\Delta\nu_S$ in terms of the spontelectric parameters introduced earlier. Firstly, **Equations 10** and **11** from before are combined and by expanding the coth function to the first order (coth(x) – 1/x = 1/3x), **Equation 23** is obtained;

$$\frac{<\mu_Z>}{\mu} = \frac{3T - 2\sqrt{\mu^2\zeta E_{sym}(E_S - E_{sym}) + 9T^2}}{2\mu\zeta E_{sym}}. \qquad \textbf{Equation 23}$$

Expanding the coth function as stated has been tested with the values found in **Table 5.7** and leads to an accuracy of better than 1 in 10^5. Once again, the E_{sym} and E_{asym} are associated with the spontelectric field and ζ is the frustration/locking term due to the

local force fields. The dipole moment of solid state CO is found to be 0.076 D as discussed previously.

Now, employing different force constants as for the N_2O calculations for these vibrational modes leads to **Equation 15** again. The CO data leads to an overall agreement of better than 0.5% (for N_2O, this accuracy was better than 0.75%). As in the previously described model, the energies (U) can be related to the spontelectric parameters where, for instance, the U_{TO} part corresponds to the local symmetrical and spontelectric effects of the $E_{sym}(1 + \zeta(<\mu_Z>/\mu)^2)$ segment of **Equation 1**. Also, since the total spontelectric field is related to the spontelectric component of the LO–TO splitting, **Equation 16** can once again be setup;

$$\frac{\Delta\nu}{\nu_{TO}} \approx \frac{\Delta\nu_S}{\Delta\nu} \times \frac{E_{asym} \times (<\mu_z/\mu>)^2}{E_{sym} \times [1 + \zeta \times (<\mu_Z>/\mu)^2]} + \frac{\Delta\nu_B}{\nu_{TO}} \qquad \textbf{Equation 16}$$

and from this, including **Equation 5** by substituting **Equation 23** through the $<\mu_Z>/\mu$ with heavy reorganisation, leads to **Equation 27**;

$$\Delta\nu_S = \nu_{TO} \frac{\mu(\Delta\nu/\Delta\nu_S)\nu_{TO}E_S T\left\{E_S\left[3T + \left(4\mu^2(\Delta\nu/\Delta\nu_S)E_{sym}(E_S - E_{sym}) + 9T^2\right)^{0.5}\right] - 6_{Esym}T\right\}}{2E_{sym}(E_S^2\mu^2\zeta + 9T^2)}.$$

Equation 23

As can be seen in **Equation 24**, both observational RAIRS data and the spontelectric parameters are included here. However, extracting values for the spontelectric parameters becomes an issue as there are too many unknowns (E_S, E_{sym} and ζ), therefore **Equation 25** is setup;

$$\Delta\nu_S = \nu_{TO} \frac{2\pi\,(\Delta\nu/\Delta\nu_S)\left\{4\pi\mu^2 - \left[9T^2\Omega^2 + 4\mu^2\left(4\mu^2\pi^2 - \Omega^2\zeta {E_{sym}}^2 + 6\pi\Omega T\right)^{0.5}\right] - 3\Omega T\right\}}{\Omega\zeta E_{sym}(4\pi\mu^2 + 3\Omega T)}.$$

Equation 25

Equations 24 and **25** are equivalent to each other when using the $E_S = (<\mu_Z>/\mu)(\mu/\varepsilon_0\Omega)$ and $E_{asym} = 4\pi\mu/\Omega$ where Ω is related to the molecular volume of CO. Also, **Equation 26** has been used for further analysis;

$$\frac{<\mu_Z>}{\mu} = \frac{\mu E_{asym} + 3T\left[1 - \left(\{1 + \mu E_{asym}/3T\}^2 - 4\zeta\mu^2 E_{sym}^2/9T^2\right)^{0.5}\right]}{2\mu\zeta E_{sym}}. \quad \textbf{Equation 26}$$

Equation 26 has also been used before, but in a different manner as when first introduced as **Equation 23**. Further to these steps in finding the spontelectric parameters and by looking at **Equation 23** we can state;

$$E_S = \left(\frac{<\mu_Z>}{\mu}\right)\left(\frac{\mu}{\varepsilon_0\Omega}\right) \text{ hence } \frac{<\mu_Z>}{\mu} = \frac{\Omega E_S}{4\pi\mu}. \quad \textbf{Equation 27}$$

Equation 27 can be used in place of the dipole orientation as used in many of the above explained equations. This simplification means the subsequent analysis for finding the spontelectric parameters for E_{sym}, ζ and Ω becomes easier before finally estimating the dipole orientation $<\mu_Z>/\mu$. The same assumptions as for the N_2O modelling have been made when modelling the CO data in that μ and ζ are constant with temperature. However, as E_{sym} (previously considered constant with temperature) and Ω are not known for CO multilayers, these values are considered variable before a definite value is assigned to them. So, in order to assign values for the spontelectric parameters which will lead to a possible surface potential of CO, four steps are involved. Firstly, an estimate of E_{sym} is made to yield a range of values of which the average is taken as the final value for E_{sym}. Then, based on the E_{sym} value, Ω is determined when considering all the temperatures used for the experiments. Thirdly, a value for the overall E_S is determined, before finally $<\mu_Z>/\mu$ is determined.

Initially, and because of the previous studies of ζ, a value of 43.8 has been chosen; this is the same value used when modelling the N_2O data. This value may at first seem random, however it has been shown that ζ can be varied from 10 to more than 10^5 with results varying less than 5%. [1]. This, considering that the dipole moments of CO and N_2O are similar, has lead to the use of 43.8 for ζ.

This means the focus will now turn towards the first step of finding a value for E_{sym}. Ignoring the data point at 26 K, due to the proximity to the desorption temperature, leads to the use of simultaneous equations for the 20, 21, 22 and 24 K data sets to find E_{sym}. By substituting the values taken from **Table 5.7** into **Equation 25** leads to

equations with only 2 unknown parameters, E_{sym} and Ω. Solving the sets of simultaneous equations for the different deposition temperature leads to an average value for E_{sym} of 4.58 ± 0.21 ×10^7 V m^{-1} and 11.8 atomic units for Ω. The uncertainties stated are due to the deposition temperature, the Gaussian fits and the error in $\Delta\nu_B$. These results were obtained by assuming that Ω is constant for the different deposition temperatures, the reason for this constant value will now be discussed.

Using the same data as before and now with the averaged value of E_{sym}, still with **Equation 25**, leads to three different values of Ω for the deposition temperatures, all summarised in **Table 5.8** [28].

Temperature / K (±0.3 K)	**Ω_1 / au × 10^4 (±0.16 × 10^4)**	**Ω_2 / au × 10^4 (±7)**	**Ω_3 / au (±0.3)**
20	5.34	341	11.8
21	5.45	310	11.8
22	5.52	282	11.8
24	5.69	236	11.8

Table 5.8: This table illustrates the variety of Ω as the deposition temperatures change when calculated through **Equation 25** [28].

As can be seen in **Table 5.8**, the second and fourth columns show the values for Ω are generally constant with temperature. This follows the assumptions based on the analysis for E_{sym}. However, Ω_1 leads to values of the order of 10^4 au which will give values for the degree of dipole orientation greater than unity which is physically unrealistic. Ω_2 can be seen to vary considerably when the deposition temperature changes, and a recent study has found that the molecular volume can be related to the polarisability [42]. Since the polarisability has been considered a constant (13.159 au for CO), the molecular volume should therefore also be constant leading to the choice of 11.8 au for Ω.

Now the third step can be embarked upon which will lead to values for the spontelectric field, E_S as based on **Equation 24** where an upper (u) branch and lower (l) branch can be found due to the nature of the equation. The results have been shown in **Table 5.9** [28].

Temperature / K (± 0.3 K)	E_{Su} / × 10^7 V m^{-1} (± 0.15 × 10^7 V m^{-1})	E_{Sl} / × 10^7 V m^{-1} (± 0.30 × 10^7 V m^{-1})
20	3.78	7.06
21	3.75	7.43
22	3.72	7.63
24	3.66	8.22

Table 5.9: This table shows how the values of E_S (upper and lower values) vary with the deposition temperature as calculated through **Equation 24** [28].

From here the dipole orientation of solid CO can be found through the simplified relationship of E_S and $<\mu_Z>/\mu$ as shown in **Equation 27**.

Temperature / K (± 0.3 K)	E_{Su} / × 10^7 V m^{-1} (± 0.15 × 10^7 V m^{-1})	$<\mu_Z>/\mu_u$ (±0.0024)	E_{Sl} / × 10^7 V m^{-1} (± 0.30 × 10^7 V m^{-1})	$<\mu_Z>/\mu_l$ (±0.0001)
20	3.78	0.0645	7.06	0.0121
21	3.75	0.0582	7.43	0.0114
22	3.72	0.0526	7.63	0.0108
24	3.66	0.0434	8.22	0.0097

Table 5.10: This table shows the values of the degree of dipole orientation as the temperature and spontelectric field vary. The subscripts *u* and *l* refer to the upper and lower branch as calculated for E_S [28].

Table 5.10 shows the response of the spontelectric field (E_S) and the dipole orientation ($<\mu_Z>/\mu$) as the deposition temperature is increased. As stated throughout this chapter, as the temperature is increased, the general behaviour of spontelectric materials leads to a decrease in the E_S and $<\mu_Z>/\mu$, this is also observed for the upper branch values. However, the lower branch values behave anomalously in that the E_S increases while the $<\mu_Z>/\mu$ (as expected) decreases as the temperature is increased. A possible answer for this behaviour can potentially be found when differentiating **Equation 24** with T, however this has not yet been attempted. The behaviour in the double–value of Ω and therefore equivalently E_S as seen for CO has also been observed through direct surface potential experiments at Aarhus University when studying propane. Here, when depositing about 2,500 ML propane, the spontelectric field switches from an upper to a lower branch of values leading to a double–valued E_S.

Although the methods of analysis for N_2O and CO differ due to lack of certain key experimental data (such as dipole orientation), the analysis as just shown for CO can be done for the N_2O data too. Suffice to say that plugging the relevant N_2O data into the recently presented equations in this subsection leads to an E_{sym} value of 4.69 ± 0.19 × 10^8 V m^{-1} which is in good agreement to the previously calculated result of 4.57 ± 0.14 × 10^8 V m^{-1}.

The last results to model are when multilayers of CO are deposited onto different types of H_2O. For simplicity, only the results will be shown as the entire model and procedure are the same as just shown for CO directly on SiO_2. The only changes are the frequencies for the LO–TO splitting as shown in **Table 5.3** and the intrinsic Berreman effect of 0.307 ± 1.589 cm^{-1} for p–ASW, 0.898 ± 1.285 cm^{-1} for c–ASW and 2.119 ± 0.104 cm^{-1} for CSW [31]. Because of the large uncertainties in the $\Delta\nu_B$ values, the largest value of 2.119 ± 0.104 cm^{-1} will be used. This will naturally have the effect of decreasing the possible surface potential meaning such a value can be regarded as a minimum value for the spontelectric effect of CO on H_2O. Following each step, **Table 5.11** [31] has been made to show the values of the upper branch spontelectric field for the different H_2O layers and deposition temperature.

H_2O type	**E_{sym} / × 10^7 V m^{-1}**	**E_S / × 10^7 V m^{-1} (± 0.15 ×10^7 V m^{-1})**			**$\langle\mu_z\rangle/\mu$ (± 0.0024)**		
		20 K	**22 K**	**24 K**	**20 K**	**22 K**	**24 K**
p–ASW	4.68 ± 0.1	3.73	3.65	3.72	0.0496	0.0401	0.0408
		3.79	3.72	3.78	0.0516	0.0417	0.0424
c–ASW	3.16 ± 0.1	1.99*	1.83	1.89	0.0102*	0.0072	0.0072
		1.96*	1.80	1.86	0.0097*	0.0068	0.0069
CSW	3.74 ± 0.1	2.89	2.84	2.77	0.0302	0.0247	0.0200
		2.85	2.79	2.72	0.0291	0.0239	0.0193

Table 5.11: This table shows the overall result of the spontelectric parameters and the dipole orientation when CO multilayers are deposited onto different types of H_2O while the deposition temperature is changed. The * marks where the deposition temperature is 21 K which is only the case for the c–ASW experiments [31].

Table 5.11 sums up the different calculations of the spontelectric field of CO on p–ASW, c–ASW and CSW. As can be seen, different values are found which are a result

of the different layers under CO. From [1] experiments have shown, the H_2O is not thought to be spontelectric because of the strong H–bonding in the films. However as already mentioned, p–ASW has also been shown to possibly harbouring a surface potential [26] from Kelvin probe measurements. If this potential is positive, as CO, then this could be the reason for the greater calculated potential for CO on p–ASW as a cumulative value would be observed as when combining different spontelectric films [1]. For the c–ASW and CSW films the nature of the H_2O surface being different could cause CO to bind in a variety of fashions leading to random orientations of CO on the surface for c–ASW as compared to the more ordered CSW. This would mean that the surface could have an effect on the overall surface potential as previously thought of as not being the case.

To summarise the different models and their results, **Table 5.12** has been created for direct comparison between the averaged values over the deposition temperatures.

Molecular system	**Measured E_S / $\times 10^7$ V m^{-1}**	**Calculated E_S / $\times 10^7$ V m^{-1}**	**Potential per Monolayer / mV ML^{-1}**
N_2O on SiO_2	6.3 ± 0.30	5.71 ± 0.30	19.4
CO on SiO_2	–	3.72 ± 0.15	12.6
CO on p–ASW	–	3.70 ± 0.15	12.6
CO on c–ASW	–	1.99 ± 0.15	6.7
CO on CSW	–	2.83 ± 0.15	9.6

Table 5.12: This table summarises the results obtained through the analysis of the RAIRS data of N_2O and CO. As can be seen for the CO data, peculiar results are obtained when the substrate is changed as already discussed in the text.

This section has discussed the use of RAIRS to investigate the spontelectric effect of dipolar molecules. Through the analysis a good agreement between observations and modelled N_2O data has been shown. The same principles have then been used to show that CO exhibits the spontelectric effect as well. Some questions are still outstanding, such as the double valued–ness of CO and the different spontelectric fields exhibited on different surfaces. However, a surface potential is believed to be present in such multilayer films.

5.5 Astrophysical Implications

While N_2O has been detected in the astronomical environment, CO is the main molecule of interest with respect to the spontelectric effect in the interstellar medium (ISM). As stated previously CO has been found in relatively pure quantities [43, 44] where the film thicknesses can reach as much as 50 to 60 ML in molecular clouds and pre–stellar cores. In these cold cores, the degree of ionisation has been estimated to be lower than other ultraviolet (UV) shielded areas of the ISM by a factor of five to ten [45]. The degree of ionisation in a cold core is due to cosmic rays inducing ionisation as they travel unobstructed through different media in the ISM. For a typical core density of about 10^5 molecules cm^{-3}, the cosmic ray induced ionisation fraction has been estimated at about 3×10^{-8} [46–48]. The degree of ionisation in these regions of the ISM has considerable impact on the chemistry; on the cooling rates when molecular clouds collapse; and on the magnetic fields during the early stage of stellar formation. A dust grain is typically thought of as having one negative charge per grain on the surface. However, a surface potential from a CO multilayer can have a great impact on this surface charge and possibly change it drastically.

The work of Nielbock *et al.* [49] and Carelli *et al.* [50] are two of many studies that discuss the observations of CO being depleted from the gas phase as it condenses onto dust grains. CO can naturally also undergo reactions to form CO_2 [51] or CH_3OH [52] and thereby be depleted in general. Hence, diminishing a potential spontelectric effect on dust grains. However, this is not considered here for simplicity. An estimate of the time taken for CO to deplete from the gas phase and form nearly 12 ML has been conducted in connection with the spontelectric potential of CO [31]. This analysis was done by considering the highly studied molecular cloud core of Barnard 68 (B68) with H_2 number density (n_{H_2}) of 10^5 molecules cm^{-3}, ratio of [CO] to [H_2] of 10^{-4} and temperature (T) of 10 K. These parameters along with the density of dust grains of 2 g cm^{-3} as observed astronomically [53, 54] and the proportion of the mass of a grain as compared to the medium of 0.013 [55] lead to the value of 12 ML. This value also considered the effect on the dust grain radius, taken to be 0.1 μm [56], and its change of radius as CO layers grow as a function of time. The overall results of this calculation are shown in **Figure 5.25** [31].

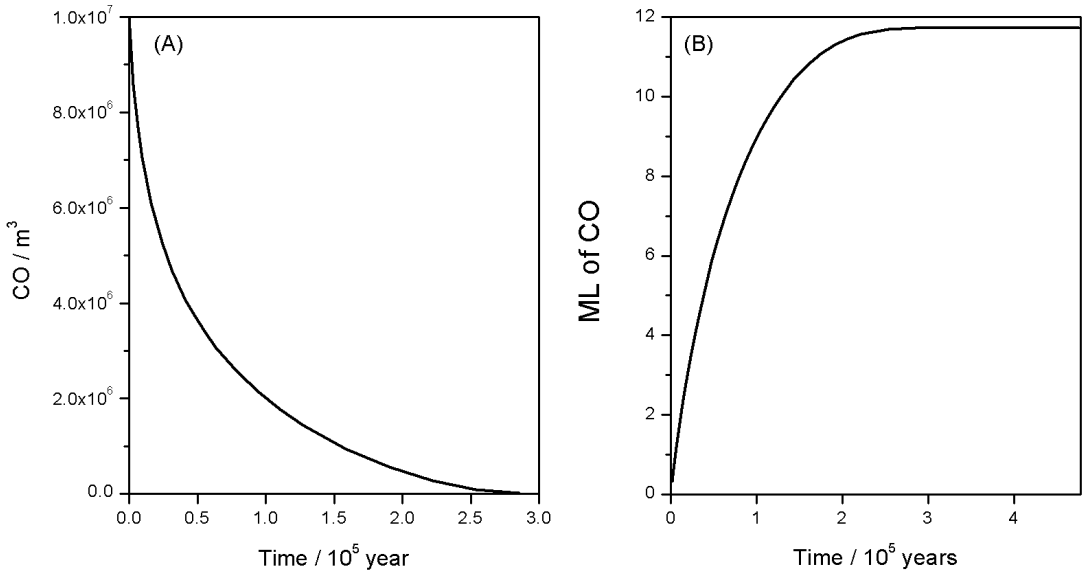

Figure 5.25: The two graphs show the depletion of CO from the gas phase **(A)** as the molecules condense onto the cold interstellar dust grain **(B)** with time. Both graphs have been done with typical astronomical conditions as found in the core of B68 [31].

As explained, **Figure 5.25 (A)** shows the depletion of CO from the gas phase while **(B)** is of CO ice growth in ML with time. As can be seen, nearly all CO is condensed onto the surface in **(A)** in a time of about 2.9×10^5 years. A monolayer is formed after about 4×10^4 years in **(B)**. Further to **Figure 5.25**, the analysis of CO on a dust grain also involves an estimate of the rate of electrons impacting a grain as based on previous work by Draine and Sutin [48]. Both of these models include a cross–section (dust grain itself), but also a factor involving the effective charge (v) of a dust grain (either repelling or attracting electrons or ions) with the reduced temperature (τ) which has all been summed up in $f(v,\tau)$. v in the case of this model relates to the charge on the dust grain divided by the charge of the incident species, either an electron or ion (specifically H^+ here). The work by Draine and Sutin resulted in **Equation 28** for the rate of collision of a species (X) per second with a dust grain surface;

$$J_X = n_X S_X \left({}^{kT_X}/_{m_X} \right)^{0.5} \times \pi a^2 \times f(v,\tau) \qquad \textbf{Equation 28}$$

where the subscript X refers to either electrons (e) or ions (i). n is the number of species present, S is the sticking coefficient of the species (set to unity [57, 58]), k is the rate constant, m is the mass of the species of interest and a is the grain radius including the increasing size of CO ice. T is the temperature of the species (of the electrons in this case) which has been estimated at 10 K as the electron equilibrates to the kinetic

temperature of the surroundings initially through electronic inelastic collisions and then elastic collision with H_2 in the gas phase. Also, $f(v,\tau)$ is equal to $[1 + (4\tau + 3v)^{-0.5}]^2 \exp((-v/(1 + v^{-0.5}))/\tau)$, $1 + (\pi/2\tau)^{0.5}$ and $(1 - (v/\tau))(1 + 2/(\tau - 2v))^{0.5}$ for negatively, neutral and positively charge dust grains.

On average, and in principle, the flux of electrons and ions should be the same over time considering how these species are produced from neutral species becoming two oppositely charged species through the interaction with cosmic rays. For this to hold, τ is set to 0.1 – 0.2, leading to an implied charge on the dust grains of –0.91 through $1/[1 + (\tau_0/\tau)^{0.5}]$ where τ_0 is 0.00139 [48]. This value implies that the grain is negatively charged, however the same calculation can be made for the removal of an electron where the grain charge becomes 1.09. For these values of grain charge, and a value of τ set to 0.2, **Table 5.13** [31] can be set up when calculating **Equation 28**.

Species	Grain Charge	Lifetime to hit grain / years
e^-	–0.91	0.32 – 0.64
e^-	0	0.03
e^-	+1.09	0.01
H^+	–0.91	0.32 – 0.64
H^+	0	1.27
H^+	+1.09	31.71 – 63.42

Table 5.13: This table sums up the estimated timescales for a species (electron or proton) to encounter an interstellar dust grain as calculated through **Equation 28** [31].

Table 5.13 shows the result of **Equation 28** when using a temperature of 10 K for the species. What can be stated from this is that the time taken for either of the charged species hitting any type of grain (neutral or charged) is much less than the time taken for an icy mantle to grow, as has been estimated being on the mega–year scale for environment such as B68.

Considering the implications of a surface potential due to spontelectric CO on a dust grain, means thinking of the icy mantle formation. CO ice will slowly form as illustrated in **Figure 5.25**, and as shown in (for instance) **Figure 5.15**, a multilayer exhibiting the LO–TO splitting is present at about 5 ML. The LO–TO splitting and its shifts with temperature being an indication of a spontelectric field means that at, say, 5

ML a surface potential is present. A value of 5 ML is chosen since the splitting is observed and because the spontelectric effect is a macroscopic effect needing a certain amount of material for it to "turn on". The time taken for a 5 ML film to be formed is about 5,000 years as seen in **Figure 5.25** and at this time, the spontelectric effect becomes active instantly creating a surface potential, ϕ, of about 33 mV (recollecting 6.695 mV ML^{-1}). This potential is equivalent to about 2.3 surface charges, q, as calculated through **Equation 29**.

$$q = 4\pi\varepsilon_0 a n_{ML} \phi \qquad \textbf{Equation 29}$$

where ε_0 is the permittivity of free space, a is the dust grain radius and n_{ML} is the number of monolayers of CO. This means that a dust grain goes from a surface charge of –0.91 to +1.4, or in other words, some grains will have a charge of +1 and others +2 with an average of +1.4. The reason for the positive potential is because of the orientation of CO on the surface [30] as mentioned earlier. With this in mind, the value of about 10^{-2} years for an electron to meet a dust grain is decreased by a factor of 1.09/2 when considering the dust grains with 2 surface charges (encounter time is now about 5×10^{-3} years). As the dust grain attracts electrons due to its positive charge, it then becomes neutral needing another 3×10^{-2} years before new electrons or ions begin to encounter the dust grain on a timescale of a further 0.32 – 0.64 years. As both electrons and ions stick to the neutral dust grain recombination reactions can occur [57], in turn creating neutral species. However, the spontelectric state of CO is still present and growing as more CO is adsorbed onto the dust grain. The cycle of electron attraction, followed by ion attraction leading to neutral species will continue and drag charge out of the gas phase. This will in effect continue until CO has been depleted from the gas phase and a film of 12 ML, as shown in **Figure 5.25**, is present. This amount of molecules equates to about 5.75 charges on the surface, meaning that 5.75 electrons will be attracted and again leading to an equal number of ion being attracted. A sketch of this can be seen in **Figure 5.26**.

Recombination between electrons and cations will involve mobility on the grain surface as discussed by Stamatellos *et al.* [59] where an electron residence time at an adsorption site was given to be about 10^5 seconds or about 3×10^{-3} years. In this time the electron can tunnel through a distance of about 20 nm, this in turn means that an electron can

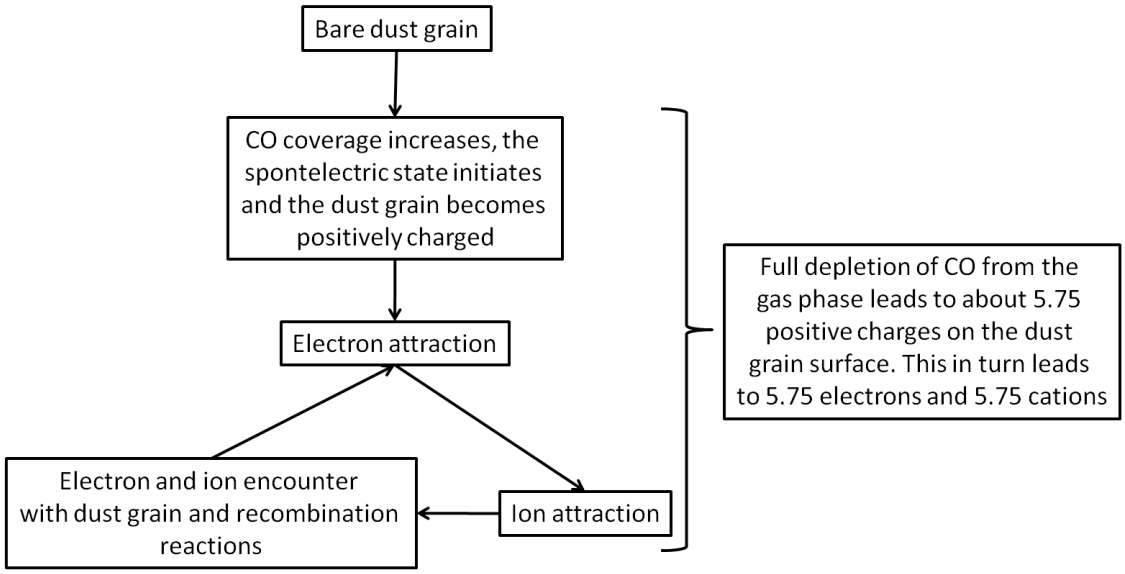

Figure 5.26: This figure shows how CO initially aggregates onto a dust grain. The spontelectric effect in CO starts when a multilayer is formed thereby creating a positively charged surface. This attracts electrons, which in turn attracts cations and together they can recombine leading to the cycle starting over.

generally cover an entire dust grain surface (with a radius of 0.1 μm) in the space of 100 residence lifetimes. Therefore, a time of $\leq 10^7$ seconds (or 0.1 years) is needed for an electron to interact with a cation. Further to this, without the spontelectric effect of CO, an average of 0.91 electrons and 0.91 cations being present on the surface will lead to recombination occurring on the timescale of $\leq 10^7$ seconds (or 0.1 years). The recombination reactions will occur as a proportionality of concentrations of the different species on the dust grain, *i.e.* $[e_{grain}] \times [cation_{grain}]$. However, as discussed, the spontelectric state of CO when 12 ML have adsorbed onto the dust grain surface will lead to an average of 5.75 charges on the surface. Therefore a new relationship will be setup where the ratio of species of non–spontelectric grains to spontelectric grains becomes 5.75:0.91, or a factor of about 6.3 increase in recombination efficiency. And, because of the balance between negatively and positively charged species over time $[e_{grain}]=[cation_{grain}]=[e_{grain}]^2$ which leads to the ratio of $(5.75/0.91)^2$ equalling about 40. This value of 40 (where the increase in efficiency of about 6.3 comes from $40^{0.5}$) is the increase in timescale for recombination, now being $\leq 2.5 \times 10^5$ seconds (or 7.9×10^{-3} years). This increase in recombination will have a direct effect on the degree of ionisation in the ISM thereby reducing it.

To illustrate this reduction of the degree of ionisation in the ISM, B68 will once again be used as an example. The rate of cosmic ray ionisation (ζ_{cr}), typically about 3×10^{-17}

s^{-1} [55], combined with H_2 density (10^5 molecules cm^{-3}) is responsible for the production of charge while recombination reactions through ion–electron processes in the gas and solid phase remove charge. In the gas phase, removal of charge is mainly seen through the $e^- + H_3^+$ route where H_3^+ itself is responsible for about 0.2% of the total ionisation [55] with a rate coefficient of recombination of about 2×10^{-7} cm^{-3} s^{-1} [60]. Multiplying these values together gives an effective rate coefficient of about 4×10^{-8} cm^3 s^{-1} which can be balanced with the cosmic ray ionisation per volume to give 8.7×10^{-3} cm^{-3} (through $(3 \times 10^{-17}$ $s^{-1} \times 10^5$ cm^{-3} / 4×10^{-8} cm^3 $s^{-1})^{0.5}$) which in turn gives an ionisation fraction of 8.7×10^{-8}. The standard ionisation fraction observed for B68 is about 5×10^{-9} meaning that pure gas–phase recombination reactions are not enough to produce the observed ionisation fraction values. This must mean that the grain surface accounts for the rest of charge removal in the cores similar to B68.

If, for the time being, only the non–spontelectric grain surface is considered, then a statement can be made that the rate of loss of ionisation is purely due to the dust grain density, n_g (0.73 m^{-3}), where the rate can be symbolised through **Equation 30**;

$$\text{rate of loss} = kn_g = 7.3 \times 10^{-12} \times kn_{H_2}. \qquad \textbf{Equation 30}$$

In this equation, k is the rate constant for this particular first order process, n_{H_2} is the H_2 density (10^5 cm^{-3}) and as can be seen n_g has been changed to n_{H_2} by considering the ratio of the two values. As there is a balance between produced charge and removed charge, this equation can be related to the previous mention of the creation of charged species ($\zeta_{cr} \times n_{H_2}$) through the **Equation 31**;

$$\zeta_{cr} n_{H_2} = 7.3 \times 10^{-12} \times kn_{H_2}. \qquad \textbf{Equation 31}$$

Now, this equation can be solved for k which yields a value of about 4.1×10^{-6} s^{-1} which can also be thought of as 2.4×10^5 s (or 7.7×10^{-3} years) between different recombination reactions. This value is very similar to the calculated value between recombination reactions on a spontelectric surface of 7.9×10^{-3} years when 5.75 charges are found on a complete 12 ML film of CO. This means that the production of charge (as calculated through ζn_{H_2}) is balanced with the removal of charge. For a non–spontelectric grain, the efficiency of charge removal would be decreased by a factor of 6.3 as discussed previously. Gas–phase charge removal combined with non–

spontelectric grain charge removal leads to an ionisation degree of about 3×10^{-8} which is not unusual for dark regions of the ISM [55, 61]. For that reason, spontelectric or not, the role of dust grains with regards to charge removal through recombination reactions in dark clouds is pivotal. However, with the presence of spontelectric CO this charge removal will be amplified by a factor of 6.3 [31] as mentioned earlier.

The recombination of charged species on dust grains has been discussed in detail in Whittet *et al.* [62] where electrons and ions on the surface are removed continuously on a timescale of about 2×10^5 years as this is close to the completion of the 12 ML CO film in **Figure 5.29**. In the model proposed by Whittet *et al.* a polarisation interaction between ions or electrons and the grain is included which is naturally of importance in this work. The model also states that the minimum grain size is important, however this is not accounted for in this work. Using equation 5.15 from Draine *et al.* [48] with a temperature of 10 K and ion mass of a proton and setting this equal to the charge loss rate on a non–spontelectric grain leads to a degree of ionisation of about 2.8×10^{-8}. This value includes the gas–phase removal of charge and can be considered the same as the degree of ionisation discussed above with 0.91 charges on a non–spontelectric grain.

The ideas set out above indicate that spontelectric CO will aid in the removal of charge from the gas phase and further decrease the degree of ionisation in cores such as B68. The decrease is on the order of about 6.3 as shown, however there are considerable uncertainties in this value and error bars cannot be simply assigned. As has been stated throughout this work, the assumption of a dust grain having a radius of 0.1 μm might need to be modified as there are more and more observational data showing that the need for the grain size distribution to be re–visited to include larger grain populations [63, 64].

5.5 Conclusion

When considering the data and analysis of the N_2O experiments, a correlation between LO and TO peak contraction is observed which can be connected to the behaviour of a spontelectric material. The model developed and explained throughout this chapter is based on the observed and measured spontelectric effect of N_2O and has been shown to follow the changes in LO–TO frequencies ($\Delta\nu$) as the deposition temperature increases as measured through RAIRS. Good agreement between the model and experimental

data indicate that the spontelectric effect can be investigated through observation of the LO–TO splitting by RAIRS. Since no surface potential is measured through RAIRS, this is an independent method of investigation and gives further credence to the proposal that the spontelectric effect is based on dipole orientation.

As has been explained, LO–TO splitting arises through the intrinsic effects of activating different phonons in a solid film as it is perturbed by the IR beam. However, as is also explained, the LO–TO splitting is enhanced due to the spontelectric effect through the vibrational Stark effect. The ratio of the splitting due to a spontelectric field with the total splitting ($\Delta\nu_S/\Delta\nu$) can be seen to decrease with temperature as the spontelectric effect decreases. This factor therefore furthers the understanding of the LO–TO splitting of solid films when temperature dependent shifts are observed. This can therefore mean that molecules exhibiting a temperature dependence on the peak positions of the LO–TO splitting can be spontelectric.

As the dependence of temperature on the LO–TO splitting has been shown to be due to the spontelectric effect, CO on SiO_2 can be stated as being spontelectric. The same behaviour is observed for CO as for N_2O, although the peak shifts are smaller. The range of temperature of these experiments is also less than that of N_2O leading to reliable data only coming from experiments in the 20 K to 24 K temperature range. Having said this, a trend is observed lending credence to the spontelectric state of CO on SiO_2. In addition to this, it has also been shown that inverting the analysis used in the case of N_2O that the surface potential arising from the spontelectric effect can be calculated through the LO–TO splitting. The size of this potential is calculated to be $5.71 \pm 0.30 \times 10^7$ V m^{-1} as compared to the directly measured experimental value of $6.30 \pm 0.30 \times 10^7$ V m^{-1}. For CO, a surface potential has been calculated to be $3.72 \pm 0.15 \times 10^7$ V m^{-1}.

CO on different multilayers of H_2O has also been studied. The relative spontelectric field of CO on SiO_2 to CO on p–ASW to CO on c–ASW to CO on CSW is 1:1:0.76:0.52 when CO is deposited at 20 K for all substrates save c–ASW. As has already been explained, p–ASW may be spontelectric itself, and if the direction of the field is the same as that of CO, an additive effect will be observed leading to a greater surface potential.

As discussed in **Chapter 4**, bare dust grain regions can become available for CO adsorption in the early stages of mantle formation. At later stages when H_2O has formed and is the dominant part of an icy mantle, CO can also adsorb onto this. CO on SiO_2 and CO on H_2O have been shown to both be spontelectric when a great enough film is formed. The effect of the spontelectric CO layer is to drag charge (ions and electrons) from the gas phase. In the solid state, electrons and cations can recombine, returning the grain to its positive charge, thereby attracting more electrons and the catalytic cycle continues. The model, as explained, suggests that the efficiency of spontelectric grains in removing charge from an interstellar cloud is increased by a factor of about 6 as compared to non–spontelectric grains.

Spontelectric CO may not be the only pathway for charge removal in interstellar clouds, and the model being based on a dust grain radius of 0.1 μm leaves it open for further modelling work with other grain radii. However, the low degree of ionisation in cold regions can be due to spontelectric CO when depleted from the gas phase. It would therefore be interesting to investigate how the models governing the physics and chemistry in dense molecular clouds, pre– and protostellar cores, low–mass star formation and planet forming disks are influenced if the spontelectric effect of CO is included.

5.6 References

[1] D. Field, O. Plekan, A. Cassidy, R. Balog, N.C. Jones and J. Dunger, *Int. Rev. Phys. Chem.*, 2013, **32**, 345

[2] R. Balog, P. Cicman, N. Jones and D. Field, *Phys. Rev. Lett.*, 2009, **102**, 2

[3] D. Field, O. Plekan, A. Cassidy, R. Balog and N. Jones, *Europhys. News*, 2011, **42**, 32

[4] O. Plekan, A. Cassidy, R. Balog, N.C. Jones and D. Field, *Phys. Chem. Chem. Phys.*, 2011, **13**, 21035

[5] O. Plekan, A. Cassidy, R. Balog, N.C. Jones and D. Field, *Phys. Chem. Chem. Phys.*, 2012, **14**, 9972

[6] A. Cassidy, O. Plekan, R. Balog, N.C. Jones and D. Field, *Phys. Chem. Chem. Phys.*, 2012, **15**, 108

[7] A. Cassidy, O. Plekan, R. Balog, J. Dunger, N.C. Jones and D. Field, *J. Phys. Chem. A*, 2014, **118**, 6615

[8] A. Cassidy, O. Plekan, J. Dunger, R. Balog, N.C. Jones, J. Lasne, A. Rosu–Finsen, M.R.S. McCoustra and D. Field, *Phys. Chem. Chem. Phys.*, 2014, **16**, 23843

[9] L.H. Jones and B.I. Swanson, *J. Phys. Chem.*, 1991, **95**, 2701

[10] M.A. Ovchinnikov and C.A. Wight, *J. Chem. Phys.*, 1993, **99**, 3374

[11] M.A. Ovchinnikov and C.A. Wight, *J. Chem. Phys.*, 1994, **100**, 972

[12] M.P. Collings, J.W. Dever, H.J. Fraser and M.R.S. McCoustra, *Astrophys. Space Sci.*, 2003, **285**, 633

[13] R.M. Escribano, G.M. Munoz Caro, G.A. Cruz–Diaz, Y. Rodriguez–Lazcano and B. Mate, *P. Natl. Acad. Sci. USA*, 2013, **110**, 12899

[14] B. Rowland, N.S. Kadagathur and J.P. Devlin, *J. Chem. Phys.*, 1995, **102**, 13

[15] E. Whalley, *Can. J. Chern.*, 1977, **55**, 3429

[16] J.P. Devlin, *J. Chem. Phys.*, 1989, **90**, 1322

[17] M.J. Wojcik, V. Buch and J.P. Devlin, *J. Chem. Phys.*, 1993, **99**, 2332

[18] J.E. Bartmess and R.M. Georgiadis, *Vacuum*, 1983, **33**, 149

[19] J. Lasne, A. Rosu–Finsen, A. Cassidy, M.R.S. McCoustra, D. Field, *Phys. Chem. Chem. Phys.*, 2015, **17**, 20971

[20] H. Schlichting and D. Menzel, *Rev. Sci. Instrum.*, 1993, **63**, 2013

[21] D.J. Burke, A.J. Wolff, J.L. Edridge and W.A. Brown, *J. Chem. Phys.*, 2008, **128**, 104702

[22] Y.S. Kim and R.I. Kaiser, *Astrophys. J.*, 2009, **181**, 543

[23] S. Shin, H. Kang, J.S. Kim and H. Kang, *J. Phys. Chem. B*, 2014, **118**, 13349

[24] A. Cassidy, M.R.V. Jørgensen, A. Rosu–Finsen, J. Lasne, J.H. Jørgensen, A. Glavic, V. Lauter, B.B. Iversen, M.R.S. McCoustra and D. Field, submitted to *J. Phys. Chem. C*

[25] A.G.G.M Tielens, *Rev. Mod. Phys.*, 2013, **85**, 1021

[26] C. Bu, J. Shi, U. Raut, E.H. Mitchell and R.A. Baragiola, *J. Chem. Phys.*, 2015, **142**, 134702

[27] M.P. Collings, J.W. Dever, H.J. Fraser, M.R.S. McCoustra and D.A. Williams, *Astrophys. J.*, 2003, **583**, 1058

[28] J. Lasne, A. Rosu–Finsen, A. Cassidy, M.R.S. McCoustra, D. Field, *Phys. Chem. Chem. Phys.*, 2015, **17**, 30177

[29] G.C. Munoz Caro, Y.–J. Chen, S. Aparicio, A. Jimenez–Escobar, A. Rosu–Finsen, J. Lasne and M.R.S. McCoustra, *Astron. Astrophys.*, 2016, **589**, A19

[30] M.P. Collings, J.W. Dever and M.R.S. McCoustra, *Phys. Chem. Chem. Phys.*, 2014, **16**, 3479

[31] A. Rosu–Finsen, J. Lasne, A. Cassidy, M.R.S. McCoustra and D. Field, *Phys. Chem. Chem. Phys.*, 2016, **18**, 5159

[32] J.E. Schaff and J.T. Roberts, *J. Phys. Chem.*, 1996, **100**, 14151

[33] J.E. Schaff and J.T. Roberts, *Langmuir*, 1999, **15**, 7232

[34] P. Jenniskens and D.F. Blake, *Science*, 1994, **265**, 753

[35] P. Jenniskens and D.F. Blake, *Astrophys. J.*, 1996, **473**, 1104

[36] Encylopedia Astronautica, http://www.astronautix.com/props/n2osolid.htm

[37] S.A. Andrews and S.G. Boxer, *J. Phys. Chem. A*, 2002, **106**, 469

[38] E.S. Park and S.G. Boxer, *J. Phys. Chem. B*, 2002, **106**, 5800

[39] I.T. Suydam and S.G. Boxer, *Biochemistry*, 2003, **42**, 12050

[40] G. Schkolnik, J. Salewski, D. Millo, I. Zebger, S. Franzen and P. Hildebrandt, *Int. J. Mol. Sci.*, 2012, **13**, 7466

[41] J. Topping, *Proc. R. Soc. London, Ser. A*, 1927, **114**, 67

[42] S.A. Blair and A.J. Thakkar, *J. Chem. Phys.*, 2014, **141**, 074306

[43] A. Brady Ford and Y. L. Shirley, *Astrophys. J.*, 2011, **728**, 144

[44] K.M. Pontoppidan, H.J. Fraser, E. Dartois, W.–F. Thi, E.F. van Dishoeck, A.C. Boogert, L. d–Hendecourt, A.G.G.M. Tielens and S.E. Bisschop, *Astron. Astrophys*,. 2003, **408**, 981

[45] S. Maret and E.A. Bergin, *Astrophys. J.*, 2007, **664**, 956

[46] E.A. Bergin, J. Alves, T. Huard, and C.J. Lada, *Astrophys. J. Lett.*, 2002, **570**, L101

[47] R.T. Garrod and T. Pauly, *Astrophys. J.*, 2011, **735**, 15

[48] B.T. Draine and B. Sutin, *Astrophys. J.*, 1987, **320**, 803

[49] M. Nielbock, R. Launhardt, J. Steinacker, A.M. Stutz, Z. Balog, H. Beuther, J. Bouwman, Th. Henning, P. Hilly–Blant, J. Kainulainen, O. Krause, H. Linz, N. Lippok, S. Ragan, C. Risacher and A. Schmiedeke, *Astron. Astrophys.*, 2012, **547**, L4

[50] F. Carelli, T. Grassi and F.A. Gianturco, *Astron. Astrophys.*, 2013, **549**, A103

[51] H.D. Nissen, N.J. Cunningham, M. Gustafsson, J. Bally, J.–L. Lemaire, C. Favre, and D. Field, *Astron. Astrophys.*, 2012, **540**, A119

[52] H.M. Cuppen, E.M. Penteado, K. Isokoski, N. van der Marel and H. Linnartz, *Mon. Not. Roy. Astron. Soc.*, 2011, **417**, 2809

[53] B.T. Draine, *Annu. Rev. Astron. Astrophys.*, 2003, **41**, 241

[54] C.A. Poteet, D.C.B. Whittet and B.T. Draine, *Astrophys. J.*, 2015, **801**, 110

[55] E.F. van Dishoeck, E. Herbst and D.A. Neufeld, *Chem. Rev.*, 2013, **113**, 9043

[56] M.P. Redman, J.M.C. Rawlings, D.J. Nutter, D. Ward–Thompson and D.A. Willams, *Mon. Not. Roy. Astron. Soc.*, 2002, **337**, L17

[57] J.F. Alves, C.J. Lada and E.A. Bergin, *Nature*, 2001, **409**, 159

[58] B. Parise, A. Belloche, F. Du, R. Gusten and K.M. Menten, *Astron. Astrophys.*, 2011, **526**, A31

[59] D.Stamatellos, A.P.Whitworth and D. Ward–Thompson, *Mon. Not. R. Astron. Soc.*, 2007, **379**, 1390

[60] J.S. Mathis, W. Rumpl and K.H. Nordsieck, *Astrophys. J.*, 1997, **217**, 425

[61] J. Steinacker, C.W. Ormel, M. Andersen and A. Bacmann, *Astron. Astrophys.*, 2014, **564**, A96

[62] D.C.B. Whittet, P.F.Goldsmith, and J.L. Pineda, *Astrophys. J.*, 2010, **720**, 259

[63] M. Guelin, W.D. Langer, R.L. Snell and H.A. Wootten, *Astrophys. J.*, 1977, **217**, L165

[64] W.D. Langer, R.W. Wilson, P.S. Henry and M. Guelin, *Astrophys. J.*, 1978, **225**, L139

Chapter 6

Concluding Remarks and Outlook

Contents of this chapter

6.1 Introduction

The general storyline of this thesis has been to study one of the solid state formation pathways of interstellar H_2O. From there, considering the initial low concentration of H_2O on an interstellar dust grain, the focus changed towards looking at how H_2O behaves on such model grains, and thus investigating how an interstellar dust grain ice mantle might build up. As time continues, the mantle grows rich with other molecules. The second most abundant molecule in such a mantle is CO. The multilayer of CO on a typical interstellar dust grain model and on various forms of H_2O was then studied with the focus of its inherent spontaneous electric field leading to a surface potential. The remainder of this brief chapter will highlight the conclusions of the individual chapters along with future work as there are yet more interesting experiments needed to further our understanding of the results presented in this thesis.

6.2 Chapter 3

Chapter 3 introduced one aspect of the mechanism of H_2O formation as discussed in [1] purely focussing on the O atom chemistry on SiO_2, porous amorphous solid water (p–ASW), compact solid amorphous water (c–ASW) and crystalline solid water (CSW). While these results are preliminary and considerable future work remains possible, a few conclusions can be drawn.

As has been shown through temperature programmed desorption (TPD) and reflection–absorption infrared spectroscopy (RAIRS), O_3 is formed on all surfaces studied (SiO_2, p–ASW, c–ASW and CSW) without an apparent preference of surface. O_2 is naturally also formed from the O atoms beam, however no evidence for H_2O_2 formation or reactive desorption of O_2 or O_3 was found to occur. The lack of reactive desorption could, however, be because of the background presence of O_2 in the main chamber from the beam source.

The RAIR spectra of O_3 formed after dosing the atomic beam for 50 minutes appear to be the same irrespective of the sample surface. The reason for the similar features could be one of three; O_3 forms islands on the investigated surfaces, O_3 has adsorbed to SiO_2 as 20 ML H_2O have not yet covered the entire SiO_2 surface or O_3 is formed in a matrix of O_2. Of these possible scenarios, O_3 in an O_2 matrix seems the most likely. In all

cases, four contributions to the O_3 feature were observed as shown in **Table 6.1** along with the corresponding literature values [2]. And, from the TPD experiments of O_2, a variety of binding energies were found as listed in **Table 6.2**.

	SiO_2 (± 1)	**p–ASW (± 1)**	**c–ASW (± 1)**	**CSW (± 1)**	**Literature (± 2)**
$[O_3...O]$ / cm^{-1}	1031	1031	1032	1032	1032
O_3 (O–O)asymmetric stretch / cm^{-1}	1036	1037	1037	1037	1037
$[O_3...O_3]$ / cm^{-1}	1045	1045	1045	1045	1042

Table 6.1: This table shows the overall results of all the RAIR spectra of O_3 and the interactions leading to the IR spectra. These values can be compared to literature values as stated in the last column.

	O_2 beam	**O atomic beam**			
	SiO_2	**SiO_2**	**p–ASW**	**c–ASW**	**CSW**
E_{des} / kJ mol^{-1}	8.5 ± 0.1	6.7 ± 0.2	7.4 ± 0.6	6.3 ± 0.4	6.7 ± 0.2
ν / molecules cm^{-2} s^{-1}	$4 \times 10^{30\pm1}$	$4 \times 10^{27\pm1}$	$1 \times 10^{25\pm2}$	$1 \times 10^{26\pm2}$	$5 \times 10^{27\pm1}$

Table 6.2: This table shows the full range of TPD results of O_2 desorption from the different surface investigated (SiO_2, p–ASW, c–ASW and CSW). The main body of the results is of O atomic beam dosing with O_2 molecular beam dosing results shown as a comparison.

As can be seen in **Table 6.2**, a spread of about 2 kJ mol^{-1} is determined in the values for the desorption energies when changing the deposition method and surface deposited onto. The reason for the discrepancy has been explained to be due to the energy transmitted to the film from the atoms and molecules in the beam and the release of energy during molecular O_2 (and O_3 to a lesser extent) formation. These energies could possibly also lead amorphisation of the CSW film as explained in **Chapter 3**.

TPD measurements on O_3 were also conducted however, individual TPD traces for O_3 gathered from the different surfaces show very little O_3 desorption. The cause for this has been explained as arising from interference of O_2 when desorbing from the cold finger. However, a cumulative TPD trace has been constructed by addition of all the O_3 TPD data. This trace yielded a desorption energy of 14.7 ± 0.5 kJ mol^{-1} which is in good agreement with literature value of 15.2 ± 0.5 kJ mol^{-1} [3, 4]. Further to this, a model has been built to show the possible extent of the O_2:O_3 being about 1:0.20 in the

presented experiments while the simulated destruction of O_3 has been judged as not being the reason for the lack of O_3 signal in the TPD experiments. Changing the experimental method to avoid the crossover signal from O_2 and O_3 desorption would show the accuracy of the ratio obtained from this model.

The O atom beam has to be fully calibrated and characterised which means placing the quadrupole mass spectrometer (QMS) in line–of–sight with the beam. Then a direct measurement of the cracking fraction can be determined by initially having a pure O_2 beam and then turning on the plasma source. The direct measurement of m/z 32 and 16 will lead to a more precise O atom cracking fraction form there, the power and flux will have to be varied to find the optimum working conditions. This while monitoring the live signal from the spectrophotometer will also show any impurities in the source chamber. With an accurate, and hopefully higher cracking fraction, the same experiments as discussed in **Chapter 3** will have to be done again for comparison if the beam characteristics have changed as a result of the calibration process. With the experiments discussed in mind, an improvement in the experimental procedure will have to be implemented. This improvement has to do with the experimental TPD results and the lack of m/z 48 signal. As O_3 comes into contact with the filament of the QMS, it breaks down into m/z 32 and 16 which can naturally be monitored with the QMS. However, a discernible difference in the m/z 32 and 16 was not measured in these experiments due to desorption of O_2 from the sample mount and cold finger in the same temperature region as O_3 desorption occurs. Therefore, attention has to be given to the applied heating ramp during a TPD experiment in the attempt to raise the sample temperature to O_3 desorption before O_2 is desorbed from the sample mount and cold finger. This was not attempted in this work due to severe time constraints, however the result of this will give much clearer indication of how much O_3 is formed and if there is a difference in concentration when using different substrates.

O atom bombardment would also be interesting to investigate as a function of the sample temperature. The formation of O_2 and O_3 as presented can be considered to go through a mixture of Langmuir–Hinshelwood and Eley–Rideal type mechanisms without the reaction products desorbing form the surface. Increasing the temperature to, say 30 or 35 K, would mean a multilayer of O_2 cannot be deposited onto SiO_2, however O_2 binding to the most favourable sites on the surface is still possible as seen in temperature programmed desorption experiments of sub–monolayer O_2 [5]. As has also

been shown in this thesis, O_3 desorption occurs at temperatures of 50 – 60 K. Increasing the temperature further to a point where the cold finger allows less O_2 to adsorb will push the O_3 formation further into the domain of the Eley–Rideal type mechanism, however this will also mean O_2 is unlikely to stick to the sample at any coverage. However, the work of He *et al.* [6] has shown that the binding energy of O atoms on H_2O and SiO_2 surfaces is of the order of about 13 – 15 kJ mol^{-1} respectively meaning that O could possible still be deposited onto the sample with O_2 in the gas–phase reacting to form solid state O_3.

When a full range of experiments with the O atomic beam on SiO_2, p–ASW, c–ASW and CSW have been done, further experiments including the H atomic beam source can be conducted. Characterising the H atomic beam the same way as done for the O atomic source and then combining the experiments will lead to a new way of looking at the H_2O formation pathway in the interstellar medium. Experiments investigating H_2O formation by use of H atoms have been done previously such as hydrogenation of O [7] and O_3 [8]. However, there is still room for further experiments to be done. Such experiments could involve looking at the 'explosive desorption' [9, 10], which as mentioned could possibly occur when H_2 forms in the bulk or near–surface of an ice. Therefore, bombarding a p–ASW film with H atoms might eventually release H_2O into the gas–phase. H atom bombardment of H_2O films could potentially also form H_2O_2. Further to this, with the H atomic beam, reactive scattering could become possible to detect if molecules such as OH are made when bombarding an O_2 or O_3 film. Detecting molecular desorption during beam dosing is also called molecular beam modulation spectrometry and can be done with the mass spectrometer in the current position leading to specular scattering. Desorption of molecules can either be due to the surface temperature or because of released energy when molecules are formed, the latter process would be similar to an Eley–Rideal type mechanism. Such experiments can yield information about surface retention times of molecules and thus their distribution of binding energies. Further to future experiments involving the atomic beam system is the addition of beam choppers. This will allow for a continuous or pulsed atomic beam as the chopper can be mounted on a z–shift and has been designed to produce a minimum pulse time of 10 μs.

An ozoniser is also available in the laboratory which can be linked to the UHV chamber to background dose pure films of O_3. This was initially attempted in this work (however

not mentioned) and a pure O_3 gas was created, however *en route* to the central chamber O_3 decomposed to O_2. Decreasing the amount of stainless steel surfaces could lead to a lesser degree of decomposition as stated in Janssen *et al.* [11].

6.3 Chapter 4

Chapter 4 introduced the idea of H_2O de–wetting from SiO_2 surfaces at cryogenic temperatures similar to what is found in the ISM. This was investigated through reflection–absorption infrared spectroscopy and showed that the energy associated with de–wetting to be close to 2 kJ mol^{-1}. De–wetting of the 0.5 ML H_2O coverage was not observed when depositing the film as compact amorphous solid water (c–ASW) or crystalline solid water (CSW). This result with the simple simulations presented show that the isolated H_2O molecules reactively accreted or deposited from the gas phase will instantaneously form clusters of H_2O irrelevant of the typical temperatures of an interstellar dust grain. This has the effect of increasing the monolayer formation time from the previous estimate of 10^4 years [7]. For that reason bare dust grain surface will be left exposed for other molecules such as CO to adsorb to. Binding energies differ between dust grain surfaces and H_2O surfaces and sub–monolayer coverages of molecules are generally found to have higher binding energies when adsorbed to SiO_2 as compared to H_2O as shown for O_2, CO and CO_2 [12]. All in all, bare dust grain surfaces could provide an additional reason for the difference in observed and calculated abundances of molecules such as O_2 as the grains act as molecular sinks [13, 14]. Further to this, bombarding a 0.5 ML coverage of porous amorphous solid water film with O atoms possibly leads to a c–ASW film due to network reconnections in the molecular film. This means that H_2O formed on a dust grain surface at typical dust grain temperatures of 10 K can still become compact through atom bombardment and molecular formation leading to one possible explanation for the c–ASW form of H_2O on dust grains in the ISM [15].

To further investigate the H_2O de–wetting process, a variety of experiments can be performed. For continued experiments with a SiO_2 surface, CO could be used as a probe molecule. Firstly, obtaining an IR spectrum of, say 0.5 ML, CO on bare SiO_2 will provide a base to which other experiments can be compared. CO has been determined to not de–wet from a SiO_2 surface [5]. Then, dosing 0.5 ML H_2O followed by CO (assuming that CO initially adsorbs randomly to both SiO_2 and H_2O) will potentially

lead to time–resolved spectra of CO migrating from H_2O to SiO_2. From these experiments, and keeping the sample at about 20 K, dosing an increased coverage of H_2O followed by CO, while comparing the CO spectra to the CO–SiO_2 spectra, will eventually lead to CO having to adsorb to H_2O at great film thicknesses. At this point the IR spectrum of CO will change due to the difference between the CO–H_2O and CO–SiO_2 interactions. The amount of H_2O introduced onto the sample will be an indication of de–wetting ability of H_2O at these cryogenic temperatures.

Changing the surface for a silicate film with metallic centres, such as Fe^{2+}, to approach a better model of interstellar dust grains will also have an effect on a film of H_2O. In theory, the H_2O clusters formed on a pure SiO_2 film can move on the surface as isolated molecules do. Adding metal centres will have the effect of anchoring these H_2O clusters, possibly producing several smaller clusters formed at metal centres instead of roaming larger clusters as might be expected on SiO_2. Keeping the temperature low should minimise H_2O dissociation as H_2O dissociation on surfaces such as FeS has been noted as only occurring at elevated temperatures of hundreds of K [16]. The same experiments can also be attempted on a highly oriented pyrolitic graphite (HOPG) surface, however sub–monolayer coverages of H_2O seem to wet these surfaces, exhibiting non–zero order desorption kinetics [17].

Another experiment involving both a SiO_2 and a graphitic surface would be to dose a sub–monolayer of D_2O. If D_2O behaves the same way as H_2O, then monomers and dimmers of D_2O at about 2400 cm^{-1} [18] could be observed as the molecular film de–wets. From such observations, an activation energy can be collected and compared to that of H_2O.

Also, to test if a c–ASW film was actually created when bombarding the H_2O film with O atoms, a thicker film is needed. As O_2 is formed, the excess reaction energy must be dissipated somehow and when the reaction takes place on a H_2O film, it is likely that the energy will be transmitted into the lattice. Conducting experiments as Collings *et al.* [19] will give a better idea of what is happening as the O atom beam bombards the H_2O film. Once again, CO can be used as a probe. Deposition of CO onto bare SiO_2 and its subsequent TPD spectrum will be the reference for such a test. Then, the same quantity of CO desorbed from p–ASW will show a variety of signals such as CO multilayer desorption, CO desorption from ASW pores, CO desorption as H_2O crystallises and co–

desorption of CO with H_2O [18]. The volcano desorption of CO as H_2O crystallises will be of interest in this set of experiments. The reason for this is that dosing a film of ASW and then bombarding this film with O atoms should close the pores. Following O atom bombardment CO will be dosed onto this H_2O film which will not be able to thermally diffuse into the H_2O pores which are now sealed. For that reason a volcano desorption of CO as c–ASW becomes CSW is not expected.

6.4 Chapter 5

Chapter 5 discussed the presence of the spontaneous electric (spontelectric) field present in solid N_2O films. Experiments conducted at Aarhus University have measured a surface potential of several V in multilayer films of this dipolar molecule. Believed to be due to dipole orientation and alignment in the film, RAIRS was used to analyse this new phenomenon further. Through the observations and measurements of the longitudinal optical and transverse optical (LO–TO) splitting of N_2O multilayers, it was seen that the peaks of these features shift with temperature. As discussed in **Chapter 5**, changes in the LO–TO splitting can be related to the dipole alignment, as the splitting contracts with increasing temperature, the alignment decreases. This is a trait also observed for spontelectric molecules (except for methyl formate). A greater contraction of the LO–TO splitting is observed when raising the deposition temperature as compared to annealing the film to the same temperature, this is also a characteristic of spontelectric materials. A model was also built from the experimental data of N_2O. This model, built from the surface potential measurements, recreates the difference in the LO–TO splitting as the deposition temperature changes which fits the presented RAIRS data very well. Through the use of this model, the surface potential was also calculated from the RAIRS data to give about $5.7 \pm 0.3 \times 10^7$ V m^{-1} as compared to the measured $6.3 \pm 0.3 \times 10^7$ V m^{-1} from Aarhus University. Next, experiments involving CO on SiO_2, p–ASW, c–ASW and CSW were done to bring the spontelectric effect into the astrophysical domain. RAIRS data show that multilayers of CO behaves in a similar fashion as N_2O with respect to its LO–TO splitting and temperature dependence. Through the model built from the N_2O data, CO was shown to exhibit a surface potential with values as stated in **Table 6.3**.

Molecular film below CO	Surface potential / V m^{-1}
SiO_2	$3.72 \pm 0.15 \times 10^7$
p–ASW	$3.70 \pm 0.15 \times 10^7$
c–ASW	$1.99 \pm 0.15 \times 10^7$
CSW	$2.83 \pm 0.15 \times 10^7$

Table 6.3: This table shows the calculated values of the spontelectric effect of CO when deposited onto SiO_2, p–ASW, c–ASW and CSW.

Such a surface potential of CO has further been shown to create positive charges (a total of 5.75 on average with 12 ML) on an interstellar dust grain in dark molecular clouds. These charges build up as the CO layers accrete on the surface and acts in a way to attract electrons from the gas phase. As electrons are attracted so, in turn, will positive ions, thereby dragging charge out of the cloud environment.

To continue the study of spontelectrics with RAIRS will need to include working with methyl formate. As has been shown in **Chapter 5**, crystalline states of matter have more clearly defined IR features. Methyl formate crystallises at about 100 K and appears to have IR peaks splitting into two distinct features [20] which could be the LO–TO splitting. However, the spontelectric state of methyl formate is unstable at temperatures about 90 K as shown in **Figure 6.1** [21, 22].

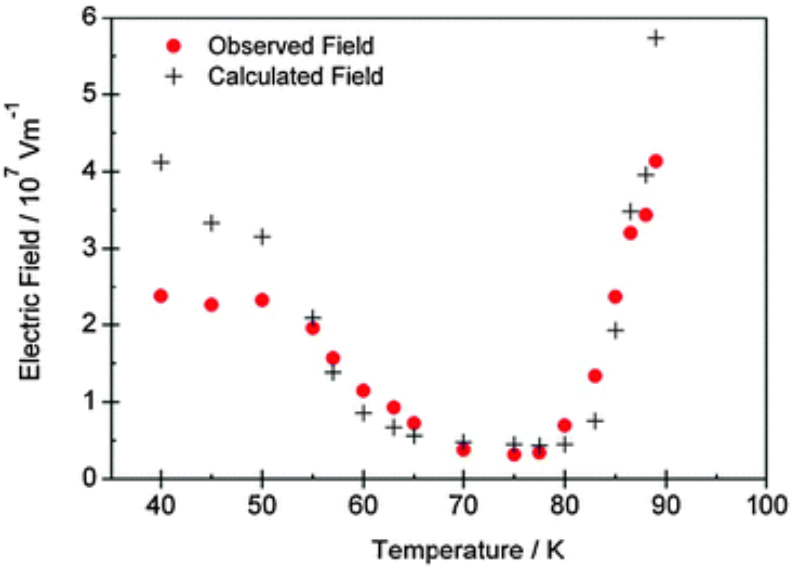

Figure 6.1: This figure shows the surface potential measurements of methyl formate as the temperature increases. As can be seen, methyl formate behaves as a typical spontelectric material initially before changing behaviour at about 70 – 80 K. Above this temperature the surface potential increases along with the temperature until the Curie point is reached at about 90 K [21, 22].

Figure 6.1 displays the behaviour of the surface potential as the deposition temperature is increased. Initially, the spontelectric effect decreases with increasing temperature as expected of a typical spontelectric material like N_2O. Then, an increase in the surface potential is observed until the field stops at the Curie point of about 90 K. If IR features are clean and defined enough, RAIRS spectra can possibly still be used to investigate the peculiar spontelectric behaviour of methyl formate in its amorphous state. Further to this, since methyl formate is no longer spontelectric at temperature above 100 K, the crystalline film will need to be investigated with respect to its LO–TO splitting. The reason for this is (as written in **Chapter 5**) that there should be no change in the splitting with temperature when the spontelectric effect is not present. The only cause for the splitting in methyl formate above 100 K should in theory be due to the intrinsic Berreman effect. This in itself would be a confirmation of using RAIRS to indirectly determine the spontelectric effect of dipolar molecules. A similar test would be to investigate a molecule without a permanent dipole moment which still exhibits an LO–TO splitting, such a molecule could be CO_2 [23]. The LO–TO splitting should behave in the same manner as crystalline methyl formate with respect to temperature.

Further work in the field of the spontelectric effect on the presented experimental equipment will involve the use of a Kelvin probe. As already mentioned, Bu *et al.* [24] have investigated p–ASW films and determined that a possible electric field is present. When fitted to the chamber initial test of the probe will be done by investigating a multilayer amount of N_2O and methyl formate. Hopefully, obtaining results similar to the ones reported from Aarhus University will lead to another way of directly investigating the spontelectric effect. Once this is done and assuming the Kelvin probe can be used as desired, tests of CO will be done to provide a more definite. Another method of indirectly investigating the spontelectric effect has been presented recently. Instead of using IR spectroscopy, vacuum ultraviolet (VUV) spectroscopy of CO films has shown similarities in UV band shifts with increasing temperature [25]. Future work in the area of VUV spectroscopy should therefore include studies of N_2O as shown in this thesis. If similar results are gathered for these VUV experiments, then spontelectric parameters could be presented and compared to the direct measurement of the surface potential and the indirectly determined values as obtained through RAIRS.

6.5 References

[1] H.M. Cuppen, S. Ioppolo, C. Romanzin and H. Linnartz, *Phys. Chem. Chem. Phys.*, 2010, **12**, 12077

[2] C.J. Bennett and R.I. Kaiser, *Astrophys. J.*, 2005, **635**, 1362

[3] D. Jing, J. He, J.R. Brucato, G. Vidali, L. Tozzetti and A. De Sio, *Astrophys J.*, 2012, **756**, 98

[4] J. He, D. Jing and G. Vidali, *Phys. Chem. Chem. Phys.*, 2014, **16**, 3493

[5] M.P. Collings, V.L. Frankland, J. Lasne, D. Marchione, A. Rosu–Finsen and M.R.S. McCoustra, *Mon. Not. Roy. Astron. Soc.*, 2015, **449**, 1826

[6] J. He, J. Shi, T. Hopkins, G. Vidali and M.J. Kaufman, *Astrophys. J.*, 2015, **801**, 120

[7] H.M. Cuppen and E. Herbst, *Astrophys. J.*, 2007, **668**, 294

[8] H. Mokrane, H. Chaabouni, M. Accolla, E. Congiu, F. Dulieu, M. Chehrouri, and J.L. Lemaire, *Astrophys. J.*, 2009, **705**, L195

[9] J.M.C. Rawlings, D.A. Williams, S. Viti, C. Cecchi–Pestellinni and W.W. Duley, *Mon. Not. Roy. Astron. Soc.*, 2013, **430**, 264

[10] C. Cecchi–Pestellini, J.M.C. Rawlings, S. Viti and D.A, Williams, *Astrophys. J.*, 2010, **725**, 1581

[11] C. Janssen, D. Simone and M. Guinet, *Rev. Sci. Instrum.*, 2011, **82**, 034102

[12] J.A. Noble, E. Congiu, F. Dulieu and H.J. Fraser, *Mon. Not. R. Astron. Soc.*, 2012, **421**, 768

[13] D. Hollenbach, M.J. Kaufman, E.A. Bergin and G.J. Melnick, *Astrophys. J.*, 2009, **690**, 1497

[14] R. Liseau, P.F. Goldsmith, B. Larsson, L. Pagani, P. Bergman, J. Le Bourlot, T.A. Bell, A.O. Benz, E.A. Bergin, P. Bjerkeli, J.H. Black, S. Bruderer, P. Caselli, E. Caux, J.–H. Chen, M. de Luca, P. Encrenaz, E. Falgarone, M. Gerin, J.R. Goicoechea, Aa. Hjalmarson, D.J. Hollenbach, K. Justtanont, M.J. Kaufman, F. Le Petit, D. Li, D.C. Lis, G.J. Melnick, Z. Nagy, A.O.H. Olofsson, G. Olofsson, E. Roueff, Aa. Sandqvist, R.L. Snell, F.F.S. van der Tak, E.F. van Dishoeck, C. Vastel, S. Viti and U.A. Yildiz, *Astron. Astrophys.*, 2012, **541**, A73

[15] E.F. van Dishoeck, E. Herbst and D.A. Neufeld, *Chem. Rev.*, 2013, **113**, 9043

[16] J.M. Guevremont, D.R. Strongin and M.A.A. Schoonen, *Am. Mineral.*, 1998, **83**, 1346

[17] A.S. Bolina, A.J. Wolff and W.A. Brown, *J. Phys. Chem.*, 2005, **109**, 16836

[18] M.J. Wojcik, V. Buch and J.P. Devlin, *J. Chem. Phys.*, 1993, **99**, 2332

[19] M.P. Collings, J.W. Dever, H.J. Fraser and M.R.S. McCoustra, *Astrophys. Space Sci.*, 2003, **285**, 633

[20] P. Modica and M.E. Palumbo, *Astron. Astrophys.*, 2010, **519**, A22

[21] D. Field, O. Plekan, A. Cassidy, R. Balog, N.C. Jones and J. Dunger, *Int. Rev. Phys. Chem.*, 2013, **32**, 345

[22] O. Plekan, A. Cassidy, R. Balog, N.C. Jones and D. Field, *Phys. Chem. Chem. Phys.*, 2012, **14**, 9972

[23] R.M. Escribano, G.M. Munoz Caro, G.A. Cruz–Diaz, Y. Rodriguez–Lazcano and B. Mate, *P. Natl. Acad. Sci. USA*, 2013, **110**, 12899

[24] C. Bu, J. Shi, U. Raut, E.H. Mitchell and R.A. Baragiola, *J. Chem. Phys.*, 2015, **142**, 134702

[25] G.C. Munoz Caro, Y.–J. Chen, S. Aparicio, A. Jimenez–Escobar, A. Rosu–Finsen, J. Lasne and M.R.S. McCoustra, *Astron. Astrophys.*, 2016, **589**, A19